A Multi-Phase Analysis of Gas Dynamics and Perturbations in the Galaxy Cluster Cores

by

Muzi Li

A thesis
presented to the University of Waterloo
in fulfillment of the
thesis requirement for the degree of
Doctor of Philosophy
in
Physics

Waterloo, Ontario, Canada, 2024

© Muzi Li 2024

Examining Committee Membership

The following served on the Examining Committee for this thesis. The decision of the Examining Committee is by majority vote.

External Examiner:	Brian W.O'Shea Professor, Dept.of Computational Mathematics, Science, and Engineering, Department of Physics and Astronomy, Facility for Rare Isotope Beams, Michigan State University
Supervisor(s):	Brian McNamara Professor, Dept. of Physics and Astronomy, University of Waterloo
Internal Member:	Will Percival Professor, Dept. of Physics and Astronomy, University of Waterloo
Internal Member:	Niayesh Afshordi Professor, Dept. of Physics and Astronomy, University of Waterloo
Internal-External Member:	Pierre-Nicholas Roy Professor, Dept. of Chemistry, University of Waterloo

Author's Declaration

This thesis consists of material all of which I authored or co-authored: see Statement of Contributions included in the thesis. This is a true copy of the thesis, including any required final revisions, as accepted by my examiners.

I understand that my thesis may be made electronically available to the public.

Statement of Contributions

This dissertation presents original research conducted by myself, Muzi Li, under the supervision of Prof. Brian McNamara, detailed in Chapters 2 and 3.

Chapter 2: 'X-ray Surface Brightness Fluctuations in Smooth Galaxy Cluster Atmospheres' Authors: Muzi Li, Brian McNamara, Irina Zhuravleva. This research is accepted by the Monthly Notices of the Royal Astronomical Society, Volume 537, Issue 2, pages 2198-2213, DOI:10.1093/mnras/staf134. I independently conducted the data reduction of Chandra X-ray observations, analyzed surface brightness fluctuations, and drafted the manuscript under Prof. McNamara's guidance. Irina Zhuravleva provided expert technical assistance and critical insights into error analysis and result interpretation, enhancing the research quality.

Chapter 3: 'Velocity Structure Correlations between the Nebular, Molecular, and Atmospheric Gases in the Cores of Four Cool Core Clusters' Authors: Muzi Li, B.R. McNamara, Alison L. Coil, Marie-Joëlle Gingras, Fabrizio Brighenti, H.R. Russell, Prathamesh D. Tamhane, S. Peng Oh, and Serena Perrotta. This paper, submitted to the Astrophysical Journal (ApJ), is under the second review. My role encompassed X-ray data reduction, multi-wavelength data analysis, and manuscript writing under the supervision of B.R. McNamara and Alison L. Coil. Marie-Joëlle Gingras and H.R. Russell provided the velocity maps of KCWI [OII] emission and ALMA CO emission, respectively. Other co-authors participated in discussions about interpreting the results and provided valuable insights that enriched the study.

In Chapter 4, I summarize my involvement in the XRISM optical blocking filter calibration and the data analysis of seven flight and flight spare filters conducted between 2019 and 2020. During this period, I participated in two on-ground synchrotron calibrations. From April to October 2019, Conor Martz and I, under the guidance of other team members, completed the modeling of parameters for these seven filters. The subsequent data analysis tasks were undertaken independently by me. This work was compiled based on calibration logs and meeting notes, with more detailed descriptions of these activities presented in the chapter's abstract.

The calibration efforts were concluded at the end of 2020, and the outcomes were summarized in the publication: 'Status of X-Ray Imaging and Spectroscopy Mission (XRISM)', 2020, in Space Telescopes and Instrumentation 2020: Ultraviolet to Gamma Ray, volume 11444, pages: 22, DOI: 10.1117/12.2565812.

Abstract

This thesis provides a detailed analysis of gas kinematics and their interactions across various phases within galaxy cluster cores. It examines the processes that generate gas perturbations and the factors that contribute to the thermal stability of the intracluster medium (ICM). A focus is placed on exploring the origins of multi-phase gas and the mechanisms—particularly AGN feedback—that either couple or decouple their motions.

Radio-mechanical AGN feedback is identified as one of the most promising heating mechanisms that prevent the cooling of gas. However, the debate on the details of the heating transport processes has remained open. The atmospheres of 5 cool-core clusters, Abell 2029, Abell 2107, Abell 2151, RBS0533 and RBS0540, have short central cooling times but little evidence of cold gas, and jet-inflated bubbles. The amplitudes of gas density fluctuations were measured using a new statistical analysis of X-ray surface brightness fluctuations within the cool cores of these 'spoil' clusters in Chapter 2. The derived velocities of gas motions, typically around 100 - 200 km s^{-1}, are comparable to those in atmospheres around central galaxies experiencing energetic feedback, such as in the Perseus Cluster, and align well with the turbulent velocities expected in the ICM. Regardless of the mechanisms driving these perturbations, turbulent heating appears sufficient to counteract radiative losses in four of the five spoiler cluster cores. We thus suggest that other mechanisms, such as gas sloshing, may be responsible for generating turbulence, offering a plausible solution to suppress cooling in these structureless atmospheres.

Multiphase filaments, key byproducts of AGN feedback, are frequently observed near central galaxies, with their morphologies and kinematics closely linked to bubbles. In Chapter 3, we analyzed the velocity structure functions (VSFs) of warm ionized gas and cold molecular gas, identified through [OII] emission and CO emissions observed by the Keck Cosmic Web Imager (KCWI) and the Atacama Large Millimeter/submillimeter Array (ALMA), respectively, in four clusters: Abell 1835, PKS 0745-191, Abell 262, and RXJ0820.9+0752. Excluding Abell 262, where gas forms a circumnuclear disk, the remaining clusters exhibit VSFs steeper than the Kolmogorov slope. The VSFs of CO and [OII] in RXJ0820 and Abell 262 show close alignment, whereas in PKS 0745 and Abell 1835, were differentiated across most scales, likely due to the churning caused by the radio-AGN. The large-scale consistency in Abell 1835 and RXJ0820, together with scale-dependent velocity amplitudes of the hot atmospheres obtained from Chandra X-ray data, may support the idea of cold gas condensation from the hot atmospheres.

X-ray observations have previously been constrained by low energy resolution, which has impeded direct measurements of velocity fields in galaxy clusters. However, the recent

release of initial data from the X-ray Imaging and Spectroscopy Mission (XRISM) provides a non-dispersive energy resolution of about 5 eV, facilitating the measurement of line broadening and shifts. In Chapter 4 of this thesis, I detail my contributions to calibrating the optical blocking filters for XRISM using synchrotron beamlines at the Canadian Light Source (CLS) and Advanced Light Source (ALS) prior to its launch, and I discuss the model-based estimation of the parameters of the calibrated filters. This capability for direct measurement of plasma velocities is expected to greatly improve our understanding of the ICM dynamics with high accuracy.

Acknowledgments

I would like to express my deepest gratitude to my advisor, Prof. Brian McNamara, for providing me with the opportunity to thrive under his guidance. His patience, continuous encouragement, and extensive knowledge have not only guided me through my academic journey but have also profoundly inspired me. I am thankful to my committee members, Prof. Mike Hudson, Prof. P. N. Roy and Prof. Will Percival, for their invaluable advice and dedication over the years. I thank Prof. Niayesh Afshordi and Prof. Brian W. O'Shea, whose involvements mark a significant milestone in my academic career. I am grateful to my collaborators, Irina Zhuravleva, Alison Coil and Helen Russell, for their efforts and insights that have greatly enriched my work. Lastly, I cherish the time spent working with my colleagues from the XRISM filter calibration team, whose camaraderie made our collaboration a truly enjoyable experience. I am also profoundly thankful to my master's advisor, Prof. Zonghong Zhu, whose support enabled me to pursue and achieve my dreams.

My time at the University of Waterloo has been incredibly enriching and memorable, filled with the companionship of friends who have made this journey unforgettable. I am profoundly grateful to my colleagues and dear friends, Prathamesh, Connor, Marie-Joelle, Neo, and Julian, for their valuable advice and the enjoyable moments spent brainstorming and learning together. Special thanks to Iurii for his guidance during the initial stages of my project, and to Tom for his assistance in analyzing ALMA data and providing insightful feedback on my research findings. I also extend my heartfelt thanks to Chegnyu, Tianyi, Nancy, Zhiwei, Rufus, Zhenwei, Chenxi, Zeren, Mengqi, Xiaomeng, Bowen, Rui, and Kiro. Your shared moments of joy, support during stressful times, encouragement through tough periods, and companionship in growth have been invaluable to me.

Though far from home, the care and support from dear friends back in my homeland have given me comfort and courage. I am especially grateful to my good friends Yue-fan, YeYan, and Bianbian, whose warmth has ensured that I never felt alone, even when far away. Their constant encouragement and thoughtfulness have been a beacon of light throughout my academic and personal adventures here.

Above all, I am most grateful to my parents, who taught me the virtues of integrity and kindness, and the importance of tolerance and understanding toward others as well as myself. No matter my circumstances or the choices I make, they have supported me with unwavering love and companionship. I am deeply thankful to Huan, my partner, my best friend, and my role model. I fondly remember my grandparents and am grateful for their nurturing. Muzi will always strive to make you proud and honor the upbringing you have given me.

Dedication

Dedicated to the important people in my life, my father, mother, and Huan, who have supported me throughout my PhD journey.

Table of Contents

Examining Committee ii

Author's Declaration iii

Statement of Contributions iv

Abstract v

Acknowledgments vii

Dedication viii

List of Figures xiii

List of Tables xxiii

1 Introduction 1

1.1 X-ray Emission from Hot Intracluster Medium 2

1.2 Cooling Flow Problem 5

1.3 AGN Feedback Mechanism 6

1.3.1 Radiative Mode 8

1.3.2 Radio Mechanical Mode 10

1.3.3 Heating Mechanisms of AGN Outbursts 12

1.4 Residual Cooling and Multi-wavelength Observations 15
1.4.1 Thermal Instability 15
1.4.2 Stimulated Cooling by Uplift 18
1.4.3 Multi-phase Gas in Cluster Cores 19
1.5 Gas Motions in ICM 21
1.5.1 Basic Turbulence 21
1.5.2 Velocity Spectrum and Density Fluctuations 23
1.5.3 Velocity Structure Function 25
1.6 This Thesis 28

2 X-ray Surface Brightness Fluctuations in Smooth Galaxy Cluster Atmospheres 30
2.1 Introduction 31
2.2 Smooth Atmosphere Clusters and X-ray Images 34
2.2.1 Sample Selection 34
2.2.2 Data Reduction 36
2.3 Surface Brightness Fluctuation Analysis 43
2.4 Results 48
2.4.1 Density Fluctuations in the Smooth Atmosphere Clusters 48
2.4.2 Velocity Power Spectrum 51
2.4.3 Turbulent Heating 53
2.5 Discussion 57
2.5.1 The Gas Perturbation Sources in Smooth Atmosphere Clusters . . . 57
2.5.2 Shape of Velocity Spectra & Mass Dependence 60
2.6 Conclusions 62

3 Velocity Structure Correlations between the Nebular, Molecular, and Atmospheric Gases in the Cores of Four Cool Core Clusters 63

3.1 Introduction . . . 64

3.2 Cluster Sample and Observational Data . . . 67

3.2.1 Cool Cluster Sample . . . 67

3.2.2 KCWI Data Reduction . . . 67

3.2.3 ALMA Observations . . . 70

3.2.4 Chandra X-ray Observations . . . 72

3.3 Results . . . 72

3.3.1 Velocity Structure Function . . . 74

3.3.2 VSF of Warm Ionized Gas . . . 75

3.3.3 VSF of the Two Velocity Components in Abell 1835 and PKS 0745-191 83

3.3.4 Molecular Gas Distribution and Kinematics . . . 86

3.3.5 Velocity Spectra of Hot ICM . . . 88

3.4 Discussion . . . 94

3.4.1 The VSF Slope and Steepening at Small Scales . . . 94

3.4.2 Projection Effects . . . 95

3.5 Conclusions . . . 97

Appendix A3: Extra Information for Chapter 3 . . . 98

A3.1.1 Window Effect on the VSF . . . 98

A3.1.2 Image Smoothing Effect on VSF . . . 99

A3.1.3 Chandra X-ray Images of KCWI Targets . . . 105

4 Calibration of XRISM Optical Blocking Filters 108

4.1 Introduction . . . 109

4.1.1 Hitomi: Predecessor of XRISM . . . 109

4.1.2 XRISM: Advancing the Legacy . . . 111

4.2 Fundamentals of Soft X-ray . . . 112

4.2.1 X-ray Absorption Fine Structure . . . 112
4.2.2 Synchrotron Radiation Facilities for X-ray Optics Calibration . . . 113
4.3 Optical Blocking Filter Calibration . . . 116
4.3.1 Optical Blocking Filter . . . 116
4.3.2 Calibration Strategy . . . 118
4.4 Model Filter Parameters . . . 124
4.5 Summary . . . 130

5 Conclusion **134**
5.1 Summary . . . 134
5.2 Future Work . . . 137

References **138**

APPENDICES **160**

A Gas perturbations in Abell 2146 **161**
A.1 Data Reduction . . . 162
A.2 Results . . . 164
A.3 Conclusion . . . 167

List of Figures

1.1 X-ray spectra with Solar abundance and at plasma temperatures 10^7 K (left) and 10^8 K (right). The spectra feature continuum contributions from bremsstrahlung (blue), recombination radiation with distinct ionization edges (green), and 2-photon radiation (red) (Boehringer et al., 1993). 4

1.2 Left: The 2 Ms background-subtracted, exposure-corrected Chandra X-ray image of Cygnus A in 0.5 - 7 keV. Right: The composite image of the Hydra A galaxy cluster. The optical starlight from cluster galaxies (in yellow), and the radio emissions from jets (in pink) originating from the central supermassive black hole, are superimposed on the X-ray emissions (in blue) from the hot ICM. Credited by: X-ray: NASA/CXC/U.Waterloo/C.Kirkpatrick et al.; Radio: NSF/NRAO/VLA; Optical: Canada-France-Hawaii-Telescope/DSS 11

1.3 Total mechanical power P_{cav} measured by cavities versus the X-ray luminosity L_{cool} within the cooling regions. Data for galaxy clusters are color-coded by their redshifts. Galaxy groups and more isolated systems are represented by grey stars, all located at $z < 0.3$. Dashed black lines indicate P_{cav} matches L_{cool} with $E_{cav} = PV,\ 4PV,\ 16PV$ from top to bottom. (Credit: Figure 4 in Hlavacek-Larrondo et al. (2022). The data are from Nulsen et al. (2009); Rafferty et al. (2006); Dunn & Fabian (2008); Hlavacek-Larrondo et al. (2012, 2015); Pandge et al. (2013, 2019, 2021); Sonkamble et al. (2015); Vagshette et al. (2017, 2019); Kadam et al. (2019); McDonald et al. (2019); Liu et al. (2020); Prasow-Émond et al. (2020); Kyadampure et al. (2021). 13

1.4 Left: Cooling time against Hα luminosity (Hogan et al., 2017). Clusters with BCGs that exhibit Hα emission are marked with black circles, while those without such emission are represented by red arrows, indicating the upper limits of emission. Right: Core entropy against Hα luminosity (Voit & Donahue, 2015). Clusters with detection are shown as blue solid circles and the upper limits of Hα emission in those without are shown as red arrows. The vertical blue dashed lines indicate the t_{cool} =1 Gyr and 30 keV cm^2 threshold, respectively. 16

1.5 Left: Comparison of velocity power spectra derived from Chandra X-ray images with direct Hitomi velocity measurements in the core of the Perseus cluster. Red and gray hatched regions represent the total velocity and velocity dispersion observed by Hitomi, respectively. The velocity amplitudes are estimated within the central 30 - 60 kpc from X-ray SB fluctuation analysis. Right: Comparison of the Velocity Structure Functions (VSF) of nebular gas traced by Hα emission (inner core: red points; outer core: green points; entire cluster: blue points), Chandra X-ray velocity analysis (purple area), and Hitomi observations (region 0: red area; region 3: green area). This Figure is adapted from Figure 4 in Li et al. (2020) 26

2.1 The background-subtracted, exposure-corrected Chandra images of our targets in the $0.5-3.5$ keV band. The cool-core radius is indicated with dashed green circles, and the inner half of the cool-core radius is marked in the green solid line. The bright point sources and the central AGNs have been masked out. The images are smoothed with a 3" Gaussian for display purposes. 37

2.2 Left: Background-subtracted, exposure-corrected mosaic Chandra images of the Perseus cluster in the $0.5-4$ keV band. The dashed green circle indicates the inner region within half cool core radius, denoted as $0 < r < r_{cool}/2$. Each image is smoothed with a 3" Gaussian for display purposes. Right: Residual X-ray image of the Perseus cluster, obtained by dividing the initial image by the best-fitting spherically symmetric β-model. The bright point sources and the central AGNs have been masked out. 38

2.3 Deprojected thermodynamic radial profiles in the $0.5-7$ keV band of sample clusters: (a) cooling timescale, (b) entropy, (c) electron temperature, (d) electron density, and (e) sound speed. The dashed vertical lines in (a) and (b) indicate a radius of 10 kpc, and the dashed horizontal lines represent the threshold values $t_{cool} = 1.0\times10^9$ yr and entropy $K = 30$ keV cm^2, respectively. 40

2.4 Power spectra of surface brightness fluctuations in the cool core of Abell 2029 derived using two different β-models. The global SB gradient has been removed by dividing the raw image with an elliptical single-β model, marked in blue points, and a double-β model, presented in green points. The horizontal dashed lines with error bars represent the Poisson noise levels, which were subtracted from the raw spectra to obtain the corrected power spectra of SB fluctuations, depicted by the shaded areas. The mean PSF spectrum, calculated from 20 simulated PSF images within the cool core of Abell 2029, is shown as a red dashed line. 42

2.5 The residual images of smooth atmosphere clusters in the 0.5 - 3.5 keV band. The underlying surface brightness gradients are removed by dividing raw images by the best-fitting $\beta-$models, summarized in Table 2.2. The cool-core radius is indicated with dashed green circles, and the inner half of the cool-core radius is marked in the green solid line. The residual images are processed with a 3" Gaussian smoothing for display purposes. The bright point sources and the central AGNs have been masked out. 44

2.6 The simulated map of the combined Chandra PSF within the mosaic image of Abell 2029. The red solid circle indicates the position of the optical axis, while the dashed green circle represents the region of interest in our analysis. 46

2.7 Gas density Fluctuation amplitudes of our five sample clusters and the Perseus Cluster. The measurements were conducted within the cool-core radius of (a) Abell 2029, (b) RBS0540, and within the inner half of the cool-core radius of (c) RBS0533, (d) Abell 2151, (e) Abell 2107, and (f) the Perseus Cluster. The central dashed lines present the mean spectra, while the widths of the shaded regions reflect the 1σ uncertainties. Displayed are measurements taken over scales that are minimally impacted by Poisson noise and PSF effect ¡ 20%. The results below the scale of 15 kpc for Abell 2107 and 20 kpc for Abell 2151, marked with hatched areas, maybe more significantly affected by PSF effects.The grey dash-dotted lines represent slopes of $k^{-1/3}$ or $k^{-1/2}$ as guidelines. 50

2.8 Amplitudes of one-component velocity with respect to wavenumber k within the cool-cores in (a) Abell 2029, (b) RBS0540, and within the inner half cool-core regions of (c) RBS0533, (d) Abell 2151, (e) Abell 2107, and (f) Perseus cluster. Velocities derived from the average sound speed in the ICM are shown as the central dashed lines. The velocity estimation below the scale of 15 kpc in Abell 2107 and 20 kpc in Abell 2151, marked with hatched areas, might be more significantly affected by PSF effects. The grey dash-dotted lines represent slopes of $k^{-1/3}$ or $k^{-1/2}$ for guidance. 54

2.9 Turbulent heating versus radiative cooling rates within the cool-core radius of Abell 2029 and RBS0540, and within the inner half cool-cores of RBS0533, Abell 2151, Abell 2107, and Perseus. For Abell 2029, the comparison is presented separately for the inner (blue) and outer (red) cool-core regions. The central points represent the Q_{cool} and Q_{turb} obtained using volume-weighted temperatures and densities. The error bars indicate 1σ uncertainties in heating rate, variations in density and temperature within the regions of interest, and deviations from the Kolmogorov spectral slope of $k^{-1/3}$. The dashed line illustrates the equilibrium where radiative cooling is balanced by turbulent heating. 56

2.10 M_{2500} versus one-component velocity $V_{1,k}$ of smooth-core clusters and Perseus cluster. The markers present the mean velocity amplitudes over the range of scales probed in each target. 61

3.1 The median velocity v_{50} maps of the [OII] emission line doublet with respect to the stellar velocity of the system. The central galaxy nucleus is designated as the reference point for each map's origin. Positive velocities indicate redshift, while negative velocities denote blueshift relative to the stellar velocity. The black solid lines indicate the integrated flux contours for 10%, 20%, 40%, and 80% of the maximum CO (3-2) emission in Abell 1835 and PKS 0745, CO (2-1) emission in Abell 262, and CO (1-0) emission in RXJ0820. Areas within the black dashed lines highlight regions where CO emissions are detected by ALMA. The dashed magenta ellipses show the positions of the X-ray cavities. 69

3.2 Velocity maps of molecular gas in the central regions of four galaxy clusters from our sample, derived from ALMA observations. The maps show CO (3-2) emission for Abell 1835 and PKS 0745, CO (2-1) emission for Abell 262, and CO (1-0) emission for RXJ0820, all detected at a signal-to-noise ratio greater than 3σ. Map origins align with the nucleus positions defined in the KCWI [OII] maps (presented in Figure 3.1). Red hatched ellipses represent the synthesized beam size and dashed magenta ellipses indicate the locations of X-ray cavities. 73

3.3 Middle: VSF analysis of warm ionized gas, traced by KCWI [OII] emission, within the core of Abell 1835. Only scales larger than seeing, and where pairs exceed 20% of the peak value, are plotted. Side panels: Distribution of velocity differences $|\delta v|$ among pixel pairs at four scales, marked as red stars in the VSF plot. The number of pairs in each $|\delta v|$ group is normalized by the total number of pairs for the entire separation bin to facilitate a comparative analysis of distribution shapes across varying scales. The best-fit log-normal profile is displayed as a solid red line over the $|\delta v|$ distribution. The vertical red dashed line represents the mean of the log-normal distribution, while the blue line shows the mean $|\delta v|$ of all pixel pairs within the given bin. . . 75

3.4 Middle: Similar to Figure 3.3, the middle panel displays the VSF for the nebular gas within the core of Abell 262. Side panels: the distributions of $|\delta v|$ within four separation bins. 78

3.5 Left panel: Continuum-subtracted [OII] flux maps with S/N $\geq$ 5 in Abell 262. Middle panel: [OII] emission velocity dispersion map. The magenta line outlines the region where ALMA CO (2-1) emission is detected. Right panel: VSFs of nebular gas with different [OII] brightness levels in Abell 262. The red points show the VSF of nebular gas within the central region where ALMA CO emission is observed. The VSF results for the top 25% brightest [OII] pixels are shown with black squares, while those for the top 50% brightest [OII] regions are indicated by green squares. 79

3.6 Middle: Similar to Figure 3.3, the middle panel displays the VSF for the nebular gas within the core of RXJ0820.9+0752. Side panels: the distributions of $|\delta v|$ within four separation bins. 81

3.7 Middle: Similar to Figure 3.3, the middle panel displays the VSF for the nebular gas within the core of PKS 0745-191. Side panels: the distributions of $|\delta v|$ within four separation bins. 82

3.8 Velocity maps and VSFs of the first Gaussian component and the second Gaussian component derived from KCWI [OII] emissions in the core of Abell 1835 (top row) and PKS 0745 (bottom row). The maps include only spaxels where emission lines can be accurately fitted by two kinematic components with a S/N $\geq$ 3. In the right panels, the VSFs for the 1st and 2nd components are represented by green and red points, respectively. 84

3.9 Comparison of the VSFs of cold molecular gas and warm ionized gas in our sample clusters, traced by ALMA CO emission and Keck [OII] line emission, respectively. The VSFs of the single component v50 (yellow points), the 1st (green dashed line) and the 2nd (red dashed line) velocity component from the Keck observations are computed within the regions covered by ALMA CO emission. For each cluster, the ALMA velocity map is smoothed with a box kernel to match the ALMA observation beam size with the KCWI seeing, and the smoothed CO emission VSF is shown as blue points. Only scales exceeding the ALMA observation beam size and KCWI seeing limits, and having a sufficient number of pixel pairs for reliable VSF calculation, are displayed here. Reference lines with slopes of 1/1, and 1/2 are also included. 89

3.10 Comparison between the VSFs of warm ionized gas traced by Keck [OII] line emission and the Chandra X-ray surface brightness fluctuation analysis in the cool cores of Abell 1835, RXJ0820.9+0752, PKS 0745-191. The VSFs of warm ionized gas are presented as the red points. Only scales exceeding the seeing limits, and with a sufficient number of pixel pairs for reliable VSF calculation, are displayed here. The power spectra of hot ICM motions are computed within the regions covered by KCWI [OII] emission, and are depicted by the blue points. The hatched regions reflect 1σ uncertainty. Only scales are least affected by systematic uncertainties and Poisson noise are shown. The X-ray results are summarized in Table 3.6 93

A3.1 Window effect on VSFs. The top panels present a Gaussian random field with a power spectrum of $\alpha = 1/2$, with dimensions of 150×150 pixels. The boxes shown on the plot indicate the sub-regions used to examine the effects of finite size. The orange box has a width of 50 pixels, while the green box has a width of 100 pixels. The VSFs calculated from the simulated map and the sub-regions are displayed in the bottom panels. The blue line represents the VSF calculated from the entire image. The VSFs of the inner 50-pixel box and 100-pixel box are indicated by the orange and green lines, respectively. The three vertical lines indicate the half-width of the corresponding windows used for analysis. The grey dash-dotted line represents the expected VSF slope of 1/2 for reference. 100

A3.2 Smoothing effect on VSFs: Top: A Gaussian field with a power spectrum characterized by an underlying power of 1/2. To investigate the effect of image smoothing on VSF, the original image (left) is subjected to Gaussian kernel smoothing with a kernel size of 5 pixels (middle) and a kernel size of 15 pixels (right). Bottom left: The corresponding VSFs are calculated from simulated Gaussian fields. The red curve represents the unsmoothed image, displaying a slope close to 1/2. The green and blue curves correspond to images smoothed with Gaussian kernels of 5-pixel and 15-pixel widths, respectively, revealing a progressive amplitude suppression, particularly on smaller scales. Bottom right: Exploring the impact of various smoothing levels on resulting VSFs. The green line and blue line illustrate the mean ratio of 50 VSFs of the unsmoothed images to those of the images blurred by a 5-pixel width Gaussian kernel and to those of the images blurred by a 15-pixel width Gaussian kernel, respectively. 101

A3.3 Velocity maps of cold molecular gas in PKS 0745 traced by ALMA CO (3-2) emission. The left panel displays the unsmoothed version of the velocity map. In the middle panel, the map is subjected to median smoothing, with a smaller beam size of 0.19". The right panel presents a velocity map that has undergone significant smoothing, with a beam size of 0.57". 102

A3.4 The VSFs are derived from different CO(3-2) velocity maps of PKS 0745 shown in Figure A3.3. The red line corresponds to the VSF of the unsmoothed PKS 0745 velocity map, while the green line and the blue line present the results of the moderately smoothed image (middle) and the heavily smoothed image (right), respectively. 102

A3.5 The smoothing effects of Gaussian and box kernel on the VSF. The VSF of the unsmoothed 50×50 pixel simulated field is presented as red crosses. It recovers the underlying slope of 12 over scales smaller than the half-width of the image, indicated by the vertical dashed line. The green and blue dashed lines show the VSF of the simulation smoothed with Gaussian kernels of $\sigma = 3$ pixels and $\sigma = 5$ pixels, respectively. The VSFs of the simulation smoothed with box kernels of widths $3\sigma + 1$ pixels are depicted as green and blue squares. The comparison demonstrates that Gaussian blurring and box blurring have analogous effects on the resultant VSFs, namely, steepening the slopes and suppressing the amplitudes. 103

A3.6 Background-subtracted, exposure-corrected mosaic Chandra images of the core of Abell 262 in the $0.5-3.5$ keV band. The dashed green circle indicates the region of interest, where [OII] emission is detected by KCWI. The image is smoothed with a 3" Gaussian for display purposes. 105

A3.7 Similar to Figure A3.6. X-ray Chandra image of the core of Abell 1835 cluster in $0.5 - 3.5$ keV. 106

A3.8 Similar to Figure A3.6. X-ray Chandra image of the core of PKS 0745-191 cluster in $0.5 - 3.5$ keV. 106

A3.9 Similar to Figure A3.6. X-ray Chandra image of the core of RXJ0820.9+0752 cluster in $0.5 - 3.5$ keV. 107

4.1 Diagram of instrument locations on Hitomi (Left) and XRISM (Right). (Image credit: JAXA/ISAS) 110

4.2 General layout of a synchrotron facility, showing the linear accelerator (LINAC), booster synchrotron, storage ring, and beamlines. Schematics is based on ALS, adapted from the ALS QuickFacts Sheet (2019). 114

4.3 The Schematic showing the arrangement of ApA and BFs on XRISM Resolve. The image is adapted from in Leutenegger (2019). 116

4.4 Left: Photograph of the OVCS flight carrier from the back, showing the coarse and fine silicon-mesh cells. Middle & Right: Dimensions of the coarse mesh cell and fine mesh cell, respectively. The images are adapted from Kilbourne et al. (2018). 117

4.5 Microscopic image of the back side of an optical blocking filter showing the non-uniform epoxy excess, which accounts for variance in X-ray transmission measurements. The image is accepted from Eckart et al. (2018). 118

4.6 The spatial uniformity maps of OVCS7 and IVCS2 at 1700 eV. The grey crosses mark the positions for the '5×5' mesh scan within each coarse mesh. The broadband transmission scans are conducted in two cells for each filter, whose locations are also highlighted. 120

4.7 Top panels: Broadband transmission curves measured in two cells for (a) OVCS7, (b) OVCS2, and (c) OVCS-S5. Bottom panels: Fractional differences in transmission between the two cells. 122

4.8 Similar to Figure 4.7. Spectral scans for IVCS filters: (a) IVCS6, (b) IVCS-G2, and (c) IVCS8. 123

4.9 Similar to Figure 4.7. Spectral scans for DMS-G1. 124

4.10 Mesh scans of the OVCS7 filter at 260 eV and 1700 eV, displaying transmission measurements within two coarse meshes labeled C3 and E2. Each position is indicated by a 5×5 grey-cross array as marked in Figure 2. The values at the bottom, calculated as $(T/T_{avg} - 1) \times 100\%$, represent the deviation from the average transmission. 125

4.11 Similar to Figure 4.10.Mesh scans of the IVCS2 filter at 260 eV and 1700 eV within cell C4 and cell D2. 126

4.12 Mass absorption coefficients as a function of energy. Left: Aluminum and Oxygen. Right: Polyimide $C_{22}H_{10}N_2O_4$ and the absorption coefficients of its constituent elements. The data is taken from CXRO (2023) 127

4.13 Top: Broadband transmission measurements (black points) and the best-fit transmission model (red dashed line) for cell C4 (left) and cell D3 (right) of the OVCS5 filter. Bottom: Residuals between the measured data and the best-fit transmission model. 130

4.14 Top: Measured and modeled transmission for cells E4 (left) and F5 (right) in the DMS-G1 filter. Bottom: Residuals between the data and model. . . 131

4.15 Top: Measured and modeled transmission for cells C4 (left) and D2 (right) in the IVCS2 filter. Bottom: Residuals between the data and model. 131

4.16 Left: Full transmission curve of the complete stack of five optical blocking filters for XRISM Resolve, spanning a broad energy range. Right: Zoomed-in view of the red-highlighted 150 – 2000 eV band, illustrating transmission features near the K-edges of key elements, including C, N, O, Al, and Si. . 132

A.1 Background-subtracted exposure-corrected Chandra image of Abell 2146 in $0.5-4$ keV. The background has been estimated and subtracted with the flux of the on-chip blank region (green dashed region). The magenta regions show the bow shock and upstream shock we analyzed in this work. The image is smoothed by 3" for display. The bright point sources and central AGN are masked out. 163

A.2 The surface brightness profiles extracted from a $225-260°$ sector across the bow shock (left) and a $55-80°$ sector across the upstream shock (right) in the $0.5-4$ keV band. The dashed red lines indicate the surface brightness profiles measured by Russell et al. (2022). The vertical green bands represent the location and width of each shock front, measured to be 17 ± 1 kpc for the bow shock and 10.7 ± 0.3 kpc for the upstream shock. 164

A.3 The amplitudes of density fluctuations near the bow shock (left) and the upstream shock (right) in Abell 2146. The dotted line is the average amplitude of density fluctuations at each spatial scale. The width of regions shows 1σ uncertainties. Only scales on which the amplitudes are least affected by Poisson noise are shown here. 165

A.4 The amplitude of one-component velocity of gas motions versus wavenumber at the bow shock (left) and the upstream shock (right). The red dashed line presents the velocities calculated from the mean density fluctuations and the mean temperature across the shocks. The solid blue regions represented velocity amplitudes when maximum and minimum temperatures were used. Black Dashed lines show the Kolmogorov slope $-1/3$. The green hatched region shows the turbulent velocity derived from the shock widths, which are 355^{+25}_{13} km s^{-1} and 290^{+30}_{-30} km s^{-1} at bow shock and at the upstream shock, respectively. 166

List of Tables

2.1 Clusters and Chandra observations in our analysis: (a). Cluster name, (b). Observations used in this analysis, (c). Redshift, (d). Right Ascension (J2000), (e). Declination (J2000), (f). Cleaned exposure after data reduction, (g). Column density, and (h) Cool-core radius. 35

2.2 The best-fitting β-model parameters of the underlying surface brightness profiles of our targets: (a). Cluster name, (b-d). Central surface brightness, Core radius, and β of the first component, (e-g). Central surface brightness, Core radius, and β of the second component, (h). The orientation angle of the observed ellipse, and (i). Eccentricity, defined as the ratio of the major to the minor axis as projected. 43

2.3 The density fluctuation amplitudes measured within the cooling regions of our sample clusters and within the inner half cool core region of Perseus: (a). Cluster name, (b). Region of interest, (c). Spatial scales least affected by Poisson noise, (d). Amplitudes of gas density fluctuations. 49

2.4 One-component velocity amplitudes of gas motion measured indirectly in the cooling regions of our targets and Perseus using SB fluctuation analysis: (a). Cluster name, (b). Cluster mass M_{2500}, (c). The region of interest, (d). Volume-weighted mean temperature in the region of interest, (e). Scales probed, (f). One-component velocity, (g). Turbulent heating rate is calculated when volume-weighted mean temperatures and densities are used, (h). Radiative cooling rate. 52

3.1 Targets details: (1). Cluster name. (2). Right ascension (RA). (3). Declination (Dec). (4). Redshift (5) Major axis of X-ray cavity. (6). Minor axis of X-ray cavity. (7). Distance from cavity center to the core. (8). Molecular gas mass. References: (5)-(7): Abell 1835: McNamara et al. (2006); Olivares et al. (2019), Abell 262: Rafferty et al. (2006); Clarke et al. (2009), RXJ0820.9+0752: Vantyghem et al. (2019), PKS 0745-191: Sanders et al. (2014). 70

3.2 The observations used in this analysis: (1). Cluster name. **KCWI observations**: (2). Seeing. (3). Field of View. (4). [OII] emission extent. **ALMA observations**: (5). CO emission line used for fitting. (6). The synthesized beam size. (7). CO emission extent. **Chandra observations**: (8). Chandra ObsIDs used in this work. (9). Cleaned exposure time. . . . 71

3.3 VSF of KCWI [OII] emission line: (1). Target. (2). Scales can be probed reliably. (3). Turnover scales shown in VSFs. (4). Scales at which the VSF slope is fitted. (5). Best-fitting slope of VSF. 77

3.4 The VSFs of the first and the second Gaussian velocity component in the Abell 1835 and PKS 0745-191, traced by Keck [OII] emission: (1). Target. (2). Component. (3). Scales can be probed reliably. (4). Turnover scales shown in VSFs. (5). Scales at which the VSF slope is fitted. (6). Best-fitting slope of VSF. 85

3.5 Comparison between the VSFs of cold molecular gas and warm ionized gas: (1). Target. (2) - (5). VSFs of CO emission: scales can be measured, measured VSF, scales for slope fitting, best-fit slope. (6) - (9). VSFs of smoothed CO emission. (10) - (13). VSFs of [OII] emission in CO detected region. 90

3.6 The velocity power spectra derived from X-ray SB fluctuation analysis using Chandra X-ray observations: (1). Cluster name, (2). Median temperature in the region of interest, (3). Spatial scales least affected by Poisson noise, (4). Velocity of gas motion. 93

4.1 The details of spectral scan and 5×5 mesh scan at CLS. 121

4.2 The best-fit mesh and film parameters of optical blocking filters: (1). Filter. (2). Cell. (3). Thickness of Al-film. (4). Polyimide thickness. (5). Surface density of oxygen. (6). Epoxy thickness. (7). Epoxy filling fraction. (8). Fine mesh filling fraction. 129

A.1 Summary of the measurements on the gas perturbations in Abell 2146: (a). Region, (b). Spatial scales least affected by Poisson noise, (c). Pre-shock temperature, (d). Post-shock temperature, (e). One-component turbulent velocity on the smallest probed scale, (f). $V_{1,k}$ on the largest probed scale, (g). the amplitude of density fluctuations 167

Chapter 1

Introduction

In the bottom-up hierarchical scenario of cosmic structure formation (Peebles, 1980), galaxy clusters originate from minor fluctuations in the universe's matter density shortly after the Big Bang. As the universe expands, these initial perturbations intensify under the influence of gravity, causing regions of higher density to attract more matter, while less dense regions become increasingly void. Following the formation of dark-matter halos, these structures continue to accrete baryonic matter that cools and condenses, eventually fueling the formation of stars and galaxies. These early galaxies and dark matter halos merge over time, leading to the formation of larger galaxy groups and, ultimately, massive galaxy clusters. Hierarchical clustering is a cornerstone of the Lambda Cold Dark Matter (ΛCDM) model. This framework is supported by extensive astronomical observations, including the abundance of clusters (e.g. Tinker et al., 2008), their distribution within the large-scale structure (e.g. Peacock, 1999; Springel et al., 2006), and the cosmic microwave background (CMB) radiation (e.g. Planck Collaboration et al., 2020), which reflects particularly the early density fluctuations that seeded all subsequent structure formation.

Galaxy clusters, the largest gravitationally bound systems in the universe, are held together by their own self-gravity after undergoing gravitational relaxation to reach virial equilibrium. Galaxy clusters typically contain hundreds to thousands of galaxies and span several megaparsecs (Mpc), with the most massive clusters reaching total masses up to $\sim 10^{15}$ $M_\odot$, where $M_\odot$ denotes the solar mass. The mass composition of galaxy clusters, with 85% dark matter and 15% observable baryons (Planck Collaboration et al., 2016), closely aligns with the observed composition of the universe, making them a robust and effective probe for constraining fundamental cosmological parameters (e.g. Abdullah et al., 2023).

The galaxies within the cluster are enveloped in a hot, diffuse plasma known as the intracluster medium (ICM), which is bound by the cluster's gravitational potential. The ICM comprises about 10% - 15% of the total mass of the cluster and represents approximately 90% of its baryonic matter, whereas the stellar mass of the galaxies accounts for only a small fraction (Lin et al., 2003).

1.1 X-ray Emission from Hot Intracluster Medium

The ICM in galaxy clusters is typically fully ionized, with temperatures ranging from 10^7 K to 10^8 K, and emits strongly in X-rays with luminosities of $L_x \sim 10^{43}$ erg s^{-1} to 10^{45} erg s^{-1}. The total mass of a galaxy cluster can be estimated from the velocity dispersion of its member galaxies. Under a model of pure gravitational collapse, a self-similar scaling relation between the mean gas temperature T and the line-of-sight velocity dispersion σ of the galaxy cluster is expected to follow $T - \sigma^2$ (Felten & Morrison, 1966). This is closely aligned with the observed relation $T-\sigma^{0.63}$ in 0.5 keV - 10 keV (e.g. Kochanek et al., 2003; Edge & Stewart, 1991). Scaling relations predict that the cluster's total mass M, mean gas temperature T and X-ray luminosity L follow the relations $M \propto T^{3/2}$ and $L \propto T^2$ (e.g. Markevitch, 1998; Giodini et al., 2013; Pérez-Martínez et al., 2021). Deviations from these scaling relations suggest the effects of non-gravitational processes, such as shock heating, supernovae, and AGN feedback (e.g. Arnaud & Evrard, 1999; Voit, 2005; Pratt et al., 2009). Consequently, X-ray emissions are crucial for probing the physical conditions and dynamics within galaxy clusters (e.g. Popesso et al., 2024).

The primary mechanism of X-ray emission in the hot ICM is thermal bremsstrahlung (Sarazin, 1988), a German term meaning 'braking radiation'. This process occurs when a fast-moving electron comes near an ion, and the Coulomb force of the nucleus alters the electron's trajectory. The change in acceleration of the electron during this interaction results in the emission of energy in the form of X-rays.

If the gravitational potential of the cluster is assumed to include contributions from both the gas and galaxies in hydrostatic equilibrium, the gas density distribution can be derived under King's approximation (King, 1962) for a self-gravitating isothermal sphere (Cavaliere & Fusco-Femiano, 1976) as follows:

$$n_e(r) = n_0 \left[1 + (r/r_c)^2\right]^{-3\beta/2}, \tag{1.1}$$

where n_0 is the central electron density, r_c is the core radius. The index β represents the square of the ratio of the velocity dispersion of galaxies to that of the gas, expressed as:

$$\beta = \frac{\mu m_p \sigma_r^2}{kT}, \tag{1.2}$$

where μ is the mean molecular mass, m_p is the proton mass, and σ_r is the one-dimensional velocity dispersion. β typically ranges between 0.4 and 1, and the most commonly observed value is ~ 0.6 (Chen et al., 2007). Then the analytical X-ray surface brightness profile is written as:

$$I_X = I_0 \left[1 + (r/r_c)^2\right]^{-3\beta+1/2}, \tag{1.3}$$

here, I_0 is the central brightness.

The single β-model inadequately captures the steep surface brightness gradients observed at the centers of cool core clusters. These clusters exhibit relaxed, dense, cold cores characterized by high metallicity, short cooling times (typically less than 1 Gyr in strong cool cores), and low entropy (Molendi & Pizzolato, 2001; Hudson et al., 2010). The entropy, expressed as $K = kT/n_e^{2/3}$, is directly dependent on both the temperature and density of the gas, making it an effective indicator for distinguishing between cool core and non-cool core clusters (Cavagnolo et al., 2009). Consequently, a second component $\mathrm{I_{X,core}}$ is introduced to $\beta-$model specifically characterize the emission excess in the cluster cores, then $\mathrm{I_X = I_{X,core} + I_{X,ambient}}$, providing a better fit for the two-phase intracluster gas (e.g. Mohr et al., 1999). Where the cluster exhibits an elliptical morphology, an additional parameter, eccentricity, defined as the ratio of the major axis to the minor axis as projected on the plane of the sky, is introduced into the β-model.

The electrons and ions interact with Coulomb collision in the ICM, making the X-ray emissivity largely independent of temperature in the soft energy band. For gas with temperatures below T > 3 keV, the surface brightness (SB) detected by X-ray instruments is directly proportional to the emission measure, $\int n_e n_H dV$, where n_e and n_H represent the electron and hydrogen number densities, respectively. This relationship effectively links the observed X-ray brightness to the square of the electron density integrated along the line of sight.

In Sections 2 and Appendix A of this thesis, we derive the gas density fluctuations in the hot atmospheres of six clusters — Abell 2029, Abell 2107, Abell 2151, RBS0540, RBS0533, and Abell 2146. This is achieved by estimating the variances of X-ray SB fluctuations in the soft energy band relative to the 'unperturbed' profiles.

The ICM contains heavier elements beyond hydrogen and helium, with a mean metallicity $\sim 1/3$ of the solar value (e.g. Mantz et al., 2017; Lovisari & Reiprich, 2019). The

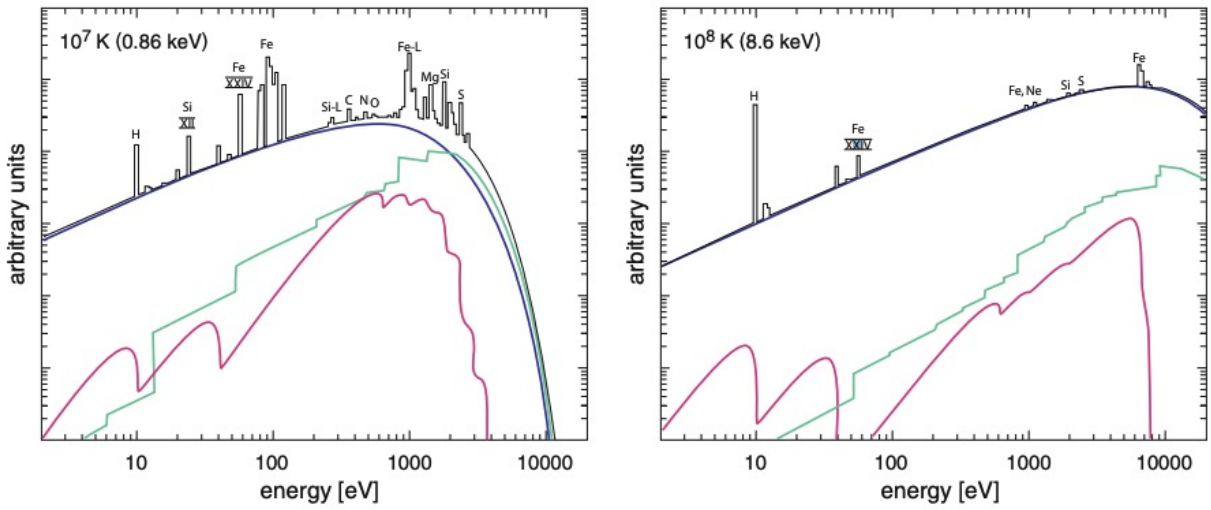


Figure 1.1: X-ray spectra with Solar abundance and at plasma temperatures 10^7 K (left) and 10^8 K (right). The spectra feature continuum contributions from bremsstrahlung (blue), recombination radiation with distinct ionization edges (green), and 2-photon radiation (red) (Boehringer et al., 1993).

X-ray spectrum of galaxy clusters features emission lines primarily from the recombination of these highly ionized metals. Figure 1.1 displays X-ray spectra with solar abundance at different plasma temperatures. One of the most frequently analyzed lines in cluster X-ray spectra is the iron K line at approximately 6.7 keV, which serves as a strong indicator of the temperature in the hot ICM. Iron L lines, emitted from lower ionization states ranging from Fe XVII to Fe XXIV, are useful for probing slightly cooler regions of the ICM compared to the iron K lines. Other lines from elements such as oxygen, silicon, sulfur, magnesium, calcium, and nickel, though less prominent, can also be detected in deeper X-ray observations. These lines significantly influence the spectrum shape in a state of thermal equilibrium and provide critical insights into the physical properties, chemical composition, and dynamical processes occurring within the ICM.

Observatories such as Chandra and XMM-Newton, along with upcoming missions like the X-Ray Imaging and Spectroscopy Mission (XRISM), provide the high spectral resolution required to distinguish these lines from the continuum and each other (e.g. Ishisaki et al., 2022; Bozzo et al., 2023; XRISM Collaboration et al., 2024).

1.2 Cooling Flow Problem

Radiative cooling significantly impacts thermodynamic properties and structure formation in systems where it is efficient. In the absence of heating, the hot intracluster gas radiates away all its thermal energy in the cooling time:

$$t_{cool} = \frac{E_{thermal}}{L_x} = \frac{3nk_BT}{2n_H^2\Lambda(T,Z)}, \tag{1.4}$$

where the mean particle density n is given by $\rho_{gas}/(\mu m_p)$, the number density of hydrogen atoms n_H is (12/27) n for a fully ionized gas, and the cooling function $\Lambda(T, Z)$ is independent of density for optically thin gas. In the densest central regions of cool-core clusters, the densities can reach up to 10^{-1} cm^{-3} with the cooling timescales often less than 1 Gyr, significantly shorter than the Hubble time (Lea et al., 1973), which is the estimated age of the Universe. This indicates that the gas is cooling rapidly, leading to a decrease in entropy. To maintain hydrostatic equilibrium, the gas density must increase, achievable only through an inward flow toward the center of the cluster's gravitational potential. This process is the classical *cooling flow* model (e.g. Cowie & Binney, 1977; Fabian et al., 1984; Fabian, 1994), in which the gas temperature rapidly drops below T $< 10^4$ K. Consequently, cool gas condenses from the surrounding hot gas, continually replenishing and forming a steady inward flow toward the central brightest cluster galaxies (BCGs).

Early evidence of cooling flows was found by early X-ray observations. Canizares et al. (1982) analyzed X-ray spectra from the Einstein Observatory's Focal Plane Crystal Spectrometer and detected the Fe L line complex in the Perseus cluster, which supported a significant amount of hot gas that could be cooling. Approximately 50% of clusters show sharp surface brightness peaks, as observed by the Einstein Observatory (Stewart et al., 1984), EXOSAT Observatory (Lahav et al., 1989), and ROSAT Observatories (Allen et al., 2001). The mass deposition $\dot{M}$ from cooling flows are estimated at a rate of $\sim$ 100 M$_\odot$ to 1000 M$_\odot$ per year (e.g. Jones & Forman, 1984; Fabian et al., 1985; Fabian, 1994; White et al., 1997; Hudson et al., 2010; Fabian et al., 2022, 2023). However, more recent observations by XMM-Newton have revealed that the emission from the coolest gas components (< 2 keV) is much lower than expected in several systems with strong cooling flows (e.g. Peterson et al., 2001; Tamura et al., 2001).

Other products of gas cooling are observed at cluster cores, but all at levels lower than predicted by classical cooling flow models. Filaments of Hα emission from warm ionized gas are detected in clusters with short cooling times (Heckman et al., 1989). Cooling at rate of 100 M$_\odot$ yr^{-1} would theoretically produce massive reservoirs of cold molecular gas

$\sim 10^{11}$ $M_\odot$. Molecular gas of $\sim 10^{10}$ $M_\odot$ has indeed been observed in BGGs, and it only fills a small volume of the core (e.g. Edge, 2001; Hayashi et al., 2018; Alberts et al., 2022). This observed amount constitutes only 5 – 10 percent of the total expected to have accumulated from these cooling flows. Star formation, fueled by the accumulated cold gas, should shine brightly in UV and optical bands due to the presence of young stars. However, observations indicate that the star formation rates in BCGs are typically only a few $M_\odot$ yr^{-1}, and only in some extreme cases in which reach up to hundreds of $M_\odot$ yr^{-1} (Johnstone et al., 1987; McNamara & O'Connell, 1989; O'Dea et al., 2004; McDonald et al., 2018).

The significant discrepancy between the predicted and observed products of cooling underscores the necessity for heating mechanisms that can suppress cooling and replenish more than 90% of the energy radiated away within galaxy clusters.

1.3 AGN Feedback Mechanism

To address the deficit of the cooling products predicted by the cooling flow model, it is crucial to have heating mechanisms that closely align with the radiative cooling rate to replenish the energy dissipated over short timescales. If heating and cooling rates are not closely coupled, the fate of the gas becomes uncertain. An excess in the heating rate would extend the central cooling time, potentially approaching the age of the system, a phenomenon that has not been observed. Thus, while various non-feedback heating mechanisms — such as conduction (e.g. Zakamska & Narayan, 2003; Voigt & Fabian, 2004; Barnes et al., 2019) , dynamical friction from galaxy motions (e.g. El-Zant et al., 2004), energy from mergers (e.g. ZuHone et al., 2010; Omiya et al., 2023), cosmic ray Su et al. (2021); Ruszkowski & Pfrommer (2023). and turbulent dissipation (e.g. Churazov et al., 2004; Howes, 2010; Liu et al., 2021)—may contribute to heating, none can independently and precisely counterbalance cooling to prevent cooling flows effectively.

The feedback from massive stars exploding as supernovae (SNe) is considered one of the crucial mechanisms regulating galaxy evolution. For a comprehensive review, please see Veilleux et al. (2005). SNe feedback is particularly significant in systems with intense star formation. It can release a substantial amount of energy, typically around 10^{51} erg per solar mass, through radiation, neutrino emission, and kinetic energy carried in stellar winds and supernova ejecta. Consequently, it has profound impacts on various scales, from individual stars to entire galaxies and even the intergalactic medium (IGM) (e.g. Bending et al., 2022).

The energy released can reheat and disperse cold gas, and then can effectively regulate the star formation within galaxies. Cole et al. (2000) show that the star formation rate is

suppressed by SN feedback when gas is reheated and expelled out of the starburst disk of the galaxy to a diffuse corona or halo. In addition, supernova feedback is a crucial mechanism in generating galactic winds, especially in low-mass galaxies where the gravitational potential well is shallower (Martin, 1999). The material in galactic winds can be in various phases, including hot ionized gas directly from the supernova, cooler gas entrained by the hot outflow, and even molecular gas (e.g. McKee & Ostriker, 1977; Hopkins et al., 2012). By removing gas from the galaxy, galactic winds can significantly reduce the raw material available for future star formation (Dekel & Silk, 1986), transport heavy elements produced in stellar interiors into the IGM (e.g. Raiteri et al., 1996; Oppenheimer & Davé, 2006, 2008; Strickland & Heckman, 2009; Mernier et al., 2016), alter the galaxy morphological characteristics, and to reproduce the observed galaxy luminosity functions (e.g. Benson et al., 2003; Cole et al., 2001).

However, supernovae feedback alone is not sufficient to counteract cooling in galaxy clusters. Simulations indicate that this feedback can partially compensate for radiative losses in central regions, resulting in lower entropy levels within the core (Springel, 2005). Borgani et al. (2005) observed that galactic winds from SN explosions are localized and fail to significantly elevate entropy at larger radii. Therefore, a feedback mechanism capable of distributing heat more diffusely across the cluster is needed. Furthermore, comparisons between observed temperature profiles of local clusters and simulations including SN feedback reveal discrepancies, especially at larger radii (Leccardi & Molendi, 2008). Simulations that integrate a variety of physical processes are more successful in reproducing the overall profile shape at these extended radii (e.g. Borgani et al., 2004; Nagai et al., 2007). Additionally, the impact of SN feedback on the evolution of both low and high-mass galaxies remains unclear. In particular, SN feedback has a limited effect on massive galaxies, largely due to the deep gravitational wells of these galaxies which prevent the escape of gas. In galaxies with high halo mass, SN feedback fails to prevent star formation (e.g. Moster et al., 2010; Kannan et al., 2014). Simulations restricted to SN feedback alone show that the stellar mass of BCGs is up to two to three times greater than observed (Borgani et al., 2008; Biffi et al., 2018).

Supermassive black holes (SMBH), residing at the centers of most massive galaxies, are believed to be essential in maintaining a long-lived balance between cooling and heating. This process, referred to as active galactic nuclei (AGN) feedback, is now widely recognized as the primary heating mechanism. Typically, the mass of a black hole correlates with the mass of its host galaxy as $M_{BH} \approx 1.4 \times 10^{-3}\ M_{gal}$ (Kormendy & Gebhardt, 2001; McConnell & Ma, 2013), indicating the co-evolution between them. The rest-mass energy of a black hole surpasses the total SN energy output of the galaxy. As the gas cools and falls toward the central SMBH, an enormous amount of energy can be released by AGN during its

lifetime as:

$$E_{BH} = \bar{\epsilon} M_{BH} c^2, \tag{1.5}$$

where efficiency factor $\bar{\epsilon} = \epsilon_r + \epsilon_m$ is the sum of the radiative efficiency ϵ_r and mechanical efficiency ϵ_m. Compared to the binding energy of its host galaxy, $E_{gal} \sim M_{gal}\sigma^2$, where σ is the galaxy velocity dispersion, it then follows that:

$$E_{BH}/E_{gal} \sim \frac{\bar{\epsilon} M_{BH}}{M_{gal}} \left(\frac{c}{\sigma}\right)^2. \tag{1.6}$$

As most massive galaxies have velocity dispersion $\sigma < 400$ km s^{-1}, the ratio $E_{BH}/E_{gal} > 10^3\bar{\epsilon}$. Therefore, even if only a small fraction of a black hole's energy is released into the surrounding gas, AGN can still be powerful enough to profoundly affect the evolution of its host galaxy by suppressing cooling flows, regulating black hole growth, and quenching star formation. Determining the value of feedback efficiency is essential for quantifying the impacts of AGN feedback. Moreover, given the relatively small size of the black hole compared to its host galaxy, understanding how feedback operates in large-scale environments presents a complex challenge. Resolving these questions depends on identifying the feedback mechanisms that channel energy into the surrounding gas, with at least two major modes currently established: *radiative mode* and *mechanical mode*. In this thesis, we provide a brief review of the physics and observational evidence of these two feedback modes. For more comprehensive discussions, please refer to McNamara & Nulsen (2007, 2012); Fabian (2012); Hlavacek-Larrondo et al. (2022).

1.3.1 Radiative Mode

The radiative feedback mode, also referred to as the quasar mode or wind mode, typically occurs in bright AGNs where the accretion rate exceeds 10% or approaches the Eddington limit $\dot{M}_{acc}$, which is the maximum accretion rate at which matter can continuously fall onto a black hole without being expelled by radiation pressure. When the accretion rate, defined as $\dot{m}_{acc} \equiv \dot{M}_{acc}/\dot{M}^{Edd}_{acc} \equiv L_{acc}/L_{Edd} \simeq 0.01-0.25$, it leads to the formation of a geometrically thin, optically thick accretion disk with high radiative efficiency of $\epsilon_r \simeq 0.05-0.2$, especially if the black hole is spinning rapidly (Kormendy & Gebhardt, 2001). Radiative mode feedback is typically linked with highly luminous quasars peaked at high redshifts $z \sim 2-3$ (e.g. Ueda et al., 2003; Hopkins et al., 2007; Rigby et al., 2011), where galaxies are typically rich in gas, which fuels the central black hole and triggers intense quasar activity, suggesting that radiative mode feedback played a significant role in earlier cosmic times (e.g. Bower

et al., 2006). The brightest quasars currently observed have the luminosity of $\sim 10^{49}$ erg s^{-1} (Wolf et al., 2024), which is much higher than the cooling rate of most massive clusters.

The observed relation between black hole mass and stellar velocity dispersion (M $-$ σ relation) can be interpreted as evidence for both radiative AGN feedback (e.g. Tremaine et al., 2002) and mechanical mode (Heckman & Best, 2023). While most observed central AGNs exhibit radiative inefficiency, there remain instances that align with the quasar mode pattern at high accretion rates above $0.01\dot{\mathrm{M}}_{\mathrm{Edd}}$ (for example: H1821+643 (Russell et al., 2010); 3C186 (Siemiginowska et al., 2005, 2010); IRAS 09104+4109 (O'Sullivan et al., 2012)).

The energy injected by AGNs can impact their host galaxies through radiation and winds. The intense radiation from the accretion disk can photoionize the circumgalactic medium (CGM) across distances up to approximately 100 kpc (e.g. Arrigoni Battaia et al., 2019). Radiation pressure primarily acts on dust near the quasar, which is partially charged and bound to the surrounding partially ionized gas. This interaction can also generate a high-velocity, pressure-driven wind that pushes gas and dust outward, eventually transferring energy into the ISM (e.g. Ishibashi et al., 2018). The wind is also likely radiatively driven, facilitated by electron scattering or UV line driving, and is closely associated with the accretion disk (e.g. Murray et al., 1995; Proga et al., 2000). The speed of these winds can reach up to 10^4 km s^{-1}, as measured by the line absorption of the quasar continuum by the intervening wind material. Wind powers, which constitute 5 - 10% of the accretion power, are sufficient to eject gas from galaxies, as supported by a broad range of indirect estimates (e.g. Dunn & Fabian, 2006; Moe et al., 2009; Tombesi et al., 2012). To understand the overall impact of these powerful winds, estimates of their duration are also required. Other energy channels include X-ray Compton heating near the accretion disk region (e.g. Sazonov et al., 2005) and collimated jets. It is also important to note that radio jets can form as part of the quasar mode feedback (e.g. Russell et al., 2014; Hlavacek-Larrondo et al., 2015; Mukherjee et al., 2018). The injected energy sweeps up material into outflows, expelling it from the host galaxy and subsequently suppressing star formation (e.g. Rupke & Veilleux, 2011). Alternatively, the gas may become trapped in the halo, where it compresses and forms a shell that can lead to star formation (van Dokkum et al., 2010).

Although the interaction between radiation and gas is more intense in the vicinity of the black hole, heating gas by radiation may only be effective on small galactic scales (Ciotti et al., 2009). For rich clusters, this is insufficient to suppress cooling. Additionally, maintaining the high accretion rate required for quasar mode, which $\dot{m}$ approaches unity, leads to rapid black hole mass growth. AGN-driven outflows will eventually deplete the cold gas reservoir that fuels SMBHs. As the accretion rate decreases, a transition to

mechanically-dominated radio mode feedback is expected at high redshift about $z = 2$ (e.g. Belloni et al., 2005; Hlavacek-Larrondo et al., 2013).

1.3.2 Radio Mechanical Mode

Central AGNs in galaxy clusters typically operate at low accretion rates of $\dot{\mathrm{M}} < 0.01$, leading to radio mode feedback driven by a geometrically thick, optically thin, and radiatively inefficient hot disk. In this mode, radiation plays a subdominant role, while mechanical energy (including jets and winds) is more significant due to its more efficient coupling with the surrounding gas. Therefore, this mode is also referred to as the radio mechanical mode or cold mode.

The radio jets, launched from the central AGN, initially propagate supersonically through the ICM (e.g. Scheuer, 1974; Blandford & Rees, 1974; Enßlin & Heinz, 2002). They eventually decelerate and cease as they achieve pressure equilibrium with the surrounding ICM. During this initial high-speed phase, relatively little of the nearby X-ray emitting gas is shocked and pushed aside, creating a narrow, elongated cavity that is difficult to detect. The cavity expands outward at a rate that matches the speed of the jet tip when the pressure within the radio lobe equals the ram pressure exerted by the jet itself, displacing a larger volume of the surrounding X-ray emitting gas and making a more spherical shape as observed. Alternatively, if the jet wanders significantly, it can carve out a larger cavity as it moves (Heinz et al., 2006). The cavity moves outward buoyantly at the terminal speed, where the buoyant force exactly balances the drag force. This speed is defined as $v_t = \sqrt{2gV/SC}$, where g is the local gravitational acceleration, V is cavity volume, S is the cavity cross-section, and C is the drag coefficient (Churazov et al., 2001).

Since the inner cavities in Perseus were first resolved by the ROSAT High Resolution Imager (HRI), many cavities have been detected in X-ray images across various systems, from individual elliptical galaxies to the most luminous clusters. These cavities appear as X-ray surface brightness deficits but as bright robes in the radio band. Generally, their sizes range from ∼1 kpc up to 200 kpc (e.g. Forman et al., 2005; Nulsen et al., 2005), extending well beyond the central cluster galaxy. Chandra X-ray observatory, with an unprecedented spatial resolution of only ~ 1.0 arcsec, has revealed the complex structures of hot ICM. A 2 Ms Chandra X-ray image of Cygnus A, the most well-documented powerful Fanaroff-Riley class II (FR II) radio galaxy, illustrates the intense interaction between the central AGN and its surrounding hot atmosphere (e.g. Boehringer et al., 1993; Snios et al., 2018), as shown in Figure 1.2 (Left). The jets collide with a wall of hot gas, creating hotspots. The cocoon shock, driven by the momentum and energy deposited by the jets,

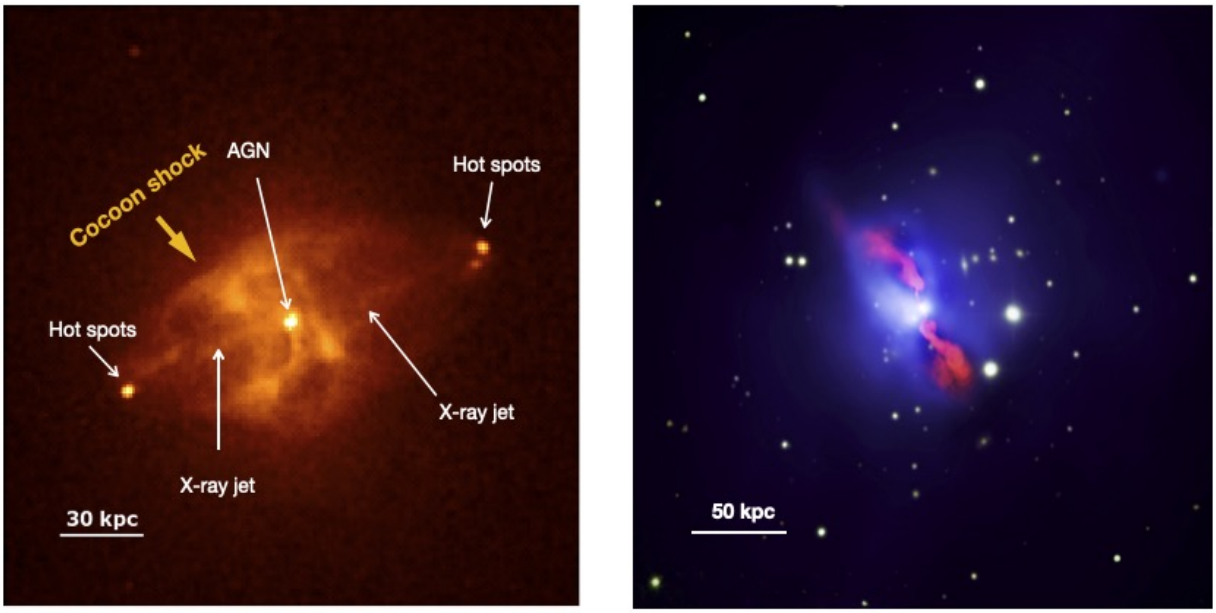


Figure 1.2: Left: The 2 Ms background-subtracted, exposure-corrected Chandra X-ray image of Cygnus A in 0.5 - 7 keV. Right: The composite image of the Hydra A galaxy cluster. The optical starlight from cluster galaxies (in yellow), and the radio emissions from jets (in pink) originating from the central supermassive black hole, are superimposed on the X-ray emissions (in blue) from the hot ICM. Credited by: X-ray: NASA/CXC/U.Waterloo/C.Kirkpatrick et al.; Radio: NSF/NRAO/VLA; Optical: Canada-France-Hawaii-Telescope/DSS

is clearly evident as a bright rim of X-ray emission that envelops the hotspots and other structures surrounding the central AGN. Nearly all Chandra X-ray observations of bright cooling flow clusters in need of heating reveal cavities and shocks near the central radio sources, suggesting that radio AGNs are likely the primary heating agents.

Considering the limitations in data for detecting cavities, it is probable that cavities exist in all cool core clusters. Coupled with their close association with radio lobes, as observed in Hydra A (in the right panel of Figure 1.2), McNamara et al. (2000) proposed that cavities observed in X-ray images essentially serve as indicators of jet power. The total mechanical energy output from the AGN is determined by measuring the work done by radio jets in creating these cavities. The total energy is calculated as the sum of the

thermal energy contained in the lobe and the work required to inflate a cavity:

$$E_{cav} = E + pV = \frac{\Gamma}{\Gamma - 1} pV, \tag{1.7}$$

where p represents the pressure inside the cavity, assumed to be equal to the surrounding pressure, and V is the cavity volume. The ratio of specific heats Γ for the ideal gas filling the lobe is 4/3 for relativistic particles and 5/3 for non-relativistic gas, respectively. And $E_{cav} = 2pV$ if lobes are dominated by magnetic field. Most of the jet power is transferred to the surrounding medium, with only a negligible fraction being radiated away (Bîrzan et al., 2008). The mean power output by AGN can then be estimated using:

$$P_{cav} = E_{cav}/t_{cav} \tag{1.8}$$

by dividing total output energy by cavity age t_{cav}. The buoyant rise time $t_{buot} \simeq R/v_t$ is commonly used as an estimate for cavity age at its late stage, which is the time required for the bubble to rise buoyantly a distance R from the cluster center at terminal velocity v_t.

The true age of the cavity depends on several uncertain factors, such as viscosity (Reynolds et al., 2005), magnetic stress (De Young, 2003), and the projection of the cavity's trajectory with respect to the plane of the sky, and is generally overestimated, causing cavity power to be underestimated. Even so, the mechanical power of radio AGN is comparable to or exceeds the mean cooling rate derived from X-ray luminosities, and thus is powerful enough to offset the cooling (e.g. Rafferty et al., 2006; Dunn & Fabian, 2006), as shown in Figure 1.3. Cavity power is plotted against the cooling power within the cooling radius of ellipticals, groups, and rich clusters, where the cooling timescale is shorter than 7.7 Gyr. The mechanical power output from AGNs finely balances the energy lost through X-radiation in the cooling regions near the centers. It suggests that the amount of energy released back into the system is correlated with the cooling rate. In the stable, long-lived AGN feedback loop, molecular gas condenses from the cooling atmosphere, forms stars, and accretes onto the central SMBH at the cluster center. This accretion releases gravitational energy, triggering a powerful radio AGN that offsets radiative losses and slows the cooling rate until the AGN eventually runs out of fuel and the cycle repeats.

1.3.3 Heating Mechanisms of AGN Outbursts

The debate over how energy is dissipated and distributed through the gas remains unresolved. Radio jets, typically narrow and highly collimated as observed in Cygnus A

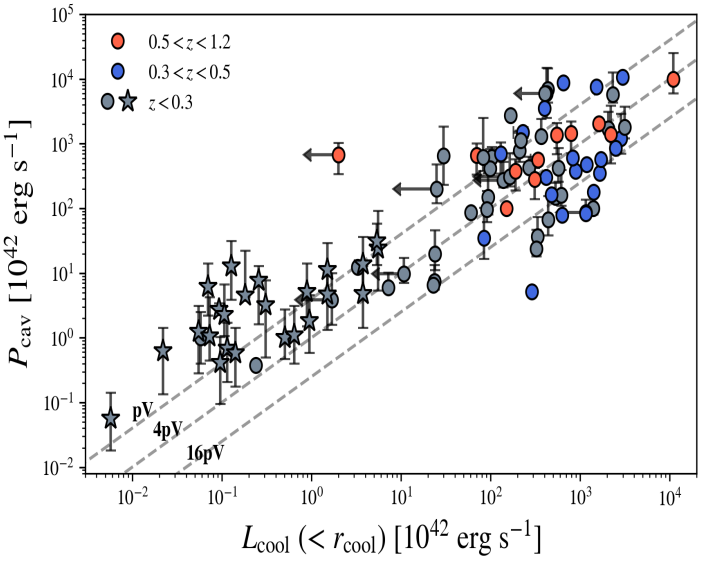


Figure 1.3: Total mechanical power P_{cav} measured by cavities versus the X-ray luminosity L_{cool} within the cooling regions. Data for galaxy clusters are color-coded by their redshifts. Galaxy groups and more isolated systems are represented by grey stars, all located at $z < 0.3$. Dashed black lines indicate P_{cav} matches L_{cool} with E_{cav} = PV, 4PV, 16PV from top to bottom. (Credit: Figure 4 in Hlavacek-Larrondo et al. (2022). The data are from Nulsen et al. (2009); Rafferty et al. (2006); Dunn & Fabian (2008); Hlavacek-Larrondo et al. (2012, 2015); Pandge et al. (2013, 2019, 2021); Sonkamble et al. (2015); Vagshette et al. (2017, 2019); Kadam et al. (2019); McDonald et al. (2019); Liu et al. (2020); Prasow-Émond et al. (2020); Kyadampure et al. (2021).

and Hydra A (refer to Figure 1.2), can penetrate the atmosphere without significant energy dissipation (e.g. Vernaleo & Reynolds, 2006). Although interactions with the ICM or changes due to jet precession can (e.g. Dunn & Fabian, 2006) quickly broaden the jet's opening angle, thereby enhancing its coupling efficiency, additional heating processes are still required.

When the expansion velocity is subsonic, the bubble detaches from the jet and rises buoyantly. The gas displaced by this movement flows inward to fill the vacated space, converting its gravitational potential energy into kinetic energy (Bîrzan et al., 2004). Alternatively, as the pressure within the cavity decreases over time, the energy is converted into kinetic energy in the flows surrounding the buoyant cavity (McNamara & Nulsen,

2007). If the viscosity is low, this kinetic energy is locally dissipated by turbulence over the turnover timescale. This process ensures that all the energy associated with the bubble is released into the surrounding gas and thermalized in its wake (Churazov et al., 2002). Using the SB fluctuation analysis method (detailed in Section 2), Zhuravleva et al. (2018) calculated turbulent dissipation rates in the cores of the brightest nearby clusters. These rates were found to effectively counterbalance radiative cooling, regardless of the initial sources of the gas motions. It suggests that turbulence may play an important role in heating processes (e.g. Dennis & Chandran, 2005; Zhuravleva et al., 2014a).

Another possibility actively discussed involves heating by weak shocks and sound waves, where the gas is compressed during the initial rapid expansion of bubbles, generating weak shock fronts with typical low Mach numbers of $\sim 1-2$. Although they can carry substantial energy, the impact of a single weak shock is minimal, with most of the energy gained from shocks converting into gravitational potential energy in the gas, thereby only slightly raising its entropy. However, in systems like M87 (Forman et al., 2007) and NGC5813 (Randall et al., 2011), multiple shocks occurring over time intervals shorter than the cooling times have been observed. The cumulative effect of repeated shock heating is significant and can compensate for the radiative loss in both systems at small radii. As the shock strength decreases with increasing radius, shock heating becomes ineffective at larger scales.

A series of outbursts generates not only weak shocks but also sound waves, which appear as concentric ripples around the cavities in X-ray images. In comparison to weak shocks, sound damping proves to be a more effective heating mechanism on larger spatial scales. The ripples have been observed in several bright clusters (e.g. Blanton et al., 2011; Sanders et al., 2016) with the most distinct case of Perseus cluster (Fabian et al., 2006), where it appears as pressure disturbances with amplitudes ranging from 5% to 10%, spreading outward over a duration of $\sim 10^7$ year. Analytical estimates (Fabian et al., 2003) and simulations (e.g. Ruszkowski et al., 2004; Sternberg & Soker, 2009) both suggest that sound waves can convert a substantial amount of AGN energy into heat, effectively counteracting cooling over the long term. However, the efficiency of sound damping depends on a transfer coefficient that is not well understood, adding uncertainty to its heating rate.

The ultimate fate of lobes is to become disrupted, with their content of relativistic particles mixing with the ICM and depositing cosmic rays and magnetic energy (Boehringer & Morfill, 1988; Hillel & Soker, 2017a, 2020). Theoretically, lobes cannot maintain stable and are quickly destroyed due to Rayleigh-Taylor and shear instabilities (e.g. Brüggen & Kaiser, 2001; Soker et al., 2002), supported by the highly irregular shapes of cavities seen in simulations. However, observations suggest that bubbles can survive for long periods (Fabian et al., 2011). This apparent inconsistency may be explained by magnetic draping (e.g. Lyutikov, 2006; Ruszkowski et al., 2007) and viscosity (Reynolds et al., 2005), which

can suppress instabilities. Additionally, surface deceleration during the early life of a jet-inflated cavity can also help prevent Rayleigh-Taylor instabilities (Pizzolato & Soker, 2006). Therefore, mixing with the gas is not an effective channel for heating the ICM due to the slow rate of energy exchange. However, cosmic rays can leak from the lobes, streaming through the ICM and exciting plasma waves (Enßlin et al., 2011). The dissipation of these waves can act as a heating source, stabilizing the cooling atmospheres (e.g. Guo & Oh, 2008).

1.4 Residual Cooling and Multi-wavelength Observations

Cool-core clusters have existed over half of the cosmic time (e.g. McDonald et al., 2013; Hlavacek-Larrondo et al., 2015; Main et al., 2017), suggesting they maintain a global thermal balance, indicating a state of global thermal equilibrium. Despite substantial AGN energy output, the formation of molecular clouds is essential for sustaining the feedback loop. Residual cooling is evidenced by the presence of nebular gas (e.g Heckman et al., 1989; McDonald et al., 2010), molecular gas (e.g Edge, 2001), and star formation (e.g. Johnstone et al., 1987; McDonald et al., 2012b; McNamara & O'Connell, 1989), suggesting that the hot ICM thus exhibits local thermal instability.

In Figure 1.4, the Hα emission luminosity is plotted against the central cooling time (left) and the central entropy (right). Bright nebular emission, commonly associated with enhanced star formation, is preferentially observed in cluster cores characterized by short central cooling time $t_{cool} < 1$ Gyr or low central entropy $K < 30$ keV cm^2 (Cavagnolo et al., 2008; Rafferty et al., 2008; Voit & Donahue, 2015). The observation suggests that the formation of cold gas is related to the properties of the surrounding hot atmosphere, potentially condensing from it as it cools. Although these two thresholds are clearly defined and distinct, the underlying physical mechanisms remain unclear. Local acceleration may also play a role in triggering thermal instability. Therefore, understanding the triggers of this thermally unstable cooling is crucial, as its cooling products directly fuel the AGN feedback loop.

1.4.1 Thermal Instability

Consider a scenario where an incompressible cold gas parcel, slightly denser than its surroundings, is displaced within a hydrostatic atmosphere where the pressure decreases with

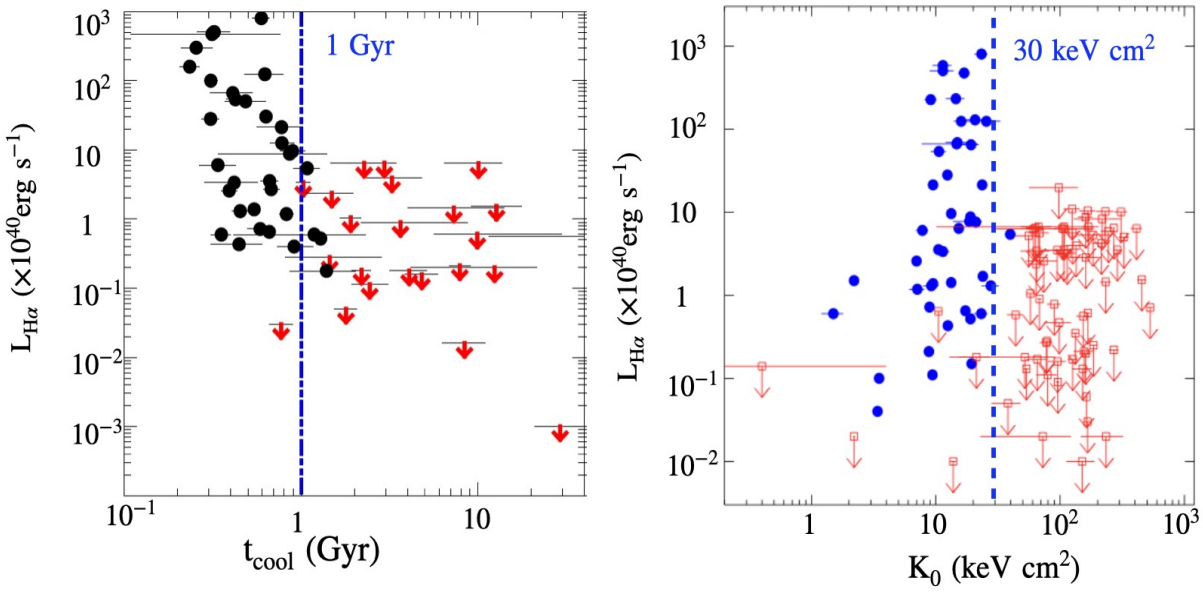


Figure 1.4: Left: Cooling time against Hα luminosity (Hogan et al., 2017). Clusters with BCGs that exhibit Hα emission are marked with black circles, while those without such emission are represented by red arrows, indicating the upper limits of emission. Right: Core entropy against Hα luminosity (Voit & Donahue, 2015). Clusters with detection are shown as blue solid circles and the upper limits of Hα emission in those without are shown as red arrows. The vertical blue dashed lines indicate the t_{cool} =1 Gyr and 30 keV cm^2 threshold, respectively.

height. Due to its lower specific entropy compared to the surrounding medium, the parcel will move downward under the influence of gravity. It will continue to descend over free-fall time t_{ff}, which represents the time scale on which gravity will cause a uniform, pressure-free, spherical cloud to collapse into a denser object, and is given by:

$$t_{ff} = \sqrt{\frac{3\pi}{32G\rho}}, \tag{1.9}$$

where G is the gravitational constant, and ρ is the mass density of the gas parcel. Then it reaches a layer where the surrounding gas has the same specific entropy but a lower density. Buoyant forces will start to push it back, causing the gas parcel to oscillate about its equilibrium position at the Brunt-Väisälä frequency.

In reality, a gas parcel is compressible, which means it cools over a timescale t_{cool} due to radiative loss. If t_{cool} is much shorter than t_{ff}, the gas parcel cools significantly and becomes denser before it reaches its equilibrium position. As a result, it continues to sink deeper into the gravitational potential well rather than oscillating without runaway cooling. Analytical arguments and simulations have consistently indicated that thermal instability occurs when the ratio of the cooling time to the free-fall time drops below unity, $t_{cool}/t_{ff} < 1$, in a plane-parallel atmosphere (e.g. Nulsen, 1986; McCourt et al., 2012).

When thermal instability occurs, gas parcels condense and become detached from the surrounding hot atmosphere, leading to cloud fragmentation within the cooling flow. Additionally, thermal instability is a fundamental concept in the formation of multi-phase gas in the ICM (McKee & Ostriker, 1977). These phases include hot plasma at $\sim 10^6$ K, warm ionized nebular gas at $\sim 10^4$ K, and cold molecular gas at $\sim 10 - 100$ K. At these temperatures, the equilibrium of the specific net cooling rate shows a weak dependence on density, but it is strongly influenced by temperature variations.

However, even within the very central regions of the clusters, the observed cooling time always exceeds the free-fall timescale, making the ratio t_{cool}/t_{ff} never fall below unity. Hogan et al. (2017) observed no case of $t_{cool}/t_{ff} < 10$ in a sample of 56 clusters, which is not consistent with the expected onset of thermal instability in hot atmospheres. In cool-core clusters with rapid cooling and detected cold gas, the ratio of cooling time to free-fall time typically ranges from 10 to 25 (Pulido et al., 2018).

Simulations modeling three-dimensional atmospheres, often referred to as the 'precipitation model', have established a higher threshold, where thermally unstable cooling occurs when the ratio $t_{cool}/t_{ff} < 10$ (e.g. Gaspari et al., 2012; Li & Bryan, 2014; Li et al., 2015; Voit et al., 2017; Voit, 2021; Wibking et al., 2025). The process unfolds as follows: when conditions for thermal instability are met, cold gas condenses and precipitates toward the

central SMBH, fueling it and simultaneously triggering star formation. The central AGN then releases a powerful jet that heats the surrounding atmosphere and lowers its density, thereby increasing the cooling time and raising the $\min(t_{cool}/t_{ff})$ above 10. This reduces accretion, suppresses star formation, and halts thermally unstable cooling. Over time, this cycle repeats, establishing a self-regulating AGN feedback loop. Li et al. (2015) found that it takes approximately 1–2 Gyr after the peak of AGN activity for the star formation rate (SFR) to begin declining. This lag in star formation behind the immediate thermal effects of AGN outbursts occurs because the persisting cold gas reservoir takes time to be depleted by star formation. The hysteresis effect results in thermal instabilities occurring when the system's $\min(t_{cool}/t_{ff})$ falls within the range of 1 - 20 (Li et al., 2015), or 4 - 20 (Voit & Donahue, 2015). This may explain why some systems with $\min(t_{cool}/t_{ff}) > 10$ still exhibit cold gas.

1.4.2 Stimulated Cooling by Uplift

As an increasing number of ALMA observations reveal, very little of the molecular gas is spatially aligned with the central AGN. Instead, most of it is distributed along elongated filaments that extend radially outward and trail buoyantly rising X-ray cavities. Inspired by these observations, McNamara et al. (2016) propose a model in which cold molecular gas condenses from low entropy gas uplifted by rising bubbles to higher altitudes, where its cooling time is shorter than its infall time t_I. The infall time is determined by the slower of its free-fall or terminal velocities, leading to an infall time that significantly exceeds the free-fall time, thereby making it easier for the t_{cool}/t_I to fall below 1.

Determining whether the molecular gas in the filaments is directly pulled from the core regions or condenses in situ from uplifted low entropy gas requires further study. Russell et al. (2019) observed that filaments typically exhibit narrow line widths and smooth velocity gradients along their lengths. This indicates that the filaments are recently formed in situ, tracing the streamlines around and behind the radio bubbles. They might retain the velocity structure of the ascending bubble or become decoupled, yet have not been significantly influenced by gravity, allowing them to slowly fall back towards the galaxy center. The quantity of molecular gas produced depends on the amount of low entropy gas uplifted, as cavities cannot lift more gas than they displace. Radio-jet-driven outflows of ionized and molecular gas in nearby radio galaxies suggest that jets can interact with dense gas clouds (e.g. Morganti et al., 2005; Alatalo et al., 2011; Morganti et al., 2015). Observations of BCGs by ALMA show that X-ray cavities are capable of lifting enough low entropy gas to higher altitudes to form molecular filaments that trail the cavities (McNamara et al., 2014, 2016; Russell et al., 2016, 2017; Vantyghem et al., 2016). The

role of bubbles in triggering cooling has also been observed in simulations. For example, Wibking et al. (2025) speculated that a driving mechanism characterized by bursty, non-Gaussian correlations might facilitate the formation of cold gas blobs. The correlated bursts can elevate low-entropy gas to higher altitudes, thereby increasing the free-fall time leading to more precipitation.

However, this process requires high coupling coefficients (e.g. Qiu et al., 2021). AGN feedback not only provides sufficient energy to heat atmospheres but also facilitates a leading mechanism, simulated cooling by uplift, to trigger the formation of cold gas.

1.4.3 Multi-phase Gas in Cluster Cores

The cool-core cluster centers are often multiphase, with hot fully ionized ICM at $\sim 10^7$ K, warm ionized atomic gas at $\sim 10^4$ K, and cold molecular gas at ~ 10 K, all coexisting around BGGs. Despite efficient AGN feedback, the presence of these cooling byproducts indicates that cooling flows are still occurring, albeit at a reduced rate.

ALMA observations: molecular gas in galaxy clusters

Although massive reservoirs of molecular gas with masses ranging from 10^9 $M_\odot$ to 10^{11} $M_\odot$ are observed in BGGs, these amounts represent only a few percent of what would be expected from the unimpeded cooling rates (Edge, 2001; Salomé & Combes, 2003). Although the molecular gas is dispersed and has a low volume-filling factor, it dominates the mass of the cold-phase gas. Early radio observations spatially resolved the cold gas in only a few nearby BCGs (e.g. Salomé & Combes, 2004; Salomé et al., 2006). Rather than being concentrated in a small region at the galactic center, the molecular gas commonly reveals a filamentary structure and shows strong spatial correlations with soft X-ray and Hα filaments (e.g. Hatch et al., 2006; Lim et al., 2012; McDonald et al., 2012a; Tamhane et al., 2022).

With the arrival of ALMA observations featuring unprecedented angular and energy resolution, it is now possible to detail the velocity structures of molecular filaments across a broad sample of central cluster galaxies (e.g. David et al., 2014; McNamara et al., 2014; Russell et al., 2016; Vantyghem et al., 2016; Russell et al., 2019). ALMA is situated on the Chajnantor plain in the Chilean Andes and consists of 66 antennas. This includes fifty 12-meter antennas (often referred to as the Atacama Compact Array (ACA) or Morita Array), twelve closely spaced 7-meter antennas (the 7-m Array), and four 12-meter antennas designated for single-dish observations (the TP Array). Interferometry is used with

baselines ranging from 150 m to ∼16 km, and the reconfigurability of ALMA enables it to achieve both a wide field of view and high spatial resolution. In the current observation cycle, ALMA covers most wavelength ranges from 84 GHz to 950 GHz. For a comprehensive description of the current setup, please refer to ALMA Technical Handbook (Remijan et al., 2019).

In its most extended configuration ∼ 16 km, ALMA can achieve sub-arcsecond angular resolution for CO emission. The molecular gas is preferentially observed to be distributed along narrow filaments following the wakes of buoyantly rising cavities (McNamara et al., 2014; Russell et al., 2016, 2019). Additionally, the molecular gas mass correlates with the X-ray gas mass at the same spatial scales (Pulido et al., 2018). Russell et al. (2019) analyzed molecular gas in 12 central cluster galaxies, using data from ALMA observations. The study found that the velocities of this molecular gas were significantly lower than those of stellar velocity dispersions, suggesting that the gas is both young and transient. Additionally, the velocities of filament bulk were observed to be below both escape and free-fall speeds, indicating that the gas is gravitationally bound and subject to deceleration. Olivares et al. (2019) explored multi-phase filamentary structures in the cores of 15 clusters by using ALMA and MUSE data. The findings indicated that these structures may be influenced by turbulence, likely induced by jets, bubbles, or mergers. The observed velocities and dispersions were low, remaining below the escape velocity, suggesting that these cold clouds are likely to fall back toward the central galaxy. Together, these observations suggest that the hot ICM serves as a reservoir for the molecular gas. The presence of narrow, redshifted absorption lines indicates that the molecular gas, formed in situ from uplifted low-energy gas, is infalling towards the central black hole and fueling star formation. This process helps maintain the AGN feedback loop.

KCWI observations: nebular gas in galaxy clusters

Warm ionized nebulae, which appear as the ionized skins of molecular filaments, are commonly observed around central galaxies (e.g. Heckman, 1981; Jaffe et al., 2005; McDonald et al., 2010; Olivares et al., 2022). These nebulae display filamentary structures extending from tens to hundreds of kpc outward, aligning spatially with observed X-ray and molecular gas (e.g. Hatch et al., 2006; McDonald et al., 2011).

The most commonly observed emission lines for warm ionized gas are the Balmer series of hydrogen, particularly the Hα line (656.3 nm). Other important lines include [O III] (500.7 nm), [N II] (654.8 nm and 658.4 nm), and [S II] (671.6 nm and 673.1 nm), which are strong indicators of ionization levels and are used to trace the distribution, temperature, and density of the ionized gas. By making assumptions about the electron density and the

volume filling factor of the gas, the observed luminosity of these lines can be converted into an estimate of the gas mass (Osterbrock & Ferland, 2006). The mass typically ranges from $\sim 10^6$ $M_\odot$ to 10^9 $M_\odot$ in the cool cores of galaxy clusters (Hatch et al., 2007; Gingras et al., 2024). Although nebular emission represents just a small fraction of the total mass involved in cooling processes, its high surface brightness makes it an invaluable tool for investigating regions where gas is thermally unstable and actively cooling, as well as for examining the dynamics of the gas.

Observations from the Keck Cosmic Web Imager (KCWI) enable detailed studies of the behaviors of warm nebular gas surrounding central galaxies. Installed on the 10 m Keck II telescope at the W. M. Keck Observatory atop Mauna Kea in Hawaii, KCWI is an optical integral field spectrograph (IFS) optimized for sensitivity in the blue band of the optical spectrum. This sensitivity is crucial for detecting emission lines such as Lyman-alpha, [O II], and [O III] from distant galaxies and intergalactic gas. KCWI covers a wavelength range from 350 - 560 nm with a spectral resolution of 1000 - 20000 and a large field of view (FoV) up to 20" $\times$ 33" (Morrissey et al., 2018). It is specifically designed to study the faint, diffuse light from the intergalactic medium and the "cosmic web", the vast network of galaxies and gaseous filaments that constitutes the large-scale structure of the universe.

1.5 Gas Motions in ICM

The hot atmospheres of galaxy clusters are influenced by a variety of processes, including mergers, plasma instabilities, the motion of galaxies, central AGN activities, and cooling, which manifest as bulk flows and turbulent eddies. Studying these gas motions across different spatial scales is crucial for unraveling the complex mechanisms that govern energy distribution, trigger multi-phase gas formation, facilitate chemical mixing, and provide stability against rapid cooling.

1.5.1 Basic Turbulence

Galaxy clusters may be turbulent environments. Before its loss, the Hitomi satellite provided unprecedented high-resolution X-ray spectroscopy of the Perseus cluster. Within the central ~ 30 kpc $- 60$ kpc, the line-of-sight velocity, measured by line centroid shift, is V $= 150 \pm 70$ km s^{-1}, and velocity dispersion, measured by line broadening, is $\sigma = 164 \pm 10$ km s^{-1}, though this lacks information on spatial scales (Hitomi Collaboration et al., 2016). Therefore, understanding turbulence is crucial for comprehending the dynamics within these clusters. For a comprehensive discussion, please refer to Tennekes &

Lumley (1972). Below, I summarized the content related to my work presented in Chapter 2 on turbulent velocity fields in the ICM.

For simplicity, the turbulence is assumed to be homogeneous, isotropic, and incompressible. This assumption may not accurately reflect conditions in ICM, which exhibits substantial variations in density across different regions. Turbulence consists of eddies of varying sizes, l, each characterized by a velocity $u(l)$ and a timescale $\tau(l) = l/u(l)$. The large eddies are unstable and break up, transferring their energy to smaller eddies.

Kolmogorov's theory of turbulence predicted that in every turbulent flow at a sufficiently high Reynolds number, the velocity field would be self-similar over a range of scales (Kolmogorov, 1941). The average velocity differences between two points are uniquely determined by energy dissipation rate ϵ_d and kinematic viscosity ν, which have dimensionalities of $[L^2T^{-3}]$ and $[L^2T^{-1}]$, respectively. The Kolmogorov length scale is the smallest size of eddies in a fluid, where the kinetic energy is dissipated due to viscosity. It can be calculated as:

$$l_K = \left(\frac{\nu^3}{\epsilon_d}\right)^{1/4}. \tag{1.10}$$

The eddies of size l_K whirl with a velocity:

$$u_K = (\nu\epsilon_d)^{1/4}. \tag{1.11}$$

The energy spectrum of Kolmogorov turbulence has the form:

$$E(k) = u_K^2 l_K E_*(l_K l), \tag{1.12}$$

where E_* is a dimensionless energy spectrum function. Within the inertial range $l_0^{-1} \ll k \ll l_K^{-1}$, kinetic energy cascades from larger to smaller eddies without significant loss. This energy transfer process continues until the Reynolds number at the Kolmogorov length scale becomes sufficiently small, resulting in the rapid dissipation of kinetic energy at the rate ϵ_d. Moreover, E_* must exhibit scale-independence, conforming to a pure power-law spectrum, expressed as: $E_*(l_K k) = \alpha(l_K k)^n$. Since the viscous forces can be negligible over the inertial range, thus, the energy spectrum $E(k)$ is independent of ν and is expressed as:

$$E(k) = \alpha\epsilon_d^{2/3}k^{-5/3}. \tag{1.13}$$

This expression describes the famous Kolmogorov spectrum $E(k) \propto k^{-5/3}$. Following dimensional analysis, the turbulent velocity $u(l)$ is:

$$u(l) \sim [E(l)/l]^{1/2} \sim \epsilon_d^{1/3} l^{1/3} = u_K (l/l_K)^{1/3} \propto k^{-1/3}. \tag{1.14}$$

Eddies have energy of order $u(l)^2$ and timescale $\tau(l) = l/u(l)$, therefore, the velocity spectra can be used to derive dissipation rate $\mathrm{Q}_{\rm turb}$:

$$\mathrm{Q}_{\rm turb} \sim \rho\epsilon \sim \rho \frac{u(l)^2}{\tau(l)} \sim \rho u(l)^3/l. \tag{1.15}$$

The RMS velocity is expressed in terms of turbulent kinetic energy as $V_{1,k} = [2kE(k)/3]^{1/2}$, we can obtain:

$$\mathrm{Q}_{\rm turb} = C_Q \rho V_{1,k}^3 k, \tag{1.16}$$

where $C_Q = 3^{3/2} 2\pi/(2C_K)^{3/2}$ is determined by Kolmogorov constant $Q_K \approx 1.65$ as experimentally measured (Sreenivasan, 1995; Kaneda et al., 2003).

Despite the widespread application of Kolmogorov's theory in astrophysics, the complexities are often overlooked in this classic model. First, the ISM / ICM are not incompressible fluids with constant density. Furthermore, many astrophysical environments are not solely hydrodynamic but also magnetohydrodynamic (MHD). Magnetic fields can significantly influence energy transfer processes, altering the dynamics of turbulence. Additionally, different physical processes can couple scales in ways that violate the locality of interactions assumed in Kolmogorov turbulence. For example, cosmic rays and radiation pressures can inject energy not only on the correlation length scale.

1.5.2 Velocity Spectrum and Density Fluctuations

A linear relationship exists between the rms density and velocity fluctuations for slow gas motions in relaxed clusters, which can be written as:

$$\left(\frac{\delta\rho_k}{\rho}\right)^2 = \eta_1 \left(\frac{V_{1,k}}{c_s}\right)^2, \tag{1.17}$$

where $\delta\rho_k/\rho$ and $V_{1,k} = V_k^2/3$ are the amplitudes of density fluctuations and one-component velocity, respectively, both measured at wavenumber k, η_1 is a dimensionless coefficient, and c_s is the sound speed. The theoretical argument is detailed in Zhuravleva et al. (2014b). The hypothesis presented is straightforward and physically motivated, only assuming that

the complexities associated with plasma effects or Magnetohydrodynamics (MHD) are neglected.

Two assumptions underlie this linear proportionality. Firstly, the turbulent injection scale is larger or comparable to the Ozmidov scale. This scale indicates the point at which the eddy turnover timescale becomes shorter than the buoyancy timescale. Assuming radiative cooling is balanced by the dissipative heating, $\mathrm{Q_{turb}} = \mathrm{Q_{cool}}$, the Ozmidov scale, l_o can be estimated using the following formula:

$$l_o = N^{-3/2}\epsilon^{1/2} = N^{-3/2}\left(\frac{\mathrm{Q_{cool}}}{\rho}\right)^{1/2}, \tag{1.18}$$

where $\epsilon = \mathrm{Q_{cool}}/\rho$ denotes the mean density-normalized dissipation rate, while N, the Brunt-Väisälä frequency, is determined by the gravitational acceleration g and the entropy scale height H_s, which is defined as $\left(\frac{d\ln S}{dr}\right)^{-1}$.

Secondly, the smallest scales at which turbulent velocity must be larger than the Kolmogorov dissipative scale l_k because gas viscosity can be neglected within the inertial range. Assuming approximate equilibrium between the cooling rate and the turbulent heating rate, the Kolmogorov dissipation scale is determined by the following expression:

$$l_K = \nu^{3/4}\epsilon^{-1/4} = \frac{\nu^{3/4}}{(\mathrm{Q_{cool}}/\rho)^{1/4}}, \tag{1.19}$$

where ν represents the viscosity calculated for ionized, unmagnetized gas, as detailed by Spitzer (1962). For more detailed information on the analytical derivation of this linear relationship, please refer to Zhuravleva et al. (2014b). The underlying concept is straightforward and physics-driven, based only on the assumption that complexities related to plasma effects and magnetohydrodynamics (MHD) can be disregarded.

They argue that linearity is maintained across a broad range of scales with the same coefficient η_1 of order unity. At larger scales, dynamics are governed by buoyancy, and η_1 is set by gravity waves, or g-modes. As scales decrease and transition to regions where turbulence dominates and the eddy turnover time is shorter than the buoyancy timescale, η_1 is determined by the ratio of the scalar dissipation rate to the flux of kinetic energy. This ratio reflects the extent to which scalar variance, relative to kinetic energy, transitions into the inertial range, characterized by energy transfer between scales without net loss. Therefore, the proportionality in both the buoyancy-dominated and turbulence-dominated regimes remains consistent. Using non-radiative cosmological simulations of relaxed clusters, the relation is calibrated to yield a proportionality of $\eta_1 \sim 1 \pm 0.3$. Zhuravleva et al.

(2023) verified this relationship using OMEGA500 simulations of 78 clusters in various dynamical states, finding it to be valid. However, the coefficient of $\eta_1 \sim 1.3 \pm 0.5$ exhibited greater scatter compared to that of relaxed clusters $\eta_1 \sim 0.9 \pm 0.2$. Direct measurements of the velocity field from the recently launched XRISM will enable us to verify and constrain this relationship with an accuracy of a few percent.

Utilizing this relationship, the velocity power spectrum of the hot ICM can be indirectly derived from existing Chandra and XMM-Newton observations accumulated over the past 20-plus years, addressing the challenge of measuring the velocity field of gas motions prior to the advent of next-generation X-ray detectors with high energy resolution. Moreover, this method is particularly valuable because it not only measures the amplitudes but also determines the corresponding spatial scales, which are hard to extract even from direct measurements.

The comparison with the direct velocity measurement of the Perseus cluster observed by Hitomi is shown in Figure 1.5. The derived velocities of gas motions vary from 110 km s^{-1} at a scale of 5 kpc to 200 km s^{-1} at a scale of 30 kpc, aligning with Hitomi's results. The same measurements in Perseus and the comparison have been also presented in Zhuravleva et al. (2014a) and Zhuravleva et al. (2018). Although the slope of the velocity spectra cannot be accurately constrained due to uncertainties, it is close to the pure Kolmogorov slope of 1/3. The typical velocities in the cooling cores of other bright, nearby relaxed clusters, derived from Chandra X-ray images, range between $\sim 100 - 150$ km s^{-1} on scales < 50 kpc, and up to ~ 300 km s^{-1} on scales of ~ 100 kpc (Zhuravleva et al., 2018), consistent with those measured in the Perseus core by Hitomi. This technique is also applied to the outer regions of relaxed cluster cores and on large scales (e.g. Hofmann et al., 2016; Eckert et al., 2017).

1.5.3 Velocity Structure Function

The Velocity Structure Function (VSF) is a versatile tool used to study the nature of gas motions, effectively quantifying the statistical properties of velocity differences across various scales. The p-th order VSF is defined as:

$$\mathrm{VSF}(r) = < |v(\vec{x} + \vec{r}) - v(\vec{x})|^p > \tag{1.20}$$

where $\vec{x}$ and $\vec{r}$ are positions and separations in the velocity maps, $<>$ denotes the ensemble average, and p is the order of VSF.

The VSF has been extensively used. The internal velocity dispersion within molecular clouds is observed to increase with their sizes, a trend typically explained by a turbulent

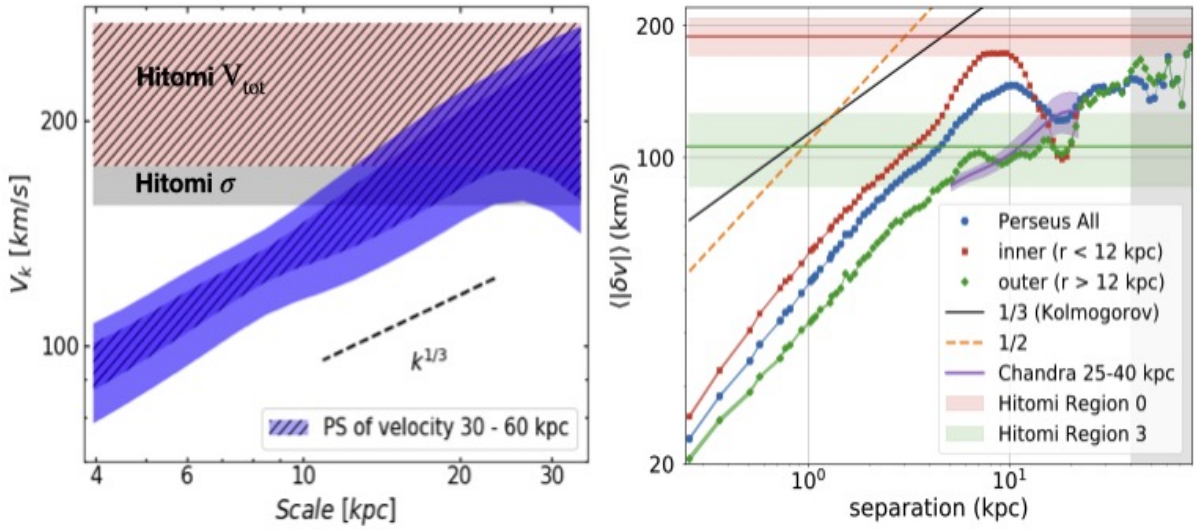


Figure 1.5: Left: Comparison of velocity power spectra derived from Chandra X-ray images with direct Hitomi velocity measurements in the core of the Perseus cluster. Red and gray hatched regions represent the total velocity and velocity dispersion observed by Hitomi, respectively. The velocity amplitudes are estimated within the central 30 - 60 kpc from X-ray SB fluctuation analysis. Right: Comparison of the Velocity Structure Functions (VSF) of nebular gas traced by Hα emission (inner core: red points; outer core: green points; entire cluster: blue points), Chandra X-ray velocity analysis (purple area), and Hitomi observations (region 0: red area; region 3: green area). This Figure is adapted from Figure 4 in Li et al. (2020)

velocity spectrum (Larson, 1981). The use of velocity centroids to constrain the structure function was first considered by von Hoerner (1951). The current generation of radio, optical, and infrared telescopes, featuring high energy and spatial resolution, enables us to statistically probe velocity differences between two points, which is key to unraveling the kinematics of nebular filaments and cold molecular clouds.

Li et al. (2020) utilized optical observations to measure VSFs of Hα filaments in the centers of three nearby clusters: Perseus, Abell 2597, and Virgo. The turnovers observed in the VSFs occur at scales consistent with the sizes of jet-inflated bubbles in the sample clusters, suggesting that the energy injection is attributed to central AGNs. Moreover, a detailed comparison between the VSF of cold phase gas in the cool core of Perseus and the velocity spectrum of the hot ICM obtained from X-ray SB fluctuation analysis is presented in Figure 1.5 (adapted from Figure 3 in Li et al. (2020)). Overall, the VSF of the warm

ionized filaments in the outer core ($r > 12$ kpc, represented by green points) aligns with the velocity spectra of the hot atmosphere measured in the region between 25 and 40 kpc (indicated by a purple band), possibly suggesting a good kinematic coupling between two phases. The coupling of kinematics may be due to: either the cold gas has recently condensed from the hot gas, thus retaining the kinematic 'memory' of the ICM, or the cold gas is diffuse, allowing it to rapidly interact with and become co-moving with the surrounding ICM. By using the VSF of cold phase gas to probe the turbulent motions of the hot ICM, the effective viscosity has been found to be significantly suppressed.

Chen et al. (2007) studied the VSFs of eight extended nebulae surrounding QSOs at redshifts $z \approx 0.5 - 1.1$, traced by [OII] or [OIII] emissions. In contrast to the slopes steeper than Kolmogorov turbulence observed in Hα filaments around BCGs (Li et al., 2020), five out of the eight nebulae displayed slopes that were consistent with or flatter than Kolmogorov predictions. This suggests that the kinematics of multiphase filaments can vary significantly depending on the environmental context.

This observation is also supported by numerous numerical simulations of the VSFs of multiphase gas in galaxy clusters. Hillel & Soker (2020) analyzed simulations of jet-inflated bubbles and found that they can induce large-scale turbulence, resulting in a VSF slope for nebular optical emissions that is steeper than the Kolmogorov slope. They also suggested that slow dissipation might indicate that heating the ICM by mixing with hot bubbles could be more efficient than heating through turbulent dissipation. Additionally, with 3D MHD simulations of self-regulated AGN feedback in a Perseus-like galaxy cluster, Wang et al. (2021) discovered that cold phase gas is dynamically linked with hot gas via magnetic fields, leading to a steeper VSF that may be influenced by gravity. Due to the inherent limitations and uncertainties of the VSF and data quality, high-resolution simulations are necessary for a clearer understanding. Fournier et al. (2025) observed no significant correlation between the behavior of the hot and cold phases of the ICM in terms of their VSFs by using XMAGNET, a suite of exascale simulations of a magnetized cool-core cluster. The power-law index for the VSFs of the cold phase shows significant variability, whereas it remains more stable for the hot phase. The VSF amplitudes and index vary significantly depending on the viewing orientation and the atmospheric conditions, suggesting that these effects must be carefully considered to assess the dynamics within cluster cores accurately. In Chapter 3, we also explore how the point spread function (PSF) and the window effect of a limited field impact VSF analysis.

In summary, by analyzing VSF, it provides us with insight into:

- Nature of turbulence: the VSF can be linked to the turbulent velocity spectrum. According to Kolmogorov theory, a first-order VSF in the inertial range has a slope

of 1/3, while the slope changes to 1/2 in supersonic turbulence.

- Energy dissipation rate: The VSF enables the examination of how energy dissipation rates vary across different scales, providing insights into the heating channels within turbulent flows.
- Gas kinematics: It reveals critical kinematic features such as rotation, shear, and bulk flows within the gas.
- Physical processes distributing energy, such as star formation, galactic motions, and AGN feedback.
- Properties of the medium: offers valuable information about the kinematic viscosity and the effective Reynolds number of the medium.

1.6 This Thesis

Central AGN activity is widely recognized as a promising solution to the cooling flow problem and plays a crucial role in the formation and evolution of galaxies. Although this concept has been extensively studied, the mechanisms by which the energy released by AGNs couples with the surrounding atmosphere and propagates on larger scales are still not well understood. Furthermore, within the context of feedback, the origins of multi-phase gas and the interactions between their movements require further investigation.

Turbulence driven by central AGN activities is considered to play an important role in heating atmospheres, though there may be additional contributors to turbulent motions. In Cavagnolo et al. (2008), several outliers were identified that disrupt the correlation between the presence of nebular gas and the typical thermodynamic properties of cool-core clusters: short cooling times and low central entropy. Martz et al. (2020) suggested that this violation is due to the absence of X-ray bubbles, which stimulate cooling by uplifting low-entropy gas. Motivated by these findings, we aim to investigate whether turbulence alone is effective enough to stabilize cooling in these structureless atmospheres.

In Chapter 2, using X-ray surface brightness fluctuation analysis, we derived the scale-dependent velocity amplitudes of gas motions in five clusters with smooth atmospheres by using Chandra observations: Abell 2029, Abell 2107, Abell 2151, RBS0533, and RBS0540. We compared the estimated turbulent dissipation heating rates with the radiative cooling rates within the rapidly cooling cores. Despite the absence of bubbles, we explore other potential sources of gas perturbations, such as sloshing induced by mergers, which are

evident in the spiral structures observed in Abell 2029 and Abell 2151, and may be a significant factor.

Another aspect we wish to investigate is the interaction between the kinematics of gas in different phases. In Chapter 3, by utilizing multi-wavelength observations—optical data from KCWI and radio data from ALMA—we study the motions of warm ionized gas and cold molecular gas via Velocity Structure Functions (VSF). Combining this with X-ray analysis, determining whether these motions are coupled or decoupled, may provide insights into the origins of the cold phase gas. X-ray observations reveal that cluster atmospheres are turbulent. Although cold gas originates from hot gas, the slope and shape of the Velocity Structure Functions (VSF) suggest that their motions are influenced by additional factors. Gravitational forces and disturbances from jets may significantly alter the motion of gas across different phases.

The motions of the hot ICM cannot be directly obtained using current measurements from X-ray spectroscopic missions. However, upcoming observations from XRISM will enable us to analyze line shifts and line broadening with a high spectral resolution of a few eV. In Chapter 4, I present the work I conducted on the calibration of optical blocking filters and the modeling of properties of filter candidates during 2019 - 2020, prior to its launch. A comprehensive understanding of the filter parameters will help us identify the most suitable candidates and provide guidance for subsequent data reduction.

Finally, Chapter 5 summarizes this thesis, presents the main conclusions of our work, and offers an outlook for future research.

Chapter 2

X-ray Surface Brightness Fluctuations in Smooth Galaxy Cluster Atmospheres

We measure surface brightness fluctuations in Chandra X-ray images of the cores of the galaxy clusters Abell 2029, Abell 2151, Abell 2107, RBS0533, and RBS0540. Their relatively structureless X-ray atmospheres exhibit the thermodynamic properties of cool cores including short central cooling times and low entropy. However, unlike typical cool-core clusters, molecular gas, star formation, and bubbles associated with radio jets are faint or absent near their central galaxies. Four clusters show typical gas density fluctuation amplitudes of ~ 10 per cent on the scales probed, apart from RBS0540, which exhibits lower amplitudes, suggesting that its gas is mildly disturbed. Under the assumption that gas density fluctuations are indicative of random gas velocities, we estimate scale-dependent velocity amplitudes of gas motions across all studied clusters, which range from 100 km s^{-1} to 200 km s^{-1} in Abell 2029, Abell 2151, and Abell 2107. These velocity estimates are comparable to the atmospheric velocity dispersion in the Perseus cluster measured by the Hitomi X-ray Observatory. The turbulent heating rates implied by our measurements are of the same order as the radiative cooling rates. Our results suggest that atmospheric sloshing and perhaps turbulent motion may aid radio jets in stabilizing atmospheric cooling.

2.1 Introduction

In the absence of reheating, the hot intracluster medium (ICM) would cool radiatively leading to cooling into molecular clouds and star formation at rates ranging from hundreds to thousands of solar masses per year (e.g. Fabian, 1994), violating observation (**?**Rafferty, McNamara, & Nulsen, 2008; Pulido, McNamara, Edge, Hogan, Vantyghem, Russell, Nulsen, Babyk, & Salomé, 2018). A variety of heat sources have been proposed to suppress cooling. The most persistent and capable heat source is the energy released from the central supermassive black hole traced by radio jets and X-ray bubbles embedded in hot atmospheres (e.g. Fabian, 2012; McNamara & Nulsen, 2007; Churazov et al., 2000). Chandra observations have shown that the energy released by buoyantly rising X-ray bubbles is able to balance atmospheric cooling over five decades of X-ray cooling luminosity (e.g. McNamara et al., 2000; Rafferty et al., 2006). However, how and how much jet energy is converted to atmospheric heating remains uncertain. Jet energy is transported throughout the atmosphere by a combination of weak shocks (e.g. Heinz et al., 1998; Fabian et al., 2006; Markevitch & Vikhlinin, 2007; **?**), sound waves (e.g. Sanders & Fabian, 2007; Sternberg & Soker, 2009; Nulsen & McNamara, 2013), and turbulence generated in wakes of the X-ray bubbles (McNamara & Nulsen, 2007; Graham, Fabian, & Sanders, 2008). Other mechanisms include heating from cosmic rays (e.g. Loewenstein et al., 1991; Guo & Oh, 2008; Pfrommer, 2013), gravity waves (Zhang, Churazov, & Schekochihin, 2018), and the release of gravitational potential energy by slow gas displacements (Hillel & Soker, 2016, 2017b). Regardless of sources that drive gas perturbations, the measurements based on power spectra analysis of X-ray surface brightness (SB) fluctuations suggest that dissipation of subsonic turbulence is, on average, sufficient enough to compensate for radiatively cooling loss and reheat ICM in cluster cores (e.g. Zhuravleva, Churazov, Schekochihin, Allen, Arévalo, Fabian, Forman, Sanders, Simionescu, Sunyaev, Vikhlinin, & Werner, 2014a; Zhuravleva, Allen, Mantz, & Werner, 2018).

As the cold, centrally accreting gas fuels the nuclear activities that suppress cooling is an essential part of the feedback loop, molecular clouds, bright nebular line emission and enhanced star formation are commonly observed in central cluster galaxies when the central entropy and cooling timescales fall below ~ 30 keV cm^2 and ~ 1 Gyr, respectively (e.g. Cavagnolo et al., 2008; Rafferty et al., 2008). The cold gas is expected to condense out of hot atmospheres when the ratio of cooling timescale to the free-fall timescale lies below the unity, $t_{cool}/t_{ff} \lesssim 1$ (e.g. Nulsen, 1986; Balbus & Soker, 1989; McCourt et al., 2011; Voit & Donahue, 2015). Nevertheless, the cooling time of the hot ambient medium pervading a massive galaxy does not drop much below ten times the free-fall timescale at any radius, even in the cores of clusters (e.g. Hogan et al., 2017; Pulido et al., 2018;

Babyk et al., 2019; Voit & Donahue, 2015). This again indicates that atmospheres are globally thermally stable. However, something must trigger thermal instability locally so that multi-phase condensation can proceed (e.g. Pizzolato & Soker, 2005, 2010; McCourt et al., 2012; McNamara et al., 2016; Gaspari et al., 2018).

Abell 2029 is the archetype in a handful of exceptions. The radiative cooling time in its inner 10 kpc falls below 5×10^8 yr, dropping to 2×10^8 yr within the central 3 kpc. Its gas density rises to 0.1 cm^{-3} yielding one of the known brightest atmospheric cusps of thermal X-ray emission. The ICM should be cooling into molecular clouds at a rate of several hundred solar mass per year (Sarazin et al., 1992). However, the optical observations are inconsistent with the relaxed cooling-flow picture of star formation, and nebular emission is absent at the levels seen in other clusters and groups with short central cooling time. Apart from a prominent swirl in its hot atmosphere associated with a cold front (Clarke et al., 2004; Paterno-Mahler et al., 2013), a feature common to many clusters with burgeoning central galaxies such as Perseus (e.g. Boehringer et al., 1993; Fabian et al., 2003), it reveals no X-ray cavities inflated by its central radio source.

McNamara et al. (2016) proposed that cold gas condenses from low entropy gas that is lifted outward from cluster cores to an altitude where its cooling time becomes shorter than its free-fall timescale, such that $t_{cool}/t_{ff} \lesssim 1$, by buoyantly rising X-ray bubbles. Martz et al. (2020) studied five cool core clusters: Abell 2029, Abell 2107, Abell 2151, RBS0533, and RBS0540 with relatively short central cooling times that show no evidence for cooling traced by nebular gas and star formation. Their analysis suggested that the absence of X-ray bubbles prevents the effective lifting of low-entropy gas to an altitude where the ratio of cooling time to free-fall time approaches unity. Thus they may temporarily be thermally stable.

The objective of this paper is to understand better why the five galaxy clusters, Abell 2029, Abell 2151, Abell 2107, RBS0533, and RBS0540, those lacking strong signatures of radio jet interaction, exhibit smooth atmospheres with short cooling times but do not appear to be cooling at appreciable rates.

Despite the absence of definitive evidence for X-ray cavities, the dissipation rate of gas turbulence, Q_{turb}, in the core of Abell 2029 generates sufficient heating to locally counteract the radiative cooling rate, Q_{cool}, although there remains considerable uncertainty (Zhuravleva et al., 2018). It suggests that turbulent dissipation driven by other processes may play an important role in preventing cooling in hot smooth atmospheres. For instance, X-ray observations frequently reveal spiral-like structures known as 'cold fronts' in the ICM of numerous clusters. These cold fronts, marked by sharp edges in temperature and density, can be seen in clusters such as Virgo (Roediger et al., 2011), Perseus (Fabian

et al., 2003, 2006), and Abell 2204 (Chen et al., 2017). The formation of these cold fronts can result from mergers with subhalos, which cause the cold gas to 'slosh' out from the cores of clusters (Markevitch & Vikhlinin, 2007). The spiral features seen in X-ray residual images of two smooth atmosphere clusters in our sample, Abell 2029, and Abell 2151, are evidence of interaction and may indicate their potential to produce sufficient turbulence (e.g ZuHone et al., 2011b; Walker et al., 2018) to prevent ICM from cooling, at least temporarily. Moreover, gas can be disturbed by jet-driven shock (Friedman et al., 2012) and by galaxy motions (Gu et al., 2013).

Using Chandra X-ray observations, we performed a new statistical analysis (Arévalo et al., 2012; Zhuravleva et al., 2014a,b) of X-ray surface brightness fluctuations in the cool-cores of these five smooth atmosphere clusters. Since this technique takes advantage of the weak temperature-dependence of the atmospheric emissivity in the soft energy band (0.5 - 3.5 keV is used in this work), the amplitudes emissivity fluctuations can be interpreted as equivalent to the amplitudes of density fluctuations measured over a range of spatial scales. (e.g. Forman et al., 2007). At higher energies (3.5 - 7 keV), emissivity depends strongly on temperature; therefore, the relative amplitudes of SB fluctuations (cross-spectrum) in the soft and hard band are sensitive to the atmosphere's effective equation of state, which enables us to understand the nature of gas perturbations (Zhuravleva et al., 2016, 2018; Churazov et al., 2016). Although high spatial-resolution Chandra observations fit in with such analysis well, pre-existing data of clusters studied here in the archive contains too few counts to yield reliable measurements on small scales where Poisson noise dominates. This lack of counts is amplified in the high energy band; hence effective equation of state of gas perturbations won't be measured in this work. Longer Chandra observations are required. To further investigate if their atmospheres in the core regions can be stabilized by turbulent dissipation, even though they lack AGN-inflated bubbles, we derive the velocity power spectra of gas motions and estimate the turbulent heating rates.

The structure of this paper is organized as follows: In Section 2.2, we describe the selected cluster samples with smooth atmospheres and outline the main steps of data reduction. Section 2.3 details the power spectrum analysis methodology. The results of the perturbation analysis are presented in Section 2.4 and discussed in Section 2.5. Finally, we provide our conclusions in Section 2.6. We here adopt ΛCDM cosmology with $\Omega_m = 0.3$, $\Omega_\Lambda = 0.7$ and $h = 0.72$ throughout this work.

2.2 Smooth Atmosphere Clusters and X-ray Images

2.2.1 Sample Selection

We focus on the X-ray surface brightness analysis in the cool cores of galaxy clusters Abell 2029, Abell 2107, Abell 2151, RBS0533, and RBS0540. These clusters were first identified as outliers from the ACCEPT database, based on the upper limits on Hα luminosity as suggested by Cavagnolo et al. (2008). Despite the absence of Hα emission and star formation at levels observed in other systems with similar thermodynamic properties, their central cooling times and central entropy fall below the thresholds of 10^9 yr and 30 keV cm^2, respectively. Our small sample spans a range of environments, from groups to rich clusters, with central densities and central pressures lying between $0.01-0.1$ cm^{-3} and $10^{-9}-10^{-10}$ erg cm^{-3}. Upon examining Chandra X-ray images of these five clusters, all atmospheres lack X-ray cavities, apart from RBS0533, which may have a potential cavity southeast of its center but with low significance. The relaxed atmospheres of Abell 2029 and Abell 2151 display spiral structures probably introduced by the 'slosh' motion of core gas arising from small infalling groups or subclusters. In this work, we study why the clusters in our sample remain thermally stable despite the absence of X-ray bubbles, which are typically associated with energetic central active galactic nucleus (AGN) activities. We explore whether contributions from other sources of turbulence might be capable of compensating for radiative cooling.

To explore the properties of gas perturbation natures of structureless atmosphere clusters in our sample, we also present the analysis within the half-cool-core region ($\sim 4.1'$ / 436 kpc) of Perseus cluster as a point of reference, using a total of 1.4 Ms of deep Chandra observations. The Chandra observations of our sample clusters and Perseus cluster are detailed in Table 2.1. The Perseus cluster is a bright, nearby galaxy cluster where the central cooling time is an order of magnitude lower than the Hubble time, and the central entropy also lies below 30 keV cm^2. Compared with our samples with smooth atmospheres, X-ray observations reveal AGN-inflated bubbles of relativistic plasma in the core of Perseus, surrounded by weak shocks (e.g Boehringer et al., 1993; Fabian et al., 2003, 2006). It indicates that the gas in the central region of the Perseus cluster is strongly disturbed, and gas turbulent motions might be triggered during the inflation and buoyant rising of those bubbles. Zhuravleva et al. (2014a) measured the amplitude of gas perturbations in the core of Perseus from its X-ray surface brightness fluctuation power spectrum. They found that central AGN activities might play a dominant role in driving gas turbulent motions in the cool core of Perseus, and the heating rate due to the dissipation of gas turbulence should be sufficient to balance radiative loss, maintaining an approximately stable state in

Cluster	ObsIDs	Redshift	BCG Position		Cleaned T_{exp}	N_H	r_{cool}
			RA (J2000)	DEC (J2000)	ks	$10^{22}cm^{-2}$	kpc
(a)	(b)	(c)	(d)	(e)	(f)	(g)	(h)
RBS0533	3186, 3187, 5800, 5801	0.0123	4:19:38.105	+2:24:35.54	107.9	0.102	58
Abell 2029	891, 4977, 6101	0.0773	15:10:56.077	+05:44:41.05	103.3	0.033	180
Abell 2151	4996, 19592, 20086, 20087	0.0366	16:04:35.758	+17:43:18.54	80.2	0.033	94
RBS0540	4183, 19593, 20862, 20863	0.0397	4:25:51.300	-8:33:38.00	61.6	0.079	115
Abell 2107	4960,24350,24351,26152, 26153,26443, 23851	0.0410	15:39:39.043	+21:46:58.55	140.0	0.045	71
Perseus	3209, 4289, 4946, 4947 - 4953, 12025, 12033, 12036, 12037	0.0176	03:19:48.160	+2:16:1.00	1335.5	0.136	174

Table 2.1: Clusters and Chandra observations in our analysis: (a). Cluster name, (b). Observations used in this analysis, (c). Redshift, (d). Right Ascension (J2000), (e). Declination (J2000), (f). Cleaned exposure after data reduction, (g). Column density, and (h) Cool-core radius.

the ICM.

2.2.2 Data Reduction

The analysis in this work is based on archival Chandra X-ray data utilizing the Advanced CCD Imaging Spectrometer (ACIS) detectors ACIS-I and ACIS-S. Observations used in this analysis are summarized in Table 2.1. All have been reprocessed following Vikhlinin et al. (2005). The observations were reduced using `CIAO` version 4.12, `CALDB` version 4.9.2. Light curves were extracted from level-2 event files above 10 keV using the `lc_clean` script to eliminate intervals affected by background flares. Blank sky files were normalized to count rates in the $10 - 12$ keV range and projected to the corresponding positions. Exposure maps were calculated to correct for varying exposure coverage caused by chip gaps and vignetting. Multiple observations were projected onto the one with the longest exposure and summed into a background-subtracted, exposure-corrected image. Point sources, including the central AGN, were identified using the `wavdetect` tool and by inspection and were removed accounting for the shape of the Point Spread Function (PSF).

The X-ray emissivity, $\Lambda(T)$ in the low energy band ($0.5 - 3.5$ keV in this work), is largely independent of the gas temperature when higher than ~ 3 keV. Therefore, surface brightness fluctuations shown in this band are used to infer ICM density fluctuations. Three clusters have a volume-weighted mean temperature lying below 3 keV within the region of interest: RBS0533 at ~ 1.2 keV, Abell 2151 at ~ 2.2 keV, and RBS0540 ~ 2.8 keV. To validate the temperature independence in each target, we employed a narrower and softer energy band of $0.5 - 1.5$ keV to measure perturbations and compared these with results from the $0.5 - 3.5$ keV band. The discrepancies between the two energy band measurements are less than 6%. The narrower energy band yields fewer counts which limits the smallest scales we can probe and amplifies the uncertainties primarily due to Poison noise. Therefore, X-ray images were prepared in the $0.5 - 3.5$ keV band given the minimal temperature dependence in this 'soft' energy band and its higher photon count contribution.

Figure 2.1 displays the reprocessed Chandra images of the sample cluster cores with smooth atmospheres in the $0.5 - 3.5$ keV band. Green dashed circles indicate the areas of the cool cores. The cool-core radius is summarized in column (h) of Table 2.1 for each target. The measurement precision within the cool cores of RBS0533, Abell 2151, and Abell 2107 is limited by their relatively low surface brightness or the existing Chandra exposure. We thus reduced our regions of interest to the inner half of cool-cores in these three objects, which are marked as solid green circles in Figure 2.1. The deep Chandra

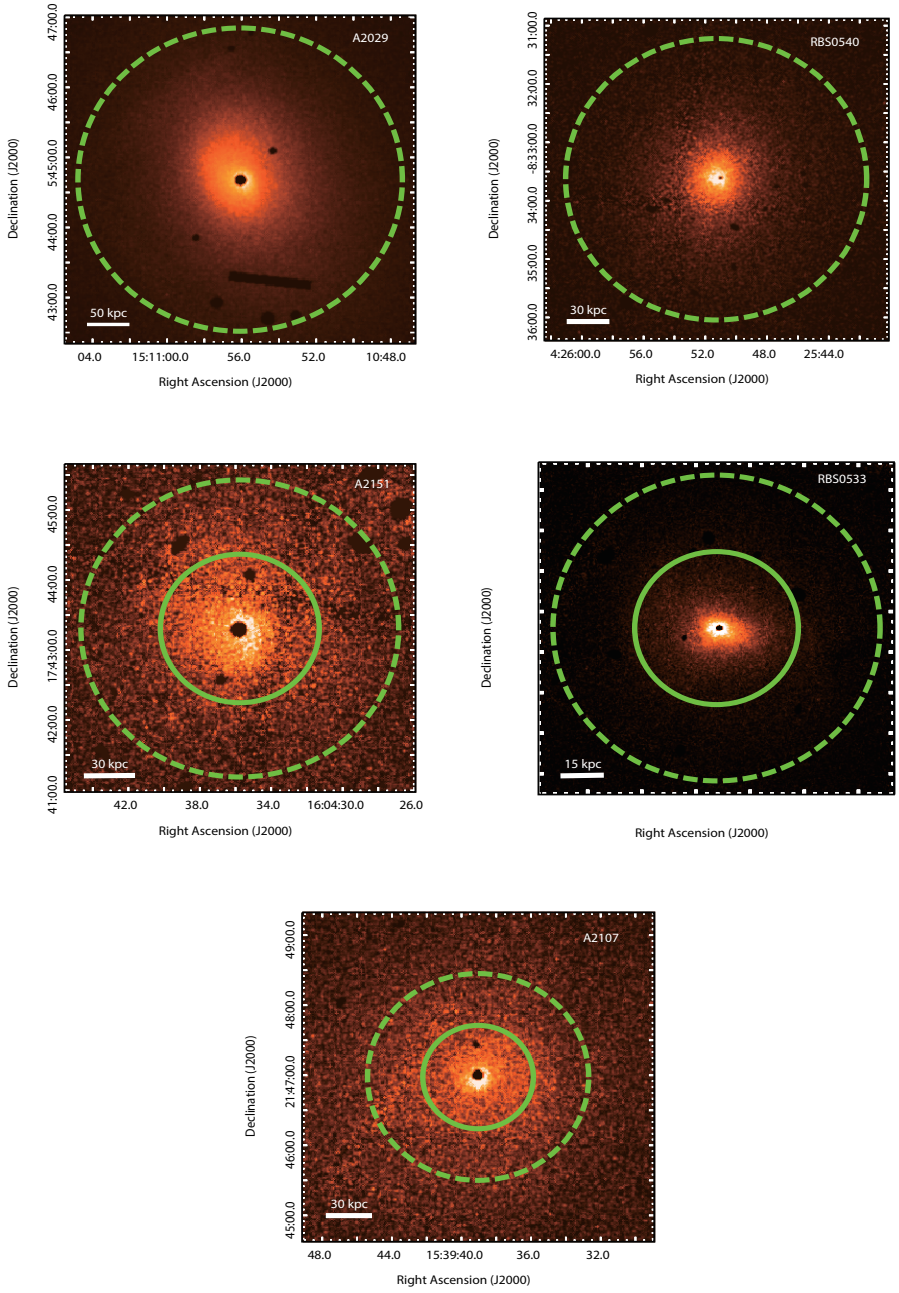


Figure 2.1: The background-subtracted, exposure-corrected Chandra images of our targets in the $0.5-3.5$ keV band. The cool-core radius is indicated with dashed green circles, and the inner half of the cool-core radius is marked in the green solid line. The bright point sources and the central AGNs have been masked out. The images are smoothed with a 3" Gaussian for display purposes.

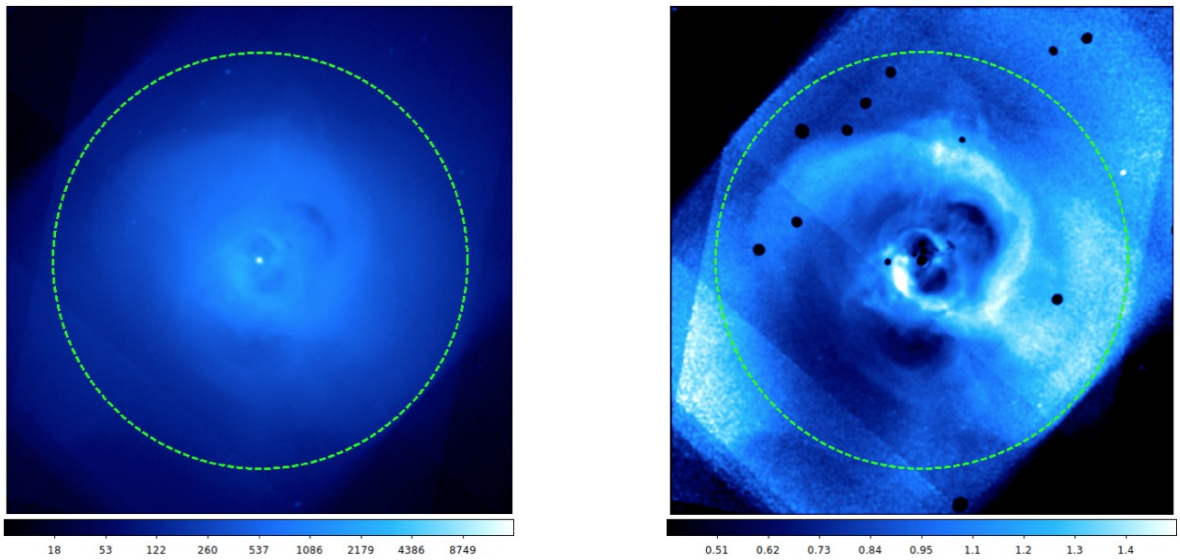


Figure 2.2: Left: Background-subtracted, exposure-corrected mosaic Chandra images of the Perseus cluster in the $0.5 - 4$ keV band. The dashed green circle indicates the inner region within half cool core radius, denoted as $0 < r < r_{\rm cool}/2$. Each image is smoothed with a 3" Gaussian for display purposes. Right: Residual X-ray image of the Perseus cluster, obtained by dividing the initial image by the best-fitting spherically symmetric β-model. The bright point sources and the central AGNs have been masked out.

X-ray mosaic of the Perseus core is created in 0.5 - 4 keV and is presented in the left panel of Figure 2.2. The green dashed circle shows the central region we studied, within the half cool-core radius ($\sim 4.1'/436$ kpc).

Deprojected Thermodynamic Profiles

Spectra were extracted from concentric circular annuli centered on the brightest cluster galaxy (BCG) within the 0.5 - 7 keV energy band, with the coordinates of the BCGs detailed in Table 2.1. The central annulus contains at least 3000 counts. The emission observed at any location contains superposed emission from hotter, overlying layers. To measure and remove the overlying emission, the spectra were deprojected using `DSDEPROJ` (Russell et al., 2008; Sanders & Fabian, 2007). Spectra were extracted separately from each observation and grouped to ensure a minimum of 30 counts per energy bin. To ensure accurate deprojected temperature measurements the net counts in subsequent annuli were set to be 1.2 times the count of the preceding one.

Thermodynamic properties were derived from spectra using an absorbed thermal model `Phabs*(apec)` built in `XSPEC`. The initial values for the galactic hydrogen column density used for fitting were based on the measurements provided by Kalberla et al. (2005), as listed in column (g) of Table 2.1. This parameter was then allowed to vary freely within each spectral bin. The heavy element abundance was treated as a free parameter.

Using the radial profiles of temperature T and electron number density n_e, we calculated the entropy index of the ICM as $K = k_B T n_e^{-2/3}$, where k_B is the Boltzmann constant. The cooling timescale was calculated using:

$$t_{cool} = \frac{3}{2}\frac{(n_e + n_i)k_B T}{n_e n_i \Lambda(T)}, \tag{2.1}$$

where $n_i = (\xi - 1)n_e$ is the ion number density with $\xi = 1.912$ for fully ionized gas. The normalized cooling function, $\Lambda(T)$, assuming $Z_\odot = 0.3$ was derived from the tabulations by Sutherland & Dopita (1993). The cool-core radius in this work denoted as r_{cool}, is defined as the distance from the center within which the cooling timescale of the ICM is shorter than the Hubble time, which is $\sim 1.36 \times 10^{10}$ yr according to the cosmological parameters we adopted.

Assuming identical ion and electron temperatures and an ideal monatomic gas, the sound speed c_s is given by:

$$c_s = \sqrt{\gamma \frac{k_B T}{\mu m_p}}, \tag{2.2}$$

where $\gamma = 5/3$ is the index for monatomic ideal gas, and $\mu = 0.61$ and m_p are the mean particle mass and the proton mass, respectively.

The deprojected radial profiles of (a) cooling timescale, (b) gas entropy, (c) temperature, (d) electron density, and (e) sound speed are depicted in Figure 2.3. All five clusters reveal both short central cooling times, less than 10^9 yr, and entropy lying below 30 keV cm^2 within the innermost 10 kpc, meeting the critical thresholds for bright nebular emission and high star formation rates. However, this does not align with our observations of smooth atmospheres, suggesting that additional processes are counteracting the expected cooling.

Underlying Surface Brightness model

The surface brightness distributions are decomposed into two components: an 'unperturbed' component, which typically peaks at the center and decreases with radius in re-

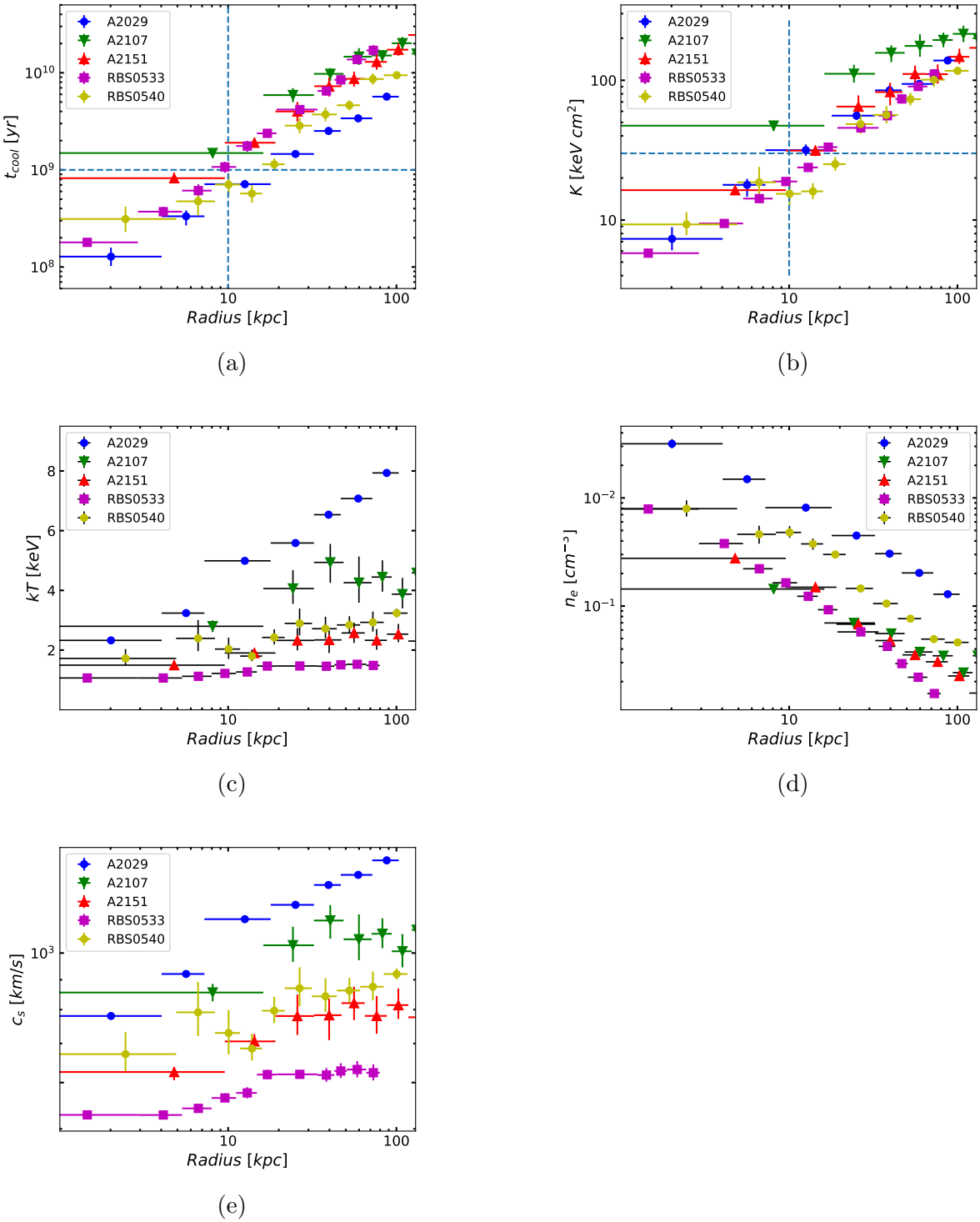


Figure 2.3: Deprojected thermodynamic radial profiles in the $0.5 - 7$ keV band of sample clusters: (a) cooling timescale, (b) entropy, (c) electron temperature, (d) electron density, and (e) sound speed. The dashed vertical lines in (a) and (b) indicate a radius of 10 kpc, and the dashed horizontal lines represent the threshold values $t_{cool} = 1.0 \times 10^9$ yr and entropy $K = 30$ keV cm^2, respectively.

laxed clusters, and a 'perturbed' component. The 'unperturbed' SB distribution reflects the global potential of the cluster in equilibrium, and is commonly described by a spherically symmetric $\beta-$model:

$$I_X(R) = I_0 \left[1 + \left(\frac{R}{r_c}\right)^2\right]^{3\beta-0.5} \tag{2.3}$$

where I_0 is the central surface brightness, r_c is the core radius, R is the projected distance from the cluster center, and β is a dimensionless parameter that determines the slope of the SB radial profile. The SB global gradient will dominate the power spectrum of raw X-ray images, resulting in high power at large scales and leakage to smaller scales. To analyze gas perturbations relative to this smooth 'unperturbed' background, the raw images were divided by the best-fitting $\beta-$models to remove the large-scale SB gradient.

A spherical β model does not capture the elliptical morphology of Abell 2029 or the slight west-east asymmetry observed in the SB of RBS0533. In addition, cool-core clusters have cusps of X-ray emission requiring a two-component β model: one for the central peak and another for the broad, shallow outer gas distribution. To assess the uncertainty caused by using an oversimplified model, we re-analyzed the SB fluctuations in the Abell 2029 cool core with an elliptical double-β model.

The comparison between two-dimensional (2D) power spectra of surface brightness fluctuations in the cool core of Abell 2029, obtained from the single $\beta-$model (in blue) and the double $\beta-$model (in green), is illustrated in Figure 2.4. This comparison reveals that the power of SB fluctuations remains almost unchanged regardless of the underlying SB model used. However, a suppressed power amplitude is observed on large spatial scales when using the double-β model. This suppression is attributed to the double β-model accounting more for features at large scales related to the underlying cluster potential rather than to perturbations. Small residuals between extracted SB profiles and best-fit profiles for both models (less than 3%) indicate an acceptable fit of the single β-model for Abell 2029. The impact of the model choice on the SB analysis of Abell 2029 is negligible. However, the choice of model depends on the specific characteristics and the scales at which the analysis is performed and is therefore evaluated for each sample cluster.

A double β-model is used for analyzing Abell 2107 and RBS0540, while the single β-model is chosen for the others. The best-fit parameters are provided in Table 2.2 for each sample. As the innermost region surrounding the AGN was removed prior to fitting, the parameters listed in Table 2.2 do not describe the properties of the cool core and the periphery.

The uncertainties associated with selecting the underlying $\beta-$models are also explored in Zhuravleva et al. (2015). Their study concludes that while more complex models might suppress the amplitude of density fluctuations across a wider range, the measurements on relatively small scales remain largely consistent, except in cases where the gas is highly disturbed. This finding is consistent with ours.

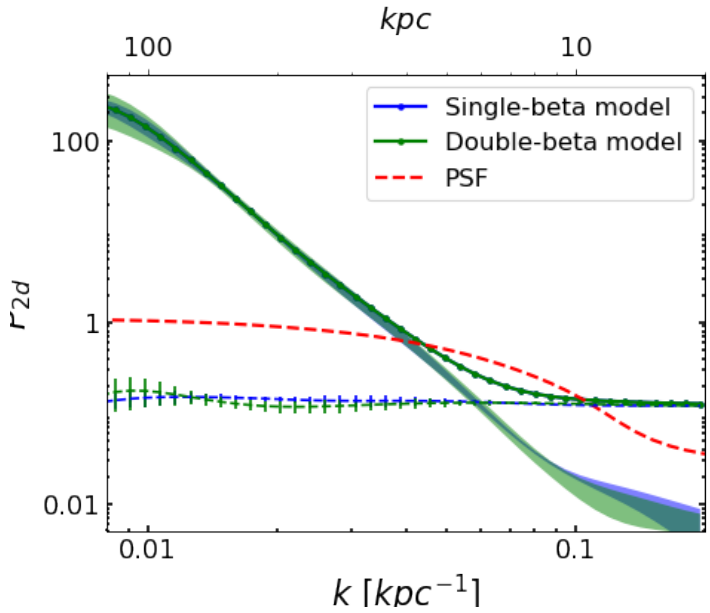


Figure 2.4: Power spectra of surface brightness fluctuations in the cool core of Abell 2029 derived using two different β-models. The global SB gradient has been removed by dividing the raw image with an elliptical single-β model, marked in blue points, and a double-β model, presented in green points. The horizontal dashed lines with error bars represent the Poisson noise levels, which were subtracted from the raw spectra to obtain the corrected power spectra of SB fluctuations, depicted by the shaded areas. The mean PSF spectrum, calculated from 20 simulated PSF images within the cool core of Abell 2029, is shown as a red dashed line.

Figure 2.5 shows the residual images of these smooth atmosphere clusters in the $0.5-3.5$ keV energy band, created by dividing the initial mosaic images shown in Figure 2.1, by the best-fitting spherically symmetric single/double $\beta-$model. Despite relatively structureless atmospheres, these X-ray residual images of sample clusters reveal structures that indicate disturbances in the ICM. RBS0533, for instance, shows a surface brightness depression to the north of its center, indicating a potential X-ray cavity. In contrast, the other four objects exhibit no prominent bubbles or cavities, typically associated with the central AGN

Cluster	I_1 cnts/arcsec^2	$R_{c,1}$ arcsec	β_1	I_2 cnts/arcsec^2	$R_{c,2}$ arcsec	β_2	ψ deg	e
(a)	(b)	(c)	(d)	(e)	(f)	(g)	(h)	(i)
RBS0533	50.2	8.2	0.40	-	-	-	-	-
Abell 2029	124.1	23.1	0.48	-	-	-	115	1.15
Abell 2151	5.5	11.7	0.37	-	-	-	-	-
Abell 2107	7.3	44.3	6.2	3.2	36.7	0.37	-	-
RBS0540	16.7	22.0	0.93	4.0	49.5	0.53	-	-

Table 2.2: The best-fitting β-model parameters of the underlying surface brightness profiles of our targets: (a). Cluster name, (b-d). Central surface brightness, Core radius, and β of the first component, (e-g). Central surface brightness, Core radius, and β of the second component, (h). The orientation angle of the observed ellipse, and (i). Eccentricity, defined as the ratio of the major to the minor axis as projected.

activities. Notably, in Abell 2029, the residual image reveals a significant spiral-like feature extending clockwise from the center to about 400 kpc at its farthest extent (Paterno-Mahler et al., 2013). Such a substructure is likely a result of gas sloshing from cluster cores, induced by small infalling groups or subclusters that gravitationally perturb the cluster core, as evidenced by similar features in numerical simulations (Ascasibar & Markevitch, 2006; ZuHone et al., 2010, 2011a). In Abell 2151, there appears to be a potential spiral feature, although it is not as distinct as the one observed in Abell 2029.

2.3 Surface Brightness Fluctuation Analysis

Gas perturbations in the X-ray residual images are quantified using the power spectrum of surface brightness fluctuations across various spatial scales. The $\Delta-$variance method as described by Arévalo et al. (2012) is used in this work, which is effective for images with irregular boundaries or significant areas missing. For a given spatial scale $k = 1/\sigma\sqrt{2\pi^2}$, the images are convolved with two Mexican hat filters of widths σ_1 and σ_2:

$$\sigma_1 = \sigma/\sqrt{1+\epsilon},\ \sigma_2 = \sigma\sqrt{1+\epsilon},\ (\epsilon \ll 1). \tag{2.4}$$

This process isolates fluctuations at scale σ by computing the differences between the two convolved images. The variances of the resulting images are then calculated as a function of the wavenumber, which serves as a measure of the power of the SB fluctuations $P_{2D}(k)$ at a given spatial scale.

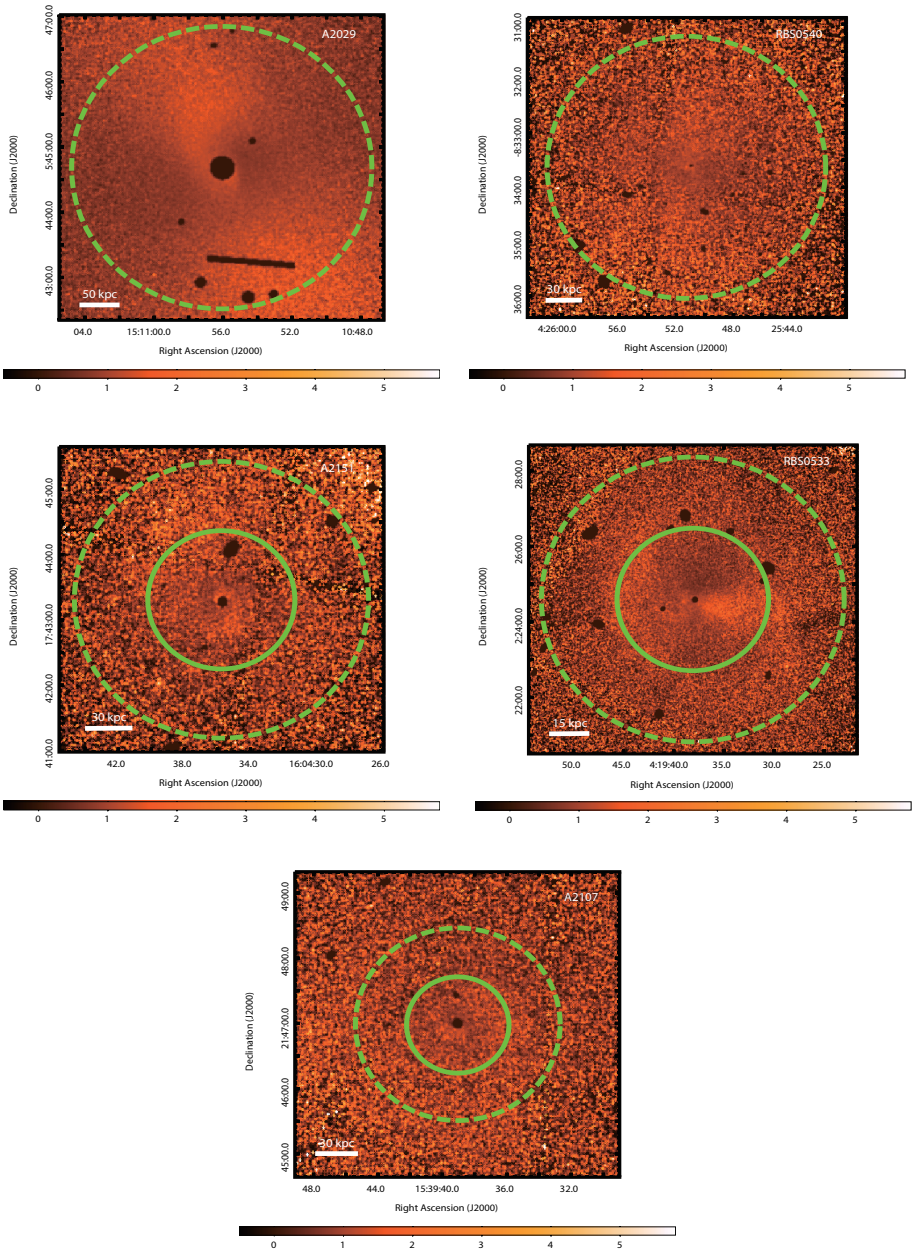


Figure 2.5: The residual images of smooth atmosphere clusters in the 0.5 - 3.5 keV band. The underlying surface brightness gradients are removed by dividing raw images by the best-fitting $\beta-$models, summarized in Table 2.2. The cool-core radius is indicated with dashed green circles, and the inner half of the cool-core radius is marked in the green solid line. The residual images are processed with a 3" Gaussian smoothing for display purposes. The bright point sources and the central AGNs have been masked out.

Poisson noise is expected to display a flat, white noise spectrum, especially dominating at smaller spatial scales. The power spectrum of Poisson noise, given the number of counts n_{cts} in each pixel, can be estimated, albeit with minor deviations due to the effects of image edges or data gaps. For this purpose, 100 mock images are generated, and each with Poisson noise simulated by multiplying the square root of the counts $\sqrt{n_{cts}}$ in each pixel by a random number from a Gaussian distribution with a mean of 0 and a variance of 1. The PS of Poisson noise is calculated for each mock image and the average is used to estimate the Poisson noise contribution. As shown by the horizontal dashed lines in Figure 2.4, the Poisson noise levels are comparable to the raw PS of SB fluctuations at large wavenumber k, thereby limiting our measurements at small spatial scales. We correct the Poisson noise by subtracting the estimated PS of Poisson noise from the raw PS. The scatter of these white noise spectra, denoted as $\sigma_{P_{wn}}$, is then scaled by the following factor:

$$\sigma_p = \sigma_{p_{wn}} \frac{P_{2D}}{P_{wn}}, \tag{2.5}$$

giving an estimation of the uncertainties in PS of SB fluctuations. In this work, we present only the measurements at scales least affected, where the power of the cleaned spectra must exceed the level of Poisson noise.

In addition, the images are smeared by the instrumental PSF. Consequently, understanding the PSF at various positions across the cluster images is critical for correcting the suppressed power at small scales and accurately determining the high-k cutoff. We use a simplified analytic model to approximate the observed PSF spectra of the Lockman Hole field for the Chandra telescope, as provided by Churazov et al. (2012):

$$P_{PSF,Chandra} = \frac{1}{\left[1 + \left(\frac{k}{0.06}\right)^2\right]^{1.1}}, \tag{2.6}$$

where the unit of wavenumber k is arcsec^{-1}. The PSF correction is applied by dividing the power spectra of the images by the power spectra of the PSF.

To accurately account for the PSF effects on the power spectrum, we generated simulated PSF maps for each cluster using the Chandra Ray Tracer (`ChaRT`) and `MARX` at various off-axis angles. The PSF for each observation is determined using Chandra's PSF libraries. The PSF images were then sampled across the field of view. The simulated map of the combined Chandra PSF of Abell 2029 is shown in Figure 2.6. The PSF exhibits distortion, especially near the edges of the image. The power spectra of simulated PSF maps are computed and used for PSF effect correction. The mean PSF spectrum is calculated from

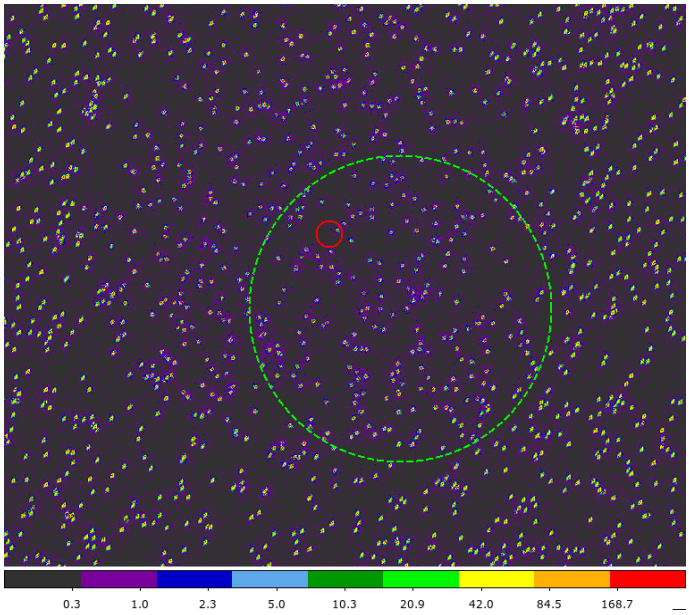


Figure 2.6: The simulated map of the combined Chandra PSF within the mosaic image of Abell 2029. The red solid circle indicates the position of the optical axis, while the dashed green circle represents the region of interest in our analysis.

20 simulated PSF images within the cool core of Abell 2029, and is shown as a red dashed line in Figure 2.4.

The contribution of unresolved point sources on the power of SB fluctuations is estimated for each target by measuring the flux distribution of point sources, following the method given in (Churazov et al., 2012; Heinrich et al., 2024). The power of unresolved point sources is much lower than that of bright point sources, which have been excluded from the residual images. In the cool core of Abell 2107, the ratio of the power of bright point sources P_{bright} to that of faint point sources $P_{unresolved}$ is around 10^9, while the ratio of other sample clusters is in range of $10^6 \sim 10^9$. Therefore, the contribution from the unresolved point sources is negligible to our analysis.

The X-ray emissivity is proportional to the integral of the square of the electron number density ($\int n_e^2 dl$) over the line of sight. Therefore, in such clusters, the amplitudes of SB fluctuations indicate the amplitudes of gas density fluctuations. We converted the 2D SB fluctuations power spectra, $P_{2D}(k)$, into 3D density fluctuations power spectra, $P_{3D}(k)$, assuming a spherically symmetric geometry of clusters. This process is discussed in detail in the works of Churazov et al. (2012) and Zhuravleva et al. (2015). The conversion factor

between the 3D power spectrum and the 2D power spectrum at each line of sight z is given by the following relationship:

$$\frac{P_{2D}(k)}{P_{3D}(k)} \approx 4 \int \left|W(k_z)^2\right| dk_z, \tag{2.7}$$

where $|W(k_z)|^2$ is the 1D power spectrum of the normalized emissivity distribution along the line of sight. The dependence of this normalization constant $\int |W(k_z)^2| \, dk_z$ in the x and y direction can be neglected in the central regions of clusters with 'flat' SB profiles, such as the Coma cluster. In our sample cool-core clusters, the SB slope is usually steep in the center and this correcting factor will vary across the region of interest. Therefore, in this work, we implemented a 'local' correction factor to account for these variations.

Rather than using the gas density power spectra $\mathrm{P_{3D}(k)}$ directly, it is often more convenient to employ the characteristic amplitude of density fluctuations:

$$\frac{\delta\rho_k}{\rho_0} \equiv A_{3D}(k) = \sqrt{4\pi P_{3D}(k) k^3}, \tag{2.8}$$

which represents the typical variations in gas density relative to the 'unperturbed' smooth density distribution, since its unit is the same as that of the variable in real space.

The velocity power spectra for gas motion can be inferred from the power spectra of density fluctuations. In a stratified ICM where perturbations are small, the one-component velocity at each wavenumber k, denoted by $V_{1,k}$, is linearly proportional to the amplitude of density fluctuations $\mathrm{A_{3D}(k)}$:

$$\frac{\delta\rho_k}{\rho_0} = \eta_1 \frac{V_{1,k}}{c_s}, \tag{2.9}$$

where $\mathrm{c_s}$ represents the sound speed in the atmosphere as given in equation (2.2). Zhuravleva et al. (2014b) provided a theoretical argument and confirmed this linear scaling relation across a broad range of scales in both buoyancy-dominated and turbulence regimes using cosmological simulations of relaxed clusters. The proportionality coefficient $\eta_1 = 1 \pm 0.3$ at scales of 30 - 300 kpc. Using simulations of 80 clusters in different dynamical states, Zhuravleva et al. (2023) verified this strong linear correlation between the gas density fluctuation amplitudes and the Mach number of gas motions in relaxed galaxy clusters. After accounting for the ellipticity of the gas distribution, the average η_1 is 0.9 ± 0.2 (1.2 ± 0.3) at scales from 60 to 300 kpc. Our clusters are well-represented by the simulated relaxed clusters in Zhuravleva et al. (2023). While simulations validate the linear scaling relation across

various conditions, they typically do not consider factors such as metallicity variations and non-thermal, spatially variable components. These elements can induce emissivity fluctuations independent of gas motion velocities, implying that the derived scale-dependent velocity amplitudes might represent upper limits.

2.4 Results

Here we present our measurements of gas density fluctuations in Section 2.4.1. We discuss indirect measurements of one-component velocity spectra derived from the power spectra of density fluctuations in Section 2.4.2. In Section 2.4.3, the turbulent heating rate for each object is estimated and compared to the radiative cooling rate to examine if turbulent dissipation is able to balance cooling in the cluster cores.

2.4.1 Density Fluctuations in the Smooth Atmosphere Clusters

The power spectra of surface brightness fluctuations in the $0.5 - 3.5$ keV band are measured to determine the density fluctuation amplitudes as a function of the wavenumber k. Figure 2.7 presents the power spectra of density fluctuations measured in the cool cores of Abell 2029, RBS0540, and within the inner half cool-core radius of RBS0533, Abell 2151, Abell 2107, and Perseus. The mean spectra are shown as the dashed lines, while the widths of the hatched regions represent the 1σ statistical uncertainties.

We excluded the measurements at large scales where amplitude flattening occurs. This flattening likely indicates leakage from the global surface brightness gradient induced by uncertainties in selecting the appropriate SB model, discussed in Section 2.2.2. The smallest scales that can be probed are determined by both the Poisson noise level and PSF distortions. The raw spectra of SB fluctuations are corrected using the estimated Poisson noise level. If the cleaned power spectrum lies below the power of Poisson noise, those measurements are excluded, and only the measurements over scales least affected by noise are retained. In addition, while equation (2.6) implies that PSF blurring effects are negligible with Chandra instruments at the low-k end ($P_{\rm PSF,Chandra} \sim 1$, presented in Figure 2.4), our analysis of the PSF effect, conducted using simulated PSF maps for each cluster as detailed in Section 2.3 reveals variations. After PSF correction, we only accept measurements over scales where the PSF suppression on 2D power spectra is less than 30%, which corresponds to less than 20% suppression on density fluctuation amplitudes. This condition ensures the reliability of the results, but measurements over scales less than 10 kpc cannot be achieved

Cluster	Region	Scales	$\frac{\delta\rho}{\rho_0}$
	kpc	kpc	per
(a)	(b)	(c)	(d)
RBS0533	1.5 - 30	$8 \sim 33$	$10.0 \sim 13.8$
Abell 2029	5 - 180	$28 \sim 216$	$5.7 \sim 14.8$
Abell 2151	3 - 47	$20 \sim 35$	$14.5 \sim 16.5$
Abell 2107	4 - 35	$15 \sim 29$	$14.6 \sim 15.3$
RBS0540	5 - 115	$54 \sim 155$	$4.9 \sim 7.8$
Perseus	5 - 87	$12 \sim 50$	$10.2 \sim 14.4$

Table 2.3: The density fluctuation amplitudes measured within the cooling regions of our sample clusters and within the inner half cool core region of Perseus: (a). Cluster name, (b). Region of interest, (c). Spatial scales least affected by Poisson noise, (d). Amplitudes of gas density fluctuations.

in the core regions of all targets, with one exception, RBS0533, where the measured gas density fluctuations at the scale of 8 kpc is 10 per cent. The high-wavenumber cutoff in its inner half cool-core is determined by the Poisson noise level, even when using strict criteria. Additionally, the PSF suppression is $\sim$ 20% at 10 kpc due to its low redshift of 0.0123 (lower than Perseus z = 0.0176). Furthermore, its cooling region is small, with $r_{cool} \sim 60$ kpc, and we only analyzed the inner half core. This means the region of interest is the very central part, where the PSF effect is relatively small. To maximize the utilization of the data, we have retained the results below the scale of 15 kpc for Abell 2107 and 20 kpc for Abell 2151 in Figure 2.7, marked with hatched areas, even though the measurements may be more significantly affected by PSF effects.

Although the ranges of measurable scales vary across the objects, the typical amplitudes of density fluctuations remain relatively small. In four out of the five clusters, the amplitudes are less than 15 per cent even on the largest scales probed. These modest amplitudes suggest mild gas perturbations. The measured gas density amplitudes are summarized in Table 2.3. An exception is observed in Abell 2151, where it reaches $\sim$ 17 per cent at a scale of 35 kpc.

The 1.4 Ms of Chandra observations of the Perseus cluster enable us to probe surface brightness fluctuations at scales of $\sim$ 12 kpc. Within the inner half cool-core region, the SB amplitudes vary from $\sim$ 10 per cent to 14 per cent at scales of 12 - 50 kpc. The residual

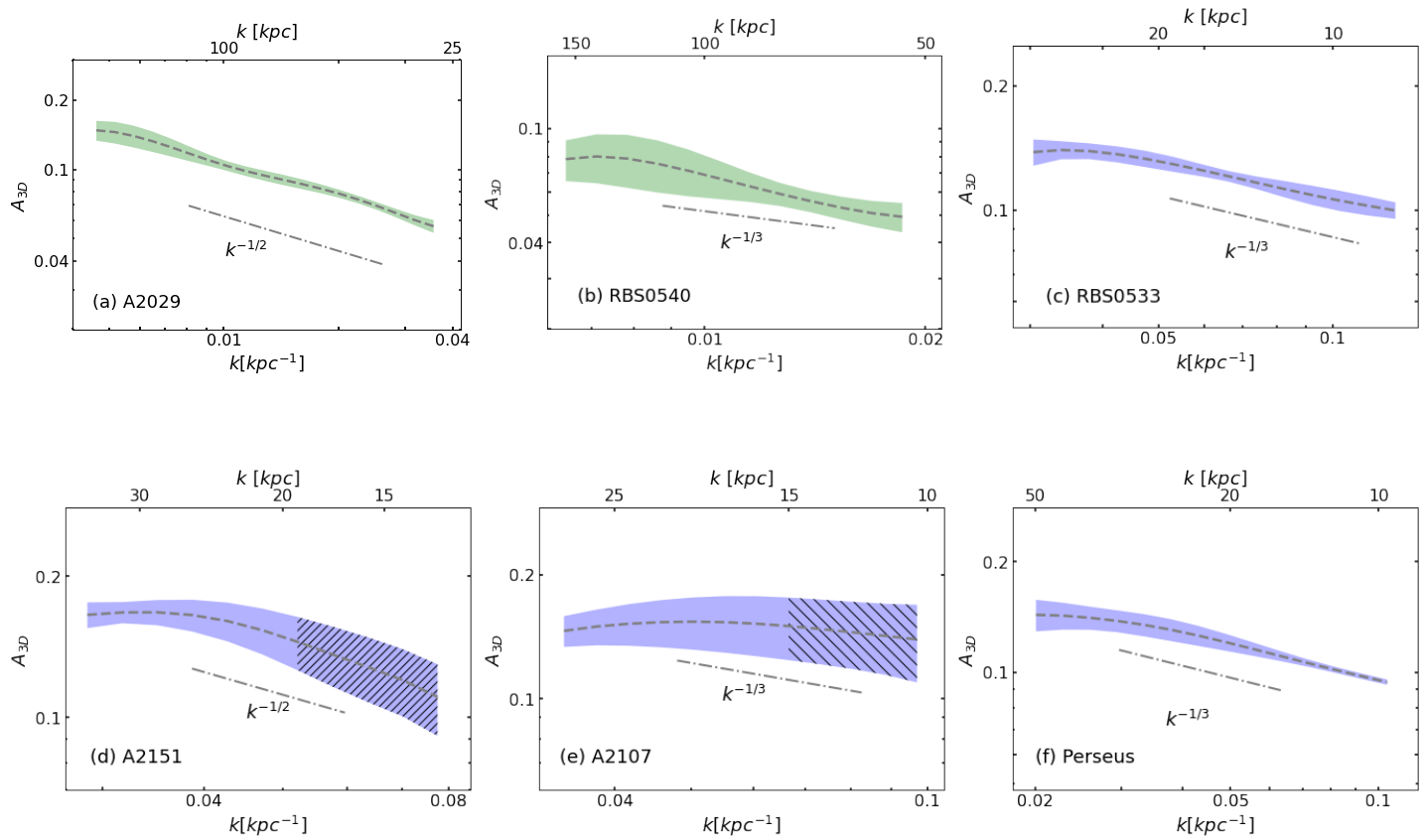


Figure 2.7: Gas density Fluctuation amplitudes of our five sample clusters and the Perseus Cluster. The measurements were conducted within the cool-core radius of (a) Abell 2029, (b) RBS0540, and within the inner half of the cool-core radius of (c) RBS0533, (d) Abell 2151, (e) Abell 2107, and (f) the Perseus Cluster. The central dashed lines present the mean spectra, while the widths of the shaded regions reflect the 1σ uncertainties. Displayed are measurements taken over scales that are minimally impacted by Poisson noise and PSF effect ¡ 20%. The results below the scale of 15 kpc for Abell 2107 and 20 kpc for Abell 2151, marked with hatched areas, maybe more significantly affected by PSF effects.The grey dash-dotted lines represent slopes of $k^{-1/3}$ or $k^{-1/2}$ as guidelines.

image of the Perseus cluster in the right panel of Figure 2.2 reveals that a significant portion of its core is filled with bubbles and sharp shock edges. These features are driving the relatively high fluctuation amplitudes. Similarly, the residual image of RBS0533 displays a surface brightness depression north of its center, identified as a possible X-ray cavity of $\sim$ 7.5 kpc in size, $\sim$ 10 kpc from the center by Martz et al. (2020). The bubble in RBS0533 is potentially capable of inducing gas turbulent motions comparable to those observed in Perseus, with amplitudes ranging from $\sim$ 9 to 14 per cent at scales of 5 - 33 kpc.

Despite the overall lack of X-ray cavities in structureless atmospheres, the observed density fluctuations are comparable to those in the Perseus cluster in four of five of our systems, except RBS0540. This suggests that other factors, such as gas sloshing, create gas perturbations. In Abell 2029, the amplitudes of density fluctuations are $\sim 5.7 - 14.8$ per cent at scales of $28 - 216$ kpc. In contrast, Abell 2151 exhibits higher density fluctuations in its core, ranging between $14.5 - 16.5$ per cent at scales of $20 - 35$ kpc, surpassing those observed in Perseus, which is known for its feature-rich X-ray images. The residual image of Abell 2029 clearly reveals a spiral feature related to a cold front, as indicated by a sharp change in surface brightness. A less distinct sloshing feature observed in the residual image of Abell 2151 suggests the possibility of an ongoing merger. These observations support the hypothesis that the gravitational disturbances induced by merging subclusters may also effectively trigger gas density fluctuations in these systems.

Due to the relatively high redshift and limited exposure, density fluctuations in our targets cannot be measured at the small scales that are possible in Perseus, complicating direct comparisons. Nonetheless, in RBS0540 the fluctuation amplitudes are lower than in the other four objects, remaining below 10 per cent across the probed range of spatial scales. These amplitudes could be even lower at smaller scales or within the outer regions where the gas is less disturbed than the core regions.

2.4.2 Velocity Power Spectrum

Using the measured power spectra of density fluctuations, the amplitudes of the one-component velocity of gas motions can be derived indirectly, following the linear scaling relation illustrated in equation 2.9. The one-component velocity spectra in the cooling regions of our targets and Perseus are presented in Figure 2.8. The dashed lines show the mean velocity spectra, obtained by using the volume-weighted sound speed of the gas, while the widths of the regions represent the 1σ uncertainties, which reflect the variances in sound speed across the cool cores of Abell 2029, RBS0540, as well as within the inner half cool-cores in RBS0533, Abell 2151, Abell 2107, and Perseus. The temperatures used

Cluster	M_{2500}	Region	T	Scales	$V_{1,k}$	Q_{turb}	Q_{cool}
	$10^{14}\ M_{\odot}$	kpc	keV	kpc	km s^{-1}	erg cm^{-3} s^{-1}	erg cm^{-3} s^{-1}
(a)	(b)	(c)	(d)	(e)	(f)	(g)	(h)
RBS0533	$0.17^{+0.02}_{-0.02}$	2 - 30	1.2	8 − 33	60 − 83	9.9×10^{-28}	9.2×10^{-28}
Abell 2029	$5.1^{+0.20}_{-0.18}$	4 - 90	6.9	16 − 105	68− 162	2.1×10^{-27}	9.5×10^{-27}
		90 - 180	8.4	44 − 217	92− 147	3.2×10^{-28}	9.6×10^{-28}
Abell 2151	$5.1^{+0.20}_{-0.18}$	4 - 47	2.2	20 − 35	112 − 126	1.8×10^{-27}	1.1×10^{-27}
Abell 2107	$1.05^{+0.23}_{-0.23}$	3 - 35	3.9	15 − 29	169 − 178	4.9×10^{-27}	1.4×10^{-27}
RBS0540	$0.32^{+0.03}_{-0.03}$	4 - 55	2.8	54 − 155	43 − 68	6.1×10^{-27}	6.5×10^{-29}
Perseus	$1.5^{+0.03}_{-0.03}$	6 - 90	3.8	12 − 50	76 − 143	1.1×10^{-26}	1.4×10^{-26}

Table 2.4: One-component velocity amplitudes of gas motion measured indirectly in the cooling regions of our targets and Perseus using SB fluctuation analysis: (a). Cluster name, (b). Cluster mass M_{2500}, (c). The region of interest, (d). Volume-weighted mean temperature in the region of interest, (e). Scales probed, (f). One-component velocity, (g). Turbulent heating rate is calculated when volume-weighted mean temperatures and densities are used, (h). Radiative cooling rate.

to calculate the mean sound speed and the measured velocities are summarized in columns (d) and (e) of Table 2.4, respectively.

In the inner half-cool-core of Perseus, the velocities of gas motion range from 76 km s^{-1} at 12 kpc to 143 km s^{-1} at 50 kpc, with some scatter. Our indirect velocity measurements are also compared with direct measurements from the Hitomi Satellite in Perseus's central 30 - 60 kpc region, where velocities varied between 110 km s^{-1} at the scale of 5 kpc to 202 km s^{-1} at the scale of 30 kpc. Notably, both indirect and direct measurement methods yield consistent results, despite the uncertainty of the dominant scale measured by Hitomi. A similar comparison in Perseus was presented by Zhuravleva et al. (2018), aligning with our results. The upcoming XRISM observations, capable of directly measuring line-of-sight gas velocities, will provide further testing and refine the relationship between density perturbations and gas motion velocity.

Despite a potential cavity structure in RBS0533, which contributes to higher density fluctuations, the measured velocities are relatively low, ranging between 60 km s^{-1} and 83 km s^{-1} at the scale of $8 - 33$ kpc. This is likely due to its low central temperature, which is less than 2 keV. Similarly, the structureless cluster RBS0540 also exhibits velocities of below 100 km s^{-1}. In contrast, the velocities measured in Abell 2029, Abell 2151, and Abell 2107 are comparable to those observed in Perseus, all exceeding 100 km s^{-1}, aligning with the expected turbulent velocities in the ICM. Notably, Abell 2029, which exhibits a spiral structure, shows velocities between 81 km s^{-1} and 211 km s^{-1} at scale of $28 - 217$ kpc, whereas Abell 2151 displays velocities of $112 - 126$ km s^{-1} at scale of $20 - 35$ kpc.

2.4.3 Turbulent Heating

The turbulent heating rate is estimated from the inferred turbulent velocity calculated using the relation $Q_{turb} \propto \rho_0 V_{1,k}^3/l$. Here, ρ_0 represents the mean gas density defined as $\rho_0 = (n_e + n_i)\mu m_p$, where n_e and n_i are the electron and ion number densities, respectively. μ is the mean molecular weight, and m_p is the mass of a proton. The scale-dependent velocity spectra $V_{1,k}$ are shown in Figure 2.8, and l is the scale within the inertia range on which the $V_{1,k} \propto l^{1/3}$, $(k \propto 1/l)$. The turbulent heating rate is then derived using:

$$Q_{turb} = \rho_0 \ \epsilon = C_Q \ \rho_0 \ V_k^3 \ k, \tag{2.10}$$

where $C_Q = 3^{3/2} \ 2\pi/(2C_K)^{3/2} \approx 5$ is a dimensionless constant where the Kolmogorov constant (Sreenivasan, 1995), C_K, is ~ 1.65. To assess the efficiency of turbulent heating in

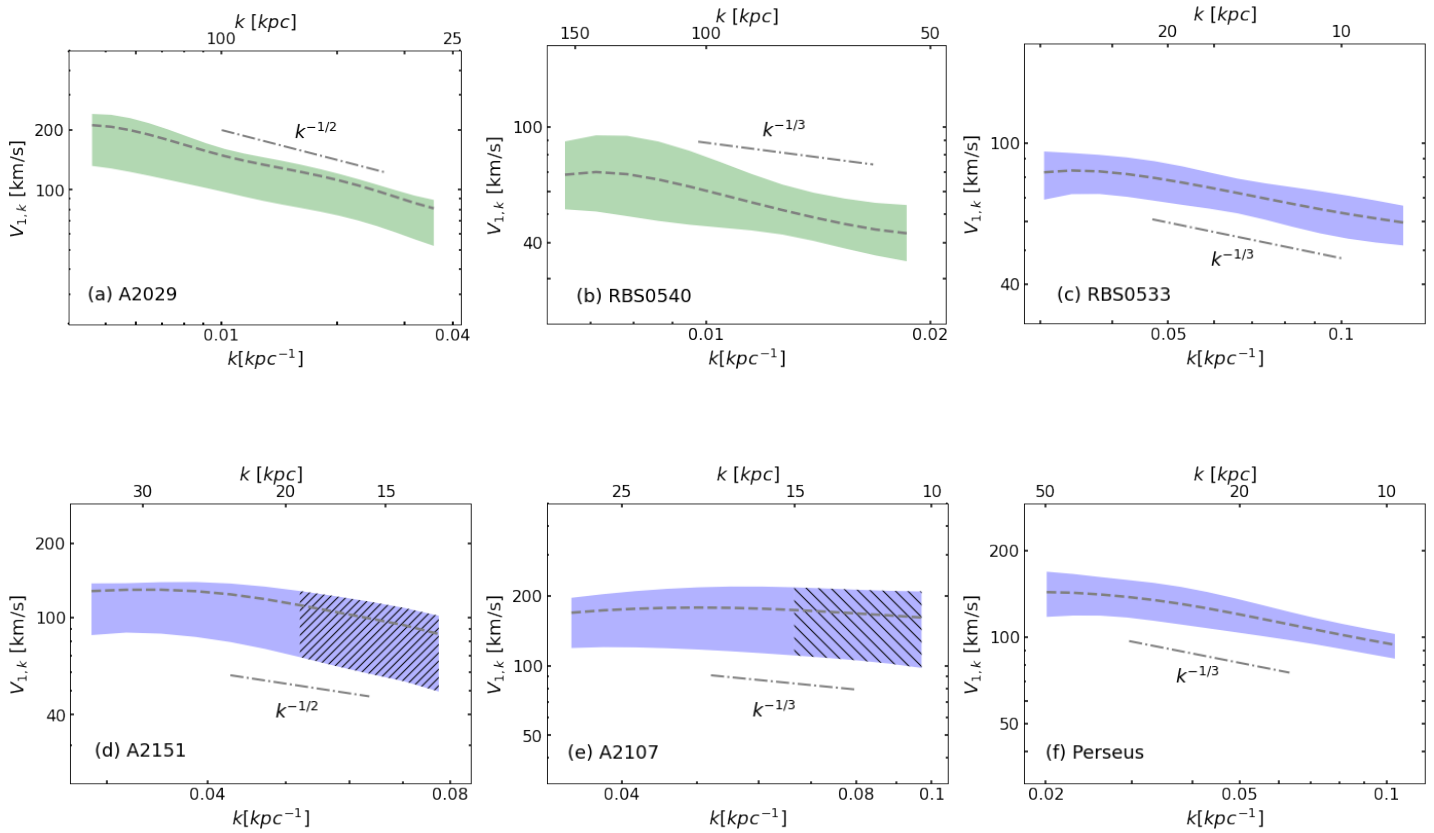


Figure 2.8: Amplitudes of one-component velocity with respect to wavenumber k within the cool-cores in (a) Abell 2029, (b) RBS0540, and within the inner half cool-core regions of (c) RBS0533, (d) Abell 2151, (e) Abell 2107, and (f) Perseus cluster. Velocities derived from the average sound speed in the ICM are shown as the central dashed lines. The velocity estimation below the scale of 15 kpc in Abell 2107 and 20 kpc in Abell 2151, marked with hatched areas, might be more significantly affected by PSF effects. The grey dash-dotted lines represent slopes of $k^{-1/3}$ or $k^{-1/2}$ for guidance.

each cluster, we compare the turbulent heating rate with the gas cooling rate. The radiatively cooling rate then is calculated as $Q_{cool} = n_e n_i \Lambda(T)$, where $\Lambda(T)$ is the normalized gas cooling function for 0.3 solar abundance.

Figure 2.9 presents a comparison between the heating and cooling rates within the cool cores of Abell 2029 and RBS0540 and within the half cool-core radius of Abell 2107, Abell 2151, RBS0533, and Perseus. The dashed lines denote equality between the heating rate and cooling rate. The central dots represent the heating and cooling rates calculated using volume-weighted mean gas temperature and density within the regions of interest. The size of each rectangle represents the 1σ uncertainties including variations in gas temperature/-density across the regions and the statistical uncertainties in measured velocity spectra. Significant uncertainties in the cooling rates arise due to the variations in gas density and temperature, which can stretch the error range and mask the tension between heating and cooling rates. To address this, we have compared the inner and outer cool core regions of Abell 2029 separately (shown in blue and red, respectively). Both the heating and cooling rates are higher in the inner cool core compared to the outer cool core, with the larger uncertainty resulting from the steeper density profile in the cluster center.

Assuming Kolmogorov-like turbulence, the cascade rate $Q_{turb} \sim V_{1,k}^3 k$ should remain approximately constant across the inertial range with a velocity spectrum $V_{1,k} \propto k^{-1/3}$. However, the velocity spectra slopes of our sample clusters depart from the Kolmogorov slope of $-1/3$, enlarging in the uncertainties in Q_{turb}. In addition, the uncertainty also arises due to the calibration of coefficient η_1 when we derived velocity spectra from the spectra of gas density fluctuations. In our analysis, we acknowledge that there is an order of magnitude uncertainty in the heating rate estimation.

Given its short central cooling time and low entropy, RBS0533 is expected to exhibit bright nebular emission. However, its H_α luminosity lies below 0.016×10^{40} erg s^{-1} in the ACCEPT database. O'Sullivan et al. (2018) found an upper limit to the molecular hydrogen mass at $M_{H_2} < 0.47 \times 10^8$ $M_\odot$. Martz et al. (2020) suggested that the bubble in RBS0533 can't lift enough cool gas to approximately 40 kpc from the cluster center where $t_{cool}/t_{ff} < 1$, thus failing to meet the cooling instability criterion and resulting in the absence of nebular emission. Moreover, as illustrated in Figure 2.9, the turbulence-induced energy within the inner half cool-core radius of RBS0533 has the potential to supply a substantial portion of the heat necessary to balance the radiative cooling. Therefore, dissipation turbulence injected by other sources might be heating the atmosphere. Our measurements are consistent with heating from the dissipation of turbulent gas motions being comparable to the radiative cooling in all systems apart from RBS0540.

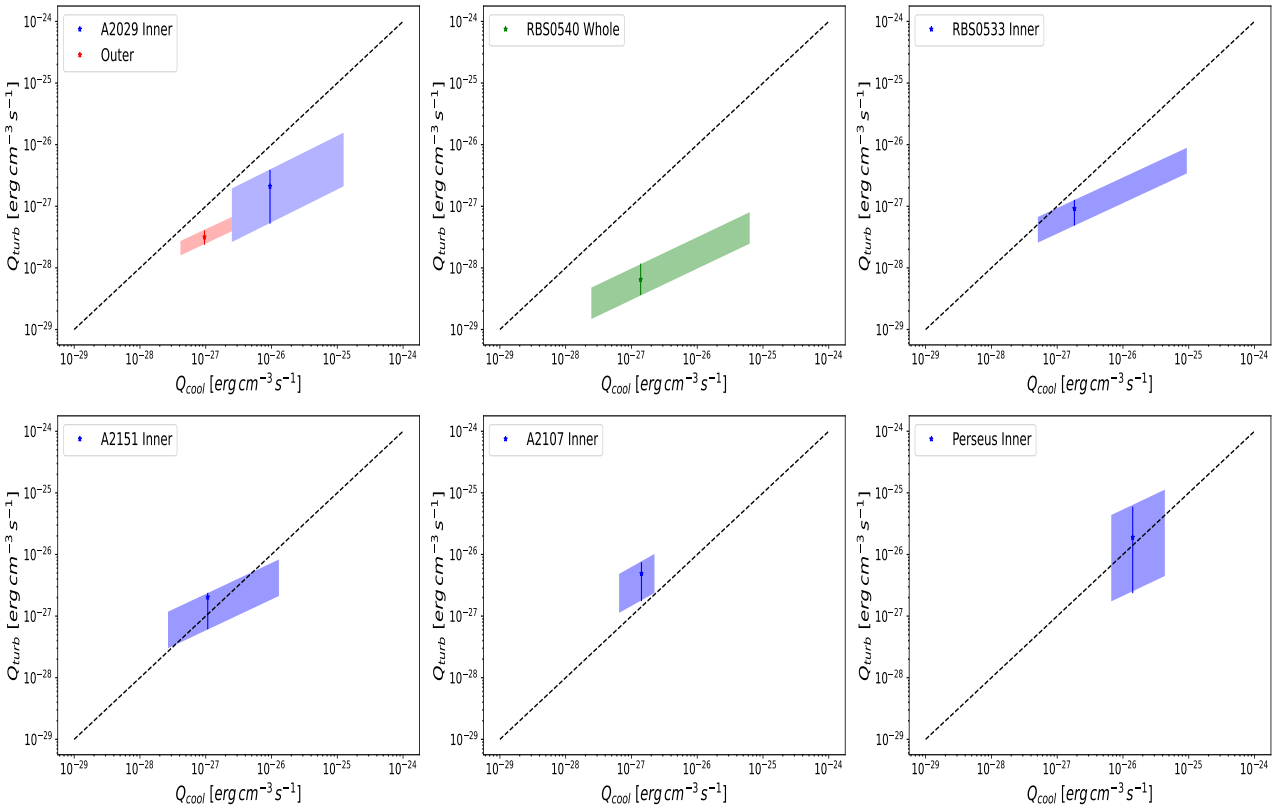


Figure 2.9: Turbulent heating versus radiative cooling rates within the cool-core radius of Abell 2029 and RBS0540, and within the inner half cool-cores of RBS0533, Abell 2151, Abell 2107, and Perseus. For Abell 2029, the comparison is presented separately for the inner (blue) and outer (red) cool-core regions. The central points represent the Q_{cool} and Q_{turb} obtained using volume-weighted temperatures and densities. The error bars indicate 1σ uncertainties in heating rate, variations in density and temperature within the regions of interest, and deviations from the Kolmogorov spectral slope of $k^{-1/3}$. The dashed line illustrates the equilibrium where radiative cooling is balanced by turbulent heating.

2.5 Discussion

2.5.1 The Gas Perturbation Sources in Smooth Atmosphere Clusters

The existing Chandra archival observations used in this work allow us to constrain density fluctuations over a limited range of spatial scales. Consequently, a direct comparison between these structureless systems and the Perseus cluster over identical scale ranges is infeasible. Nevertheless, based on the results shown in Figure 2.7, it can be inferred that typical density fluctuations within the clusters with smooth atmospheres are generally modest across the range of measurable scales. Noteworthy exceptions are observed in Abell 2151 which range from $\sim$ 10 per cent to 17 per cent at scales of $12 - 35$ kpc, and in RBS0540, ranging from $\sim$ 6 per cent to 8 per cent at scales of $33 - 155$ kpc. By comparison, the core of the Perseus cluster exhibits density fluctuations ranging between 8 and 14 percent at scales of $4 - 50$ kpc, suggesting that the perturbation levels in Perseus are comparable to, or slightly exceed, those in tranquil-core clusters. The absence of pronounced bubble structures in our targets, perhaps apart from RBS0533, raises questions about the underlying mechanisms responsible for generating the observed levels of gas perturbations in these systems.

In the central region of Abell 2029, the ratio of cooling time to free-fall time consistently remains above 15 - 20, suggesting a thermally stable environment but one that is susceptible to precipitation. Nevertheless, a heating mechanism is required to account for the absence of cooling products such as nebular emission and star formation. Studies of turbulent dissipation in the central regions of more than ten nearby brightest cool-core clusters, including Perseus, have indicated that turbulence can sufficiently offset radiative cooling on average (Zhuravleva et al., 2018). Central AGN activity likely plays a role by transferring energy to the ICM through turbulence induced by jets and bubbles.

Despite the absence of prominent X-ray cavities, we infer from Figure 2.9 that the dissipation of turbulence in the core of Abell 2029 somewhat balances its cooling rate. The cD galaxy in Abell 2029, IC1101, harbors a relatively powerful radio source, PKS 1508+059 (Taylor et al., 1994; Becker et al., 1995), with jet power of $P_{1.4} \sim 10^{41}$erg s^{-1} and a size of $\sim$15 - 22 kpc. Radio sources of comparable power and size have been known to inflate X-ray cavities or bubbles. If PKS 1508+059 is indeed heating the ICM in Abell 2029 without creating bubbles, we would expect to observe stronger fluctuations near the radio source and lower amplitudes further away. We measured the inner and outer cooling regions separately in Abell 2029's core and observed higher gas density fluctuations in the

inner regions. At a scale of $\sim$ 100 kpc, the density fluctuation is around 12 per cent in the inner region and 10 percent in the outer region. However, comparisons over smaller scales cannot be conducted. The reason why smooth atmospheres, such as Abell 2029, exhibit gas perturbation levels similar to those in Perseus remains unclear. To accurately measure density fluctuation amplitude down to the scale of the radio source, a substantially longer exposure of approximately 1.4 Ms for Abell 2029 would be necessary.

An alternative possibility is that gas sloshing induces density fluctuations. A prominent spiral is clearly visible in Abell 2029, identified as a cold front. The relaxed atmosphere of Abell 2029 shows no obvious indication of a major merger. The cold front is likely created by a 'slosh' motion induced by merging halos, which is displacing low-entropy gas from the cluster cores. This sloshing is likely to disturb the ICM and heat the cluster core by mixing hot gas from the outer regions with the cooler gas in the core. ZuHone et al. (2010) used high-resolution N-body/Eulerian hydrodynamic simulations to model gas sloshing initiated by mergers with subclusters in galaxy clusters closely resembling Abell 2029. Their results indicate that gas sloshing can facilitate the inflow of heat to the cluster core by mixing hot gas from the cluster outskirts with the cool-core gas. This process redistributes gas in cooling cores, thereby reducing the efficiency of radiative cooling. The impact of gas sloshing varies with viscosity and the frequency of mergers, but they suggest that a cooling catastrophe can be prevented for intervals of approximately 1–3 Gyr.

Walker et al. (2018) conducted an analysis of the Perseus cluster using simulated Chandra observations tailored to examine gas sloshing effects. Their findings indicate that the density fluctuations observed beyond the central 60 kpc align closely with those expected from sloshing phenomena alone. Furthermore, their analysis translated these surface brightness fluctuations into estimates of turbulent heating rates. Remarkably, across the annuli examined beyond 60 kpc, the estimated heating rates were found to either match or exceed the cooling rates.

Similarly, the residual image of Abell 2151 exhibits a possible spiral feature that extends radially to approximately 81 kpc. To determine whether these interactions are driving gas turbulence and to assess their relative contributions to the total variance, an 'effective' equation of state can be used to study the nature of gas perturbations. This equation, which illustrates the correlation between density fluctuations and temperature fluctuations, can be derived by measuring fluctuations in both the soft energy band ($0.5 - 3.5$ keV) and the hard energy band ($3.5 - 7$ keV). The equation is defined as follows (**?**):

$$\frac{\delta T}{T} = (\xi_i - 1)\frac{\delta \rho}{\rho}, \tag{2.11}$$

where ξ_i represents the effective adiabatic index. Given that emissivity is more strongly temperature-dependent at higher energies, surface brightness fluctuations in the hard band are used to characterize temperature fluctuations. The gas perturbations are classified into three types according to their origins. Isothermal perturbations ($\xi_i = 1$), manifesting as variations in thermal gas density at a constant temperature, are typically associated with bubbles of relativistic plasma. Isobaric fluctuations ($\xi_i = 0$), often induced by slow gas displacements such as the motion of galaxies and mergers, are sensitive to entropy changes while maintaining pressure equilibrium with the surrounding atmosphere. Adiabatic fluctuations ($\xi_i = 5/3$), produced by shock fronts, sound waves, and other mildly transonic disturbances, are characterized by constant gas entropy.

Isobaric perturbations, predominant in the core of Abell 2029 on scales of $60 - 90$ kpc, constitute more than 70 percent of the total variation, measured by (Zhuravleva et al., 2016), suggesting that slow motions of gas or gas cooling might significantly contribute to these gas disturbances in the core. They also estimated that approximately 80 percent of perturbations in the core are isobaric at scales of $\sim 8 - 70$ kpc in the core of Perseus, where a similar spiral feature is observed. It indicates that the central AGN activity is not the only driver of gas perturbations in the ICM. However, the existing exposure of Chandra observations does not provide sufficient counts in the hard band, preventing us from determining the nature of gas perturbations in the remaining four clusters.

While we have not observed significant X-ray cavities in the five clusters studied, it is possible that the dissipation timescale of perturbations produced by feedback processes is long. This implies that we could have a mix of both AGN feedback and other mechanisms, such as gas sloshing, contributing to the generation of turbulence. Future observations and more detailed analyses will be required to determine the relative contributions of these processes.

On the other hand, mild turbulence has been suggested as a potential trigger for thermal instabilities (Voit, 2018; Gaspari et al., 2018). However, the lack of cooling products in Abell 2029 and Abell 2151 could imply that the mergers occurring in these clusters may not generate sufficient turbulence levels to induce thermally unstable cooling.

The variation of metallicity can also cause emissivity variation, which might further lead to an overestimation of density fluctuations. The nuclear metallicity of Abell 2029 lies near the solar value and then drops to $\sim 0.4\ Z_\odot$ at 100 kpc. Kirkpatrick & McNamara (2015) found evidence for enhanced metallicity compared to the ambient value with an amplitude of $\sim$ 0.1 $Z_\odot$ in several regions along the radio axis. While the magnitude of this signal is comparable to the measurement errors, its systematic presence across multiple regions is notable. This apparent excess spans several tens of kpc in altitude.

Nevertheless, at this level, metallicity variations are unlikely to significantly contribute to the observed emissivity/density variations in Abell 2029. Furthermore, in the other four clusters, significant metallicity variance was also not observed. The density fluctuations due to cooling don't trace velocity, however, it can be neglected because the eddy turnover timescale t_{eddy} is typically shorter than cooling timescale t_{cool}.

The mechanisms contributing to the observed emissivity/density fluctuation spectra in these smooth atmospheres remain elusive. Future research, potentially involving more simulations of clusters lacking radio bubbles yet with short central cooling times will aim to quantify the effects of halo disturbances and galaxy motions. More insight will come from direct high-resolution X-ray spectroscopy including the X-ray Imaging and Spectroscopy Mission (XRISM), which has recently published its initial results featuring a non-dispersive resolution of ~ 5 eV.

2.5.2 Shape of Velocity Spectra & Mass Dependence

For pure hydrodynamic turbulence, the energy spectrum $E(k_1)$, where $k_1 = 2\pi/l = 2\pi k$, depends solely on the wavenumber k_1 and the mean density-normalized dissipation rate is $\epsilon = Q_{turb}/\rho_0$ within the inertial scale range. This relationship is expressed as $E(k_1) = C_K \epsilon^{2/3} k_1^{-5/3}$, with C_K representing the universal Kolmogorov constant. In the case of isotropic turbulence, the mean square component of the velocity field is uniform in all directions, and as such, $V_{1,k} = V_k/3 = [2k_1 E(k_1)/3]^{1/2}$ can be approximated as $\sim k^{-1/3}$.

Pure turbulence in this setting may be unrealistic as the effects of gravity and bulk motions should lead to departures from the Kolmogorov spectrum. The errors in Figure 2.7 are consistent with a range of slopes, including $\propto k^{-1/3}$. So we cannot exclude pure turbulence. However, the surface brightness fluctuations may not be caused entirely by turbulent motions. Therefore, the measurements presented in Figure 2.8 should be considered upper limits on turbulent velocities. Assuming that gas perturbations are caused only by turbulence, the heating rates would be in the same order as the cooling rates, as shown in Figure 2.9.

Several interesting theoretical possibilities exist to explain slope variance. They include turbulent energy injected at multiple spatial scales, and a time-dependent evolution of turbulent atmospheric motions (Chen et al., 2023). The steepening may indicate partial dissipation of certain modes or suppression of power on small scales. For instance, magnetic fields can steepen the kinetic power spectrum when magnetic stresses suppress the kinetic energy cascade (Bambic et al., 2018). However, when including magnetohydrodynamic (MHD) effects, plasma effects should also be considered, in which the pressure anisotropy

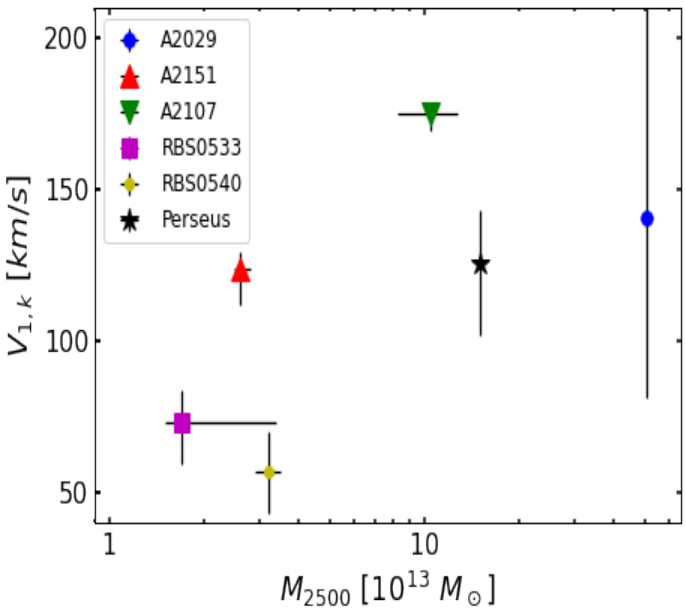


Figure 2.10: M_{2500} versus one-component velocity $V_{1,k}$ of smooth-core clusters and Perseus cluster. The markers present the mean velocity amplitudes over the range of scales probed in each target.

causes the turbulent plasma to resist changes in magnetic-field strength, thereby preserving the spectrum slope (Squire et al., 2019).

It is also worth noting that the Δ-variance method used in X-ray surface brightness fluctuation analysis may introduce slope bias (Arévalo et al., 2012; Romero, 2024). Furthermore, the depth of the Chandra exposures limits the attainable accuracy. These considerations restrict our measurements to a relatively narrow scale range and prevent us from accurately constraining the spectral slopes.

Finally, we examine the trend between cluster mass and turbulent velocity shown in Figure 2.10. Total mass estimates are found by Martz et al. (2020) using the Navarro–Frenk–White (NFW) potential model. Their masses range between 10^{13} $M_\odot$ and 10^{14} $M_\odot$ as detailed in the column (b) of Table 2.4. The vertical error bars reflect the 1σ uncertainties in the turbulent velocity; the horizontal error bars reflect the uncertainties in mass profile fitting. No significant correlation between mass and turbulent velocity is found.

2.6 Conclusions

In this work, we studied gas perturbations in the atmospheres of five cool-core clusters, which have short central cooling times and low entropy but show little evidence of cold gas and bubbles inflated by AGN feedback. Assuming that the detected density fluctuations reflect underlying random gas motions, the amplitudes of gas density fluctuations estimated from X-ray surface brightness fluctuations are used to derive the velocity spectra of gas motions. We estimated the dissipation heating rates and further explored the impact of turbulent dissipation in reheating and stabilizing the atmospheres of the structureless clusters. The uncertainties due to the limited exposure times, the choice of the underlying SB models, and the deviation from the Kolmogorov slope are also examined. The key conclusions drawn from our research are as follows:

- The characteristic amplitude of density fluctuations is ~ 10 per cent at the scale of the cool core. Amplitudes rise to ~ 15 per cent at the scale of ~ 216 kpc in Abell 2029 and ~ 17 per cent at the scale of ~ 35 kpc in Abell 2151. Despite the absence of structures associated with central AGN activity, our results are comparable to the gas density fluctuations measured in the core of the Perseus cluster, where a large fraction of the core area is occupied by bubbles, shocks, and spirals.

- The measured power spectra are consistent with a broad range of slopes, making it impossible to confirm or rule out alignment with the Kolmogorov turbulence.

- The velocity amplitudes lie below 100 km s^{-1} in RBS0540 and RBS0533 but rise to ~ 178 km s^{-1} at scales of ~ 30 kpc in Abell 2107 and ~ 211 km s^{-1} at scales of ~ 220 kpc in Abell 2029. These velocity amplitudes are consistent with turbulent velocities expected in hot atmospheres.

- No relationship is found between cluster mass, M_{2500}, and the velocity amplitudes.

- The turbulent heating rates implied by our measurements are of the same order as the radiative cooling rates. Our results suggest that atmospheric sloshing and perhaps turbulent motion may aid radio jets in stabilizing atmospheric cooling.

Chapter 3

Velocity Structure Correlations between the Nebular, Molecular, and Atmospheric Gases in the Cores of Four Cool Core Clusters

We investigate the velocity structure of nebular gas in the central galaxies of four clusters: Abell 1835, PKS 0745-191, Abell 262, and RXJ0820.9+0752, using data from the Keck Cosmic Web Imager (KCWI). Velocity structure functions (VSFs) of the [OII] emission line are compared to VSFs of molecular clouds observed with the Atacama Large Millimeter/submillimeter Array (ALMA). Apart from Abell 262 where the gas is located in a circumnuclear disk, the nebular gas in the remaining galaxies lies in off-nuclear filamentary structures with VSFs steeper than the Kolmogorov slope. This steepening may be plausibly attributed to gravity although other factors, such as magnetic stresses and bulk motion, may be significant. The VSFs of CO and [OII] emission are similar in RXJ0820 and Abell 262, indicating close coupling of the nebular and molecular gases. In contrast, the nebular and molecular gases are differentiated on most scales in PKS 0745 and Abell 1835. This discrepancy is likely due to the radio-AGN churning the gas. We compare the scale-dependent velocity amplitudes of the hot atmospheres constrained by X-ray surface brightness fluctuation analysis using Chandra observations to the nebular VSFs. The large-scale consistency in Abell 1835 and RXJ0820 is consistent with condensation from the hot atmospheres. We explore substantial systematic biases, including projection effects, windowing, and smoothing effects when comparing VSFs using different telescopes and instruments.

3.1 Introduction

Galaxy clusters, the universe's largest gravitationally bound structures, are filled with ionized hot atmospheres with temperatures between 10^7 K and 10^8 K. Within the cores of these clusters, an increase in gas density is expected to lead to substantial accumulations of cold gas, enable the condensation of molecular clouds at rates exceeding 100 $M_\odot$ yr^{-1}, and thereby foster vigorous star formation but is unseen (Cowie & Binney, 1977; Cavagnolo et al., 2008; Rafferty et al., 2008; Peterson & Fabian, 2006). Despite central radiative cooling timescales often being shorter than the ages of clusters, their hot atmospheres are globally stable, remaining in both hydrostatic and thermal equilibrium (McCourt et al., 2012). One or more heat sources are required to maintain this stability. The most prevalent heating mechanism is radio-mechanical Active Galactic Nucleus (AGN) feedback, in which the energy is injected from central supermassive black holes (SMBHs), interacting with the intercluster medium (ICM) via jet-inflated bubbles of relativistic plasma, seen as cavities in X-ray images (Voit & Donahue, 2005; Fabian, 2012; Bîrzan et al., 2012). The AGN energy associated with the cavity alone is enough to offset radiative cooling, as shown by measuring the surrounding pressure and volume of the cavities using the X-ray data (Rafferty et al., 2006). However, the process by which this energy is transferred to the ICM is not well understood.

Turbulence is thought to be an important channel for coupling feedback to the environment (Churazov et al., 2002; Omma et al., 2004; Gaspari et al., 2014). The analysis of X-ray surface brightness (SB) fluctuations indicates that the ICM in the cluster cores is turbulent, consistent with the Hitomi Doppler line broadening measurements (Hitomi Collaboration et al., 2016). Turbulent dissipation may be sufficient to compensate for cooling losses, although measurement uncertainties prevent a conclusive determination (Zhuravleva et al., 2014a). Other possibilities for channeling energy to the ICM include shocks (Heinz et al., 1998; Fabian et al., 2006; Markevitch & Vikhlinin, 2007; Randall et al., 2011), sound waves (Sternberg & Soker, 2009; Sanders & Fabian, 2007; Nulsen & McNamara, 2013), streaming and diffusion of cosmic ray protons (Loewenstein et al., 1991; Guo & Oh, 2008; Pfrommer, 2013), radiative heating (Nulsen & Fabian, 2000; Ciotti & Ostriker, 2001), and the mixing of gas between the ICM and the hot content of bubbles (Hillel & Soker, 2016, 2017b). Many or all may contribute to heating.

Despite suppression of cooling by heating processes in groups and clusters, the detection of cool-phase gas within the atmospheres of the brightest cluster galaxies (BCGs) and giant elliptical galaxies indicates significant cooling. Massive molecular gas reservoirs in excess of 10^9 $M_\odot$ are observed near the nucleus of some clusters, which fuels star formation and sustains the feedback loop (Edge, 2001; Salomé & Combes, 2003; Rafferty et al., 2008;

Russell et al., 2019; Olivares et al., 2019). ALMA observations of central galaxies in clusters show that the molecular gas preferentially lies around and in the wakes of buoyantly rising bubbles (McNamara et al., 2014; Russell et al., 2017, 2019; Olivares et al., 2019). However, if and how the molecular gas couples to the bubbles is not understood. The cold dense gas may be accelerated outward from the center. Alternatively, with the difficulty of lifting high column density clouds, the molecular gas might cool from the hotter gas lifted behind bubbles (McNamara et al., 2016). Moreover, optical line emission at $\sim 10^4$ K is commonly observed in the centers of cool-core clusters (Heckman et al., 1989; Crawford et al., 1999; Cavagnolo et al., 2008; McDonald et al., 2011; Gingras et al., 2024). This filamentary nebular emission, tracing warm ionized envelopes of many cold molecular gas clouds (Jaffe et al., 2005), wraps around both the radio jet and the X-ray cavities (Salomé et al., 2008; McNamara et al., 2014; Vantyghem et al., 2016; Russell et al., 2017). Such a spatial coupling is consistent with a top-down multi-phase condensation cascade, within which both the warm ionized and cold molecular components are cooling products that rain from the hot ambient plasma. Their kinematics are predicted to retain the "memory" of the hot gas from which they condense (Gaspari et al., 2017, 2018; Voit, 2018).

The velocity structure function (VSF) provides a powerful tool to characterize gas motions and dynamical processes. The kinematics of multi-phase filaments in three nearby galaxy clusters, Perseus, Abell 2597, and Virgo, have been examined by Li et al. (2020). Their results indicate that the cold filaments in these clusters are well coupled to the turbulent nature of the hot gas that is present. The agreement between the turnover scales of the VSF and the dimensions of the observed bubbles inflated by jets suggests that activity from the central supermassive black hole drives turbulent gas motions in cluster cores, highlighting the potential role of turbulence in channeling feedback energy to the ICM. In contrast, Hillel & Soker (2020) noticed that the VSFs of cold filaments in these three clusters were steeper than the Kolmogorov slope of 1/3, typical for classical turbulent cascades, leading them to claim that turbulence may not be a major heating mechanism in these clusters due to long dissipation timescales. Instead, they concluded that mixing with hot gas from the bubbles is more effective in counteracting radiative cooling. By comparing with 3D hydrodynamical simulations of jet-inflated hot bubbles, as studied in (Hillel & Soker, 2016), they suggested that jets could directly induce turbulence with a VSF slope steeper than 1/3. By examining magnetohydrodynamical (MHD) simulations of self-regulated AGN feedback in a Perseus-like cluster, Wang et al. (2021) found that the cold phase ($T \sim 10^4$ K) VSF was steeper than predicted by Kolmogorov's theory and attributed this steepening to gravitational acceleration acting on cold clouds. The results imply that the turbulence in the surrounding hot medium may be driven by the motion of precipitating cold filaments and by AGN jets. Furthermore, by varying initial outflow

properties in hydrodynamical simulations Hu et al. (2022) discovered that a supersonic turbulent velocity structure with VSF slope of 1/2, can be generated and be "frozen" within the Hα-emitting filaments emerging from fast AGN-driven hot outflows. Gravitational interaction tends to flatten the VSF of the cold phase over a short timescale, approximately 10 Myr, indicating that the lack of flattened VSF reflects the short-lived nature of the Hα emitting phase.

The nebular emission from the core regions of four galaxy clusters—Abell 1835, Abell 262, PKS 0745-191, and RXJ0820.9+0752—has been analyzed using new optical observations from the Keck Cosmic Web Imager (KCWI) (Morrissey et al., 2018; Gingras et al., 2024). As the [OII] emission line doublet is the highest luminosity line observed in the KCWI data, Gingras et al. (2024) focused on the [OII]3726,9 Å, also incorporated data from previous multiwavelength studies, including radio and X-ray observations, to examine the morphology and dynamics of the nebular gas. In this work, we continued our VSF analysis by utilizing this integral field spectroscopy (IFS) data, which offers a larger field-of-view (FOV) and relatively high spectral resolution compared to earlier studies. This enables us to effectively probe the dynamical processes affecting the gas across a broad range of spatial scales. Furthermore, the velocity structures of the multi-phase filaments may reflect the origins of the filaments and the interactions between AGN feedback and the intracluster medium (ICM). Therefore, we have also incorporated multi-wavelength observations to provide a detailed analysis of the kinematics of both molecular gas and the hot gas, and to conduct a thorough comparison with the warm ionized gas. The molecular gas in these clusters was observed by ALMA and is traced by J = 1 - 0, J = 2 - 1, and J = 3 - 2 rotational transitions of CO with high spatial and velocity resolution. Additionally, by comparing the VSF feature scales with the structures identified in the X-ray images observed by the Chandra X-ray Observatory, we can explore the correlations between their dynamics and the jet-inflated bubbles within these systems.

The line-of-sight velocity dispersion of the hot ICM has been measured directly in the core of Perseus by Hitomi (Hitomi Collaboration et al., 2016) with relatively low spatial resolution. Under certain assumptions, the scale-dependent velocity amplitude of the hot gas motion can be derived indirectly from the measured power spectra of X-ray surface brightness fluctuations. In this work, we analyze the velocity power spectra of hot gas motion obtained from Chandra observations and compare them to the VSFs of filaments observed with KCWI. This analysis provides us with insights into the role of turbulence in reheating the ICM and the connection between the motion of gas in different phases and the activity of the central SMBHs.

In Section 3.2 we introduce the central galaxies studied in this work and provide a summary of the data processing procedures. In Section 3.3 we present the results of

the VSF measurements based on KCWI and ALMA observations, analyzing their shapes, slopes, and amplitudes, and comparing them to Kolmogorov turbulence theory and hot ICM motions obtained from X-ray SB analysis. In Section 3.4 we discuss the shape of measured VSFs, as well as the the interaction between gas in different phases. Finally, we conclude this work in Section 3.5. Throughout the paper we assume a standard ΛCDM cosmology with $H_0 = 70$ km s^{-1} Mpc^{-1}, $\Omega_{\rm m} = 0.3$, and $\Omega_\Lambda = 0.7$.

3.2 Cluster Sample and Observational Data

3.2.1 Cool Cluster Sample

Though limited to only four clusters, the sample in this study is adequately representative of the broader cool cluster population and was chosen to encompass a broad range of feedback properties. The details are listed in the Table 3.1. The redshifts lie between $z = 0.0165$ and $z = 0.2512$. The cluster atmospheres have central cooling times below 1 Gyr and harbor substantial reservoirs of molecular gas with masses ranging between 10^8 M$_\odot$ and 10^{10} M$_\odot$. The central galaxy of Abell 1835 is experiencing powerful radio-mode feedback and has a high star formation rate (McNamara et al., 2006). A powerful radio source is in the core of PKS 0745, more than ten times higher than those of other clusters in our sample. CO emission emitted from molecular gas in these clusters spatially overlaps the nebular gas in all sample clusters, allowing us to directly compare the kinematics of these gas phases. In RXJ0820, the molecular and nebular gases show a significant spatial offset from the central galaxy. Both gas phases in Abell 262 exhibit a disk-like structure that rotates around the nucleus. Combined with the detection of X-ray cavities in these clusters, which result from previous central AGN activity, the multi-wavelength observations allow us to study the dynamics of different phases of the ICM and their interconnection in the AGN feedback model.

3.2.2 KCWI Data Reduction

Details of the KCWI observations and data reduction of these four central galaxies are presented in Gingras et al. (2024); here we report the most relevant details. The properties of KCWI observations are given in column (2) - (4) of Table 3.2. The data was reduced using the KCWI IDL Data Extraction and Reduction Pipeline (KDERP). The data was resampled onto a $0.29'' \times 0.29''$ spaxel grid, and a mosaic was created from the individual pointings observed for each cluster.

The stellar continuum and emission lines in each spaxel were simultaneously fit using the `IFSFIT` IDL library. To obtain the stellar velocity in the innermost 1" region of the central galaxy, which was used as the systemic velocity of the system, a spatially-integrated spectrum was created by summing the spectra from spaxels with a strong stellar continuum in the central galaxy. Emission lines were masked out and the stellar continuum was fit using the Penalized Pixel-Fitting method `PPXF` (Cappellari & Emsellem, 2004). The stellar component is matched to stellar population synthesis (SPS) models (González Delgado et al., 2005). The best-fit SPS models across all stellar ages were then summed to obtain the stellar continuum fit in the spatially-integrated spectrum.

The stellar continuum and emission lines were fit simultaneously. Using `MPFIT` (Markwardt, 2009), the line profiles were convolved with the KCWI spectral resolution to fit the emission lines. The flux ratio of [OII] doublet was fixed at 1.2, based on an assumed electron density of $400\,\mathrm{cm}^{-3}$ (McLaughlin & Bell, 1998; Pradhan et al., 2006). A flux threshold of signal-to-noise ratio (S/N) > 5 per spaxel was applied to all the flux and kinematic maps of the [OII] 3726,9 Å doublet presented here.

In performing the emission line fitting, a second component is included when the Bayesian Information Criterion (BIC) for the two-component fit is less than that for the one-component fit and when neighboring spaxels also require a second kinematic component. Of the four cooling clusters observed, only one kinematic component is required for Abell 262 and RXJ0820, while a second kinematic component is needed for Abell 1835 and PKS0745. More details are provided in Gingras et al. (2024).

Figure 3.1 presents the median velocity v_{50}, which is the 50th percentile of the cumulative velocity profiles of the [OII] emission line doublet in the four cooling cluster cores. Positive velocities indicate a redshift when compared to the systemic redshift of the central galaxy, while negative velocities are blueshifted. The nucleus of the central galaxy, located at the origin of the images, corresponds to the brightest spaxel in the stellar continuum flux map of Abell 1835, PKS 0745 and RXJ0820. The location of the nucleus in Abell 262 is determined from the spaxel with the highest stellar velocity dispersion, as a strong central dust lane leads to substantial extinction in this central galaxy. Most of the nebular gas is redshifted with respect to the stars by approximately 150 km s^{-1} in Abell 1835, 135 km s^{-1} in PKS 0745, and 150 km s^{-1} in RXJ0820. The nebular gas in Abell 262 is blueshifted in the south and redshifted in the north, with median velocities ranging between $-$ 314 km s^{-1} and $+$ 422 km s^{-1}. This clear velocity gradient demonstrates ordered motion along the north-south axis.

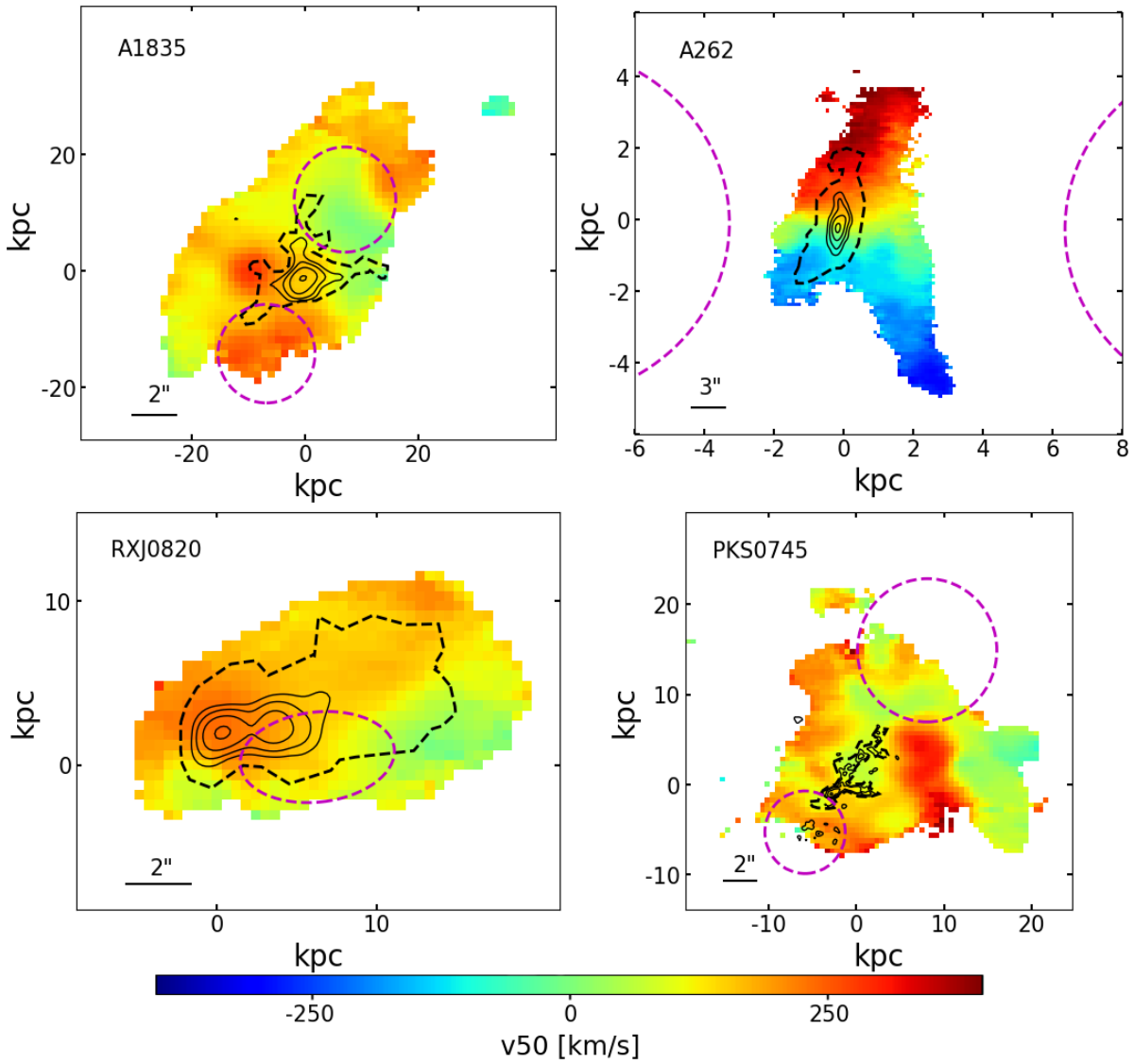


Figure 3.1: The median velocity v_{50} maps of the [OII] emission line doublet with respect to the stellar velocity of the system. The central galaxy nucleus is designated as the reference point for each map's origin. Positive velocities indicate redshift, while negative velocities denote blueshift relative to the stellar velocity. The black solid lines indicate the integrated flux contours for 10%, 20%, 40%, and 80% of the maximum CO (3-2) emission in Abell 1835 and PKS 0745, CO (2-1) emission in Abell 262, and CO (1-0) emission in RXJ0820. Areas within the black dashed lines highlight regions where CO emissions are detected by ALMA. The dashed magenta ellipses show the positions of the X-ray cavities.

Target	R.A. (J2000)	Dec. (J2000)	z	a (kpc)	b (kpc)	D (kpc)	M_{mol} (10^8 $M_\odot$)
(1)	(2)	(3)	(4)	(5)	(6)	(7)	(8)
Abell 1835	14:01:02.1	+02:52:43	0.2514	14	10	17	500
				16	12	23	
Abell 262	01:52:46.5	+36:09:07	0.0160	11	10	8	3.4
				11	10	10	
RXJ0820.9+0752	08:21:02.3	+07:51:47	0.1103	9	5	6	390
PKS 0745-191	07:47:31.3	−19:17:40	0.1024	10	10	6	46
				17	17	20	

Table 3.1: Targets details: (1). Cluster name. (2). Right ascension (RA). (3). Declination (Dec). (4). Redshift (5) Major axis of X-ray cavity. (6). Minor axis of X-ray cavity. (7). Distance from cavity center to the core. (8). Molecular gas mass. References: (5)-(7): Abell 1835: McNamara et al. (2006); Olivares et al. (2019), Abell 262: Rafferty et al. (2006); Clarke et al. (2009), RXJ0820.9+0752: Vantyghem et al. (2019), PKS 0745-191: Sanders et al. (2014).

3.2.3 ALMA Observations

We use archival ALMA observations of the four cooling cluster cores in sample to compare the dynamic properties of the cold molecular gas with the warm ionized gas. Details of these observations are listed in column (5) - (7) of Table 3.2. The data were calibrated using the ALMA pipeline reduction scripts with `CASA` version 4.7.2. Standard phase calibration was performed, and the data cube was binned in 10 km s^{-1} resolution. The black dashed contours in Figure 3.1 represent the region of the CO emission detected at a 3σ level by ALMA. While the observed molecular gas spatially overlaps with the nebular gas, it is more concentrated near the central galaxy of each cluster (Gingras et al., 2024).

Figure 3.2 presents the velocity maps of the molecular gas traced by CO emission. These velocity fitting results are published in Russell et al. (2019). Gaussian smoothing over the synthesized beam was applied. The origins are consistent with those in Figure 3.1, indicating the locations of the nuclei of the central galaxies. CO emission shown was detected at a S/N $> 3\sigma$ threshold. When multiple CO lines are detected, we present either the stronger line or the line with higher spatial resolution over a larger area, whichever is

Target	KCWI Observations			ALMA observations			Chandra Observations	
	Seeing	FOV	Emission extent	CO line	Beam size	Emission extent	ObsIDs	Clean T_{exp}
	(")	(" × ")	(kpc × kpc)		(" × ")	(kpc × kpc)		ks
(1)	(2)	(3)	(4)	(5)	(6)	(7)	(8)	(9)
Abell 1835	0.8	35 × 33	62 × 51	J = 3 - 2	0.45 × 0.6	25 × 22	6880, 6881, 7370	178
Abell 262	0.9	30 × 32	5.5 × 8.9	J = 2 - 1	0.6 × 1.0	2 × 4	/	/
RXJ0820.9+0752	0.9	21 × 24	41 × 26	J = 1 - 0	0.7 × 0.7	18 ×11	17194, 17563	60
PKS 0745-191	1.2	26 × 31	33 × 30	J = 3 - 2	0.2 × 0.3	11 × 14	2427, 6103,7694, 12881, 19572 - 5	176

Table 3.2: The observations used in this analysis: (1). Cluster name. **KCWI observations**: (2). Seeing. (3). Field of View. (4). [OII] emission extent. **ALMA observations**: (5). CO emission line used for fitting. (6). The synthesized beam size. (7). CO emission extent. **Chandra observations**: (8). Chandra ObsIDs used in this work. (9). Cleaned exposure time.

more suitable for our purposes. The specific CO emission line used for each object is listed in column (5) of Table 3.2.

3.2.4 Chandra X-ray Observations

To investigate the dynamics of the hot atmospheres in the cores of these clusters, we measured its velocity power spectra within the KCWI [OII] emission regions based on archival Chandra X-ray data available in the archive, observed by the Advanced CCD Imaging Spectrometer (ACIS). Details of the Chandra observations are listed in column (8) - (9) of Table 3.2. Each observation was reduced by `CIAO` 4.15 with the latest `CALDB 4.15` calibration, following the standard algorithm described by Vikhlinin et al. (2005). Intervals contaminated by background flares were removed from each observation using the light curves extracted from `level-2` event files above 10 keV. The X-ray background files were estimated using blank sky files, which were re-normalized to align with the count rates in the 10 - 12 keV band. To measure the gas density fluctuations, the exposure-corrected, background-subtracted images of each observation were generated in the $0.5 - 3.5$ keV band. In this energy range, the X-ray emissivity is independent of gas temperature for clusters with a mean temperature T $>\sim$3 keV. For each target, all observations were reprojected onto the observation with the largest exposure time and summed up into a single mosaic image. The background-subtracted exposure-corrected images within the cores of our targets are presented in Appendix A3.1.3. The bright point sources identified using `wavdetect` tool, as well as the central AGNs, were masked out from subsequent SB analysis.

3.3 Results

In Section 3.3.1, we first introduce the methods used for VSF analysis in this study. Section 3.3.2 presents the VSFs of v_{50} for four central galaxies. Each Gaussian velocity component is analyzed for Abell 1835 and PKS 0745 in Section 3.3.3. Comparisons between the VSFs of warm ionized gas and the cold molecular gas traced by ALMA CO emission are detailed in Section 3.3.4. Additionally, velocity spectra of hot gas observed by Chandra X-ray observations are discussed in Section 3.3.5.

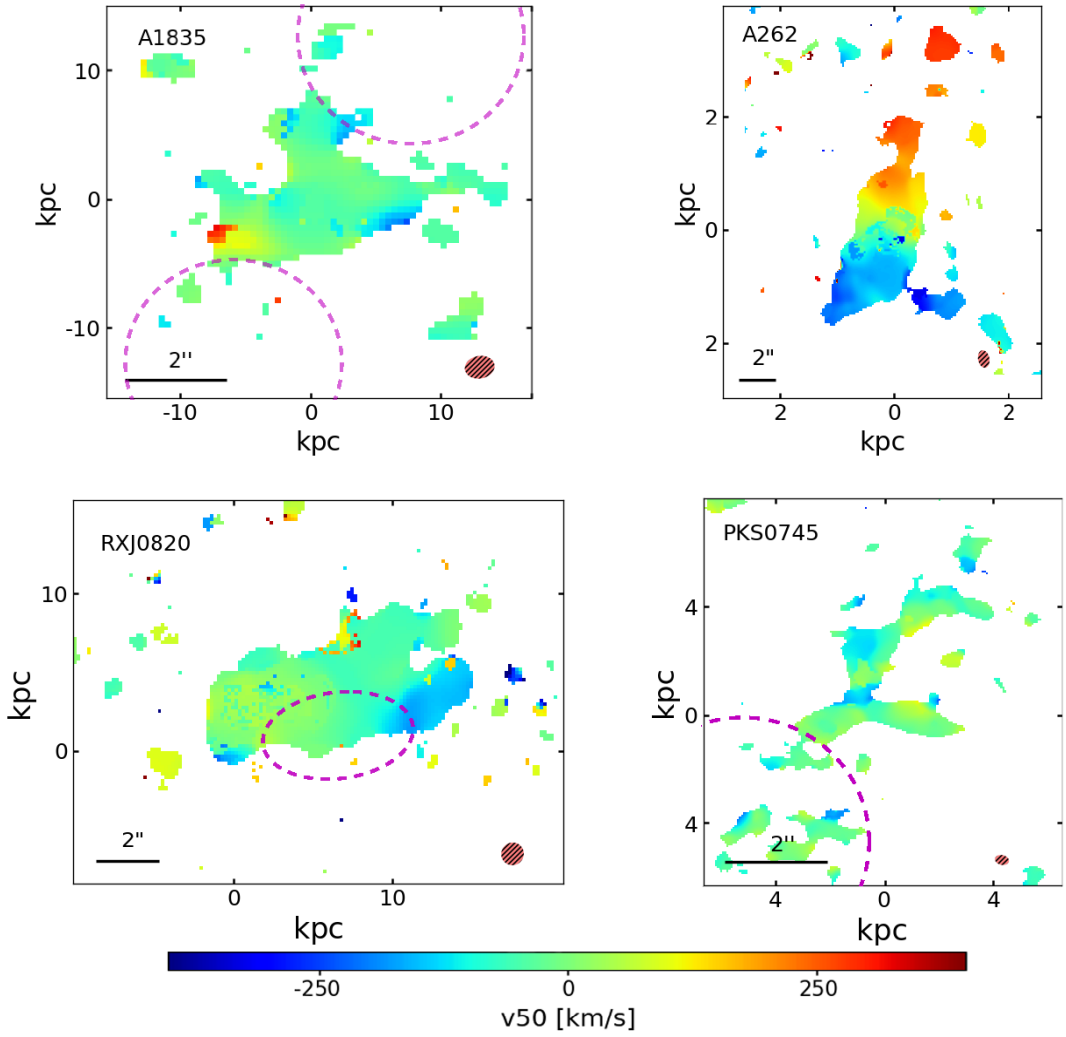


Figure 3.2: Velocity maps of molecular gas in the central regions of four galaxy clusters from our sample, derived from ALMA observations. The maps show CO (3-2) emission for Abell 1835 and PKS 0745, CO (2-1) emission for Abell 262, and CO (1-0) emission for RXJ0820, all detected at a signal-to-noise ratio greater than 3σ. Map origins align with the nucleus positions defined in the KCWI [OII] maps (presented in Figure 3.1). Red hatched ellipses represent the synthesized beam size and dashed magenta ellipses indicate the locations of X-ray cavities.

3.3.1 Velocity Structure Function

The VSF is a powerful analytical tool that extends beyond turbulence studies. It provides insights into the kinematics of gas, allowing us to identify and quantify the physical processes driving the observed motions such as rotational dynamics, gravitational effects, and interactions with external forces.

For VSF calculation, the projected separation, denoted by l, and the absolute velocity difference $|\delta v| = |v_i - v_j|$ is determined for all possible combinations of selected pixels. These pixel pairs are then grouped into distinct bins based on their separation l. Within each bin, the average of the velocity differences $\langle|\delta v|\rangle$is computed to determine the VSF amplitude at that specific scale. We experimented with evenly grouping pairs across the scales of interest and confirmed that the VSF results remain consistent.

The measurements are taken only at scales exceeding the point spread function (PSF). The bins with an insufficient number of pixel pairs can undermine the reliability of VSF measurements, especially at larger separations where the constraints of the image size become a limiting factor. To address this, bins where pairs drop below 20% of the peak value are excluded. This threshold ensures that sufficient pairs are included at each separation. The turnover scale refers to the point where the VSF amplitude reaches a local maximum. This scale may indicate the scale where energy is injected into the system and subsequently dissipates onto smaller scales, or it may be related to other factors such as bulk motions. Our findings indicate that the VSF is reliable up to scales no larger than half the extent of the map. Significant slope changes or turnovers may be influenced by insufficient pixel pairs at large separations — a limitation resulting from the restricted image size. This phenomenon, referred to as the 'window effect', stems from statistical uncertainty due to limited data size.The impact of the window effect on VSF measurements is further explored and discussed in Appendix A3.1.1.

The velocity differences $|\delta v|$ spread over a wide range within each bin. Simply using the mean difference does not adequately represent the $|\delta v|$ among all pairs. Therefore, to obtain a more comprehensive understanding, we analyze the $|\delta v|$ distribution at each measured scale. This detailed examination enhances our understanding of the characteristics of the resulting VSFs as well as the kinematics of gas within the cluster cores. We group the pairs into 10 km s^{-1} bins, ranging between 0 and the maximum $|\delta v|$ for each object. To allow for an efficient comparison analysis, each $|\delta v|$ bin count is normalized by the total number of pairs at that scale, ensuring value ranges between 0 and unity, allowing for comparison across scales.

Three of the clusters exhibit distributions with a peak at lower values and an extended tail reaching toward higher values. This shape resembles a log-normal distribution, which

describes a dataset where the logarithm of the values follows a Gaussian distribution. We fit the $|\delta v|$ distribution in each separation bin to a log-normal profile. By using the parameters from the best-fit model, we reconstruct the VSFs based on the mean of the log-normal distribution.

3.3.2 VSF of Warm Ionized Gas

Abell 1835

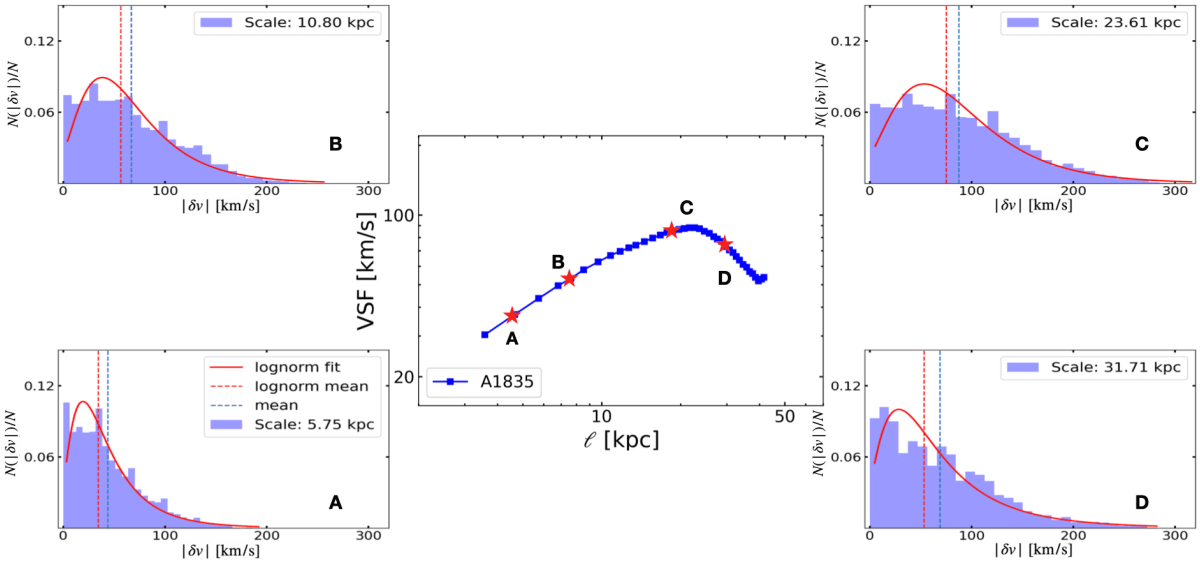


Figure 3.3: Middle: VSF analysis of warm ionized gas, traced by KCWI [OII] emission, within the core of Abell 1835. Only scales larger than seeing, and where pairs exceed 20% of the peak value, are plotted. Side panels: Distribution of velocity differences $|\delta v|$ among pixel pairs at four scales, marked as red stars in the VSF plot. The number of pairs in each $|\delta v|$ group is normalized by the total number of pairs for the entire separation bin to facilitate a comparative analysis of distribution shapes across varying scales. The best-fit log-normal profile is displayed as a solid red line over the $|\delta v|$ distribution. The vertical red dashed line represents the mean of the log-normal distribution, while the blue line shows the mean $|\delta v|$ of all pixel pairs within the given bin.

Abell 1835 is a typical example of a cool core cluster where the central galaxy is undergoing intense radio-mode feedback. X-ray observations have revealed two cavities as surface brightness depressions: one with a radius of ∼16 kpc, located ∼23 kpc northwest of the center, and another with a radius of 14 kpc, situated ∼17 kpc to the southwest (McNamara et al., 2006). Furthermore, Abell 1835 is characterized by strong nebular emission, with an Hα luminosity of 1.7×10^{42} erg s^{-1} (Wilman et al., 2006). The [OII] emission traced by KCWI extends over a wide area, reaching beyond $\sim$ 45 kpc in right ascension and $\sim$ 50 kpc in declination. As seen in the upper left panel of Figure 3.1, the nebular gas closely reflects the alignment of the X-ray bubbles, extending approximately 50 kpc along the axis of the bubbles. The median velocity of the [OII] emitting gas ranges between -30 km s^{-1} and +290 km s^{-1}. Most nebular gas is redshifted, indicating a consistent movement away from the observer relative to the central stellar velocity (Gingras et al., 2024).

The middle panel of Figure 3.3 displays the VSF of nebular gas in Abell 1835. The VSF ranges from 30 km s^{-1} on the smallest scale of $\sim$ 4 kpc to 88 km s^{-1} at a scale of 22 kpc. The turnover presented at a scale of $\sim$ 23 kpc suggests the driving scale of turbulence, which corresponds to the distance from the X-ray bubble to the nucleus of Abell 1835, indicating a potential link to radio-mechanical AGN feedback. Below this scale, the VSF increases steadily with a slope of approximately 0.39 at scales between 10 kpc and 20 kpc and steepens at scales below 10 kpc. A summary of the [OII] VSF measurements for Abell 1835, as well as those for the other three clusters, is presented in Table 3.3.

The side panels of Figure 3.3 illustrate the distributions of velocity differences $|\delta v|$ at four distinct scales to present the characteristic shapes as the scale varies. The mean $|\delta v|$ of all pairs is indicated by the blue vertical dashed line, corresponding to the VSF amplitude, marked by a red star in the middle panel. The histograms typically show a left-skewed peak towards the lower velocity differences, while the extended tails indicate a significant number of pixel pairs with high $|\delta v|$. As the separation scale grows from panels A to D, the tail of the distribution broadens, with $|\delta v|$ values reaching up to approximately 290 km s^{-1} at a scale of 32 kpc. This trend is consistent with the expectation that larger separations correlate with higher velocity differences. However, at smaller scales, such as the 5.75 kpc scale shown in panel A, a notably high $|\delta v|$ tail extends to nearly 200 km s^{-1}, far exceeding the mean of $\sim$ 44 km s^{-1}. This may be attributed to projection effects where pixel pairs close in projection but not in three-dimensional space exhibit large velocity differences. The red solid line in the histograms represents a log-normal fit to the distribution of $|\delta v|$. The means derived from the log-normal fits, denoted by the vertical red dashed lines, are consistently ∼14% to 22% lower than the direct mean of all pairs, suggesting that VSFs reconstructed by log-normal fitting can mitigate the influence of the extended tails, especially at smaller scales where these tails are more pronounced. Based

Target	Scales (kpc)	Turnover scale (kpc)	Scales for fit (kpc)	Slope
(1)	(2)	(3)	(4)	(5)
Abell 1835	3.6 - 43	22	3.6 - 22	0.58
			3.6 - 12	0.70
			12 - 22	0.39
Abell 262	0.6 - 5.9	/	0.6 - 5.9	1.0
RXJ0820.9+0752	2 - 17	9	2.0 - 8.7	0.60
PKS 0745-191	3.1 - 24	9	3.1 - 8.1	0.50
		17	17 - 24	0.86

Table 3.3: VSF of KCWI [OII] emission line: (1). Target. (2). Scales can be probed reliably. (3). Turnover scales shown in VSFs. (4). Scales at which the VSF slope is fitted. (5). Best-fitting slope of VSF.

on the comparison of the best-fit profiles and the distributions, the log-normal fit provides a reasonable approximation of these distributions in Abell 1835.

Abell 262

VSF can be measured at scales below 1 kpc due to the low redshift of Abell 262 and are plotted and shown in the middle panel of Figure 3.4. The mean velocity differences, ranging between 47 km s^{-1} at a 0.56 kpc scale and 510 km s^{-1} at a scale of 5.9 kpc, are substantially higher than the other three targets which have velocity differences $\sim$100 km s^{-1}. The continuous rise seen here with a slope of $\sim$1 suggests that the absolute velocity difference between two points increases linearly with their separation distance. This pattern is typical for systems where the velocity structure is dominated by rotation, rather than random turbulent motion.

The side panels of Figure 3.4 display velocity difference distributions at four specific separations. At small scales (in panels A and B), the distribution is fitted well by a log-normal profile, shown as the red solid line. However, at intermediate scales (in panel C), the distribution begins to widen and flatten, suggesting a more diverse mixture of velocity differences due to the varied orientations of pixel pairs across the map. At larger scales (in panel D, $\sim$ 5 kpc), the peak of the distribution shifts toward higher $|\delta v|$ values, marking

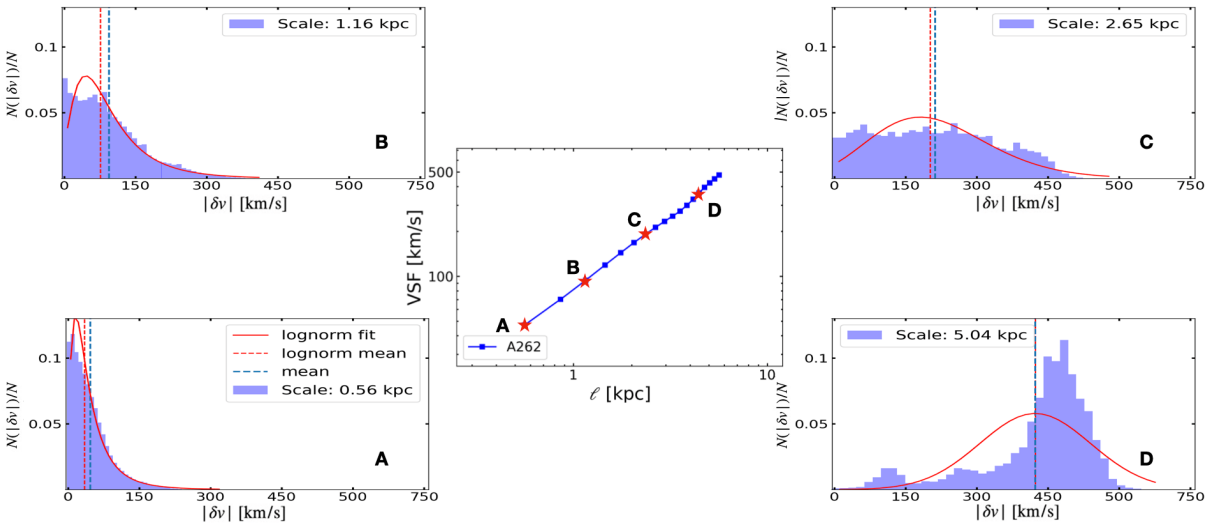


Figure 3.4: Middle: Similar to Figure 3.3, the middle panel displays the VSF for the nebular gas within the core of Abell 262. Side panels: the distributions of $|\delta v|$ within four separation bins.

a significant departure from the log-normal fit. This shift is indicative of increasing velocity differences with separation, consistent with the ordered, large-scale rotational motion within the ionized gas.

To further explore the motion of nebular gas in the core of Abell 262, we compare the VSFs of different [OII] brightness components within the central region where ALMA CO emission is observed. The continuum-subtracted [OII] flux map, presented in the left panel of Figure 3.5, reveals that the pixels with the highest 25% brightness in [OII] emission are concentrated near the nucleus of Abell 262, surrounded by the outer top 50% brightness component. The [OII] emission velocity dispersion map, illustrated in the middle panel of Figure 3.5, reveals a central high dispersion region extending along the axis of the AGN-driven radio jets. This suggests that the enhanced velocity dispersion may be a result of the jets colliding with the rotating gas disk (Gingras et al., 2024).

The right panel of Figure 3.5 shows that the VSFs of all [OII] brightness components exhibit identical slopes of ~ 1, suggesting coherent rotation around the center. The region

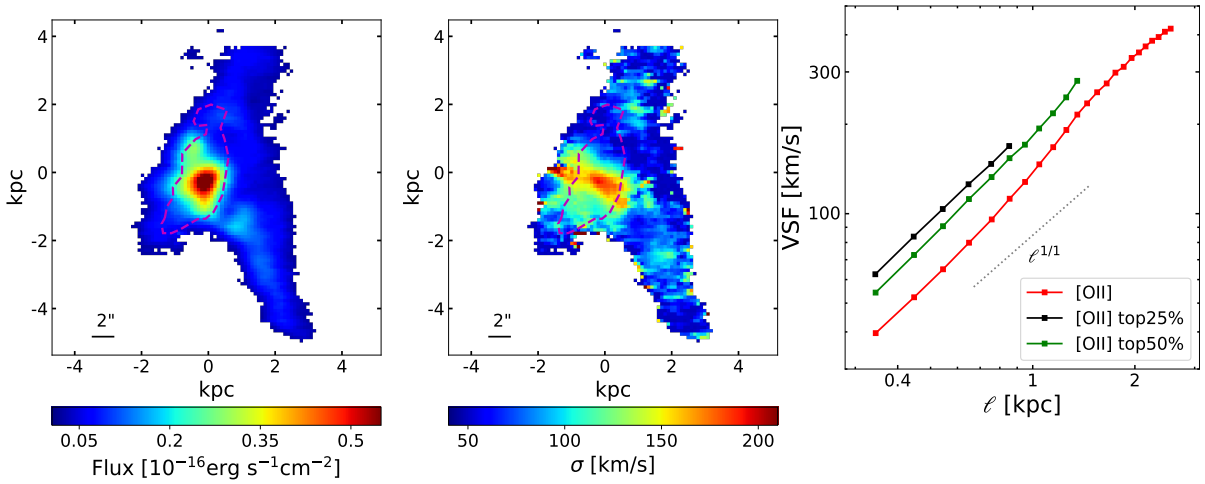


Figure 3.5: Left panel: Continuum-subtracted [OII] flux maps with S/N $\geq$ 5 in Abell 262. Middle panel: [OII] emission velocity dispersion map. The magenta line outlines the region where ALMA CO (2-1) emission is detected. Right panel: VSFs of nebular gas with different [OII] brightness levels in Abell 262. The red points show the VSF of nebular gas within the central region where ALMA CO emission is observed. The VSF results for the top 25% brightest [OII] pixels are shown with black squares, while those for the top 50% brightest [OII] regions are indicated by green squares.

containing the top 25% brightest [OII] emission has the highest VSF amplitudes, shown as the black points. A plausible explanation for the observed variation in VSF amplitudes is the differential rotation of ionized gas around the cluster's center, with higher angular velocities at the center contributing to the higher mean velocity differences observed in the brightest [OII] regions. Another possible reason is the projection effect, which will be discussed in detail in Section 3.4.2. The central 25% of the brightest [OII] emission is located in the high-density environment of the cluster core. More gas velocity components are aligned along the line of sight, which is consistent with the high velocity dispersion and contributes to the elevated VSF amplitudes measured.

RXJ0820.9+0752

RXJ0820 contains one of the most gas-rich central galaxies known. However, as seen in the bottom left panel of Figure 3.1, unlike the rest of the sample in this study, the [OII] line emission is not centered on the cluster nucleus but is instead offset to the northwest of the central galaxy, extending 24 kpc in RA and 15 kpc in DEC. A secondary galaxy located at ∼8 kpc SE to the main galaxy, moves at a relative velocity of ∼ 100 km s^{-1} (Bayer-Kim et al., 2002; Olivares et al., 2019). Therefore, it is plausible that sloshing motions, induced by the interaction with this nearby galaxy, might also contribute to the formation of and significant offset of cold gas reservoirs in RXJ0820 (Vantyghem et al., 2019).

The median velocity of [OII] emission is substantially redshifted compared to the central stellar velocity, ranging between −12 km s^{-1} and +286 km s^{-1}. The region with the highest median velocity is located approximately 4 kpc north of the nucleus, while the gas with the lowest velocities is found ∼ 14 kpc west of the nucleus. Given that the nebular gas is largely undisturbed, with velocity dispersion below 100 km s^{-1}, only a single Gaussian component is required to fit the velocity distribution of the ionized gas. This smooth velocity map, which lacks complex structures, is in a quiescent phase.

Figure 3.6 presents the VSF for the nebular gas in the core of RXJ0820. The amplitude of the VSF increases from below 30 km s^{-1} to 85 km s^{-1} over the scales spanning from 2 kpc to 17 kpc. The VSF is linear with a slope of ∼ 0.61 on scales of 2 - 8 kpc. The slope flattens progressively at larger scales around 9 kpc, which is close to the size of the X-ray bubble in RXJ0820, suggesting that the central AGN activity may drive the motion of nebular gas. The log-normal distribution can adequately describe the $|\delta v|$ distributions within the measured scales, as shown by the red solid lines in the side panels of Figure 3.6. This suggests that the high $|\delta v|$ tails, which are likely due to projection effects on small scales, can be mitigated by using a log-normal fit.

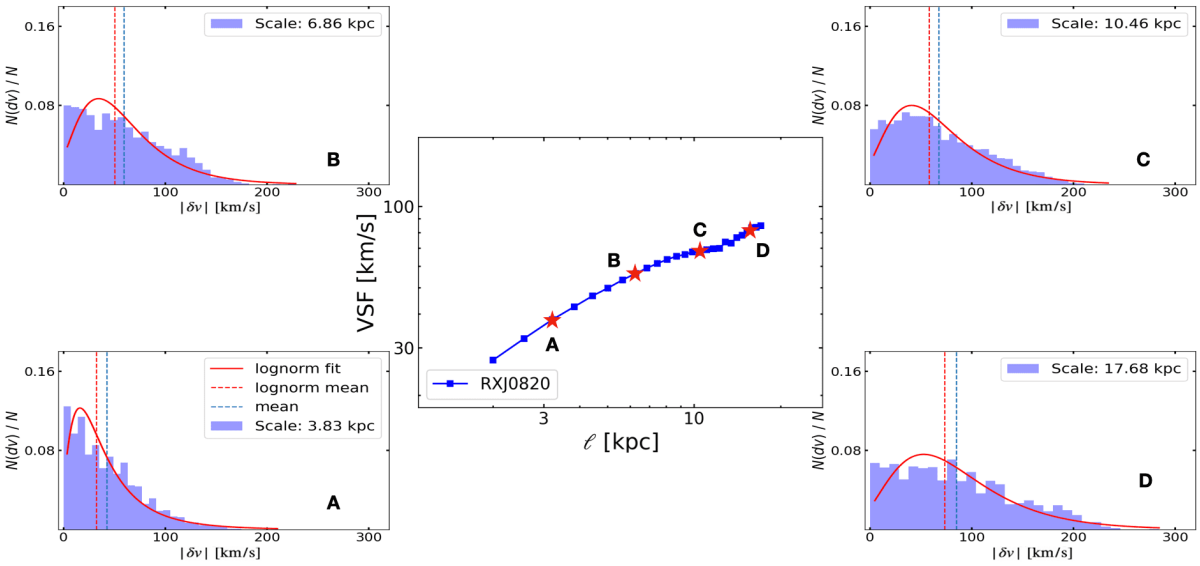


Figure 3.6: Middle: Similar to Figure 3.3, the middle panel displays the VSF for the nebular gas within the core of RXJ0820.9+0752. Side panels: the distributions of $|\delta v|$ within four separation bins.

PKS 0745-191

The bottom right panel of Figure 3.1 displays the nebular median velocity map of the core of PKS 0745. The nebular gas shows an average redshift of $\sim$ 135 km s^{-1} relative to the systemic stellar velocity, ranging from - 75 km s^{-1} to + 400 km s^{-1}. PKS 0745 has the broadest emission lines among four central galaxies, indicative of a highly disturbed environment with velocity dispersion up to 400 km s^{-1}. As a result, the line profiles of about 16% of the spaxels need to be modeled with two Gaussian velocity components. The dynamics of each gas component will be further discussed in Section 3.3.3. The central galaxy of PKS 0745 contains a powerful radio source, emitting energy ten times higher than the other targets (Pulido et al., 2018). The X-ray cavities, with diameters $\sim$ 10 kpc and 17 kpc and located approximately 6 kpc and 20 kpc from the center along the NW - SE axis, are asymmetrically positioned relative to the nucleus (Sanders et al., 2014), closely following the [OII] emission distribution, which spans 33 kpc in RA and 30 kpc in DEC. The core of PKS 0745 contains 4.9×10^9 M$_\odot$ of cold molecular gas, observed by ALMA CO

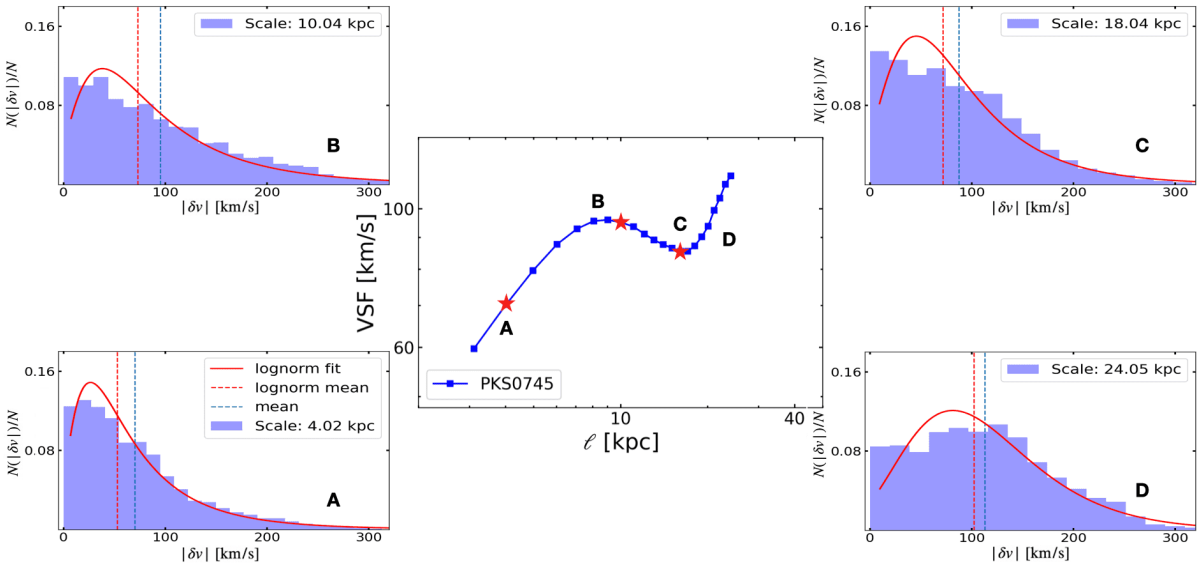


Figure 3.7: Middle: Similar to Figure 3.3, the middle panel displays the VSF for the nebular gas within the core of PKS 0745-191. Side panels: the distributions of $|\delta v|$ within four separation bins.

(3-2) emission line within 5 kpc of the nucleus (Russell et al., 2016), as indicated by the central black contours. It is mostly concentrated in the brightest nebular emission areas and lies in filaments trailing behind the X-ray cavities in the system.

Figure 3.7 illustrates the VSF of the nebular gas in PKS 0745. Starting from the smallest measured scales of 3 kpc to 8 kpc, the VSF rises linearly from around 60 km s^{-1} to a peak of approximately 95 km s^{-1} with a slope of 0.50. The VSF displays a turnover at a scale of $\sim$ 9 kpc, which is comparable to the size of the innermost cavity, which is 6 kpc southeast to the nucleus. It then drops to a minimum of 85 km s^{-1} at $\sim$15 kpc before rising again to over 120 km s^{-1} at the largest measured scale of 24 kpc. The limited FOV restricts the measurement of VSFs at larger scales. However, the complex VSF characteristics observed in PKS 0745 may indicate that the gas motions are driven by multiple cycles of central AGN activities. In side panels, all four $|\delta v|$ distributions exhibit left-skewed peaks with extended tails, and are well modeled by log-normal profiles, similar to those observed in RXJ0820 and Abell 1835.

3.3.3 VSF of the Two Velocity Components in Abell 1835 and PKS 0745-191

Emission line velocity profiles reveal the gas kinematics. A single Gaussian component often inadequately represents the line profile in the presence of multiple kinematic components. Two Gaussian velocity components were detected in Abell 1835 and PKS 0745 (Gingras et al., 2024), described in Section 3.2.2. The first Gaussian component, representing the "core" of the emission line, is typically narrower than the second component, which often has a broad wing at the base of the emission line. Multiple gas complexes along the line of sight can contribute to the line broadening. Turbulence introduces random motions resulting in a broadened velocity distribution. Additional broadening may arise from bulk motions associated with outflows, inflows, ordered motion (disks), dynamical stirring, supernovae, and AGN. To understand the kinematics of each component in Abell 1835 and PKS 0745, we calculate the VSFs of both velocity components of the ionized gas individually.

The top left and middle panels of Figure 3.8 show the median velocity of the first and second Gaussian kinematic components in the core of Abell 1835 (top row) and PKS 0745 (bottom row), respectively. Only pixels with both components detected at a significance of S/N > 3 are presented. The narrow component likely reflects the more extensive outer, quiescent region of the nebula, while the broad component, which is embedded within the narrow component, is primarily associated with the central region near the radio bubbles (Gingras et al., 2024) in Abell 1835 and PKS 0745-191 (Gingras et al., 2024).

The second kinematic component exhibits a significantly larger velocity variance across the field compared to the quiescent first component. A velocity gradient is observed in the median velocity map of the second component along the NW-SE axis of the X-ray cavities in Abell 1835 (Gingras et al., 2024). Additionally, highly redshifted gas with velocities exceeding 500 km s^{-1} is detected to the NW, E, and SE of the nucleus in the velocity map of the second component for PKS 0745, following the positions of X-ray cavities.

The right panels of Figure 3.8 show the VSFs for the first and second Keck [OII] components in Abell 1835 and PKS 0745. The second component, indicated by the red points, consistently shows higher VSF amplitudes across all scales, while the VSFs of the first component, represented by the green points, exhibit lower amplitudes, reflecting its milder variance compared to the second component. A summary of the VSF measurements is provided in Table 3.4.

In Abell 1835, both velocity components exhibit approximately linear growth as the scale increases, with a steeper progression observed at larger scales, approaching a slope of

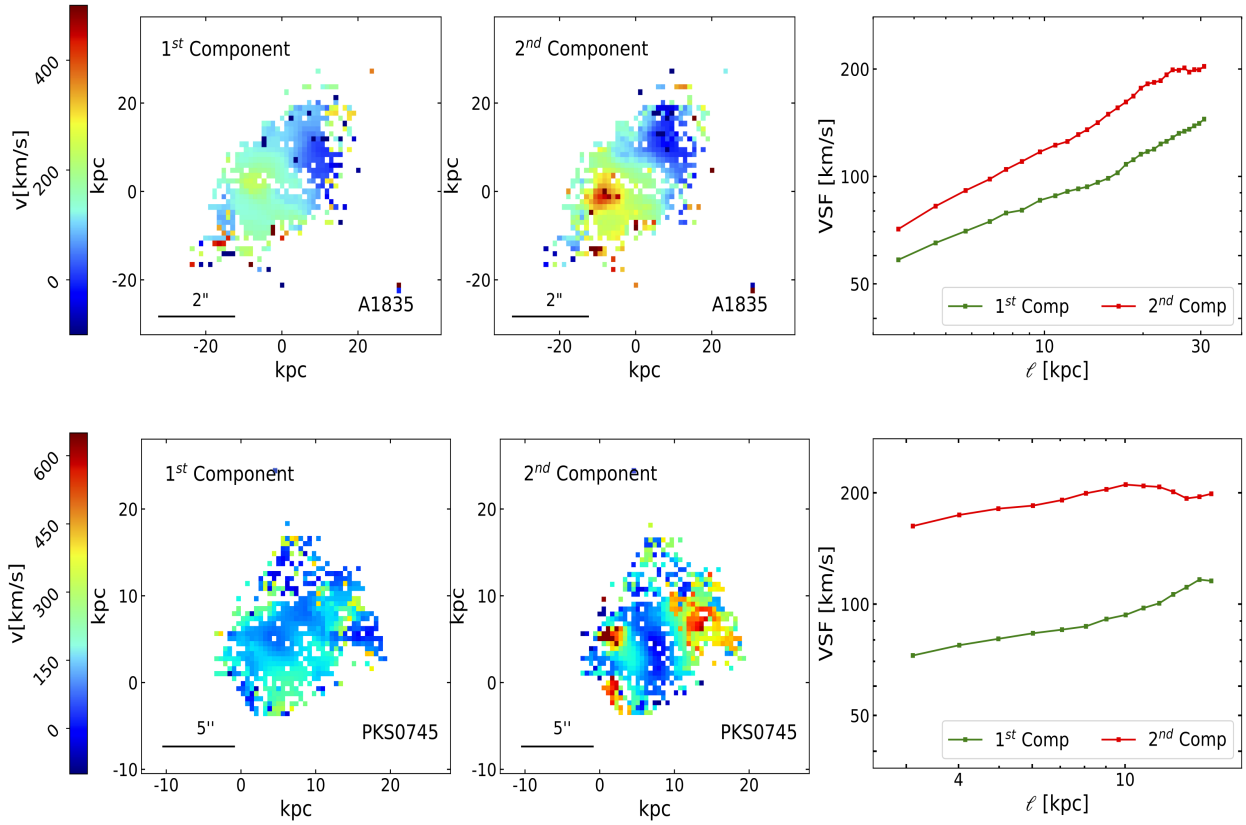


Figure 3.8: Velocity maps and VSFs of the first Gaussian component and the second Gaussian component derived from KCWI [OII] emissions in the core of Abell 1835 (top row) and PKS 0745 (bottom row). The maps include only spaxels where emission lines can be accurately fitted by two kinematic components with a S/N $\geq$ 3. In the right panels, the VSFs for the 1st and 2nd components are represented by green and red points, respectively.

Target	Component	Scales	Turnover scale	Scales for fit	Slope
		kpc	(kpc)	(kpc)	
(1)	(2)	(3)	(4)	(5)	(6)
Abell 1835	1st	4 - 30	/	4 - 17 / 17 - 30	0.35 / 0.53
	2nd	4 - 30	23	4 - 23	0.53
PKS 0745-191	1st	3 - 15	/	3 - 8 / 8 - 15	0.19 / 0.43
	2nd	3 - 15	10	3 - 10	0.21

Table 3.4: The VSFs of the first and the second Gaussian velocity component in the Abell 1835 and PKS 0745-191, traced by Keck [OII] emission: (1). Target. (2). Component. (3). Scales can be probed reliably. (4). Turnover scales shown in VSFs. (5). Scales at which the VSF slope is fitted. (6). Best-fitting slope of VSF.

1/2. This steepening at larger scales may be attributed to the gravitational acceleration of the gas, as discussed in more detail in Section 3.4.1. Additionally, the VSF of the second component begins to flatten beyond the $\sim$ 23 kpc scale, which corresponds to the distance of the X-ray bubbles from the center of Abell 1835. In A1853, the VSFs of [OII] emission obtained using both components, as presented in Figure 3, also exhibit a turnover at this scale. It suggests that the scale of energy injection into the gas motions is closely linked to the rising bubbles and the dynamics of the turbulent component.

A similar pattern for both components is observed in PKS 0745. The first component shows comparable linear growth with a slope of $\sim$0.2 at scales below 8 kpc, followed by a steeper increase of $\sim$0.43. Meanwhile, the VSF of the second component, represented by the red points, exhibits a significantly higher amplitude. A turnover is observed at the scale of 10 kpc, which is close to the size of the secondary southeast X-ray cavity in PKS 0745. A turnover is also observed at the same scale in the VSFs of PKS0745, which uses a double-component V50, as shown in Figure 3.7. This observation further supports the idea that gas motions are induced by AGN activity.

Overall, these findings suggest that the two different Gaussian components trace two distinct kinematic components with different origins. The second component likely reflects the turbulent motion of gas driven by AGN activity in the galaxy. Additionally, gravity likely also has a significant influence on the motion of both components.

3.3.4 Molecular Gas Distribution and Kinematics

Here we compare the kinematics of the nebular gas to the cold molecular gas. Figure 3.2 shows the line of sight velocity maps of the dominating component of CO emission observed by ALMA in our samples. The CO emission distribution is filamentary, clumpy, and asymmetric. Most of the gas lies in extended filaments outside of the nucleus surrounding or extending towards X-ray cavities inflated by radio jets.

In PKS 0745, 4.6×10^9 $M_\odot$ molecular gas is observed in three filaments extending in the N, SW, and SE directions (Russell et al., 2016). The N and SW molecular filaments extend up to 5.7 kpc and 3.6 kpc, respectively, towards the X-ray cavities. Abell 1835 contains 5×10^{10} $M_\odot$ of molecular gas, detected by CO(3-2) and CO(1-0) emission with ALMA (McNamara et al., 2006). The molecular gas is concentrated around the central galaxy and three filaments extending 35 kpc in RA and ∼25 kpc in DEC. Two filaments, projecting towards the NW and SE X-ray cavities, appear to be part of a bipolar outflow with a mass of around 10^{10} $M_\odot$, which may be driven outwards by the mechanical energy from the buoyantly rising bubbles.

In contrast, the molecular clouds in RXJ0820 are displaced northward 3 kpc from the nucleus, similar to the nebular gas. The cold gas is concentrated into two bright clumps. The brighter clump is approximately 3 kpc north of the BCG center, while the secondary clump is 4.6 kpc west of the primary clump. The cavity is too feeble to lift enough low-entropy gas to explain the observed gas via simulated cooling. Instead, the sloshing motions in the ICM, induced by the close passage of a nearby galaxy, might contribute to the condensation of the cold gas and its displacement (Vantyghem et al., 2019). Abell 262 is the only system here with a gaseous, circumnuclear disk approximately 3 kpc across, whose angular momentum axis lies approximately perpendicular to the radio jets and X-ray bubbles (Gingras et al., 2024).

To investigate the relationship between different gas phases and their roles in AGN feedback, we calculate the VSF of the cold gas observed by ALMA and compare it with that of the warm ionized gas, as illustrated in Figure 3.9. Here the median velocity of the Keck [OII] emission is modeled using a single Gaussian component for all four targets, including Abell 1835 and PKS 0745, as the velocity of the molecular gas is similarly characterized by a single dominant component. To ensure accuracy, we focused only on central regions where both CO and [OII] emissions are detected, as indicated by the black dashed lines in Figure 3.1. The yellow points represent the VSF of warm nebular gas. Due to the compact nature of the CO emission, the measurements are confined to scales of approximately 10 kpc in all targets. A measurement summary is provided in Table 3.5.

We examined and accounted for the systematic effects of telescope resolution, seeing,

and smoothing applied during data processing to the comparison of VSFs obtained from multiple instruments. Smoothing determines the low separation cut-off, the VSF slope, and amplitude. It decreases the velocity differences across the field, leading to amplitude suppression, particularly at scales below the smoothing kernel width, further steepening the slope. The smoothing effect on VSF is detailed in Appendix A3.1.2.

The KCWI data has a lower spatial resolution than ALMA. Its smallest spatial scale probed for VSF measurement is determined by the seeing for each object. The ALMA observations are smoothed by their synthesized beam sizes during data reduction. For a direct and meaningful comparison, we smoothed the ALMA maps using box kernels to match their synthesized beam size to the seeing of the KCWI observations. Due to the asymmetry of the synthesized beam, we applied smoothing based on the length of its major axis. The VSFs of the smoothed CO emission are presented as the blue points in Figure 3.9. The unsmoothed CO emission VSFs are not shown, but the measurements are summarized in Table 3.5.

The VSF of the ALMA CO (2-1) emission in Abell 262 ranges from 39 km s^{-1} at a scale of 0.2 kpc to 397 km s^{-1} at a scale of 2.6 kpc, with a slope of ~ 0.97. The smoothed ALMA VSF slope increases to ~ 1.12, as shown by the blue points in the upper right panel of Figure 3.9, nearly aligning with the KCWI VSF of 1.21. Despite slight differences observed at smaller scales, the molecular gas VSF exhibits similar amplitudes to that of the nebular gas, represented by the yellow points. This consistency suggests that the warm and cold gas phases are dynamically coupled in their rotation around the nucleus.

The cold molecular and nebular gases in RXJ0820 also exhibit a close coupling. The smoothed VSF of CO (1–0) emission ranges from 33 km s^{-1} to 91 km s^{-1} at scales of 1.8 to 12.5 kpc, with a slope of ~ 0.53. The KCWI [OII] VSF within the CO emission region exhibits a slightly steeper slope of 0.62 but with lower amplitudes, particularly at smaller scales. Nonetheless, both phases increase similarly as scales increase and show no turnover. Considering both cold molecular and nebular gas offset from the cluster center, although mild differentiation between the two gas phases is seen, their kinematics, overall, are similar.

The right panel of Figure 3.10 shows the one-component velocities of hot gas motions observed within the [OII] emission-detected area in the core of Abell 1835, ranging from 71 km s^{-1} at 18 kpc scale to 92 km s^{-1} at a 35 kpc scale. Although the energy injection scale cannot be constrained from the SB fluctuation analysis, the velocity spectrum and VSF of [OII] emission show consistency around the [OII] VSF turnover scales of ~ 20 kpc, close to the bubble size in this system. Combined with the cold gas distribution along the cavity axis, it suggests that the nebular filaments likely condensed from the turbulent

hot ICM due to thermal instability, triggered by the inflation of X-ray bubbles related to central AGN activities in Abell 1835.

The velocity structure of the CO (3-2) line emission, resolved into three main filaments that contain roughly 90 percent of the total molecular gas mass in the BCG of PKS 0745, is used to compute the VSF of the cold phase gas, and compared to the [OII] emission in the bottom right panel of Figure 3.9. The VSF of the smoothed ALMA CO emission, shown as the blue points, varies from 52 km s^{-1} to 62 km s^{-1} at scales of 2.0 kpc to 7.6 kpc, which is lower than that measured in the other three targets. This is consistent with the low velocity dispersion of less than 150 km s^{-1}, which is significantly lower than the typical stellar velocity dispersion of such a massive BCG. The [OII] emission VSF differs in amplitude from the molecular gas, and at some points has opposite signs, indicating the two gas phases are moving separately. Due to the limited extent of CO emission, we are unable to measure its VSF on the characteristic scales of bubbles in this system.

The comparison between the first and second velocity components of [OII] emission in Abell 1835 and PKS 0745 and the dominant component of molecular gas, as shown in Figure 3.9, presents both intriguing insights and challenges for interpretation. The first (green dashed line) and second [OII] (red dashed line) components in both systems exhibit slopes similar to those of the single Gaussian VSFs but differ in amplitude by more than a factor of two. Notably, these components appear to be disconnected from the molecular gas, a phenomenon that remains difficult to understand. A major factor may be sensitivity, as nebular emission is more sensitive to gas mass by two to three orders of magnitude. Therefore, more sensitive ALMA observations would be required to probe these components at the level of detail provided by the [OII] observations.

In summary, the nebular and molecular gas VSFs for Abell 262 and RXJ0820, apart from mild differentiation, are broadly consistent indicating strongly coupled kinematics on all scales. However, the VSFs for PKS 0745 and Abell 1835, which are experiencing strong radio-AGN feedback, are more complex. The gases are correlated only at some scales in Abell 1835 but are differentiated at all scales in PKS 0745.

3.3.5 Velocity Spectra of Hot ICM

We use existing Chandra X-ray observations to estimate the velocity spectra of hot ICM motion in our targets. The X-ray emissivity in the soft energy band (0.5 - 3.5 keV is used in this work) is weakly dependent on temperature when the electron temperature exceeds 3 keV. Therefore, the SB fluctuations observed in X-ray images reflect gas density fluctuations. First, the 'unperturbed' SB gradient is removed by dividing the raw images by the

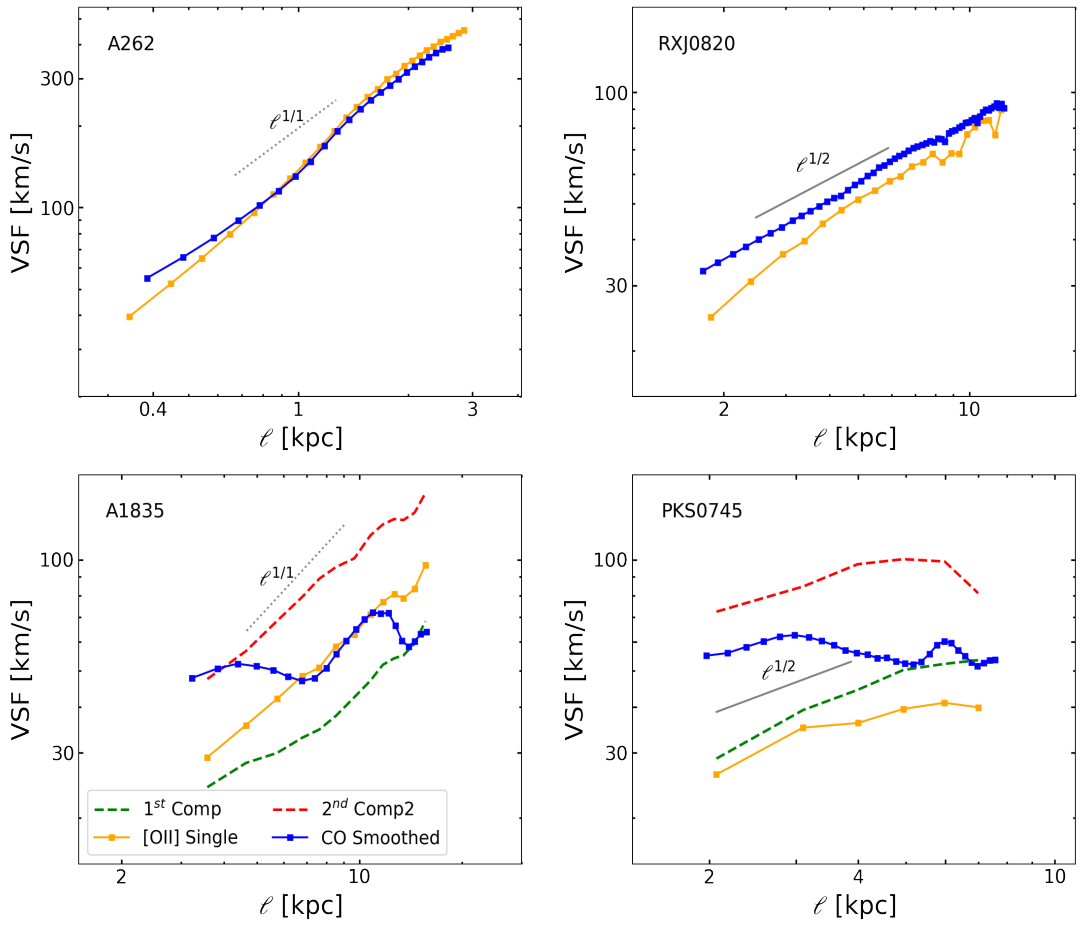


Figure 3.9: Comparison of the VSFs of cold molecular gas and warm ionized gas in our sample clusters, traced by ALMA CO emission and Keck [OII] line emission, respectively. The VSFs of the single component v50 (yellow points), the 1st (green dashed line) and the 2nd (red dashed line) velocity component from the Keck observations are computed within the regions covered by ALMA CO emission. For each cluster, the ALMA velocity map is smoothed with a box kernel to match the ALMA observation beam size with the KCWI seeing, and the smoothed CO emission VSF is shown as blue points. Only scales exceeding the ALMA observation beam size and KCWI seeing limits, and having a sufficient number of pixel pairs for reliable VSF calculation, are displayed here. Reference lines with slopes of 1/1, and 1/2 are also included.

Target	CO emission				Smoothed CO emission				[OII] emission			
	Scales	$\|\delta v\|$	Scale for fit	Slope	Scales	$\|\delta v\|$	Scale for fit	Slope	Scales	$\|\delta v\|$	Scale for fit	Slope
	(kpc)	(km s^{-1})	(kpc)		(kpc)	(km s^{-1})	(kpc)		(kpc)	(km s^{-1})	(kpc)	
(1)	(2)	(3)	(4)	(5)	(6)	(7)	(8)	(9)	(10)	(11)	(12)	(13)
Abell 1835	1.4 - 15.8	36 - 77	6.8 - 11.6	0.83	3.3 - 15.8	48 - 72	6.8 - 11.6	0.92	3.3 - 15.6	28 - 97	3.3 - 15.6	0.85
Abell 262	0.2 - 2.6	39 - 397	0.2 - 2.6	0.97	0.4 - 2.6	55 - 391	0.4 - 2.6	1.12	0.4 - 2.8	40 - 452	0.4 - 2.8	1.21
RXJ0820.9+0752	0.5 - 12.5	21 - 98	0.5 - 12.5	0.48	1.8 - 12.5	33 - 91	1.8 - 12.5	0.53	1.8 - 12.3	25 - 90	1.8 - 12.3	0.62
PKS 0745-191	0.6 - 7.6	48 - 71	/	/	2.0 - 7.6	52 - 63	/	/	2.4 - 7.3	30 - 43	4.2 - 6.8	0.43

Table 3.5: Comparison between the VSFs of cold molecular gas and warm ionized gas: (1). Target. (2) - (5). VSFs of CO emission: scales can be measured, measured VSF, scales for slope fitting, best-fit slope. (6) - (9). VSFs of smoothed CO emission. (10) - (13). VSFs of [OII] emission in CO detected region.

best-fit spherically symmetric β-model. Then, the rms of SB fluctuations at wavenumber k in the residual images are calculated using the modified Δ-variance method (Arévalo et al., 2012), and are deprojected to derive the scale-dependent amplitudes of gas density fluctuations, $A_{3D}(k)$ (Churazov et al., 2012).

Using cosmological simulations of relaxed galaxy clusters, Zhuravleva et al. (2014b) provide a theoretical argument and confirm the linear scaling relation between the amplitudes of gas density fluctuations and velocity fluctuations across a wide range of scales:

$$A_{3D}(k) \equiv \frac{\partial \rho_k}{\rho_0} = \eta_1 \frac{V_{1,k}}{c_s}, \tag{3.1}$$

where c_s is the sound speed in the atmosphere, and $\eta_1 \approx 1 \pm 0.3$ is the proportionality coefficient. The velocity spectra $V_{1,k}$ in this work are defined as velocity fluctuation at scale $l \equiv k^{-1}$, rather than the energy distribution of velocity fluctuations obtained from the Fourier transform of the velocity field. This method overcomes the challenge of directly measuring gas velocity due to the low spectral resolution of current X-ray observations. The indirect velocity spectra measurements (Zhuravleva et al., 2018) are consistent with the direct measurements of line-of-sight velocity dispersion obtained by Hitomi (Hitomi Collaboration et al., 2016) within the central 30 - 60 kpc of the Perseus cluster.

The projected areas where CO emission is detected are too small for X-ray SB analysis, therefore, a direct comparison to cold molecular gas is not included in this work. The velocity amplitudes of hot atmosphere motions are estimated within the KCWI [OII] emission detected regions, marked as blue points in Figure 3.10. The width of the blue regions reflects the 1σ statistical uncertainty. Due to the predominance of Poisson noise at small scales, we only present measurements at scales where the power of X-ray SB fluctuations is larger than that of the Poisson noise. Deeper observations are needed to accurately constrain gas perturbations on smaller scales, allowing us to compare multi-phase gas dynamics across a wider range of scales. Table 3.6 lists the X-ray measurements in each cluster. Given the similar rotational kinematics observed between the molecular and nebular gas in the core of Abell 262, both demonstrate clear signs of ordered motion. Additionally, the X-ray observation of the core of Abell 262 in the soft energy band is illustrated in Figure A3.6. Notably, two cavities inflated by the AGN jet, manifesting as SB depressions, are distinctly visible on the eastern and western sides of the center. The ICM distribution at the center also aligns with the rotation axis, indicating interactions with the cold gas disk. These dynamic features go beyond what can be analyzed through X-ray SB analysis alone; therefore, we focused our analysis on the other three targets, excluding Abell 262.

The right panel of Figure 3.10 shows the one-component velocities of hot gas motions observed within the [OII] emission-detected area in the core of Abell 1835, ranging from 71 km s^{-1} at a 57 kpc scale to 92 km s^{-1} at a 139 kpc scale. Although the energy injection scale cannot be constrained from the SB fluctuation analysis, the velocity spectrum and VSF of [OII] emission show consistency around the [OII] VSF turnover scales of $\sim$ 20 kpc, close to the bubble size in this system. Combined with the cold gas distribution along the cavity axis, it suggests that the nebular filaments likely condensed from the turbulent hot ICM due to thermal instability, triggered by the inflation of X-ray bubbles related to central AGN activities in Abell 1835.

The velocity spectrum of RXJ0820 ranges between 68 km s^{-1} at a 17 kpc scale and 192 km s^{-1} at a 40 kpc scale, shown in the middle panel of Figure 3.10. The FOV of [OII] emission observations limits direct comparison between the VSF of the nebular gas and the X-ray velocity spectrum at large scales. Nevertheless, at the 17 kpc scale, where overlap occurs, the VSF amplitude of the nebular gas and the derived velocity of hot atmospheric motion are both measured at approximately 80 km s^{-1}, indicating their potential coupling. Given that the motion of cold filaments is also closely coupled with that of the nebular gas, there are two possible scenarios in which the filaments could share similar turbulent motions with the hot ICM: (1) the filaments form from the hot atmospheres, allowing them to retain the turbulent characteristics of the hot gas, or (2) the filaments, even though formed independently, evolve to be co-moving with the hot gas over time.

In the right panel of Figure 3.10, the hot atmosphere in PKS 0745 exhibits a velocity spectrum ranging between 107 km s^{-1} and 151 km s^{-1} at scales of 8 kpc to 30 kpc. The VSF of the nebular emission is lower than that of the hot ICM, and the turnover at the scale of 9 kpc seen in the ionized gas is not observed in the X-ray measurements.

The slope of the velocity spectra may be affected by the Δ-variance method used in the X-ray surface brightness analysis. Furthermore, the considerable uncertainties presented in Figure 3.10 correspond to a broad spectrum of slopes, preventing us from confirming or ruling out Kolmogorov turbulence.

In summary, in Abell 1835, RXJ0820, and PKS0745, the velocity amplitudes of gas motion in the hot atmospheres determined by X-ray SB analysis range from $\sim$ 100 km s^{-1} to $\sim$ 200 km s^{-1}, aligning with the expected turbulent velocities of the ICM. The cold and hot gas in Abell 1835 and RXJ0820, exhibit consistent kinematics at large scales, indicating a potential relationship in their formation and evolution. It suggests that the interaction and co-evolution of different gas phases play a significant role in the dynamics of galaxy cluster cores.

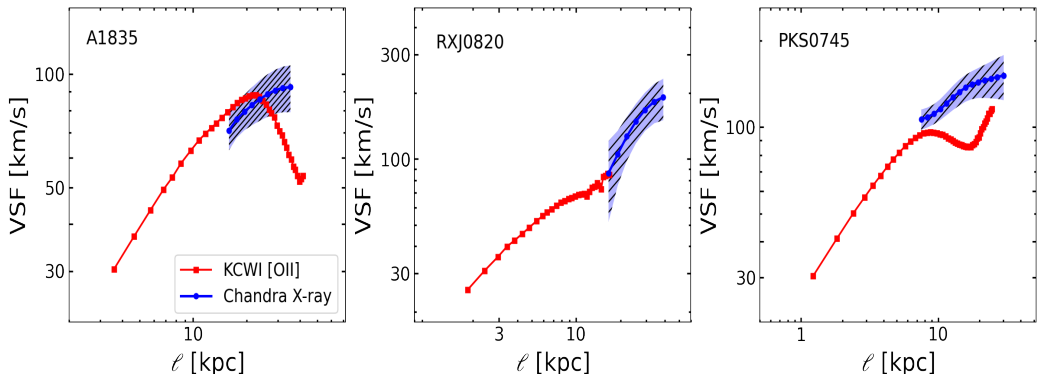


Figure 3.10: Comparison between the VSFs of warm ionized gas traced by Keck [OII] line emission and the Chandra X-ray surface brightness fluctuation analysis in the cool cores of Abell 1835, RXJ0820.9+0752, PKS 0745-191. The VSFs of warm ionized gas are presented as the red points. Only scales exceeding the seeing limits, and with a sufficient number of pixel pairs for reliable VSF calculation, are displayed here. The power spectra of hot ICM motions are computed within the regions covered by KCWI [OII] emission, and are depicted by the blue points. The hatched regions reflect 1σ uncertainty. Only scales are least affected by systematic uncertainties and Poisson noise are shown. The X-ray results are summarized in Table 3.6

Target	T	Scales	V_{turb}
	(keV)	(kpc)	(km s^{-1})
(1)	(2)	(3)	(4)
Abell 1835	2.7	16 - 35	71 - 92
RXJ0820.9+0752	1.3	17 - 40	68 - 192
PKS 0745-191	2.6	8 - 30	107 - 151

Table 3.6: The velocity power spectra derived from X-ray SB fluctuation analysis using Chandra X-ray observations: (1). Cluster name, (2). Median temperature in the region of interest, (3). Spatial scales least affected by Poisson noise, (4). Velocity of gas motion.

3.4 Discussion

3.4.1 The VSF Slope and Steepening at Small Scales

The VSFs of gas in all phases in Abell 262 exhibit clear characteristics of ordered motion, with a slope of ~ 1, consistent with disk rotation. Therefore, our discussion focuses on the VSFs in the other three filament-dominated objects. In these clusters, the VSFs are steeper than the 1/3 slope of classic Kolmogorov turbulence in an incompressible fluid. We do not necessarily expect the VSF slopes of the warm and cold gas phases to follow the ideal Kolmogorov slope, which serves as a reference for comparison.

The VSFs of filamentary nebular structures with slopes $\geq 1/2$ are reported in the centers of Perseus, A2579, and Virgo (Li et al., 2020). The VSFs of multiphase filaments in the centers of 10 galaxy clusters have been measured, and in all systems, the slopes are found to be steeper than those expected by classical Kolmogorov theory (Ganguly et al., 2023). Supersonic turbulence, which has a characteristic slope of 1/2 has been seen in simulations of of galaxy clusters and AGN feedback, indicating that cold gas may fragment out of a supersonic outflow driven by AGN jets or winds, forming the extended filamentary nebulae (Qiu et al., 2020). These supersonic turbulent structures can become 'frozen' in the cold gas and flatten rapidly over a short timescale of approximately 10 Myr (Hu et al., 2022). Our observations reveal nebular and molecular gas speeds significantly below the hot atmospheres' sound speeds.

For warm ionized gas at a temperature of $\sim 10^4$ K, the sound speed is ~ 10 km s^{-1}; thus, the VSF amplitudes measured are highly supersonic. However, the velocities we have observed pertain to external gas motions, and the filaments themselves do not inherently exhibit supersonic characteristics. Thus, it is still uncertain whether the steep VSF can be directly linked to the supersonic nature of the originating outflows.

Despite excluding measurements significantly affected by the smoothing effect, amplitude suppression persists across all ranges, not just contributing to the VSF steepening at smaller scales (as detailed in Appendix A3.1.2). Other factors may also play a role.

Gravity will steepen the VSF. We investigated the influence of gravity following the methodology of Wang et al. (2021): test particles with identical initial velocities fall from the same height, overshoot the center while decelerating outward and oscillate. We sample the particles over different time intervals and find that the VSF slopes are sensitive to the time interval sampled, with the slope approaching a maximum of ~ 1 during the phase before the particles return toward the center. Over a longer trajectory, which includes several oscillation periods, the VSF of gravity-dominated motion flattens over time. However,

it does not consistently converge to 1/2 or 1/3, as suggested by Wang et al. (2021), but rather approaches zero.

If the cold filaments condense out of the hot atmosphere, they may retain the memory of the initial conditions of the hot gas and fall toward the center under gravity. However, they may not overshoot the center via ballistic motion and continue oscillating around it. The infalling filaments may collide with pre-existing cold gas clouds, leading to a reduction in their velocity or their disruption before reaching the center. The freefall of cold gas can also be slowed by magnetic stresses, or velocity kicks due to bulk motion. Therefore, during the infall process, the VSF slope of the cold-phase gas is likely to remain close to 1 or below. The steep slope due to gravity is more pronounced on larger scales because the velocity differences accumulate over greater displacements. This phenomenon may explain the decreasing differences in the VSFs of cold molecular gas and warm ionized gas at large scales, as observed in Figure 3.9.

Magnetic fields can stabilize gas motion by suppressing the growth of hydrodynamic instabilities through a mechanism known as 'magnetic draping'. This stabilization can steepen the VSF of turbulence generated by AGN-driven bubbles, as the energy cascade to smaller scales is hindered. Additionally, magnetic fields introduce anisotropy into the velocity field, with more significant suppression along the field lines (Bambic et al., 2018). Mohapatra et al. (2022) used simulations of homogeneous isotropic subsonic turbulence to study the VSF of multiphase gas. They found that in the hot phase, the gas remains more isotropic and is less constrained by magnetic tension forces. However, in the cold phase, magnetic pressure dominates, leading to a much steeper VSF, especially at smaller scales.

Some quasars exhibit Kolmogorov or shallower slopes. Chen et al. (2023) found that among the four quasi-stellar object (QSO) nebulae studied, only TXS0206-048's VSF follows the Kolmogorov slope, while the others are shallower. The flatter VSFs may indicate multiple energy injection scales (ZuHone et al., 2016) including AGN, mergers, magnetic field stresses (Wang et al., 2021), or geometrical projection (see below in Section 3.4.2). The conclusive interpretation is unclear, but the agents governing the VSF of the quasars in (Chen et al., 2023) differ from the central galaxies studied here.

3.4.2 Projection Effects

After accounting for smoothing, the VSFs of nebular emission and molecular gas are broadly similar in the cores of Abell 262 and RXJ0820, indicating the coupling of gas kinematics. However, the VSFs of [OII] emission, shown as yellow points in Figure 3.9, are consistently smaller and steeper than those derived from ALMA CO emission, shown

as blue points, across all four targets, particularly at smaller scales. Projection is likely responsible for these scale-dependent differences. Although the VSFs of gas in both phases are computed within the same projected region near the cluster center, the measured VSFs are influenced by the depth of the cloud along the line of sight L. At a given scale $l < \mathrm{L}$, the VSF is expected to be steepened, and the intrinsic slope generally recovers at larger scales $l > \mathrm{L}$ (O'Dell & Castaneda, 1987; Xu, 2020). This effect is similar to the smoothing effect discussed in AppendixA3.1.2 and is usually termed 'projection smoothing'. The nebular gas envelops the cold molecular gas, thus having a larger depth and being more significantly affected by projection smoothing. It is consistent with the relatively large amplitude differences at small scales and the observed steepening of the KCWI VSF below the scale of ∼6 kpc in RXJ0820.

The clearest example of a projection bias is seen in Abell 262, as shown in Figure 3.5. There the brightest [OII] emission has the highest velocity amplitude and is thus closer to the nucleus where the gas density is highest. The lower speeds of the fainter emission along any line of sight indicate emission further from the center where the gas density is lower.

The kinematics in Abell 1835 and PKS0745 are distinct from Abell 262. The large velocity differences observed at small scales cannot be fully explained by projection effects alone, indicating that the distinctions between the nebular and molecular gas are real. Feedback acting on gases with significant variations in temperature, density, and volume filling factor may play a contributing role.

Zhang et al. (2022) found that projection in compact emission sources flattens the VSF rather than steepens it. The velocity difference distribution plots reveal the presence of high $|\delta v|$ tails, even at small scales. These pixel pairs may correspond to two physically distant points that appear close in projection, potentially leading to an overestimation of the VSF amplitude at small scales and thereby flattening the slope.

Both types of projection effects may occur simultaneously, but the resulting net effect depends on the distribution of clouds and the kinematics of their gas. We cannot recover the intrinsic slope by correcting for projection effects because we lack specific knowledge about these properties. In this study, we merely propose potential explanations for the discrepancies observed in the VSFs of [OII] and CO emissions across different scales, presented in Figure 3.9.

3.5 Conclusions

The VSFs of [OII] emission are compared to cold molecular gas probed by CO emission along common lines of sight in four systems. In addition, the velocity spectra of the surrounding hot atmospheres are estimated from surface brightness fluctuations observed with the Chandra X-ray observatory. These comparative analyses enable us to explore correlations between gas phases from temperatures ranging between 30 K and 10^7 K. Several technical issues that can bias the interpretation of the VSF analyses are explored. The main conclusions are as follows:

- The VSF of KCWI [OII] emission shows that the nebular gas is disturbed in three of four clusters. Abell 262 is the exception, where the gas is rotating about the nucleus.
- The cold molecular gas, traced by ALMA CO emission, is spatially aligned with [OII] emission in each central galaxy. A comparison of the VSFs in RXJ0820 and Abell 262, where the gas is either in rotation or relatively quiescent, shows similar motions across all scales, but with minor differences. These similarities in motion may indicate common dynamics and perhaps a similar origin of formation.
- In Abell 1835, the VSFs of cold and warm gas differentiate at small scales, while in PKS 0745, they differentiate across all scales. The differentiation may occur during interactions between the cold and warm media and the radio jets and X-ray bubbles.
- In Abell 262, the VSF slopes of the [OII] emission and CO emission of ~ 1, consistent with ordered motion in a ring or disk. In contrast, the VSFs in the remaining three systems are steeper than the classical Kolmogorov turbulence slope of 1/3. The steepening may be caused by a variety of factors including magnetic stresses and gravity, as well as potential artifacts introduced by windowing, smoothing, and projection effects.
- The scale-dependent amplitudes of hot atmospheric velocities are derived indirectly from the surface brightness fluctuations using Chandra X-ray observations within the KCWI [OII] emission regions. The velocity amplitudes are $100 - 200$ km s^{-1}, comparable to direct Hitomi measurements of ICM velocity dispersion in the Perseus cluster. Due to Poisson noise, measurements cannot be made on scales accessible by KCWI data. However, we find a consistent and similar trend in amplitude at large spatial scales in Abell 1835 and RXJ0820, suggesting that the cold phase gas condensed from the hot atmospheres.

- Using simulations of Gaussian random fields with known underlying power spectra, we explore the impact of a restricted field of view on VSF measurements. We find that when the spatial scale measured exceeds half the width of the observation area, the declining number of pixel pairs can distort the shape of the VSFs, potentially introducing unphysical features. Therefore, characteristics appearing on large scales in VSFs should be interpreted with caution. Given the observational constraints of KCWI and ALMA, we are unable to precisely constrain an energy injection scale leading to turbulence. However, a careful examination reveals that the turnovers in the KCWI [OII] emission VSFs in Abell 1835, RXJ0820, and PKS 0745 correspond closely with the characteristic scales of X-ray cavities present in the system. This suggests that AGN activity may drive the gas motion in the core and could play a significant role in energy injection and transfer.

- The VSFs comparisons between data taken with different instruments must account for differences in spatial and spectral resolution. We find that coarse spatial resolution and smoothing of the data tend to suppress the VSF amplitude, particularly at spatial scales smaller than the PSF and/or the smoothing kernel, which in turn leads to VSF steepening.

Appendix A3: Extra Information for Chapter 3

A3.1.1 Window Effect on the VSF

The smallest measurable scale in our analysis is constrained by the observational PSF, while the largest scale is limited by the FOV of the data. As the separation increases, the number of pixel pairs decreases, thereby reducing the statistical reliability of the VSF and leading to distortion at larger scales. To mitigate these statistical uncertainties, we include only measurements at scales where bins exceed 20% of peak values (with a minimum of 2000 pixel pairs for KCWI [OII] VSFs). Additionally, any finite-sized dataset has a 'window function' due to its boundaries, which can distort the true VSF shape. The scales at which VSFs exhibit turnovers or changes in slope are indicative of the underlying drivers of motion. This is particularly evident when these turnovers correspond to distinct physical features, such as the sizes of X-ray cavities within the system, suggesting a direct relationship between gas motions and AGN feedback mechanisms. However, if the VSF turnover scale approaches the image extent, it raises questions about their reliability. To determine whether these features represent true physical phenomena or artifacts, we used

simulated Gaussian random fields to explore the influence of the dataset's limited size on the VSF.

We employed `PowerBox`, a Python code designed for generating density grids with an arbitrary two-point distribution, to simulate 50 Gaussian random fields characterized by known power-law power spectra. The simulated fields, each measuring 150×150 pixels and featuring power spectra with a spectral index of $1/2$, are displayed in the top row of Figure A3.1. The values within the field are dimensionless and centered around a zero mean. Pixels with positive and negative values simulate spaxels with redshifted and blueshifted velocities, respectively. The width of the outer green box is 100 pixels, twice that of the central yellow box. To investigate the effects introduced by limited sampling, we calculated the VSF for the entire map and compared it with those derived from sub-regions. The comparison is presented in the bottom panels.

The blue line depicts the VSF derived from the entire map, while the orange and green lines represent the VSF for the 50-pixel and 100-pixel boxes, respectively. A grey dash-dotted reference line with a slope of $1/2$ indicates the expected VSF slope underlying the Gaussian random field shown above. At smaller scales, the VSFs across all areas closely follow the $1/2$ power-law behavior, confirming the VSF analysis's ability to accurately recover the underlying two-point distribution. However, turnovers and deviations from the $1/2$ slope are observed at larger scales near the half-widths of the analysis window, marked by the dashed vertical lines in their respective colors. These distortions, observed in all 50 realizations, result from the finite size of the regions from which the VSF is calculated. We conclude that the decrease in pair numbers at larger separations, along with window effects, causes changes in VSF slope and distortions in VSF shape. Therefore, the features in measured VSFs are considered reliable only up to scales no larger than half the image extent.

A3.1.2 Image Smoothing Effect on VSF

We compare the VSF computed from ALMA and KCWI observations to study the coupling between the motion of warm and cold gas, as seen in Figure 3.9. The higher spatial resolution of CO ALMA observations allows the VSF measurements at smaller scales than [OII] emission detected by KCWI. The PSF and image smoothing during data reduction introduce correlations between adjacent pixels, that thus affect velocity difference measurements, and change the shape and slope of the VSFs.

To examine the smoothing effect on the VSF measurement, we generated multiple 50×50 pixel simulated Gaussian random fields with a power-law power spectrum characterized

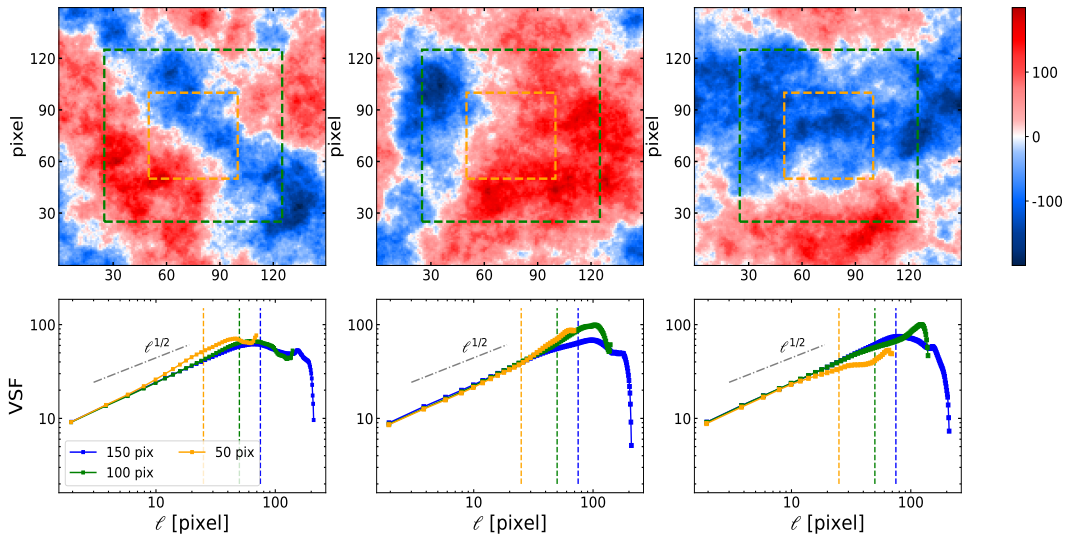


Figure A3.1: Window effect on VSFs. The top panels present a Gaussian random field with a power spectrum of $\alpha = 1/2$, with dimensions of 150×150 pixels. The boxes shown on the plot indicate the sub-regions used to examine the effects of finite size. The orange box has a width of 50 pixels, while the green box has a width of 100 pixels. The VSFs calculated from the simulated map and the sub-regions are displayed in the bottom panels. The blue line represents the VSF calculated from the entire image. The VSFs of the inner 50-pixel box and 100-pixel box are indicated by the orange and green lines, respectively. The three vertical lines indicate the half-width of the corresponding windows used for analysis. The grey dash-dotted line represents the expected VSF slope of 1/2 for reference.

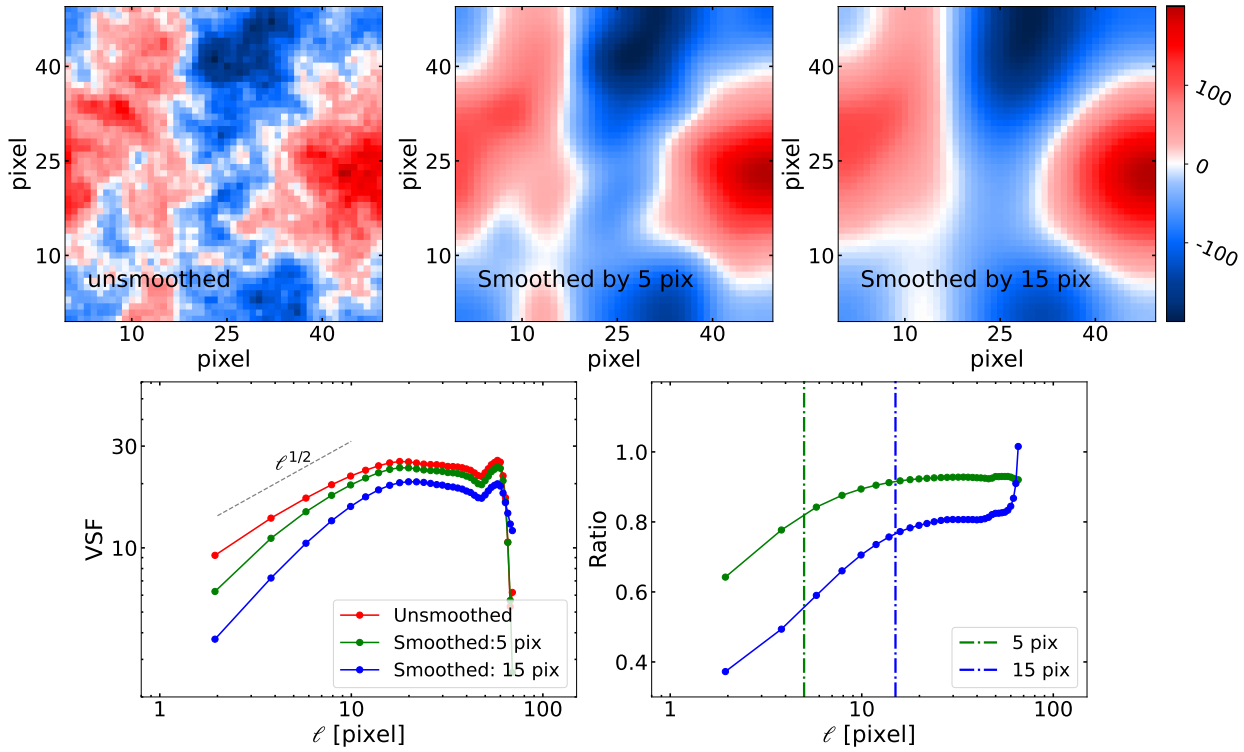


Figure A3.2: Smoothing effect on VSFs: Top: A Gaussian field with a power spectrum characterized by an underlying power of 1/2. To investigate the effect of image smoothing on VSF, the original image (left) is subjected to Gaussian kernel smoothing with a kernel size of 5 pixels (middle) and a kernel size of 15 pixels (right). Bottom left: The corresponding VSFs are calculated from simulated Gaussian fields. The red curve represents the unsmoothed image, displaying a slope close to 1/2. The green and blue curves correspond to images smoothed with Gaussian kernels of 5-pixel and 15-pixel widths, respectively, revealing a progressive amplitude suppression, particularly on smaller scales. Bottom right: Exploring the impact of various smoothing levels on resulting VSFs. The green line and blue line illustrate the mean ratio of 50 VSFs of the unsmoothed images to those of the images blurred by a 5-pixel width Gaussian kernel and to those of the images blurred by a 15-pixel width Gaussian kernel, respectively.

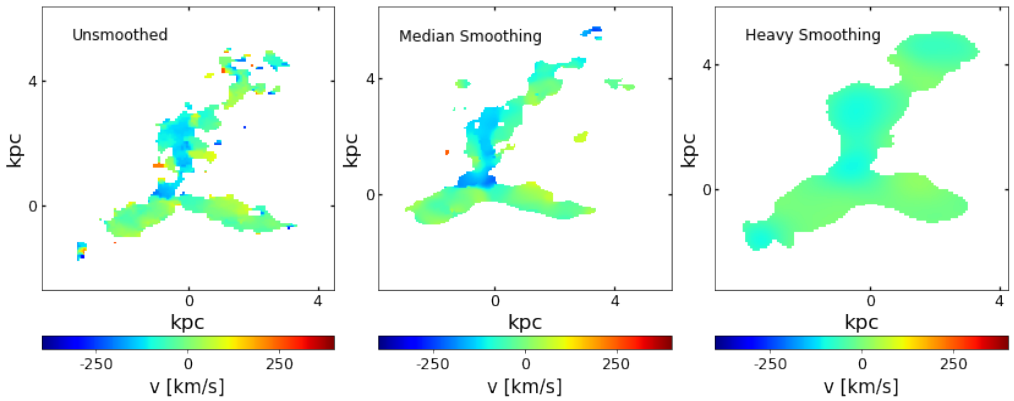


Figure A3.3: Velocity maps of cold molecular gas in PKS 0745 traced by ALMA CO (3-2) emission. The left panel displays the unsmoothed version of the velocity map. In the middle panel, the map is subjected to median smoothing, with a smaller beam size of 0.19". The right panel presents a velocity map that has undergone significant smoothing, with a beam size of 0.57".

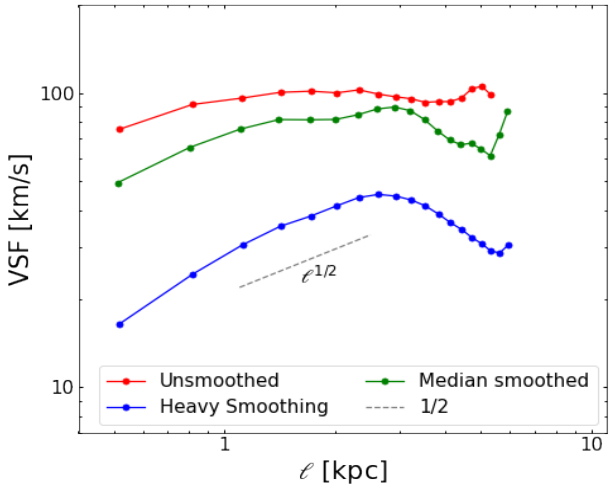


Figure A3.4: The VSFs are derived from different CO(3-2) velocity maps of PKS 0745 shown in Figure A3.3. The red line corresponds to the VSF of the unsmoothed PKS 0745 velocity map, while the green line and the blue line present the results of the moderately smoothed image (middle) and the heavily smoothed image (right), respectively.

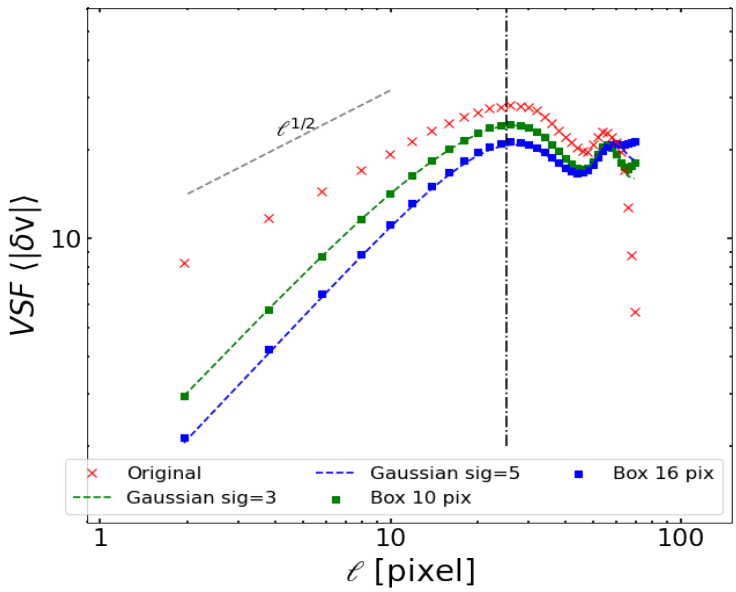


Figure A3.5: The smoothing effects of Gaussian and box kernel on the VSF. The VSF of the unsmoothed 50×50 pixel simulated field is presented as red crosses. It recovers the underlying slope of 12 over scales smaller than the half-width of the image, indicated by the vertical dashed line. The green and blue dashed lines show the VSF of the simulation smoothed with Gaussian kernels of $\sigma = 3$ pixels and $\sigma = 5$ pixels, respectively. The VSFs of the simulation smoothed with box kernels of widths $3\sigma + 1$ pixels are depicted as green and blue squares. The comparison demonstrates that Gaussian blurring and box blurring have analogous effects on the resultant VSFs, namely, steepening the slopes and suppressing the amplitudes.

by an underlying power of 1/2. The realization is depicted in the top row of Figure A3.2. The left panel shows the original, unsmoothed image, while the middle and right panels display the image smoothed by Gaussian kernel of $\sigma = 5$ pixel width and $\sigma = 15$ pixel width, respectively. From left to right, the progressive blurring of delicate structures and the apparent reduction in image fluctuations are evident.

The VSFs, computed from the simulated fields smoothed at different levels, are presented in the left panel of the bottom row in Figure A3.2. The VSF of the unsmoothed image (shown as the red line) maintains a slope of approximately 1/2 up to scales of $\sim$20

pixel.

For the VSFs of smoothed images, as represented by the green and blue lines, we observe an amplitude suppression relative to the true VSF. The amplitude suppression is consistent with the reduced fluctuations due to smoothing, which decreases the differences between pixels. This impact is dependent on the scales measured and the kernel width. The amplitudes are more heavily suppressed at small scales comparable to or less than the kernel width, leading to a slope steepening, and converging at larger scales. The steepest slope is observed in the VSFs of the images smoothed by the 15-pixel width kernel (blue line), resulting from the heaviest suppression of the smoothing effect at small scales.

The scale-dependent impact is clearly presented by the VSF ratio of the smoothed to the unsmoothed images, as shown in the right panel of the bottom row in Figure A3.2. The green line illustrates the mean ratio of 50 VSFs obtained from the unsmoothed images to those from images blurred by a 5-pixel width Gaussian kernel, while the blue line represents the ratio for images blurred by a 15-pixel width Gaussian kernel. The vertical dashed lines indicate the widths of the kernels. The amplitudes are reduced more significantly at scales below the kernel widths, with ratios becoming almost constant at larger scales and approaching 1 as they near the largest pixel separation detectable. The range of scales impacted broadens as the kernel width increases.

Consistent with the results from the simulated fields, a similar trend is observed in the VSFs derived from the velocity maps of PKS 0745, which are created using the same ALMA CO observation but with varying degrees of image smoothing applied during data reduction, shown in Figure A3.3. From the left to right panel, the maps progressively reveal a decreasing level of noise as the heavier smoothing is applied. The corresponding VSFs are shown in Figure A3.4, with the more significant differences observed at small scales. The amplitude of the VSFs decreased as the image smoothing increased, resulting in a stronger suppression of small-scale structures and a steeper slope shown in the more heavily smoothed map.

Figure A3.5 shows the comparison of the smoothing effects on VSF between the Gaussian and box kernel. The smoothing effect on the VSF is independent of the type of kernel used. This test is critical, as it supports our methodology of applying a box kernel to smooth ALMA observations in section 3.3.4. Such smoothing is necessary to match the coarser spatial resolution of Keck observations, allowing for a direct and meaningful comparison between the datasets. By confirming that the smoothing effect is kernel-independent, we ensure that the comparison between VSF of Keck [OII] observations and the smoothed ALMA CO emission is not biased by the choice of smoothing technique.

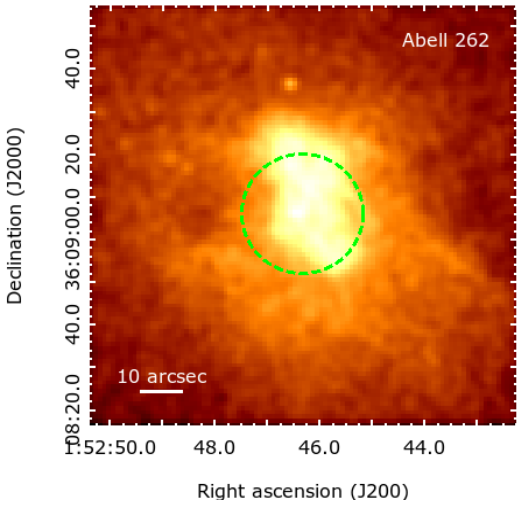


Figure A3.6: Background-subtracted, exposure-corrected mosaic Chandra images of the core of Abell 262 in the $0.5 - 3.5$ keV band. The dashed green circle indicates the region of interest, where [OII] emission is detected by KCWI. The image is smoothed with a 3" Gaussian for display purposes.

A3.1.3 Chandra X-ray Images of KCWI Targets

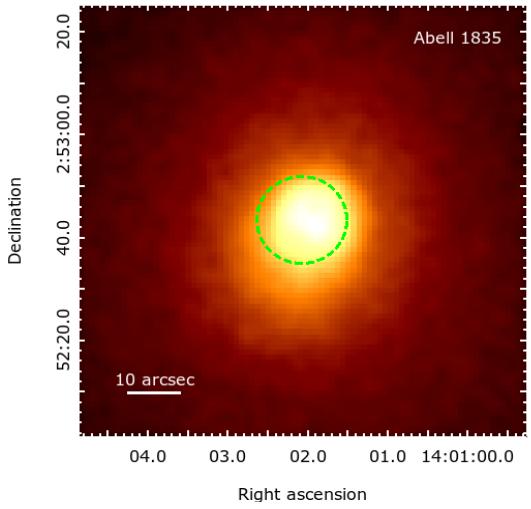


Figure A3.7: Similar to Figure A3.6. X-ray Chandra image of the core of Abell 1835 cluster in $0.5 - 3.5$ keV.

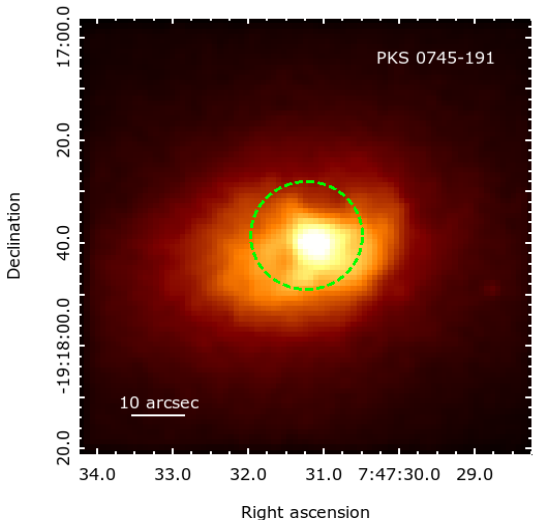


Figure A3.8: Similar to Figure A3.6. X-ray Chandra image of the core of PKS 0745-191 cluster in $0.5 - 3.5$ keV.

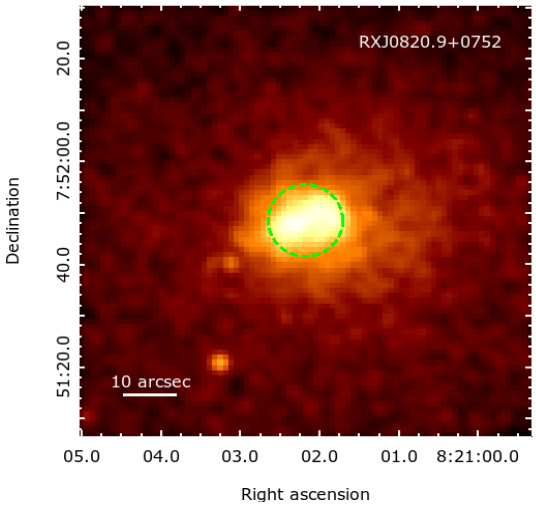


Figure A3.9: Similar to Figure A3.6. X-ray Chandra image of the core of RXJ0820.9+0752 cluster in $0.5 - 3.5$ keV.

Chapter 4

Calibration of XRISM Optical Blocking Filters

From April 2019 to May 2020, I had the privilege of contributing to the X-ray Imaging and Spectroscopy Mission (XRISM), a project led by the Japanese Aerospace Exploration Agency (JAXA) and widely participated in by the international community. During this period, I worked alongside my supervisor, Prof. Brian McNamara[1], and colleagues Dr. Iurii Babyk[1] and Connor Martz[1] at the University of Waterloo. Together, we collaborated closely with a team of experts, including Dr. Megan E. Eckart[2], Dr. Natalie Hell[2], Dr. Maurice Leutenegger [3], and Dr. Sawada Makoto[3]. Our collaborative efforts were dedicated to the on-ground calibration and analysis of flight-candidate optical blocking filters for Resolve.

During my involvement in the XRISM project, I actively participated in multiple filter calibration runs, the data from these were crucial for subsequent filter modeling efforts. My specific contributions mainly included:

- Participated in the calibration of multiple IVCS, OVCS, DMS flight-candidate mesh filters, and thermal shields at the Advanced Light Source (ALS) from May 8th to 10th, 2019.
- Engaging in the calibration of multiple light-candidate mesh filters and witness samples at the Canadian Light Source (CLS) from July 23rd to 28th, 2019.

[1]University of Waterloo, Ontario N2L 3G1, Waterloo, Canada
[2]Lawrence Livermore National Laboratory, CA 94550, USA
[3]NASA / Goddard Space Flight Center, MD 20771, USA

- Analyzing the properties of candidate filters through modeling parameters such as thickness, uniformity, and mesh filling factor based on the data gathered from multiple calibration runs. This included filters: IVCS8, IVCS6, OVCS7, and OVCS2 (calibrated at CLS from January to February 2019), and IVCS_G2, OVCS5, and DMS_C1 (calibrated in July 2019 at CLS).

The scripts for filter parameter fitting used in my analysis were provided by Dr. Maurice Leutenegger and were based on the model described in Eckart et al. (2018). Connor Martz and I were responsible for data analysis, and we regularly updated and discussed our results during our online project meetings. Dr. Megan E. Eckart, Dr. Natalie Hell, and Dr. Maurice Leutenegger provided essential feedback on our fitting results, ensuring their accuracy and relevance. The research documented in this thesis was meticulously compiled from the observational logs of calibration sessions and records of our online discussions. Additionally, the analysis results for the IVCS6 and OVCS7 filters have been detailed in the master thesis of Connor Martz, which was completed in October 2019.

4.1 Introduction

4.1.1 Hitomi: Predecessor of XRISM

Hitomi, initially named Astro-H and also known as NeXT, was the sixth in the series of X-ray astronomy missions developed by the Japan Aerospace Exploration Agency (JAXA). It was launched into low Earth orbit on February 17, 2016.

The design of Hitomi included four focusing telescopes and six detectors, offering unparalleled capabilities in high-energy astrophysics. Two of the telescopes, known as Soft X-ray Telescopes (SXTs) and each with a focal length of 5.6 m, were respectively aligned with a Soft X-ray Spectrometer (SXS) and a Soft X-ray Imager (SXI). The other two telescopes were Hard X-ray Telescopes (HXTs) with a 12 m focal length, which direct X-rays to two Hard X-ray Imaging detectors (HXIs) located on a 6 m extendable optical bench. To expand its detection capabilities, Hitomi was equipped with two Soft Gamma-ray Detectors (SGD), mounted as non-focusing detectors on opposite sides of the satellite. This configuration, as shown in the left panel of Figure 4.1, enabled the most sensitive wideband observations across an energy range from 0.3 keV to 600 keV.

Furthermore, Hitomi was designed to deliver unprecedented spectral resolution for spatially extended cosmic X-ray sources as well as for all cosmic X-ray sources within the Fe-K

band around 6 keV. To achieve this, the SXS employed an advanced micro-calorimeter array, operating at a temperature of approximately 50 mK to facilitate detailed spectroscopic observations (Shirron et al., 2016). This setup allows for the measurement of subtle temperature changes that occur when an X-ray photon is absorbed, thereby enabling precise determination of the photon's energy. The SXS offered an exceptional non-dispersive resolution of ∼7 eV across the 0.3 - 10 keV bandpass and maintained a field of view of about 3 arcminutes.

The most notable observation made by Hitomi was of the core of the Perseus galaxy cluster. It revealed a remarkably quiescent atmosphere with a line-of-sight dispersion of 164 ± 19 km s^{-1} within the central 30 kpc to 60 kpc, as determined by spectral line-width measurement (Hitomi Collaboration et al., 2016). This observation underscored Hitomi's advanced capabilities in studying the dynamics of hot gas within galaxy clusters. Before its unfortunate loss, Hitomi had also successfully gathered data from six celestial objects: Perseus, N132D, IGR-J16318-4848, RXJ1856.5-3754, G21.5-0.9, and the Crab, along with observations of the blank sky, totaling about one month of operational data collection.

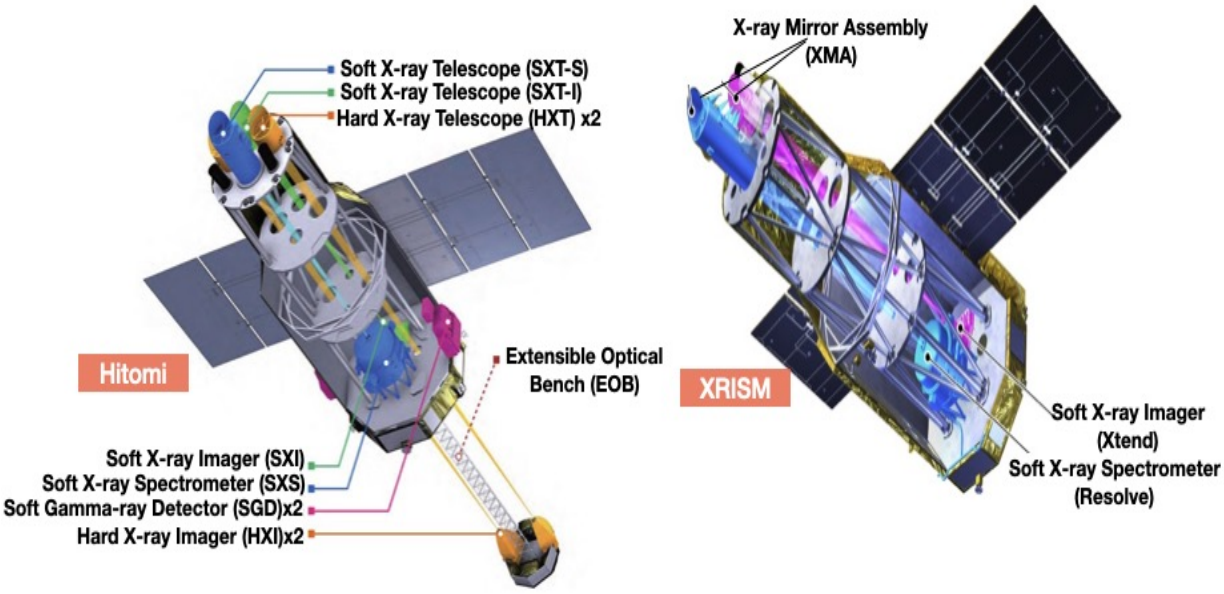


Figure 4.1: Diagram of instrument locations on Hitomi (Left) and XRISM (Right). (Image credit: JAXA/ISAS)

4.1.2 XRISM: Advancing the Legacy

Motivated by the loss of Hitomi, the XRISM mission is designed to recover and expand upon the scientific opportunities that were curtailed by Hitomi's premature termination.

XRISM is viewed as both a continuation and an advancement of Hitomi's scientific legacy, inheriting improved technology and lessons learned from Hitomi's shortcomings. The right panel of Figure 4.1 shows the illustration of instrument mounting locations on XRISM. Resolve, the micro-calorimeter aboard XRISM, is specifically designed to succeed and enhance the high-resolution X-ray spectroscopy capabilities previously established by Hitomi's SXS. It provides non-dispersive energy resolution of ~ 5 eV in 0.3 - 12 keV band with a FOV of $\sim 3'$. Resolve is also a cryogenic thermometer with high sensitivity operating at temperatures close to absolute zero.

Resolve's high sensitivity enables it to detect not only X-rays but also a broader range of photons from the entire electromagnetic spectrum, as well as particles. To minimize contamination, it is crucial to shield the instrument from thermal radiation, as well as optical and ultraviolet (UV) light from the sky. It is also essential to protect the instrument's coldest stages from thermal radiation emitted by its warmer stages. Building on the design of Hitomi's SXS, Resolve incorporates five thin-film radiation-blocking filters (BFs) anchored in the detector dewar (Kilbourne et al., 2018). These filters effectively block unwanted optical / UV photons while permitting X-rays to pass through with minimal absorption.

During the design, development, and production phases of XRISM's filters, it is necessary to conduct X-ray transmission spectroscopy and imaging measurements to calibrate X-ray transmission, thickness uniformity, and mesh filling factor (e.g. Eckart et al., 2018; Puccio et al., 2020). These calibrations are pivotal, not only for verifying that the filters meet the main scientific requirements but also for deepening our understanding of the instrument's intricate response mechanisms. To mitigate the risk of accidental damage to the filters, each one is supported by four backup candidates, all of which also require calibration.

In this chapter, I outline my efforts to calibrate XRISM's optical blocking filters at both the Canadian Light Source (CLS) and the Advanced Light Source (ALS). In Section 4.2, I explore the fundamentals of soft X-ray technology and the utilization of synchrotron facilities for the calibration of X-ray optics. Sections 4.3 and section 4.4 detail the calibration experiments conducted at CLS and ALS, respectively, describing the methodologies and the process of fitting parameters. Finally, Section 4.5 provides a summary of the project along with considerations for future work.

4.2 Fundamentals of Soft X-ray

The soft X-ray spectrum, typically ranging from about 0.1 keV to 10 keV, is essential for analyzing the composition and temperature of intracluster gas, as well as studying the properties of stellar coronae and black holes. This regime is characterized by primary atomic resonances and absorption edges of most elements with low or intermediate atomic numbers. In the design of optical blocking filters, it is crucial to ensure high X-ray transmission; this requires a careful balance where thin films must minimize absorption while also providing effective out-of-band shielding, and maintaining mechanical and thermal robustness. Therefore, a thorough understanding of the fine structure of soft X-rays is essential for comprehending the spectral response of filters, which is briefly introduced in Section 4.2.1. To achieve precise calibration of these filters, high-energy resolution transmittance measurement is typically performed at synchrotron facilities, a process extensively detailed in Section 4.2.2.

4.2.1 X-ray Absorption Fine Structure

When an X-ray photon with energies up to 30 keV passes through a thin film, the photoelectric effect predominates as the absorption mechanism. This is because such photon energies are sufficient to remove electrons from the inner atomic orbitals, but not high enough to cause more complex processes like resonance scattering. As a result, X-ray photons transfer their energy to core electrons, which are then ejected from their orbits, creating distinct absorption edges. The K-edge, L-edge, and M-edge, correspond to the most tightly bound innermost electrons in the atomic shells, with principal quantum numbers of n=1, 2, and 3, respectively.

The Beer-Lambert law quantitatively describes the exponential decrease in X-ray intensity as it traverses a homogeneous medium, which can be expressed as:

$$I = I_0 \, e^{-\rho\mu t}, \tag{4.1}$$

where I_0 is the incident intensity, I is the transmitted intensity, t is the sample thickness, and μ is the mass absorption coefficient, which represents the probability of X-ray absorption by the material (Attwood, 2000). The coefficients heavily depend on the atomic number Z and the photon energy E, and are experimentally derived and tabulated for many elements (Hubbell, 2006)

The transmission of a filter is defined as:

$$T = \frac{I}{I_0} = e^{-\rho\mu t}, \tag{4.2}$$

where ρ is material density. For filters composed of multiple materials, the overall transmission is calculated by summing the contributions from each element:

$$T = e^{-\Sigma\rho_i\mu_i t_i}, \tag{4.3}$$

where ρ_i, μ_i and t_i correspond to the density, mass absorption coefficient, and thickness of the i-th element, respectively. Therefore, the X-ray absorption fine structure (XAFS) of a sample can be directly measured by evaluating its transmission.

When an X-ray photon's energy matches the core-level binding energy of a specific element, the mass absorption coefficients increase sharply, forming distinct absorption edges in the X-ray spectrum. Typically, within 30 eV of the main absorption edge, the spectrum features X-ray Absorption Near-Edge Structures (XANES). Beyond this, the Extended X-ray Absorption Fine Structure (EXAFS) extends for several keV past the edge, providing insights into the local structural environment of absorbing atoms.

To thoroughly understand the instrument's response, X-ray transmission spectroscopy and imaging measurements of filters are essential. These include a broadband transmittance scan and a detailed examination of near-edge fine structures of the chemical elements that compose the filters. To accurately resolve the edge region, the energy step in the measurement process should be significantly finer than the instrument's expected resolution. For example, the design resolution target for Resolve is ~ 5 eV, which requires transmission near the absorption edges to be scanned with even finer precision using a high-resolution synchrotron beamline, achieving spectral resolutions of ~ 1 eV.

4.2.2 Synchrotron Radiation Facilities for X-ray Optics Calibration

The performance of filters can be assessed using the collimated monochromatic beams provided by synchrotron facilities. Therefore, understanding the capabilities of the chosen synchrotron beamlines is essential before initiating any filter calibration.

A synchrotron, a type of particle accelerator, produces extremely bright light spanning a broad spectrum from infrared to X-rays. This is achieved by accelerating electrons to velocities approaching the speed of light. While designs vary, the operating principles

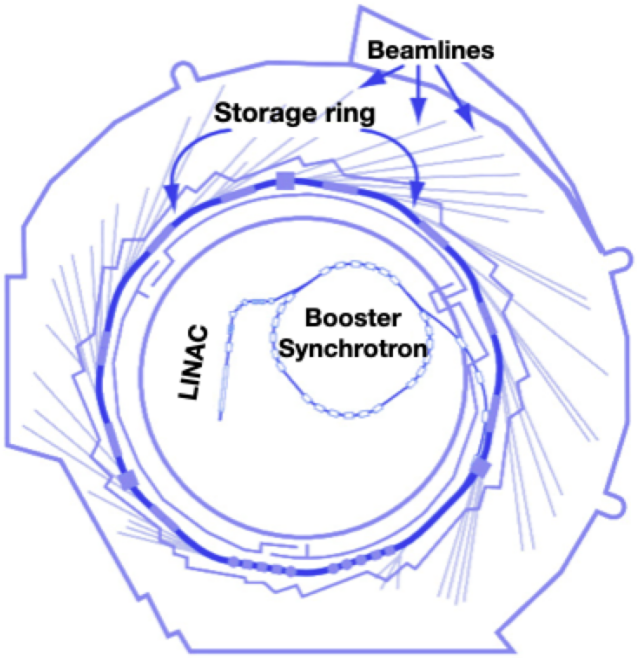


Figure 4.2: General layout of a synchrotron facility, showing the linear accelerator (LINAC), booster synchrotron, storage ring, and beamlines. Schematics is based on ALS, adapted from the ALS QuickFacts Sheet (2019).

remain similar. A schematic layout of ALS is shown in Figure 4.2. Although the layout of CLS has some differences, its overall structure is fundamentally similar.

This process begins with a tungsten button cathode heated to incandescence, which generates electrons energetic enough to leave its surface. Once these 'boiling' electrons are produced, they are accelerated in the linear accelerator (LINAC) before being transferred to the booster Ring, where the electrons are further energized by radio frequency cavities as they circulate. This boosts them to nearly the speed of light, preparing them for injection into the storage ring for synchrotron light production.

Electrons typically travel in straight lines; however, their trajectories are redirected in the storage ring, which features a series of straight sections punctuated by large magnets at each turn. Guided by the magnetic fields, the electrons circulate, continuously emitting synchrotron light for several hours. Within these sections, insertion devices such as wigglers and undulators refine the light by intensifying its brightness and tuning its spectrum. The enhanced light is then channeled into specific beamlines, serving a wide range of scientific

applications.

Everything from the electron gun to the beamlines is under vacuum to avoid electrons from colliding into particles and disappearing. During operation, the storage ring at CLS maintains a beam current of 220 mA (Cutler et al., 2017), whereas ALS sustains a higher beam current of 500 mA. However, the number of electrons in the storage ring inevitably declines over time due to the unavoidable imperfections in the vacuum. To counter this, both CLS and ALS employ 'Top-Up' mode (Boland & Le Pimpec, 2022; Baptiste et al., 2010), automatically injecting small amounts of electrons to maintain a stable ring current. At CLS, electron injections occur at intervals of a few minutes to replenish the beam, while ALS operates continuously in top-off mode, maintaining a beam current decline below 0.3%. This technique guarantees a consistently stable beam current, thereby enhancing the reliability of scientific experiments by preserving beam quality, and minimizing the need for frequent recalibrations.

Finally, synchrotron light is directed to 22 beamlines at CLS, while at ALS, it is distributed across 40 beamlines. Each beamline consists of an optics hutch, where the light is focused and its wavelength precisely selected, and an experimental hutch housing an endstation uniquely designed for specific research applications.

In May 2019, I participated in a calibration at ALS using beamline 6.3.2, which operates within an energy range of 50 to 1300 eV with a high spectral resolution (relative spectral bandwidth $\Delta\lambda/\lambda \leq 7000$), obtained using a variable-line spaced plane grating monochromator. The beamline features a beam size of 10 mm by 300 mm and offers positioning accuracy of 4 mm along three axes. Designed specifically for precise studies of thin films and surfaces, beamline 6.3.2 excels in controlling light wavelengths and minimizing beam divergence, ensuring accurate and repeatable measurements.

Later, in July 2019, I was involved in a calibration using the Resonant Elastic and Inelastic X-ray Scattering (REIXS) beamline at CLS. REIXS typically operates in the soft X-ray range of 95 eV to 2000 eV, effectively covering key absorption edges such as the O K-edge, N K-edge, and the L-edges of transition metals like Fe, Co, and Ni. The full beam size on the sample is 450 µm (horizontal) by 300 µm (vertical). It offers exceptional energy resolution, often better than 0.1 eV for X-ray absorption spectroscopy, enabling detailed examinations near absorption edges.

For more detailed information about the synchrotron facilities and beamlines of CLS and ALS, please refer to the introduction on their websites (CLS, 2024; ALS, 2024).

4.3 Optical Blocking Filter Calibration

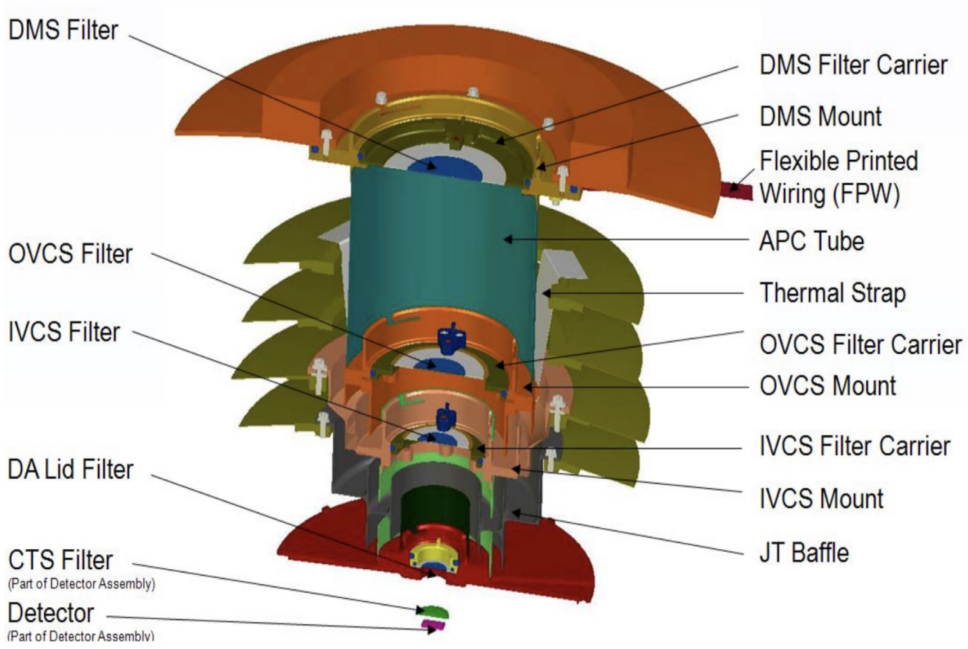


Figure 4.3: The Schematic showing the arrangement of ApA and BFs on XRISM Resolve. The image is adapted from in Leutenegger (2019).

Resolve is an advanced soft X-ray calorimeter array aboard the XRISM satellite, offering an exceptional energy resolution of $\sim 5 - 7$ eV across the $0.3 - 12$ keV band. It is anchored to a 50 mK heat sink, and the dewar main shell operates at ~ 300 K in orbit. To maintain its high performance, the detector, which is the coldest stage of the instrument, must be shielded from thermal radiation emitted by the warmer components. Additionally, given its sensitivity to the full range of the electromagnetic spectrum and various particles, Resolve requires shielding to protect against optical/UV photons that originate from the sky background.

4.3.1 Optical Blocking Filter

An aperture assembly (ApA), equipped with a set of thin-film blocking filters (BFs), is designed to protect the detector from water vapor, infrared, optical, and ultraviolet photons

while minimizing X-ray absorption to preserve its performance. Figure 4.3 illustrates the schematic arrangement of the ApA and the five blocking filters mounted on Resolve, along with the associated mechanical, thermal, and electrical hardware. The filters are divided into two groups from the innermost layer near the detector to the outermost layer adjacent to the dewar main shell. The inner filters, comprising the detector enclosure and heat sink (CTS) filter and the detector assembly (DA) filter, are made of freestanding aluminized polyimide (Al/PI) films mounted on aluminum frames. The three outer filters — inner vapor-cooled shield (IVCS) filter, outer vapor-cooled shield (OVCS) filter, and dewar main shell (DMS) filter — are also made of the same Al/PI films but are larger in size. To enhance their structural strength, these filters are supported by two-level silicon meshes bonded with epoxy.

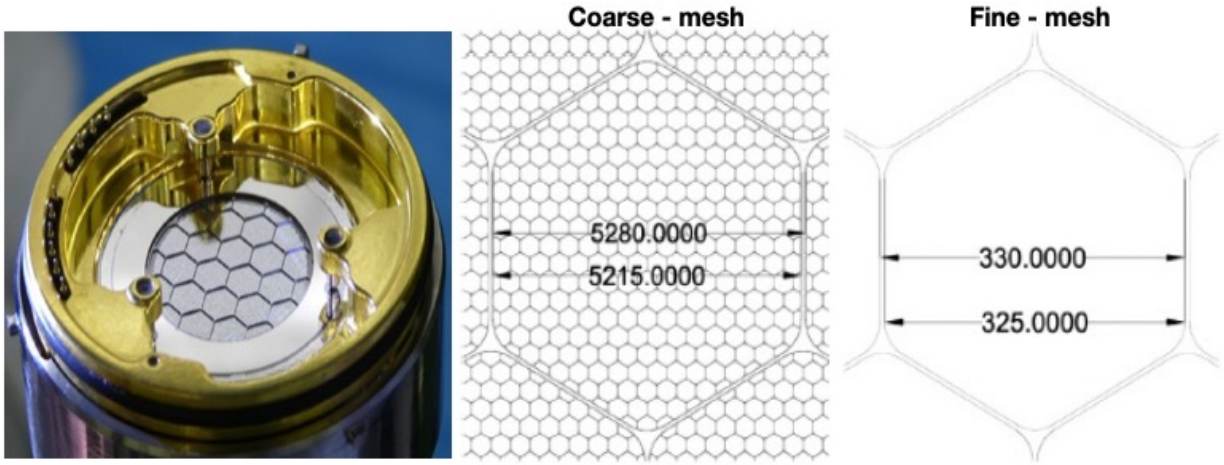


Figure 4.4: Left: Photograph of the OVCS flight carrier from the back, showing the coarse and fine silicon-mesh cells. Middle & Right: Dimensions of the coarse mesh cell and fine mesh cell, respectively. The images are adapted from Kilbourne et al. (2018).

The thin films used in the outer filters have a thickness of ∼200 nm. Figure 4.4 illustrates the two-level mesh design, consisting of a 'coarse' hexagonal mesh with 5.28 mm cell spacing and 65-micron bar width. Within each coarse mesh are 'fine' meshes that are 25 microns thick (8 microns for the DMS filter), featuring 0.33 mm cell spacing and 5-micron bar width (Kilbourne et al., 2018).

The aluminized polyimide films are highly reflective in visible and infrared light, while the attenuation of UV light depends on the combined thickness of the aluminum layer and polyimide layer. The assumed chemical composition of polyimide is $C_{22}H_{10}N_2O_4$. The precise thickness of each thin-film component needs to be determined through the trans-



Figure 4.5: Microscopic image of the back side of an optical blocking filter showing the non-uniform epoxy excess, which accounts for variance in X-ray transmission measurements. The image is accepted from Eckart et al. (2018).

mission analysis of absorption structures using synchrotron calibration measurements. For the outer filters supported by meshes, parts of the filter are partially covered by the coarse mesh bars and the epoxy used to bind the fine meshes to the Al/PI film. Furthermore, the epoxy bleeds beyond the 5-micron fine mesh bars, creating non-uniform coverage across the filter surface. As a result, the IVCS, OVCS, and DMS filters require additional three modeling parameters: the covering fraction due to the coarse mesh and the filling fraction caused by the fine mesh, as well as the epoxy thickness.

4.3.2 Calibration Strategy

Each of the five optical blocking filters has four flight candidates, totaling 20 filters, whose spectral response and spatial homogeneity require calibration through X-ray transmission spectroscopy and imaging measurements conducted at synchrotron facilities.

Filter calibration is typically carried out in the following stages:

1. Measure calibration standards: determine the optical constants of the materials used in the filter fabrication process. This requires high-resolution scans of the photo-electric absorption edges for all chemical elements present in the filters within the

energy band of interest and must be conducted using standards that have thicknesses equivalent to those specified in the flight filter design.

2. Calibrate the witness sample of the outer filters: To minimize the risk of potential damage to the flight and flight spare filters during calibration, broadband transmission measurements are conducted on smaller, representative samples known as witness samples. These samples are fabricated from the same coated membranes as the full-sized filters and provide representative results for the filter models.

3. Calibration of flight and flight spare filters prior to integration: verify uniformity across the filters and determine the filling factor of the meshes. The transmission of the complete set of five optical blocking filters is measured as well to identify and correct any systematic errors present in the individual filter measurements.

The REIXS beamline at the CLS was utilized as the primary X-ray source for the calibration of the Resolve optical blocking filters. The REIXS beamline at the CLS was utilized as the primary X-ray source for the calibration of the Resolve optical blocking filters. The key characteristics of these two beamlines are detailed in Section 4.2.2. The filter modeling analysis I participated in focused on the IVCS, OVCS, and DMS filters calibrated at CLS. Therefore, the analysis and calibration processes of the inner freestanding filters conducted at ALS are not discussed in detail. The following sections exclusively summarize the calibration of meshed filters at CLS.

Position scan

Prior to each calibration session, a position scan is performed to ensure that the beam avoids the coarse mesh bars. Figure 4.6 displays the spatial uniformity maps of the OVCS7 filter and IVCS2 at 1700 eV, calibrated in February and July 2019 at CLS, respectively. The arrangements of the coarse mesh and its bars are clearly visible. The horizontal and vertical positions of the sample within the chamber are marked on the x and y axes. The beam size of the REIXS beamline at CLS is 450μm $\times$ 300μm, which is large enough to average over the fine mesh while being small enough to scan through the openings of the coarse mesh without striking the bars.

Broadband Transmission Scan

The broadband transmission of each filter was measured over the energy range of 260 eV to 2100 eV. To prevent overheating of the monochromator and to enhance the spectral

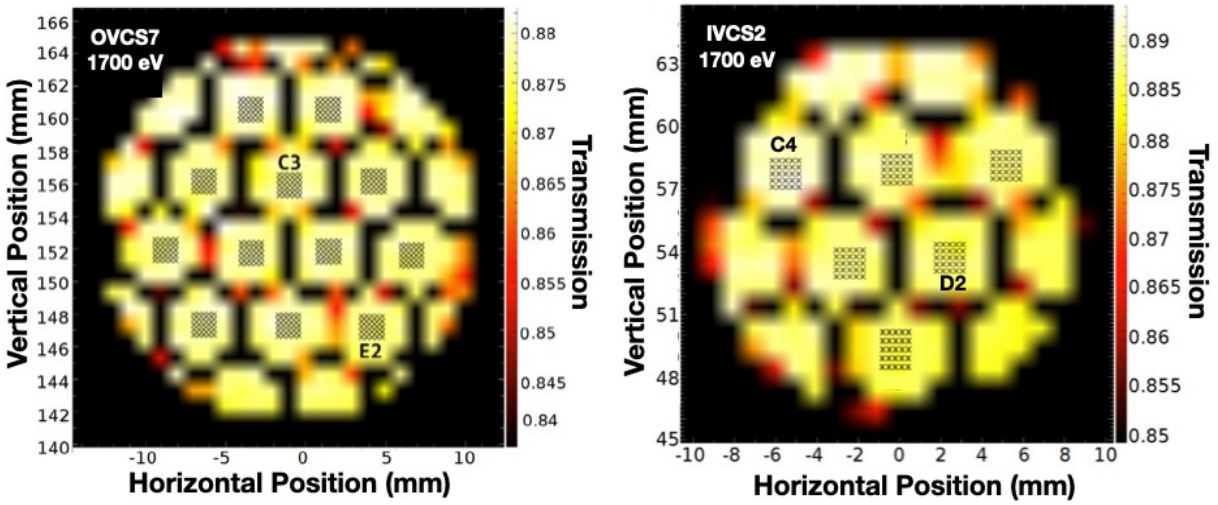


Figure 4.6: The spatial uniformity maps of OVCS7 and IVCS2 at 1700 eV. The grey crosses mark the positions for the '5 × 5' mesh scan within each coarse mesh. The broadband transmission scans are conducted in two cells for each filter, whose locations are also highlighted.

purity of the beam, the broadband scan was divided into six segments. Each segment was scanned either with a selected high-order suppression (HOS) filter inserted into the beam path or with the beam path left open. The transmission curves were sampled with steps of $\sim$ 5 eV to 50 eV across different segments. Table 4.1 details the energy scan ranges, sampling steps, and the specific HOS filters used for each segment.

The transmission at a given energy is calculated using the following equation:

$$T(E) = (I_m/I_d)/(I_{m0}/I_{d0}), \tag{4.4}$$

where I_m and I_d represent the intensities measured by the monitor and detector, respectively. The subscript '0' denotes measurements taken at the open-hole position, which serves as a reference for normalization.

The full energy scans are typically conducted on two cells of each filter, both to minimize errors and to confirm the filter's spatial uniformity by comparing their transmission curves. Figures 4.7, 4.8, and 4.9 present the broadband scans for the OVCS, IVCS, and DMS filters calibrated at CLS, which I analyzed. To better assess spatial uniformity, broadband transmission measurements are typically performed on two widely separated cells within each filter. Since the high spectral resolution measurements of absorption edges were completed

Full Energy Scan			5 ×5 Mesh Scan	
Energy	Step	Filter	Energy	Filter
eV	eV		eV	
(1)	(2)	(3)	(4)	(5)
250 - 350	25	V	260	V
290 - 440	15	Cr	330	Cr
360 - 500	10	Fe	510	Ni
430 - 850	30	Ni	600	open
800 - 1600	30	open	1400	open
1500 - 2100	20	open	1700	open

Table 4.1: The details of spectral scan and 5×5 mesh scan at CLS.

during the calibration of standards, only broadband transmission data are collected at this stage. These scans include the absorption edges of key filter elements, including C K, N K, O K, and Al K, all of which are clearly visible in the transmission curves shown in the top panels. During data analysis, data points located near the absorption edges are excluded due to their relatively higher measurement uncertainties.

The fractional differences in transmission between the two cells, shown in the bottom panels, are consistently below 2% across the entire energy range for all calibrated OVCS, IVCS, and DMS filters. Additionally, the transmission consistency between all cells becomes even more pronounced at higher energy bands.

Mesh Scan

To further constrain the spatial uniformity across the filters, transmission data were systematically collected at fixed energies within a 5×5 position grid for each coarse mesh. These energies and the corresponding HOS filters used in calibration are specified in Table 4.1. Figure 4.10 and 4.11 display the mesh scans of OVCS7 and IVCS2 at 260 eV and 1700 eV, respectively. At high energy, the filters exhibit greater transparency. The percentage difference from the average transmission, calculated as $(T/T_{avg} - 1) \times 100\%$, is also depicted at the bottom of each grid point, demonstrating the consistency of filter uniformity with differences in transmission across the coarse mesh cells remaining below 1%.

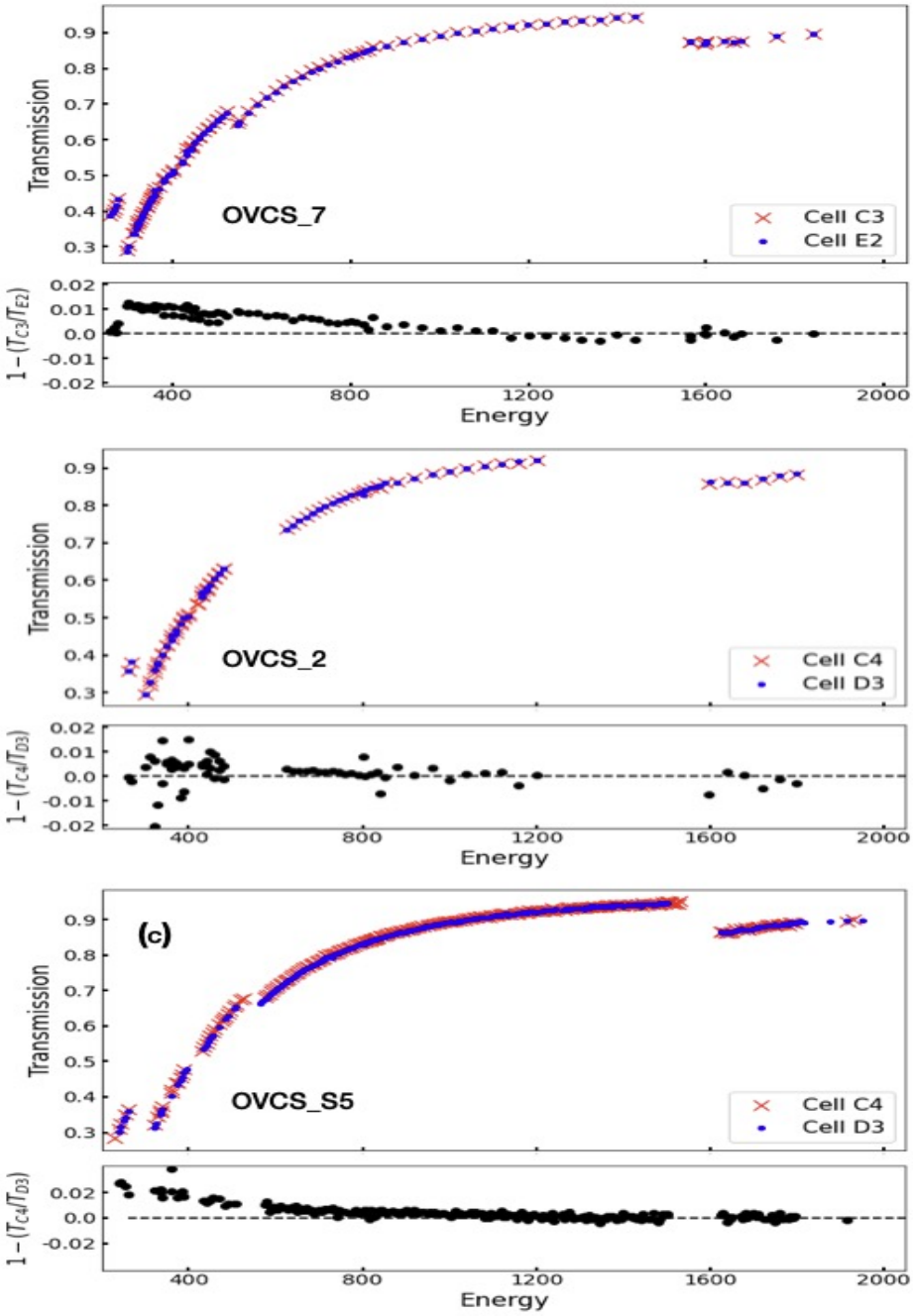


Figure 4.7: Top panels: Broadband transmission curves measured in two cells for (a) OVCS7, (b) OVCS2, and (c) OVCS-S5. Bottom panels: Fractional differences in transmission between the two cells.

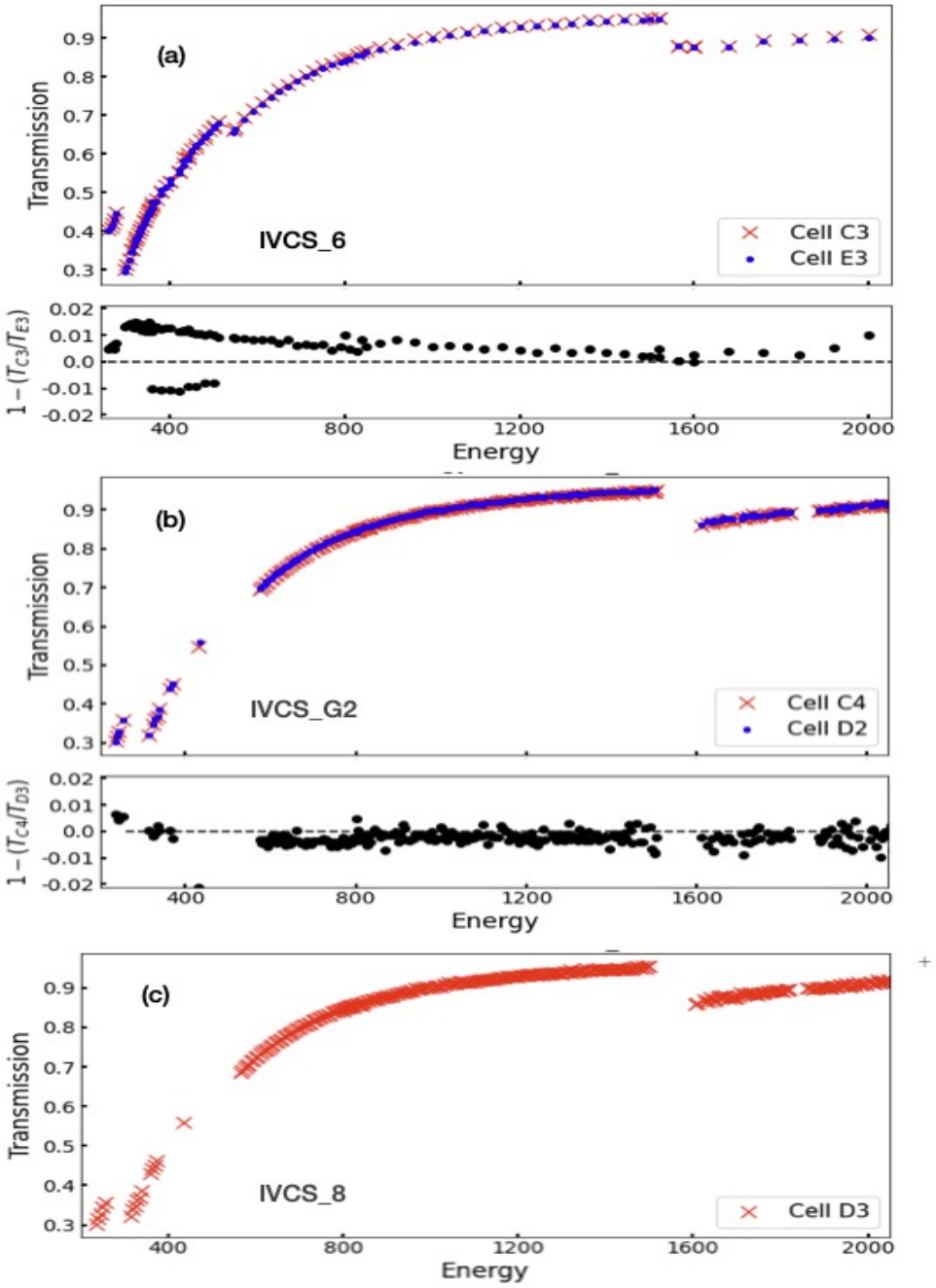


Figure 4.8: Similar to Figure 4.7. Spectral scans for IVCS filters: (a) IVCS6, (b) IVCS-G2, and (c) IVCS8.

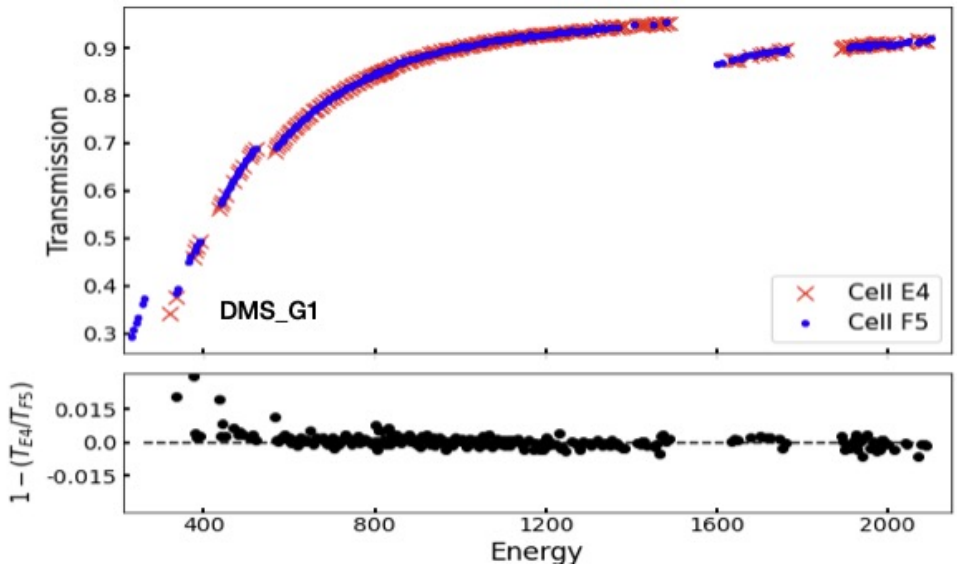


Figure 4.9: Similar to Figure 4.7. Spectral scans for DMS-G1.

Measure Transmission of Filter Stack

The transmission of the complete five-filter stack is measured to identify any systematic errors that may have arisen during the individual calibration of each filter and to ensure that the assembled stack satisfies the design requirement.

4.4 Model Filter Parameters

The model previously developed for calibrating the blocking filters of Hitomi's SXS is applied here for XRISM filter calibration (Eckart et al., 2018). The broadband transmission, measured during the spectral scan which is described in Section 4.3.2, is fitted by the model to determine the polyimide thickness, aluminum thickness, surface oxide contamination on the aluminum films, mesh filling fraction, epoxy filling fraction, and epoxy thickness.

The mass absorption coefficients of aluminum and oxygen, tabulated by Henke et al. (1993) and based on data from CXRO (2023), are presented in the left panel of Figure 4.12. Similarly, the mass absorption coefficient of polyimide ($C_{22}H_{10}N_2O_4$) is calculated by summing the contributions from its individual components and is shown in the right panel of Figure 4.12.

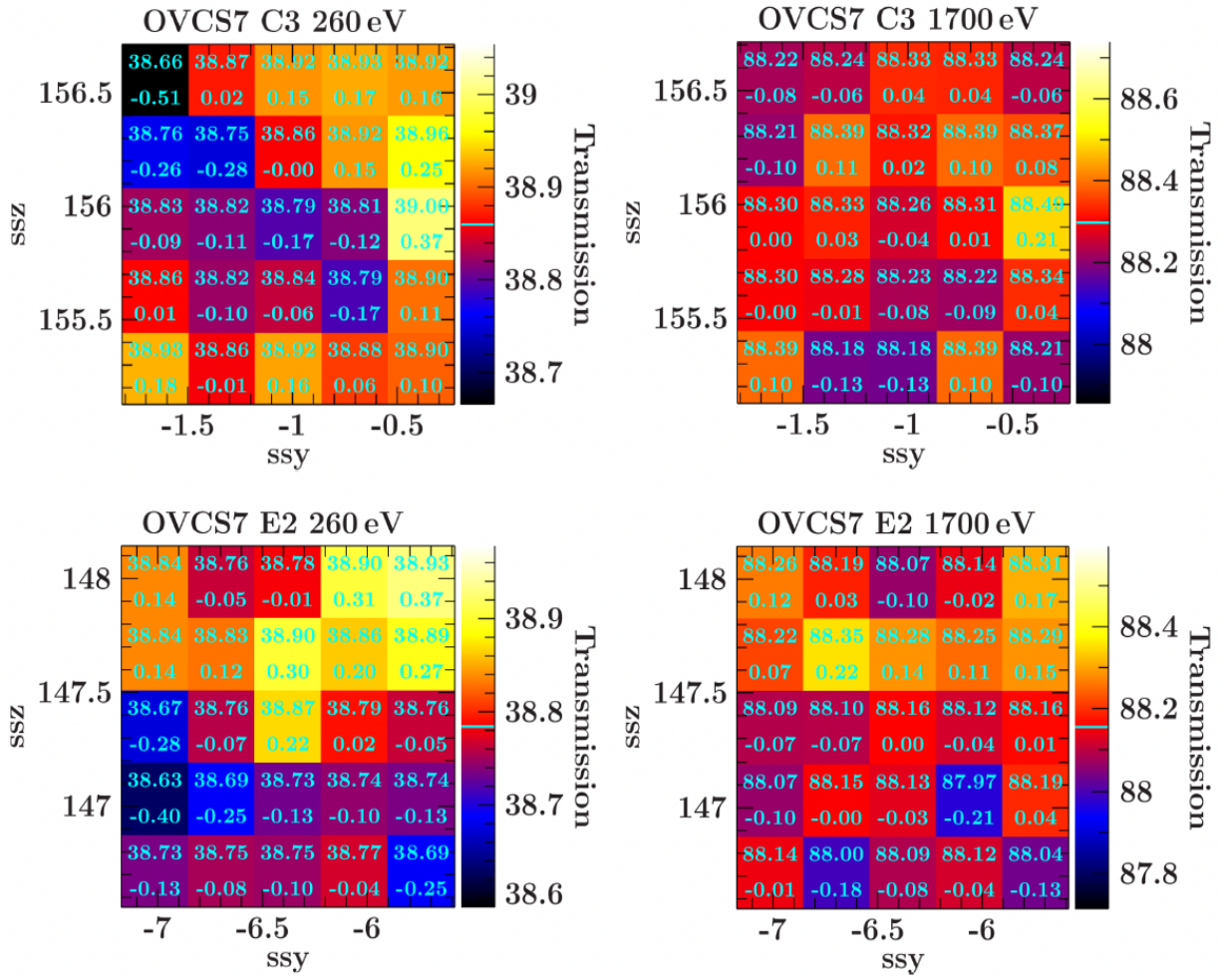


Figure 4.10: Mesh scans of the OVCS7 filter at 260 eV and 1700 eV, displaying transmission measurements within two coarse meshes labeled C3 and E2. Each position is indicated by a 5×5 grey-cross array as marked in Figure 2. The values at the bottom, calculated as $(T/T_{avg} - 1) \times 100\%$, represent the deviation from the average transmission.

When X-rays pass through aluminum thin films, the transmission is described by the equation:

$$T_{Al} = \exp(-\Sigma_{Al}\mu_{Al}), \tag{4.5}$$

where Σ_{Al} represents the surface density of aluminum, and μ_{Al} is the energy-dependent mass

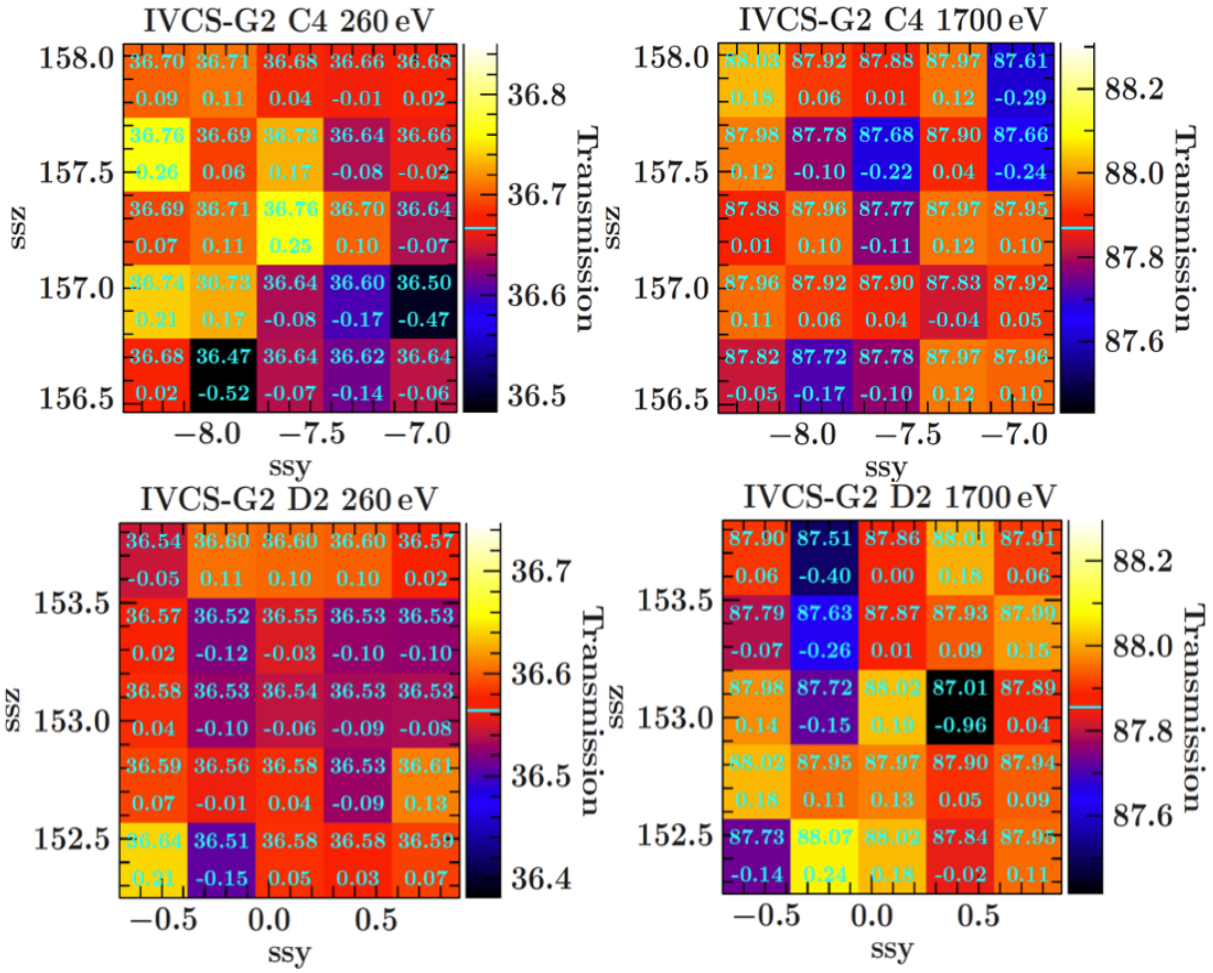


Figure 4.11: Similar to Figure 4.10.Mesh scans of the IVCS2 filter at 260 eV and 1700 eV within cell C4 and cell D2.

absorption coefficient. Given the density of aluminum $\rho_{\mathrm{Al}} = 2.7$ g cm^{-3}, the thickness of the aluminum film can be calculated using:

$$t_{\mathrm{Al}} = \frac{\Sigma_{\mathrm{Al}}}{\rho_{\mathrm{Al}}}. \tag{4.6}$$

Similarly, the thickness of polyimide is calculated using the equation:

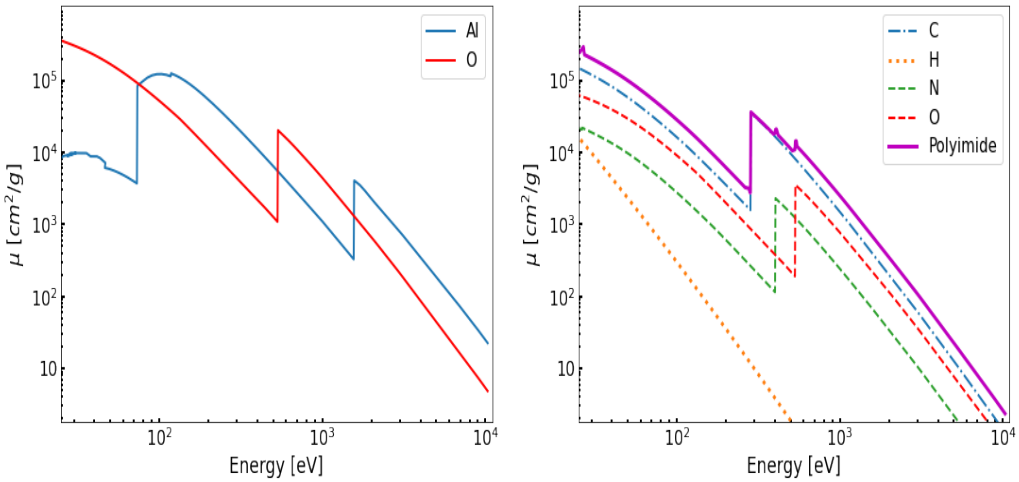


Figure 4.12: Mass absorption coefficients as a function of energy. Left: Aluminum and Oxygen. Right: Polyimide $C_{22}H_{10}N_2O_4$ and the absorption coefficients of its constituent elements. The data is taken from CXRO (2023)

$$t_{Pl} = \frac{\Sigma_{Pl}}{\rho_{Pl}}, \tag{4.7}$$

where the density of polyimide ρ_{Pl} is assumed to be 1.43 g cm^{-3}.

The surface oxygen contamination due to epoxy bleed also absorbs X-rays, and its transmission is given by:

$$T_O = \exp(-\Sigma_O \mu_O). \tag{4.8}$$

The filters are partially blocked by the silicon mesh bars of both fine and coarse meshes. To accurately fit the transmission curve, the mesh filling fraction f should be treated as a free parameter. The transmission due to the mesh bars is expressed as:

$$T_{mesh} = (1 - f) + f \exp(-\Sigma_{Si} \mu_{Si}). \tag{4.9}$$

The thickness of fine mesh and coarse mesh is fixed as 25 μm and 225 μm, thus the silicon surface density is calculated as $\Sigma_{Si} = \rho_{Si} t_{Si}$, where $\rho_{Si} = 2.33$ g cm^{-3} and $t_{Si} = 25$ μm.

Epoxy bleed extended beyond the 5-micron-wide silicon bars of the fine mesh and exhibited non-uniform distribution across different sections of each filter, as illustrated in Figure 4.5. Consequently, the epoxy thickness t_{ep} and epoxy filling factor f_{ep} were included as free parameters in the transmission fitting. Assuming the epoxy has the same composition as polyimide, it contributes to the overall transmission model:

$$T_{ep} = 1 - f_{ep}\left[1 - \frac{2}{\Sigma_{ep}\mu_{Pl}} + \frac{2}{\exp(-2\Sigma_{ep}\mu_{Pl})}\left(1 - \exp(-\Sigma_{ep}\mu_{Pl})\right)\right]. \tag{4.10}$$

Fitting Results of Filter Properties

Here, I present the analysis of seven flight spare filters, which include three IVCS filters, three OVCS filters, and one DMS filter. As part of the collaborative filter analysis effort, the results for OVCS7 and IVCS6 have previously been detailed in Martz's master's degree thesis (Martz, 2019).

The broadband transmission measured in two cells of filters OVCS5, IVCS2, and DMS-G1 is represented by black points, with the corresponding best-fit models shown as red dashed lines in the top panels of Figure 4.13, Figure 4.14, and Figure 4.15, respectively. Data points near absorption edges were excluded from the fitting due to the high uncertainties. The bottom panels of each figure display the residuals between the calibration data and the fitted models, clearly demonstrating a high degree of agreement with discrepancies maintained below 2%.

The fitting results for the mesh and film properties of the filters are summarized in Table 4.2. With the exception of OVCS2, the aluminum and polyimide thicknesses measured in the two cells of each filter are very similar, demonstrating high spatial uniformity with non-uniformity levels of $\sim 2\%$. The coarse mesh filling fraction was estimated from microscopic measurements, while the epoxy filling fraction f_{ep} and fine mesh bar filling fraction f_{fine} were determined from synchrotron-based filter transmission data. The fine mesh filling factors remain consistent among cells at ~ 0.03 but are slightly lower than the values estimated for the Hitomi SXS blocking filters (Eckart et al., 2018), particularly in the case of IVCS6.

The epoxy filling factor shows greater variability between different cells compared to the fine mesh filling factor. This is likely due to the inherently uneven distribution of excess epoxy, leading to localized differences across the filter. Our estimates indicate that the typical epoxy filling factor is less than 1.0%, which is even lower than the values reported for the Hitomi SXS flight filters: $f_{ep} = 1.6\%,\ 1.0\%,\ 2.2\%$ for the IVCS, OVCS, and DMS filters, respectively (Eckart et al., 2018). This significant reduction suggests the improvements in

Filter	Cell	t_{Al} $\mathring{A}$	t_{Pl} $\mathring{A}$	Σ_O 10^6 g cm^2	t_{ep} μm	f_{eq}	f_{fine}
(1)	(2)	(3)	(4)	(5)	(6)	(7)	(8)
OVCS7	C3	925.9	950.3	2.00	8.9	0.013	0.029
	E2	925.9	965.9	1.99	8.4	0.012	0.028
OVCS2	C4	926.5	949.7	1.48	25.0	0.004	0.029
	D3	988.5	985.2	2.52	25.0	0.008	0.029
OVCS5	C4	930.1	1189.0	1,18	11.7	0.003	0.030
	D3	945.2	1220.6	1.14	11.6	0.010	0.027
IVCS6	C3	843.6	980.9	2.20	8.3	0.040	0.013
	E3	844.5	998.6	2.39	8.3	0.045	0.014
IVCS2	C4	919.5	1122.9	0.83	12.5	0.004	0.026
	D2	926.0	1106.0	0.69	12.5	0.007	0.029
IVCS8	D3	876.6	1210.6	1.07	9.7	0.010	0.029
DMS-G1	E4	911.4	1040.4	1.17	8.0	0.004	0.030
	F5	909.2	1078.1	0.97	8.0	0.005	0.029

Table 4.2: The best-fit mesh and film parameters of optical blocking filters: (1). Filter. (2). Cell. (3). Thickness of Al-film. (4). Polyimide thickness. (5). Surface density of oxygen. (6). Epoxy thickness. (7). Epoxy filling fraction. (8). Fine mesh filling fraction.

the low-energy transmission of the blocking filters, likely due to advancements in fabrication techniques.

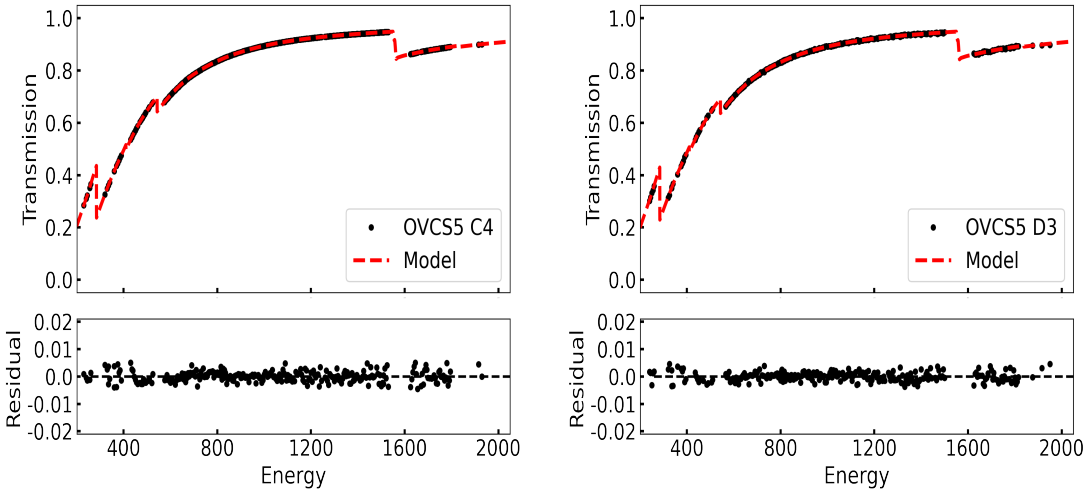


Figure 4.13: Top: Broadband transmission measurements (black points) and the best-fit transmission model (red dashed line) for cell C4 (left) and cell D3 (right) of the OVCS5 filter. Bottom: Residuals between the measured data and the best-fit transmission model.

Modeled Transmission of the Whole Stack

Figure 4.16 presents the modeled transmission curve for the full stack, derived from calibrations of CTS-2F (ALS, Dec 2018), DA-D (NSLS, Oct/Nov 2012), IVCS19 (ALS, May 2019), OVCS11 (ALS, May 2019), and DMS-G10 (CLS, July 2019). This model has been released and incorporated into the XRISM HEASARC Calibration Database (CALDB, 2024). The shallow depth of the Si K edge is attributed to the low filling fraction of the fine mesh combined with the relatively thin silicon layer.

4.5 Summary

In this chapter, I detailed my calibration work on the XRISM Resolve optical blocking filters. This included participating in synchrotron calibrations of flight and flight spare

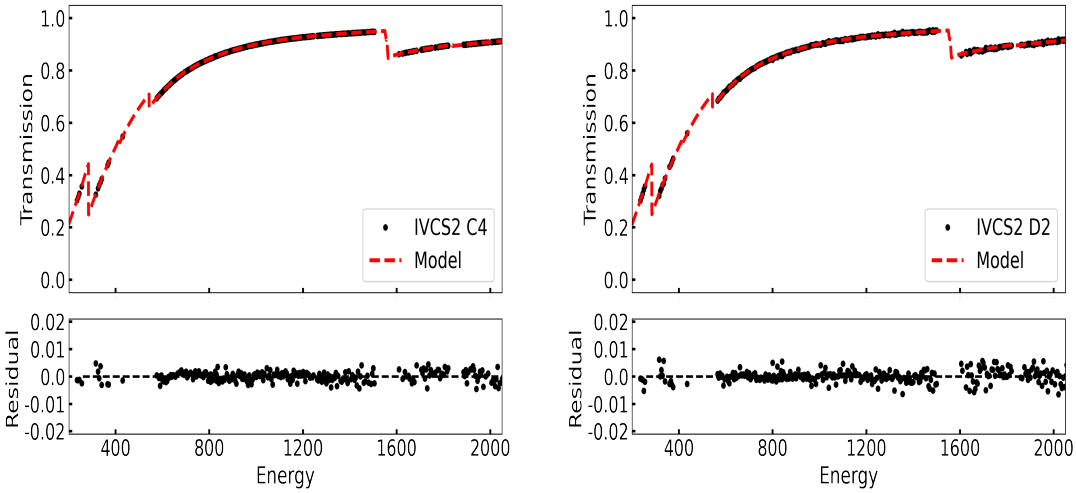


Figure 4.14: Top: Measured and modeled transmission for cells E4 (left) and F5 (right) in the DMS-G1 filter. Bottom: Residuals between the data and model.

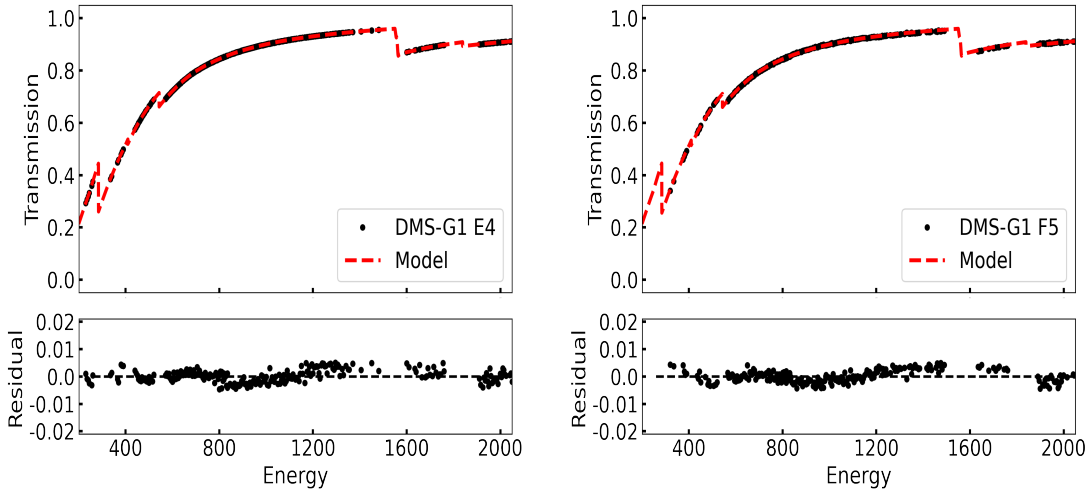


Figure 4.15: Top: Measured and modeled transmission for cells C4 (left) and D2 (right) in the IVCS2 filter. Bottom: Residuals between the data and model.

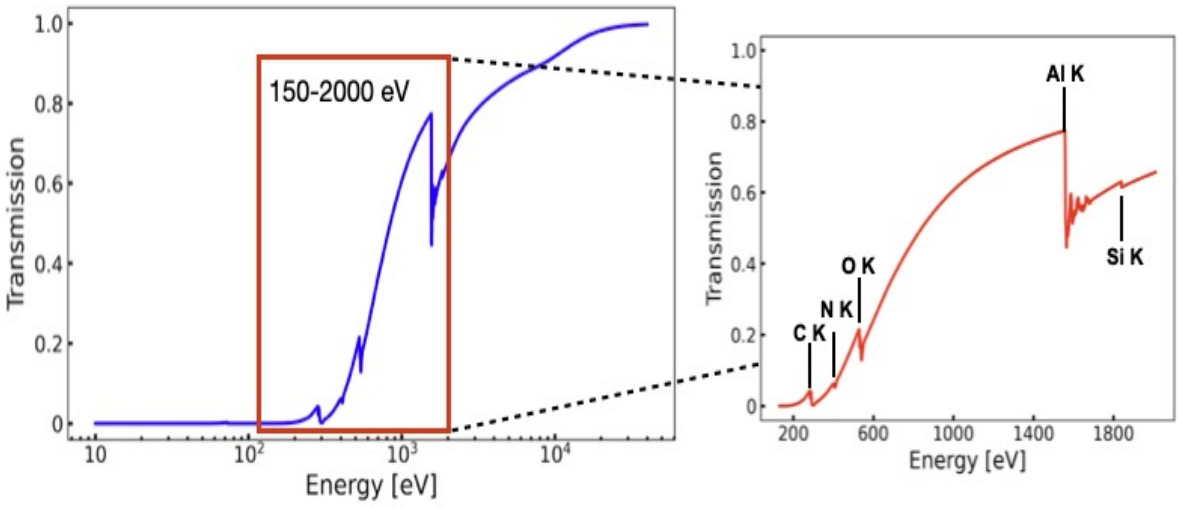


Figure 4.16: Left: Full transmission curve of the complete stack of five optical blocking filters for XRISM Resolve, spanning a broad energy range. Right: Zoomed-in view of the red-highlighted 150 – 2000 eV band, illustrating transmission features near the K-edges of key elements, including C, N, O, Al, and Si.

filters at the Canadian Light Source and the Advanced Light Source in July and May 2019, respectively. I was also involved in analyzing synchrotron-based transmission to model filter properties. Here, I present the analysis of three OVCS filters (OVCS7, OVCS2, and OVCS5), three IVCS filters (IVCS6, IVCS2, and IVCS8), and one DMS filter (DMS-G1). The analysis of IVCS6 and OVCS7 was collaboratively conducted with my colleague Connor Martz, with findings summarized in his master's thesis. These filters underwent microscopic imaging and high-resolution X-ray spectral measurements in January-February and July 2019 at the CLS.

For all filters, transmission measurements were performed at a series of fixed energies within each coarse mesh using a 5×5 mesh scan. The resulting spatial uniformity maps indicate that transmission variances within the coarse meshes are much below 1%. Furthermore, broadband transmission for each filter is measured in two distinct cells via a full spectral scan over the range of 260 eV to 2100 eV. The comparison of the transmission curves revealed differences of less than 2%, confirming the uniformity across the filters.

The key filter parameters were determined by fitting broadband transmission curves. The best-fit thicknesses of the aluminum and polyimide films are consistent with the design specification of $\sim$100 nm and show uniformity across the filters. The filling fractions of the

fine mesh are $\lesssim 3\%$, slightly lower than those estimated for the blocking filters installed on Hitomi SXS. In contrast, the epoxy filling factor exhibits significant variation between cells, reflecting the non-uniform distribution of epoxy. Despite this, the epoxy filling factor remains below 1% for all filters except IVCS6, indicating progress in mitigating the issue of epoxy excess.

The calibration campaign for the optical blocking filters was completed in 2020.The model transmission curve of the entire five-filter stack was released to support Resolve data reduction. Following XRISM's launch in September 2023, the nominal phase of observations has demonstrated an exceptional energy resolution of ~ 5 eV, surpassing the design goal of ~ 7 eV. This achievement sets the stage for XRISM to advance its scientific goals effectively, including probing the structure of the Universe, understanding the mechanics of galaxy cluster formation, and investigating black hole physics with unprecedented clarity and precision.

Chapter 5

Conclusion

5.1 Summary

Radio AGN feedback is widely recognized as a promising mechanism that helps offset cooling flows. The energy released by the central black hole is sufficient to balance radiative cooling, though it does not completely stop it. The jet-inflated X-ray bubbles can lift low-entropy gas from the cluster cores to higher altitudes, where cold gas condenses out of the hot atmosphere as thermal instabilities are triggered (e.g. McNamara et al., 2016). The trailing multiphase filaments observed in these regions provide compelling evidence for the scenario of stimulated cooling (McNamara et al., 2014; Vantyghem et al., 2019; Russell et al., 2019). However, several key questions remain unclear. How is the energy released via radio AGN feedback converted into thermal energy that ultimately couples with and heats the intracluster medium? Could turbulence dissipation provide a viable heating mechanism, and if so, is it efficient enough to account for the observed thermal balance? Besides central AGN activities, are other processes triggering turbulence within the cluster cores? Lastly, are the kinematics of gas in multiple phases within the AGN feedback loop interconnected?

To explore the issues raised, this thesis provides a detailed investigation of gas kinematics and their interactions within galaxy cluster cores using multi-wavelength observations. It examines the processes that potentially generate gas perturbations and estimates the resulting dissipation rates. Additionally, this study focuses on exploring the origins of multi-phase gas and the mechanisms—particularly AGN feedback—that influence the coupling or decoupling of their motions.

In Chapter 2, I investigated gas perturbations within the atmospheres of five galaxy cluster cores, Abell 2029, Abell 2107, Abell 2151, RBS0533, and RBS0540, observed by the Chandra X-ray Observatory. These clusters display the typical thermodynamic properties of cool core clusters, including short cooling times and low central entropy. However, contrary to expectations, they lack significant star formation and nebular emission. This discrepancy may be explained by the absence of buoyant bubbles, which are often responsible for lifting cooler gas from the cluster centers (Martz et al., 2020).

X-ray surface brightness fluctuation analysis is utilized to compensate for the lack of direct velocity measurements of the hot ICM. Due to the low energy resolution of current X-ray images, accurately measuring spectral line shifts or line widths is challenging. This method is effective as X-ray emissivity is strongly dependent on gas density at temperatures above keV. By analyzing the surface brightness fluctuations presented in X-ray images at specific scales, we estimate the amplitude of gas density fluctuations. Combined with the linear relationship between the gas density fluctuation amplitude and the one-component velocity of hot gas, velocity spectra are derived and further used to constrain the turbulent dissipation rates. The turbulent heating rates for ten nearby bright clusters are calculated by Zhuravleva et al. (2018) and found to be sufficient to counterbalance the radiative cooling rates.

Despite the absence of cavities, the gas density fluctuations measured in five clusters with smooth atmospheres are comparable to those observed in the Perseus-like cluster. This suggests that factors other than AGN-inflated bubbles may efficiently drive gas perturbations in these systems. For example, the spiral structures observed in Abell 2029 and Abell 2151 are believed to be triggered by mergers with nearby subclusters. The typical velocity amplitudes of hot gas motions, ranging from 100 $\mathrm{km/s^{-1}}$ to 200 $\mathrm{km/s^{-1}}$, align well with direct velocity measurements within the cores of Perseus and Abell 2029 obtained by Hitomi and XRISM, respectively.

No correlation is observed between cluster mass and gas turbulent velocity in our sample. Interestingly, the latest XRISM observations have found a similar trend. The velocity dispersion measured in the cool core of Abell 2029 is akin to that observed in the core of Perseus (XRISM Collaboration, 2025), although Abell 2029 is a much more massive cluster with a higher ICM temperature exceeding 7 keV.

Furthermore, regardless of the mechanisms driving these perturbations in the ICM, the turbulent dissipation rates are roughly of the same order as the radiative cooling rates in these smooth atmospheres. This suggests that turbulent heating can significantly contribute to balancing cooling and maintaining thermal stability. However, with large uncertainties, many aspects of these interactions remain ambiguous.

In Chapter 3, the focus is on the multiphase filaments commonly observed at the centers of cool core clusters. Unlike X-ray observations, which rely on indirect methods to infer gas motions, the velocity fields of cold molecular gas and nebular gas can be directly measured. The recently released KCWI observations of the four central cluster galaxies: Abell 1835, PKS 0745-191, Abell 262, and RXJ0820.9+0752, offer high spatial and spectral resolution along with a large field of view, making them well-suited for VSF analysis. Complementary data from ALMA's CO emission detections and Chandra X-ray observations allow for a multi-wavelength investigation, providing a detailed view of the gas motions in these systems.

Analysis and comparison of the VSFs from KCWI [OII] emission and ALMA CO emission reveal a strong coupling between gas motions in both phases for Abell 262 and RXJ0820. In Abell 262, the gas in both phases exhibits rotational motion around the nucleus, while in RXJ0820, the motions are predominantly influenced by sloshing caused by the passage of a nearby subcluster. In Abell 1835 and PKS 0745, which are both experiencing strong radio AGN feedback, the gas motions appear decoupled due to their complex environments. However, their turnover scales in the VSFs of nebular gas closely correspond with their bubble sizes, suggesting energy injection from AGN activity. This finding is further supported by the alignment of cold gas distribution along the cavity axes in both systems. The velocity spectra of hot gas were derived using X-ray surface brightness analysis for three of our targets, excluding Abell 262. When compared with the VSFs of nebular gas, Abell 1835 and RXJ0820 show consistent amplitude trends at large spatial scales, suggesting that the cold-phase gas may originate from the hot atmospheres.

Direct velocity measurements of cluster atmospheres have become possible with the launch of the XRISM satellite in September 2023. XRISM is equipped with Resolve, an advanced soft X-ray calorimeter operating at an ultra-low temperature of 50 mK. To ensure optimal performance, a set of optical blocking filters is required to shield the detector from thermal radiation emitted by warmer parts of the instrument and from optical and UV photons from the sky, while minimizing X-ray absorption. Between April 2019 and May 2020, I participated in the on-ground calibration and analysis of the flight and flight spare optical blocking filters for XRISM Resolve. This work was critical for verifying filter performance against design specifications and understanding their spectral responses. Early science results of the Perseus cluster, released in March 2024, demonstrated an impressive energy resolution of 5 eV, exceeding the original design target of 7 eV. This enhanced capability provides new opportunities for understanding the dynamics of cluster hot atmospheres.

5.2 Future Work

Although upcoming XRISM observations now enable direct measurements of hot ICM velocities, the indirect derivation of velocity spectra through X-ray SB fluctuation analysis remains scientifically valuable. Firstly, it provides critical scale-dependent information on gas motions, allowing us to investigate the nature of gas perturbations—insights that are challenging to obtain even with direct measurements from instruments like Hitomi or XRISM. Additionally, Chandra's exceptional performance over the past two decades has built an extensive observational archive, offering a ready-made database for studying the kinematics of hot gas across a wide variety of galaxy clusters. Thus, future work will involve utilizing this method and existing data to expand the study of hot ICM in a wider range of clusters. For example, Abell 2029 and Cygnus A, both high-priority targets in XRISM's Performance Verification Phase, have accumulated substantial datasets in the Chandra archive. These studies will further enhance our understanding of the role of AGN feedback and other processes in driving gas perturbations and their contributions to reheating the ICM. Additionally, comparing velocity spectra derived from X-ray surface brightness fluctuations with direct spectral measurements from XRISM will shed light on their differences, potentially providing insights into new physics.

Future efforts will continue to utilize multi-wavelength observations to comprehensively investigate the kinematics of multi-phase filaments in cluster cores, providing insights into the origins and formation of cold phases within AGN feedback. The inherent properties of each analytical method and observational dataset must be further clarified to avoid systematic errors. This thesis also explores the limitations and uncertainties of VSF analysis, including the window effect due to limited image size, which distorts the VSF shape at large scales, and the impacts of data smoothing during reduction and differing spatial resolutions between telescopes. Further in-depth studies might incorporate numerical simulations to enhance our understanding.

References

Abdullah, M. H., Wilson, G., Klypin, A., & Ishiyama, T. 2023, ApJ, 955, 26, doi: 10.3847/1538-4357/ace773

Alatalo, K., Blitz, L., Young, L. M., et al. 2011, ApJ, 735, 88, doi: 10.1088/0004-637X/735/2/88

Alberts, S., Adams, J., Gregg, B., et al. 2022, ApJ, 927, 235, doi: 10.3847/1538-4357/ac48f6

Allen, S. W., Fabian, A. C., Johnstone, R. M., Arnaud, K. A., & Nulsen, P. E. J. 2001, MNRAS, 322, 589, doi: 10.1046/j.1365-8711.2001.04135.x

ALS. 2024, Advanced Light Source Synchrotron and Beamlines. Available at. https://als.lbl.gov/about/about-the-als/

ALS QuickFacts Sheet. 2019, ALS Quick Facts Sheet, Lawrence Berkeley National Laboratory. https://als.lbl.gov/wp-content/uploads/2018/11/QuickFacts2019.pdf

Arévalo, P., Churazov, E., Zhuravleva, I., Hernández-Monteagudo, C., & Revnivtsev, M. 2012, MNRAS, 426, 1793, doi: 10.1111/j.1365-2966.2012.21789.x

Arnaud, M., & Evrard, A. E. 1999, MNRAS, 305, 631, doi: 10.1046/j.1365-8711.1999.02442.x

Arrigoni Battaia, F., Hennawi, J. F., Prochaska, J. X., et al. 2019, MNRAS, 482, 3162, doi: 10.1093/mnras/sty2827

Ascasibar, Y., & Markevitch, M. 2006, ApJ, 650, 102, doi: 10.1086/506508

Attwood, D. 2000, Soft x-rays and extreme ultraviolet radiation: principles and applications (Cambridge university press)

Babyk, I. V., McNamara, B. R., Tamhane, P. D., et al. 2019, ApJ, 887, 149, doi: 10.3847/1538-4357/ab54ce

Balbus, S. A., & Soker, N. 1989, ApJ, 341, 611, doi: 10.1086/167521

Bambic, C. J., Morsony, B. J., & Reynolds, C. S. 2018, ApJ, 857, 84, doi: 10.3847/1538-4357/aab558

Baptiste, K., Balagot, M., Barry, W., et al. 2010. https://api.semanticscholar.org/CorpusID:111385605

Barnes, D. J., Kannan, R., Vogelsberger, M., et al. 2019, MNRAS, 488, 3003, doi: 10.1093/mnras/stz1814

Barret, D., Lam Trong, T., den Herder, J.-W., et al. 2016, in Society of Photo-Optical Instrumentation Engineers (SPIE) Conference Series, Vol. 9905, Space Telescopes and Instrumentation 2016: Ultraviolet to Gamma Ray, ed. J.-W. A. den Herder, T. Takahashi, & M. Bautz, 99052F, doi: 10.1117/12.2232432

Bayer-Kim, C. M., Crawford, C. S., Allen, S. W., Edge, A. C., & Fabian, A. C. 2002, MNRAS, 337, 938, doi: 10.1046/j.1365-8711.2002.05969.x

Becker, R. H., White, R. L., & Helfand, D. J. 1995, ApJ, 450, 559, doi: 10.1086/176166

Belloni, T., Homan, J., Casella, P., et al. 2005, A&A, 440, 207, doi: 10.1051/0004-6361:20042457

Bending, T. J. R., Dobbs, C. L., & Bate, M. R. 2022, MNRAS, 513, 2088, doi: 10.1093/mnras/stac965

Benson, A. J., Bower, R. G., Frenk, C. S., et al. 2003, ApJ, 599, 38, doi: 10.1086/379160

Biffi, V., Mernier, F., & Medvedev, P. 2018, Space Sci. Rev., 214, 123, doi: 10.1007/s11214-018-0557-7

Bîrzan, L., McNamara, B. R., Nulsen, P. E. J., Carilli, C. L., & Wise, M. W. 2008, ApJ, 686, 859, doi: 10.1086/591416

Bîrzan, L., Rafferty, D. A., McNamara, B. R., Wise, M. W., & Nulsen, P. E. J. 2004, ApJ, 607, 800, doi: 10.1086/383519

Bîrzan, L., Rafferty, D. A., Nulsen, P. E. J., et al. 2012, MNRAS, 427, 3468, doi: 10.1111/j.1365-2966.2012.22083.x

Blandford, R. D., & Rees, M. J. 1974, MNRAS, 169, 395, doi: 10.1093/mnras/169.3.395

Blanton, E. L., Randall, S. W., Clarke, T. E., et al. 2011, ApJ, 737, 99, doi: 10.1088/0004-637X/737/2/99

Boehringer, H., & Morfill, G. E. 1988, ApJ, 330, 609, doi: 10.1086/166497

Boehringer, H., Voges, W., Fabian, A. C., Edge, A. C., & Neumann, D. M. 1993, MNRAS, 264, L25, doi: 10.1093/mnras/264.1.L25

Böhringer, H., & Werner, N. 2010, A&A Rev., 18, 127, doi: 10.1007/s00159-009-0023-3

Boland, M., & Le Pimpec, F. 2022, JACoW, IPAC2022, TUPOMS003, doi: 10.18429/JACoW-IPAC2022-TUPOMS003

Borgani, S., Fabjan, D., Tornatore, L., et al. 2008, Space Sci. Rev., 134, 379, doi: 10.1007/s11214-008-9322-7

Borgani, S., Finoguenov, A., Kay, S. T., et al. 2005, MNRAS, 361, 233, doi: 10.1111/j.1365-2966.2005.09158.x

Borgani, S., Murante, G., Springel, V., et al. 2004, MNRAS, 348, 1078, doi: 10.1111/j.1365-2966.2004.07431.x

Bower, R. G., Benson, A. J., Malbon, R., et al. 2006, MNRAS, 370, 645, doi: 10.1111/j.1365-2966.2006.10519.x

Bozzo, E., Huenemoerder, D. P., Produit, N., et al. 2023, MNRAS, 522, L66, doi: 10.1093/mnrasl/slad040

Brüggen, M., & Kaiser, C. R. 2001, MNRAS, 325, 676, doi: 10.1046/j.1365-8711.2001.04494.x

CALDB. 2024, the XRISM HEASARC Calibration Database (CALDB), Available at the XRISM HEASARC CALDB provided by XRISM Science Data Center (SDC). https://heasarc.gsfc.nasa.gov/docs/xrism/calib/

Canizares, C. R., Clark, G. W., Jernigan, J. G., & Markert, T. H. 1982, ApJ, 262, 33, doi: 10.1086/160393

Cappellari, M., & Emsellem, E. 2004, PASP, 116, 138, doi: 10.1086/381875

Cavagnolo, K. W., Donahue, M., Voit, G. M., & Sun, M. 2008, ApJ, 683, L107, doi: 10.1086/591665

—. 2009, ApJS, 182, 12, doi: 10.1088/0067-0049/182/1/12

Cavaliere, A., & Fusco-Femiano, R. 1976, A&A, 49, 137

Chen, H., Jones, C., Andrade-Santos, F., ZuHone, J. A., & Li, Z. 2017, ApJ, 838, 38, doi: 10.3847/1538-4357/aa64de

Chen, M. C., Chen, H.-W., Rauch, M., et al. 2023, MNRAS, 518, 2354, doi: 10.1093/mnras/stac3193

—. 2024, ApJ, 962, 98, doi: 10.3847/1538-4357/ad1406

Chen, Y., Reiprich, T. H., Böhringer, H., Ikebe, Y., & Zhang, Y. Y. 2007, A&A, 466, 805, doi: 10.1051/0004-6361:20066471

Churazov, E., Arevalo, P., Forman, W., et al. 2016, MNRAS, 463, 1057, doi: 10.1093/mnras/stw2044

Churazov, E., Brüggen, M., Kaiser, C. R., Böhringer, H., & Forman, W. 2001, ApJ, 554, 261, doi: 10.1086/321357

Churazov, E., Forman, W., Jones, C., & Böhringer, H. 2000, A&A, 356, 788, doi: 10.48550/arXiv.astro-ph/0002375

Churazov, E., Forman, W., Jones, C., Sunyaev, R., & Böhringer, H. 2004, MNRAS, 347, 29, doi: 10.1111/j.1365-2966.2004.07201.x

Churazov, E., Sunyaev, R., Forman, W., & Böhringer, H. 2002, MNRAS, 332, 729, doi: 10.1046/j.1365-8711.2002.05332.x

Churazov, E., Vikhlinin, A., Zhuravleva, I., et al. 2012, MNRAS, 421, 1123, doi: 10.1111/j.1365-2966.2011.20372.x

Ciotti, L., & Ostriker, J. P. 2001, ApJ, 551, 131, doi: 10.1086/320053

Ciotti, L., Ostriker, J. P., & Proga, D. 2009, ApJ, 699, 89, doi: 10.1088/0004-637X/699/1/89

Clarke, T. E., Blanton, E. L., & Sarazin, C. L. 2004, ApJ, 616, 178, doi: 10.1086/424911

Clarke, T. E., Blanton, E. L., Sarazin, C. L., et al. 2009, ApJ, 697, 1481, doi: 10.1088/0004-637X/697/2/1481

CLS. 2024, Canadian Light Source Synchrotron and Beamlines. Available at https://www.lightsource.ca/public/what-is-a-synchrotron.phpLearnMore

Cole, S., Lacey, C. G., Baugh, C. M., & Frenk, C. S. 2000, MNRAS, 319, 168, doi: 10.1046/j.1365-8711.2000.03879.x

Cole, S., Norberg, P., Baugh, C. M., et al. 2001, MNRAS, 326, 255, doi: 10.1046/j.1365-8711.2001.04591.x

Cowie, L. L., & Binney, J. 1977, ApJ, 215, 723, doi: 10.1086/155406

Crawford, C. S., Allen, S. W., Ebeling, H., Edge, A. C., & Fabian, A. C. 1999, MNRAS, 306, 857, doi: 10.1046/j.1365-8711.1999.02583.x

Cutler, J., Chapman, D., Dallin, L., & Lamb, R. 2017, Quantum Beam Science, 1, 4, doi: 10.3390/qubs1010004

Cutler, J., Hallin, E., de Jong, M., Thomlinson, W., & Ellis, T. 2007, Nuclear Instruments and Methods in Physics Research A, 582, 11, doi: 10.1016/j.nima.2007.08.086

CXRO. 2023, X-Ray Interactions With Matter, NIST Physical Measurement Laboratory. https://henke.lbl.gov/optical_constants/

David, L. P., Lim, J., Forman, W., et al. 2014, ApJ, 792, 94, doi: 10.1088/0004-637X/792/2/94

De Young, D. S. 2003, MNRAS, 343, 719, doi: 10.1046/j.1365-8711.2003.06719.x

Dekel, A., & Silk, J. 1986, ApJ, 303, 39, doi: 10.1086/164050

Dennis, T. J., & Chandran, B. D. G. 2005, ApJ, 622, 205, doi: 10.1086/427424

Dunn, J. P., Bautista, M., Arav, N., et al. 2010, ApJ, 709, 611, doi: 10.1088/0004-637X/709/2/611

Dunn, R. J. H., & Fabian, A. C. 2006, MNRAS, 373, 959, doi: 10.1111/j.1365-2966.2006.11080.x

—. 2008, MNRAS, 385, 757, doi: 10.1111/j.1365-2966.2008.12898.x

Eckart, M. E., Adams, J. S., Boyce, K. R., et al. 2018, Journal of Astronomical Telescopes, Instruments, and Systems, 4, 021406, doi: 10.1117/1.JATIS.4.2.021406

Eckert, D., Gaspari, M., Vazza, F., et al. 2017, ApJ, 843, L29, doi: 10.3847/2041-8213/aa7c1a

Edge, A. C. 2001, MNRAS, 328, 762, doi: 10.1046/j.1365-8711.2001.04802.x

Edge, A. C., & Stewart, G. C. 1991, MNRAS, 252, 414, doi: 10.1093/mnras/252.3.414

El-Zant, A. A., Kim, W.-T., & Kamionkowski, M. 2004, MNRAS, 354, 169, doi: 10.1111/j.1365-2966.2004.08175.x

Enßlin, T., Pfrommer, C., Miniati, F., & Subramanian, K. 2011, A&A, 527, A99, doi: 10.1051/0004-6361/201015652

Enßlin, T. A., & Heinz, S. 2002, A&A, 384, L27, doi: 10.1051/0004-6361:20020207

Fabian, A. C. 1994, ARA&A, 32, 277, doi: 10.1146/annurev.aa.32.090194.001425

—. 2012, ARA&A, 50, 455, doi: 10.1146/annurev-astro-081811-125521

Fabian, A. C., Ferland, G. J., Sanders, J. S., et al. 2022, MNRAS, 515, 3336, doi: 10.1093/mnras/stac2003

Fabian, A. C., Nulsen, P. E. J., & Canizares, C. R. 1984, Nature, 310, 733, doi: 10.1038/310733a0

Fabian, A. C., Sanders, J. S., Allen, S. W., et al. 2003, MNRAS, 344, L43, doi: 10.1046/j.1365-8711.2003.06902.x

Fabian, A. C., Sanders, J. S., Ferland, G. J., et al. 2023, MNRAS, 521, 1794, doi: 10.1093/mnras/stad507

Fabian, A. C., Sanders, J. S., Taylor, G. B., et al. 2006, MNRAS, 366, 417, doi: 10.1111/j.1365-2966.2005.09896.x

Fabian, A. C., Arnaud, K. A., Nulsen, P. E. J., et al. 1985, MNRAS, 216, 923, doi: 10.1093/mnras/216.4.923

Fabian, A. C., Sanders, J. S., Allen, S. W., et al. 2011, MNRAS, 418, 2154, doi: 10.1111/j.1365-2966.2011.19402.x

Felten, J. E., & Morrison, P. 1966, ApJ, 146, 686, doi: 10.1086/148946

Forman, W., Nulsen, P., Heinz, S., et al. 2005, ApJ, 635, 894, doi: 10.1086/429746

Forman, W., Jones, C., Churazov, E., et al. 2007, ApJ, 665, 1057, doi: 10.1086/519480

Fournier, M., Grete, P., Bruggen, M., et al. 2025, 'XMAGNET: Velocity structure functions in AGN-driven turbulence of the multiphase intracluster medium', Submitted to A&A.

Friedman, S. H., Heinz, S., & Churazov, E. 2012, ApJ, 746, 112, doi: 10.1088/0004-637X/746/1/112

Ganguly, S., Li, Y., Olivares, V., et al. 2023, Frontiers in Astronomy and Space Sciences, 10, 1138613, doi: 10.3389/fspas.2023.1138613

Gaspari, M., Churazov, E., Nagai, D., Lau, E. T., & Zhuravleva, I. 2014, A&A, 569, A67, doi: 10.1051/0004-6361/201424043

Gaspari, M., Ruszkowski, M., & Sharma, P. 2012, ApJ, 746, 94, doi: 10.1088/0004-637X/746/1/94

Gaspari, M., Temi, P., & Brighenti, F. 2017, MNRAS, 466, 677, doi: 10.1093/mnras/stw3108

Gaspari, M., McDonald, M., Hamer, S. L., et al. 2018, ApJ, 854, 167, doi: 10.3847/1538-4357/aaaa1b

Gingras, M.-J., Coil, A. L., McNamara, B. R., et al. 2024, arXiv e-prints, arXiv:2404.02212, doi: 10.48550/arXiv.2404.02212

Giodini, S., Lovisari, L., Pointecouteau, E., et al. 2013, Space Sci. Rev., 177, 247, doi: 10.1007/s11214-013-9994-5

González Delgado, R. M., Cerviño, M., Martins, L. P., Leitherer, C., & Hauschildt, P. H. 2005, MNRAS, 357, 945, doi: 10.1111/j.1365-2966.2005.08692.x

Graham, J., Fabian, A. C., & Sanders, J. S. 2008, MNRAS, 386, 278, doi: 10.1111/j.1365-2966.2008.13027.x

Gu, L., Gandhi, P., Inada, N., et al. 2013, Astronomische Nachrichten, 334, 453, doi: 10.1002/asna.201211879

Guo, F., & Oh, S. P. 2008, MNRAS, 384, 251, doi: 10.1111/j.1365-2966.2007.12692.x

Hatch, N. A., Crawford, C. S., & Fabian, A. C. 2007, MNRAS, 380, 33, doi: 10.1111/j.1365-2966.2007.12009.x

Hatch, N. A., Crawford, C. S., Johnstone, R. M., & Fabian, A. C. 2006, MNRAS, 367, 433, doi: 10.1111/j.1365-2966.2006.09970.x

Hayashi, M., Tadaki, K.-i., Kodama, T., et al. 2018, ApJ, 856, 118, doi: 10.3847/1538-4357/aab3e7

Heckman, T. M. 1981, ApJ, 250, L59, doi: 10.1086/183674

Heckman, T. M., Baum, S. A., van Breugel, W. J. M., & McCarthy, P. 1989, ApJ, 338, 48, doi: 10.1086/167181

Heckman, T. M., & Best, P. N. 2023, Galaxies, 11, 21, doi: 10.3390/galaxies11010021

Heinrich, A., Zhuravleva, I., Zhang, C., et al. 2024, MNRAS, 528, 7274, doi: 10.1093/mnras/stae208

Heinz, S., Brüggen, M., Young, A., & Levesque, E. 2006, MNRAS, 373, L65, doi: 10.1111/j.1745-3933.2006.00243.x

Heinz, S., Reynolds, C. S., & Begelman, M. C. 1998, ApJ, 501, 126, doi: 10.1086/305807

Henke, B. L., Gullikson, E. M., & Davis, J. C. 1993, Atomic Data and Nuclear Data Tables, 54, 181, doi: 10.1006/adnd.1993.1013

Hillel, S., & Soker, N. 2016, MNRAS, 455, 2139, doi: 10.1093/mnras/stv2483

—. 2017a, ApJ, 845, 91, doi: 10.3847/1538-4357/aa81c5

—. 2017b, MNRAS, 466, L39, doi: 10.1093/mnrasl/slw231

—. 2020, ApJ, 896, 104, doi: 10.3847/1538-4357/ab9109

Hitomi Collaboration, Aharonian, F., Akamatsu, H., et al. 2016, Nature, 535, 117, doi: 10.1038/nature18627

Hlavacek-Larrondo, J., Fabian, A. C., Edge, A. C., et al. 2013, MNRAS, 431, 1638, doi: 10.1093/mnras/stt283

—. 2012, MNRAS, 421, 1360, doi: 10.1111/j.1365-2966.2011.20405.x

Hlavacek-Larrondo, J., Li, Y., & Churazov, E. 2022, in Handbook of X-ray and Gamma-ray Astrophysics, ed. C. Bambi & A. Sangangelo, 5, doi: 10.1007/978-981-16-4544-0_122-1

Hlavacek-Larrondo, J., McDonald, M., Benson, B. A., et al. 2015, ApJ, 805, 35, doi: 10.1088/0004-637X/805/1/35

Hofmann, F., Sanders, J. S., Nandra, K., Clerc, N., & Gaspari, M. 2016, A&A, 585, A130, doi: 10.1051/0004-6361/201526925

Hogan, M. T., McNamara, B. R., Pulido, F. A., et al. 2017, ApJ, 851, 66, doi: 10.3847/1538-4357/aa9af3

Hopkins, P. F., Quataert, E., & Murray, N. 2012, MNRAS, 421, 3488, doi: 10.1111/j.1365-2966.2012.20578.x

Hopkins, P. F., Richards, G. T., & Hernquist, L. 2007, ApJ, 654, 731, doi: 10.1086/509629

Howes, G. G. 2010, MNRAS, 409, L104, doi: 10.1111/j.1745-3933.2010.00958.x

Hu, H., Qiu, Y., Gendron-Marsolais, M.-L., et al. 2022, ApJ, 929, L30, doi: 10.3847/2041-8213/ac6601

Hubbell, J. H. 2006, Physics in Medicine and Biology, 51, R245, doi: 10.1088/0031-9155/51/13/R15

Hudson, D. S., Mittal, R., Reiprich, T. H., et al. 2010, A&A, 513, A37, doi: 10.1051/0004-6361/200912377

Ishibashi, W., Fabian, A. C., & Maiolino, R. 2018, MNRAS, 476, 512, doi: 10.1093/mnras/sty236

Ishisaki, Y., Kelley, R. L., Awaki, H., et al. 2022, in Society of Photo-Optical Instrumentation Engineers (SPIE) Conference Series, Vol. 12181, Space Telescopes and Instrumentation 2022: Ultraviolet to Gamma Ray, ed. J.-W. A. den Herder, S. Nikzad, & K. Nakazawa, 121811S, doi: 10.1117/12.2630654

Jaffe, W., Bremer, M. N., & Baker, K. 2005, MNRAS, 360, 748, doi: 10.1111/j.1365-2966.2005.09073.x

Jiang, D. T., Shu, D., & Sheng, W. 2007, in American Institute of Physics Conference Series, Vol. 879, Synchrotron Radiation Instrumentation, ed. J.-Y. Choi & S. Rah (AIP), 1022–1025, doi: 10.1063/1.2436236

Johnstone, R. M., Fabian, A. C., & Nulsen, P. E. J. 1987, MNRAS, 224, 75, doi: 10.1093/mnras/224.1.75

Jones, C., & Forman, W. 1984, ApJ, 276, 38, doi: 10.1086/161591

Kadam, S. K., Sonkamble, S. S., Pawar, P. K., & Patil, M. K. 2019, MNRAS, 484, 4113, doi: 10.1093/mnras/stz144

Kalberla, P. M. W., Burton, W. B., Hartmann, D., et al. 2005, A&A, 440, 775, doi: 10.1051/0004-6361:20041864

Kaneda, Y., Ishihara, T., Yokokawa, M., Itakura, K., & Uno, A. 2003, Physics of Fluids, 15, L21, doi: 10.1063/1.1539855

Kannan, R., Stinson, G. S., Macciò, A. V., et al. 2014, MNRAS, 437, 3529, doi: 10.1093/mnras/stt2144

Kilbourne, C. A., Adams, J. S., Arsenovic, P., et al. 2018, Journal of Astronomical Telescopes, Instruments, and Systems, 4, 011215, doi: 10.1117/1.JATIS.4.1.011215

King, I. 1962, AJ, 67, 471, doi: 10.1086/108756

Kirkpatrick, C. C., & McNamara, B. R. 2015, MNRAS, 452, 4361, doi: 10.1093/mnras/stv1574

Kochanek, C. S., White, M., Huchra, J., et al. 2003, ApJ, 585, 161, doi: 10.1086/345896

Kolmogorov, A. 1941, Akademiia Nauk SSSR Doklady, 30, 301

Kormendy, J., & Gebhardt, K. 2001, in American Institute of Physics Conference Series, Vol. 586, 20th Texas Symposium on relativistic astrophysics, ed. J. C. Wheeler & H. Martel (AIP), 363–381, doi: 10.1063/1.1419581

Kyadampure, A., Vagshette, N. D., & Patil, M. K. 2021, Serbian Astronomical Journal, 202, 17, doi: 10.2298/SAJ2102017K

Lahav, O., Edge, A. C., Fabian, A. C., & Putney, A. 1989, MNRAS, 238, 881, doi: 10.1093/mnras/238.3.881

Larson, R. B. 1981, MNRAS, 194, 809, doi: 10.1093/mnras/194.4.809

Lea, S. M., Silk, J., Kellogg, E., & Murray, S. 1973, ApJ, 184, L105, doi: 10.1086/181300

Leccardi, A., & Molendi, S. 2008, A&A, 486, 359, doi: 10.1051/0004-6361:200809538

Leutenegger, M. A. 2019, Calibration of the XRISM/Resolve instrument. https://iachec.org/wp-content/presentations/2019/sessionIII_Leutenegger.pdf

Li, Y., & Bryan, G. L. 2014, ApJ, 789, 54, doi: 10.1088/0004-637X/789/1/54

Li, Y., Bryan, G. L., Ruszkowski, M., et al. 2015, ApJ, 811, 73, doi: 10.1088/0004-637X/811/2/73

Li, Y., Gendron-Marsolais, M.-L., Zhuravleva, I., et al. 2020, ApJ, 889, L1, doi: 10.3847/2041-8213/ab65c7

Lim, J., Ohyama, Y., Yan, C.-H., Dinh-V-Trung, & Wang, S.-Y. 2012, ApJ, 744, 112, doi: 10.1088/0004-637X/744/2/112

Lin, Y. T., Mohr, J. J., & Stanford, S. A. 2003, ApJ, 591, 749, doi: 10.1086/375513

Liu, H., Fabian, A. C., Pinto, C., et al. 2021, MNRAS, 505, 1589, doi: 10.1093/mnras/stab1372

Liu, W., Sun, M., Nulsen, P. E. J., et al. 2020, MNRAS, 492, 3156, doi: 10.1093/mnras/staa005

Loewenstein, M., Zweibel, E. G., & Begelman, M. C. 1991, ApJ, 377, 392, doi: 10.1086/170369

Lovisari, L., & Reiprich, T. H. 2019, MNRAS, 483, 540, doi: 10.1093/mnras/sty3130

Lyutikov, M. 2006, MNRAS, 373, 73, doi: 10.1111/j.1365-2966.2006.10835.x

Main, R. A., McNamara, B. R., Nulsen, P. E. J., Russell, H. R., & Vantyghem, A. N. 2017, MNRAS, 464, 4360, doi: 10.1093/mnras/stw2644

Mantz, A. B., Allen, S. W., Morris, R. G., et al. 2017, MNRAS, 472, 2877, doi: 10.1093/mnras/stx2200

Markevitch, M. 1998, ApJ, 504, 27, doi: 10.1086/306080

Markevitch, M., & Vikhlinin, A. 2007, Phys. Rep., 443, 1, doi: 10.1016/j.physrep.2007.01.001

Markwardt, C. B. 2009, in Astronomical Society of the Pacific Conference Series, Vol. 411, Astronomical Data Analysis Software and Systems XVIII, ed. D. A. Bohlender, D. Durand, & P. Dowler, 251. https://arxiv.org/abs/0902.2850

Martin, C. L. 1999, ApJ, 513, 156, doi: 10.1086/306863

Martz, C. G. 2019, Master's thesis: X-ray astrophysics: The spoiler clusters and xrism synchrotron calibrations, University of Waterloo

Martz, C. G., McNamara, B. R., Nulsen, P. E. J., et al. 2020, ApJ, 897, 57, doi: 10.3847/1538-4357/ab96cd

McConnell, N. J., & Ma, C.-P. 2013, ApJ, 764, 184, doi: 10.1088/0004-637X/764/2/184

McCourt, M., Parrish, I. J., Sharma, P., & Quataert, E. 2011, MNRAS, 413, 1295, doi: 10.1111/j.1365-2966.2011.18216.x

McCourt, M., Sharma, P., Quataert, E., & Parrish, I. J. 2012, MNRAS, 419, 3319, doi: 10.1111/j.1365-2966.2011.19972.x

McDonald, M., Gaspari, M., McNamara, B. R., & Tremblay, G. R. 2018, ApJ, 858, 45, doi: 10.3847/1538-4357/aabace

McDonald, M., Veilleux, S., & Mushotzky, R. 2011, ApJ, 731, 33, doi: 10.1088/0004-637X/731/1/33

McDonald, M., Veilleux, S., & Rupke, D. S. N. 2012a, ApJ, 746, 153, doi: 10.1088/0004-637X/746/2/153

McDonald, M., Veilleux, S., Rupke, D. S. N., & Mushotzky, R. 2010, ApJ, 721, 1262, doi: 10.1088/0004-637X/721/2/1262

McDonald, M., Bayliss, M., Benson, B. A., et al. 2012b, Nature, 488, 349, doi: 10.1038/nature11379

McDonald, M., Benson, B. A., Vikhlinin, A., et al. 2013, ApJ, 774, 23, doi: 10.1088/0004-637X/774/1/23

McDonald, M., McNamara, B. R., Voit, G. M., et al. 2019, ApJ, 885, 63, doi: 10.3847/1538-4357/ab464c

McKee, C. F., & Ostriker, J. P. 1977, ApJ, 218, 148, doi: 10.1086/155667

McLaughlin, B. M., & Bell, K. L. 1998, Journal of Physics B Atomic Molecular Physics, 31, 4317, doi: 10.1088/0953-4075/31/19/017

McNamara, B. R., & Nulsen, P. E. J. 2007, ARA&A, 45, 117, doi: 10.1146/annurev.astro.45.051806.110625

—. 2012, New Journal of Physics, 14, 055023, doi: 10.1088/1367-2630/14/5/055023

McNamara, B. R., & O'Connell, R. W. 1989, AJ, 98, 2018, doi: 10.1086/115275

McNamara, B. R., Russell, H. R., Nulsen, P. E. J., et al. 2016, ApJ, 830, 79, doi: 10.3847/0004-637X/830/2/79

McNamara, B. R., Wise, M., Nulsen, P. E. J., et al. 2000, ApJ, 534, L135, doi: 10.1086/312662

McNamara, B. R., Rafferty, D. A., Bîrzan, L., et al. 2006, ApJ, 648, 164, doi: 10.1086/505859

McNamara, B. R., Russell, H. R., Nulsen, P. E. J., et al. 2014, ApJ, 785, 44, doi: 10.1088/0004-637X/785/1/44

Mernier, F., de Plaa, J., Pinto, C., et al. 2016, A&A, 595, A126, doi: 10.1051/0004-6361/201628765

Moe, M., Arav, N., Bautista, M. A., & Korista, K. T. 2009, ApJ, 706, 525, doi: 10.1088/0004-637X/706/1/525

Mohapatra, R., Jetti, M., Sharma, P., & Federrath, C. 2022, MNRAS, 510, 2327, doi: 10.1093/mnras/stab3429

Mohr, J. J., Mathiesen, B., & Evrard, A. E. 1999, ApJ, 517, 627, doi: 10.1086/307227

Molendi, S., & Pizzolato, F. 2001, ApJ, 560, 194, doi: 10.1086/322387

Morganti, R., Oosterloo, T., Oonk, J. B. R., Frieswijk, W., & Tadhunter, C. 2015, A&A, 580, A1, doi: 10.1051/0004-6361/201525860

Morganti, R., Tadhunter, C. N., & Oosterloo, T. A. 2005, A&A, 444, L9, doi: 10.1051/0004-6361:200500197

Morris, R. G., & Fabian, A. C. 2005, MNRAS, 358, 585, doi: 10.1111/j.1365-2966.2005.08822.x

Morrissey, P., Matuszewski, M., Martin, D. C., et al. 2018, ApJ, 864, 93, doi: 10.3847/1538-4357/aad597

Moster, B. P., Somerville, R. S., Maulbetsch, C., et al. 2010, ApJ, 710, 903, doi: 10.1088/0004-637X/710/2/903

Mukherjee, D., Bicknell, G. V., Wagner, A. Y., Sutherland, R. S., & Silk, J. 2018, MNRAS, 479, 5544, doi: 10.1093/mnras/sty1776

Murray, N., Chiang, J., Grossman, S. A., & Voit, G. M. 1995, ApJ, 451, 498, doi: 10.1086/176238

Nagai, D., Vikhlinin, A., & Kravtsov, A. V. 2007, ApJ, 655, 98, doi: 10.1086/509868

Nulsen, P., Jones, C., Forman, W., et al. 2009, in American Institute of Physics Conference Series, Vol. 1201, The Monster's Fiery Breath: Feedback in Galaxies, Groups, and Clusters, ed. S. Heinz & E. Wilcots (AIP), 198–201, doi: 10.1063/1.3293033

Nulsen, P. E. J. 1986, MNRAS, 221, 377, doi: 10.1093/mnras/221.2.377

Nulsen, P. E. J., & Fabian, A. C. 2000, MNRAS, 311, 346, doi: 10.1046/j.1365-8711.2000.03038.x

Nulsen, P. E. J., & McNamara, B. R. 2013, Astronomische Nachrichten, 334, 386, doi: 10.1002/asna.201211863

Nulsen, P. E. J., McNamara, B. R., Wise, M. W., & David, L. P. 2005, ApJ, 628, 629, doi: 10.1086/430845

O'Dea, C. P., Baum, S. A., Mack, J., Koekemoer, A. M., & Laor, A. 2004, ApJ, 612, 131, doi: 10.1086/422402

O'Dea, K. P., Quillen, A. C., O'Dea, C. P., et al. 2010, ApJ, 719, 1619, doi: 10.1088/0004-637X/719/2/1619

O'Dell, C. R., & Castaneda, H. O. 1987, ApJ, 317, 686, doi: 10.1086/165314

Oegerle, W. R., Cowie, L., Davidsen, A., et al. 2001, ApJ, 560, 187, doi: 10.1086/322246

Olivares, V., Salome, P., Combes, F., et al. 2019, A&A, 631, A22, doi: 10.1051/0004-6361/201935350

Olivares, V., Salomé, P., Hamer, S. L., et al. 2022, A&A, 666, A94, doi: 10.1051/0004-6361/202142475

Omiya, Y., Nakazawa, K., Matsushita, K., et al. 2023, PASJ, 75, 37, doi: 10.1093/pasj/psac087

Omma, H., Binney, J., Bryan, G., & Slyz, A. 2004, MNRAS, 348, 1105, doi: 10.1111/j.1365-2966.2004.07382.x

Oppenheimer, B. D., & Davé, R. 2006, MNRAS, 373, 1265, doi: 10.1111/j.1365-2966.2006.10989.x

—. 2008, MNRAS, 387, 577, doi: 10.1111/j.1365-2966.2008.13280.x

Osterbrock, D. E., & Ferland, G. J. 2006, Astrophysics of gaseous nebulae and active galactic nuclei

O'Sullivan, E., Giacintucci, S., Babul, A., et al. 2012, MNRAS, 424, 2971, doi: 10.1111/j.1365-2966.2012.21459.x

O'Sullivan, E., Combes, F., Salomé, P., et al. 2018, A&A, 618, A126, doi: 10.1051/0004-6361/201833580

Pandge, M. B., Sebastian, B., Seth, R., & Raychaudhury, S. 2021, MNRAS, 504, 1644, doi: 10.1093/mnras/stab384

Pandge, M. B., Sonkamble, S. S., Parekh, V., et al. 2019, ApJ, 870, 62, doi: 10.3847/1538-4357/aaf105

Pandge, M. B., Vagshette, N. D., Sonkamble, S. S., & Patil, M. K. 2013, Ap&SS, 345, 183, doi: 10.1007/s10509-013-1366-9

Paterno-Mahler, R., Blanton, E. L., Randall, S. W., & Clarke, T. E. 2013, ApJ, 773, 114, doi: 10.1088/0004-637X/773/2/114

Peacock, J. A. 1999, Cosmological Physics

Peebles, P. J. E. 1980, The large-scale structure of the universe

Pérez-Martínez, J. M., Ziegler, B., Dannerbauer, H., et al. 2021, A&A, 646, A53, doi: 10.1051/0004-6361/201936456

Peterson, J. R., & Fabian, A. C. 2006, Phys. Rep., 427, 1, doi: 10.1016/j.physrep.2005.12.007

Peterson, J. R., Paerels, F. B. S., Kaastra, J. S., et al. 2001, A&A, 365, L104, doi: 10.1051/0004-6361:20000021

Pfrommer, C. 2013, ApJ, 779, 10, doi: 10.1088/0004-637X/779/1/10

Pizzolato, F., & Soker, N. 2005, ApJ, 632, 821, doi: 10.1086/444344

—. 2006, MNRAS, 371, 1835, doi: 10.1111/j.1365-2966.2006.10803.x

—. 2010, MNRAS, 408, 961, doi: 10.1111/j.1365-2966.2010.17156.x

Planck Collaboration, Ade, P. A. R., Aghanim, N., et al. 2016, A&A, 594, A13, doi: 10.1051/0004-6361/201525830

Planck Collaboration, Aghanim, N., Akrami, Y., et al. 2020, A&A, 641, A6, doi: 10.1051/0004-6361/201833910

Popesso, P., Biviano, A., Bulbul, E., et al. 2024, MNRAS, 527, 895, doi: 10.1093/mnras/stad3253

Pradhan, A. K., Montenegro, M., Nahar, S. N., & Eissner, W. 2006, MNRAS, 366, L6, doi: 10.1111/j.1745-3933.2005.00119.x

Prasow-Émond, M., Hlavacek-Larrondo, J., Rhea, C. L., et al. 2020, AJ, 160, 103, doi: 10.3847/1538-3881/ab9ff3

Pratt, G. W., Croston, J. H., Arnaud, M., & Böhringer, H. 2009, A&A, 498, 361, doi: 10.1051/0004-6361/200810994

Proga, D., Stone, J. M., & Kallman, T. R. 2000, ApJ, 543, 686, doi: 10.1086/317154

Puccio, E., Todaro, M., Lo Cicero, U., et al. 2020, Journal of Astronomical Telescopes, Instruments, and Systems, 6, 038003, doi: 10.1117/1.JATIS.6.3.038003

Pulido, F. A., McNamara, B. R., Edge, A. C., et al. 2018, ApJ, 853, 177, doi: 10.3847/1538-4357/aaa54b

Qiu, Y., Bogdanović, T., Li, Y., McDonald, M., & McNamara, B. R. 2020, Nature Astronomy, 4, 900, doi: 10.1038/s41550-020-1090-7

Qiu, Y., McNamara, B. R., Bogdanović, T., Inayoshi, K., & Ho, L. C. 2021, ApJ, 923, 256, doi: 10.3847/1538-4357/ac2ede

Rafferty, D. A., McNamara, B. R., & Nulsen, P. E. J. 2008, ApJ, 687, 899, doi: 10.1086/591240

Rafferty, D. A., McNamara, B. R., Nulsen, P. E. J., & Wise, M. W. 2006, ApJ, 652, 216, doi: 10.1086/507672

Raiteri, C. M., Villata, M., & Navarro, J. F. 1996, A&A, 315, 105

Randall, S. W., Forman, W. R., Giacintucci, S., et al. 2011, ApJ, 726, 86, doi: 10.1088/0004-637X/726/2/86

Remijan, A., Biggs, A., Cortes, P. A., et al. 2019, ALMA Technical Handbook,ALMA Doc. 7.3, ver. 1.1, 2019, ALMA Technical Handbook,ALMA Doc. 7.3, ver. 1.1ISBN 978-3-923524-66-2, doi: 10.5281/zenodo.4511522

Reynolds, C. S., McKernan, B., Fabian, A. C., Stone, J. M., & Vernaleo, J. C. 2005, MNRAS, 357, 242, doi: 10.1111/j.1365-2966.2005.08643.x

Rigby, E. E., Best, P. N., Brookes, M. H., et al. 2011, MNRAS, 416, 1900, doi: 10.1111/j.1365-2966.2011.19167.x

Roediger, E., Brüggen, M., Simionescu, A., et al. 2011, MNRAS, 413, 2057, doi: 10.1111/j.1365-2966.2011.18279.x

Romero, C. 2024, arXiv e-prints, arXiv:2405.06489, doi: 10.48550/arXiv.2405.06489

Rupke, D. S. N., & Veilleux, S. 2011, ApJ, 729, L27, doi: 10.1088/2041-8205/729/2/L27

Russell, H. R., Fabian, A. C., Sanders, J. S., et al. 2010, MNRAS, 402, 1561, doi: 10.1111/j.1365-2966.2009.16027.x

Russell, H. R., Sanders, J. S., & Fabian, A. C. 2008, MNRAS, 390, 1207, doi: 10.1111/j.1365-2966.2008.13823.x

Russell, H. R., McNamara, B. R., Edge, A. C., et al. 2014, ApJ, 784, 78, doi: 10.1088/0004-637X/784/1/78

Russell, H. R., McNamara, B. R., Fabian, A. C., et al. 2016, MNRAS, 458, 3134, doi: 10.1093/mnras/stw409

—. 2017, MNRAS, 472, 4024, doi: 10.1093/mnras/stx2255

—. 2019, MNRAS, 490, 3025, doi: 10.1093/mnras/stz2719

Russell, H. R., Nulsen, P. E. J., Caprioli, D., et al. 2022, MNRAS, 514, 1477, doi: 10.1093/mnras/stac1055

Ruszkowski, M., Brüggen, M., & Begelman, M. C. 2004, ApJ, 611, 158, doi: 10.1086/422158

Ruszkowski, M., Enßlin, T. A., Brüggen, M., Heinz, S., & Pfrommer, C. 2007, MNRAS, 378, 662, doi: 10.1111/j.1365-2966.2007.11801.x

Ruszkowski, M., & Pfrommer, C. 2023, A&A Rev., 31, 4, doi: 10.1007/s00159-023-00149-2

Salomé, P., & Combes, F. 2003, A&A, 412, 657, doi: 10.1051/0004-6361:20031438

—. 2004, A&A, 415, L1, doi: 10.1051/0004-6361:20031744

Salomé, P., Combes, F., Revaz, Y., et al. 2008, A&A, 484, 317, doi: 10.1051/0004-6361:200809493

Salomé, P., Combes, F., Edge, A. C., et al. 2006, A&A, 454, 437, doi: 10.1051/0004-6361:20054745

Sanders, J. S., & Fabian, A. C. 2007, MNRAS, 381, 1381, doi: 10.1111/j.1365-2966.2007.12347.x

Sanders, J. S., Fabian, A. C., Hlavacek-Larrondo, J., et al. 2014, MNRAS, 444, 1497, doi: 10.1093/mnras/stu1543

Sanders, J. S., Fabian, A. C., Taylor, G. B., et al. 2016, MNRAS, 457, 82, doi: 10.1093/mnras/stv2972

Sarazin, C. L. 1988, X-ray emission from clusters of galaxies

Sarazin, C. L., O'Connell, R. W., & McNamara, B. R. 1992, ApJ, 389, L59, doi: 10.1086/186348

Sazonov, S. Y., Ostriker, J. P., Ciotti, L., & Sunyaev, R. A. 2005, MNRAS, 358, 168, doi: 10.1111/j.1365-2966.2005.08763.x

Scheuer, P. A. G. 1974, MNRAS, 166, 513, doi: 10.1093/mnras/166.3.513

Shen, X., L.O.Dallin, Silzer, R. M., T.Summers, & de Jong, M. S. 2008. https://api.semanticscholar.org/CorpusID:114238265

Shirron, P. J., Kimball, M. O., James, B. L., et al. 2016, in Society of Photo-Optical Instrumentation Engineers (SPIE) Conference Series, Vol. 9905, Space Telescopes and Instrumentation 2016: Ultraviolet to Gamma Ray, ed. J.-W. A. den Herder, T. Takahashi, & M. Bautz, 99053O, doi: 10.1117/12.2231301

Siemiginowska, A., Burke, D. J., Aldcroft, T. L., et al. 2010, ApJ, 722, 102, doi: 10.1088/0004-637X/722/1/102

Siemiginowska, A., Cheung, C. C., LaMassa, S., et al. 2005, ApJ, 632, 110, doi: 10.1086/432871

Snios, B., Nulsen, P. E. J., Wise, M. W., et al. 2018, ApJ, 855, 71, doi: 10.3847/1538-4357/aaaf1a

Soker, N., Blanton, E. L., & Sarazin, C. L. 2002, ApJ, 573, 533, doi: 10.1086/340799

Sonkamble, S. S., Vagshette, N. D., Pawar, P. K., & Patil, M. K. 2015, Ap&SS, 359, 21, doi: 10.1007/s10509-015-2508-z

Spitzer, L. 1962, Physics of Fully Ionized Gases

Springel, V. 2005, MNRAS, 364, 1105, doi: 10.1111/j.1365-2966.2005.09655.x

Springel, V., Frenk, C. S., & White, S. D. M. 2006, Nature, 440, 1137, doi: 10.1038/nature04805

Squire, J., Schekochihin, A. A., Quataert, E., & Kunz, M. W. 2019, Journal of Plasma Physics, 85, 905850114, doi: 10.1017/S0022377819000114

Sreenivasan, K. R. 1995, Physics of Fluids, 7, 2778, doi: 10.1063/1.868656

Sternberg, A., & Soker, N. 2009, MNRAS, 395, 228, doi: 10.1111/j.1365-2966.2009.14566.x

Stewart, G. C., Fabian, A. C., Jones, C., & Forman, W. 1984, ApJ, 285, 1, doi: 10.1086/162470

Strickland, D. K., & Heckman, T. M. 2009, ApJ, 697, 2030, doi: 10.1088/0004-637X/697/2/2030

Su, K.-Y., Hopkins, P. F., Bryan, G. L., et al. 2021, MNRAS, 507, 175, doi: 10.1093/mnras/stab2021

Sutherland, R. S., & Dopita, M. A. 1993, ApJS, 88, 253, doi: 10.1086/191823

Tamhane, P. D., McNamara, B. R., Russell, H. R., et al. 2022, MNRAS, 516, 861, doi: 10.1093/mnras/stac2168

Tamura, T., Kaastra, J. S., Peterson, J. R., et al. 2001, A&A, 365, L87, doi: 10.1051/0004-6361:20000038

Taylor, G. B., Barton, E. J., & Ge, J. 1994, AJ, 107, 1942, doi: 10.1086/117006

Tennekes, H., & Lumley, J. L. 1972, First Course in Turbulence

Tinker, J., Kravtsov, A. V., Klypin, A., et al. 2008, ApJ, 688, 709, doi: 10.1086/591439

Tombesi, F., Cappi, M., Reeves, J. N., & Braito, V. 2012, MNRAS, 422, L1, doi: 10.1111/j.1745-3933.2012.01221.x

Tremaine, S., Gebhardt, K., Bender, R., et al. 2002, ApJ, 574, 740, doi: 10.1086/341002

Ueda, Y., Akiyama, M., Ohta, K., & Miyaji, T. 2003, ApJ, 598, 886, doi: 10.1086/378940

Vagshette, N. D., Naik, S., & Patil, M. K. 2019, MNRAS, 485, 1981, doi: 10.1093/mnras/stz476

Vagshette, N. D., Naik, S., Patil, M. K., & Sonkamble, S. S. 2017, MNRAS, 466, 2054, doi: 10.1093/mnras/stw3227

van Dokkum, P. G., Whitaker, K. E., Brammer, G., et al. 2010, ApJ, 709, 1018, doi: 10.1088/0004-637X/709/2/1018

Vantyghem, A. N., McNamara, B. R., Russell, H. R., et al. 2016, ApJ, 832, 148, doi: 10.3847/0004-637X/832/2/148

—. 2019, ApJ, 870, 57, doi: 10.3847/1538-4357/aaf1b4

Veilleux, S., Cecil, G., & Bland-Hawthorn, J. 2005, ARA&A, 43, 769, doi: 10.1146/annurev.astro.43.072103.150610

Vernaleo, J. C., & Reynolds, C. S. 2006, ApJ, 645, 83, doi: 10.1086/504029

Vikhlinin, A., Markevitch, M., Murray, S. S., et al. 2005, ApJ, 628, 655, doi: 10.1086/431142

Voigt, L. M., & Fabian, A. C. 2004, MNRAS, 347, 1130, doi: 10.1111/j.1365-2966.2004.07285.x

Voit, G. M. 2005, Reviews of Modern Physics, 77, 207, doi: 10.1103/RevModPhys.77.207

—. 2018, ApJ, 868, 102, doi: 10.3847/1538-4357/aae8e2

—. 2021, ApJ, 908, L16, doi: 10.3847/2041-8213/abe11f

Voit, G. M., & Donahue, M. 2005, ApJ, 634, 955, doi: 10.1086/497063

—. 2015, ApJ, 799, L1, doi: 10.1088/2041-8205/799/1/L1

Voit, G. M., Meece, G., Li, Y., et al. 2017, ApJ, 845, 80, doi: 10.3847/1538-4357/aa7d04

von Hoerner, S. 1951, ZAp, 30, 17

Walker, S. A., Sanders, J. S., & Fabian, A. C. 2018, MNRAS, 481, 1718, doi: 10.1093/mnras/sty2390

Wang, C., Ruszkowski, M., Pfrommer, C., Oh, S. P., & Yang, H. Y. K. 2021, MNRAS, 504, 898, doi: 10.1093/mnras/stab966

White, D. A., Jones, C., & Forman, W. 1997, MNRAS, 292, 419, doi: 10.1093/mnras/292.2.419

Wibking, B. D., Voit, G. M., & O'Shea, B. W. 2025, MNRAS, 537, 739, doi: 10.1093/mnras/staf092

Wilman, R. J., Edge, A. C., & Swinbank, A. M. 2006, MNRAS, 371, 93, doi: 10.1111/j.1365-2966.2006.10658.x

Wolf, C., Lai, S., Onken, C. A., et al. 2024, Nature Astronomy, 8, 520, doi: 10.1038/s41550-024-02195-x

XRISM Collaboration. 2025, arXiv e-prints, arXiv:2501.05514, doi: 10.48550/arXiv.2501.05514

XRISM Collaboration, Audard, M., Awaki, H., et al. 2024, PASJ, 76, 1186, doi: 10.1093/pasj/psae080

Xu, S. 2020, MNRAS, 492, 1044, doi: 10.1093/mnras/stz3092

Zakamska, N. L., & Narayan, R. 2003, ApJ, 582, 162, doi: 10.1086/344641

Zhang, C., Churazov, E., & Schekochihin, A. A. 2018, MNRAS, 478, 4785, doi: 10.1093/mnras/sty1269

Zhang, C., Zhuravleva, I., Gendron-Marsolais, M.-L., et al. 2022, MNRAS, 517, 616, doi: 10.1093/mnras/stac2282

Zhuravleva, I., Allen, S. W., Mantz, A., & Werner, N. 2018, ApJ, 865, 53, doi: 10.3847/1538-4357/aadae3

Zhuravleva, I., Chen, M. C., Churazov, E., et al. 2023, MNRAS, 520, 5157, doi: 10.1093/mnras/stad470

Zhuravleva, I., Churazov, E., Schekochihin, A. A., et al. 2014a, Nature, 515, 85, doi: 10.1038/nature13830

Zhuravleva, I., Churazov, E. M., Schekochihin, A. A., et al. 2014b, ApJ, 788, L13, doi: 10.1088/2041-8205/788/1/L13

Zhuravleva, I., Churazov, E., Arévalo, P., et al. 2015, MNRAS, 450, 4184, doi: 10.1093/mnras/stv900

—. 2016, MNRAS, 458, 2902, doi: 10.1093/mnras/stw520

ZuHone, J., Markevitch, M., & Brunetti, G. 2011a, Mem. Soc. Astron. Italiana, 82, 632, doi: 10.48550/arXiv.1101.4627

ZuHone, J. A., Markevitch, M., & Johnson, R. E. 2010, ApJ, 717, 908, doi: 10.1088/0004-637X/717/2/908

ZuHone, J. A., Markevitch, M., & Lee, D. 2011b, ApJ, 743, 16, doi: 10.1088/0004-637X/743/1/16

ZuHone, J. A., Markevitch, M., & Zhuravleva, I. 2016, ApJ, 817, 110, doi: 10.3847/0004-637X/817/2/110

APPENDICES

Appendix A

Gas perturbations in Abell 2146

In the study by (Russell et al., 2022), a deep 2 Ms Chandra observation of the galaxy cluster Abell 2146 is presented, providing significant insights into the structure of merger shocks in clusters. Abell 2146 is observed to host two massive merger shock fronts, each with a Mach number of ~ 2 and spanning roughly 500 kpc, making them some of the largest known shock fronts in clusters. For the first time, the widths of these shock fronts are resolved: the bow shock has a measured width of 17 ± 1 kpc, while the upstream shock is narrower, at 10.7 ± 0.3 kpc. These measurements align with expectations for collisionless shocks. The observed width indicates minimal collisional broadening, suggesting that plasma-wave interactions and turbulent gas motions dominate the dynamics at these scales.

The gas motion velocities around both shock fronts were determined to be 290 ± 30 km s^{-1} by examining the blurring effect of turbulent gas motions on the observed shock width using the measured electron density profiles. The results indicate that the electron heating in Abell 2146 is primarily due to adiabatic compression with minimal non-adiabatic electron heating, consistent with collisional equilibration models. This finding supports the view that collisionless shocks in high-beta cluster environments largely dissipate kinetic energy through adiabatic processes rather than through additional electron heating mechanisms, aligning with results from solar wind and supernova remnant shock studies.

In my work, which also relies on the deep Chandra X-ray observations of Abell 2146 detailed by (Russell et al., 2022), we apply SB fluctuation analysis to quantify the turbulence levels around the two shock fronts. This method enables a detailed examination of the turbulent structure within the ICM surrounding these shocks, refining our understanding of gas dynamics in this merging cluster environment.

We measure gas density fluctuations in the ICM to assess the local turbulence around

each shock front and further derive gas motion velocities. This derivation uses the linear relationship between density fluctuations and the one-component velocity amplitude of gas motions, providing an indirect measure of the turbulent gas dynamics associated with the shocks. The methodology is described comprehensively in Section 2 of this thesis. Through this analysis, we aim to gain a clearer insight into the role that shocks play in triggering gas motions and driving energy dissipation within merging galaxy clusters. This enhances our knowledge of the thermodynamic and dynamical states of the ICM, thereby contributing to our understanding of high-energy processes in astrophysical environments.

A.1 Data Reduction

The Chandra observation of the cluster merger Abell 2146 has an exposure time of 1.93 Ms split over 67 separate observations on the ACIS-I detector between June 2018 and August 2019. Combined with the earlier ACIS-I observations taken in 2010 (Russell et al., 2022), the total exposure is 2.31 Ms. All observations are reprocessed following the standard algorithm described by Vikhlinin et al. (2005) and were reduced with CIAO version 4.12 using the calibration CALDB version 4.9.2. Using the `lc_clean` script, light curves extracted from level-2 events above 10 keV were carefully cleaned to remove any intervals affected by background flares. Background counts, estimated from the on-chip region, were subtracted from the raw images. The exposure maps, calculated in the same energy band, were used to correct for non-uniform exposures and gaps in the observations. Multiple observations are reprojected to the one with the longest exposure time and are combined into a summed background-subtracted exposure-corrected image used to identify point source candidates using the `wavdetect` tool. Each identified point source is visually inspected in DS9 before being removed. Accounting for the combined PSF shape, the point sources and the central AGN are excised from subsequent analysis using the procedure.

The reprocessed Chandra X-ray images of Abell 2146 in the 0.5 - 4 keV band are presented in Figure A.1. The bow shock front and the upstream shock front are clearly visible, located SE approximately 150 kpc ahead of the subcluster core and at the far northwest edge of the primary cluster, respectively.

We removed the large-scale SB gradient by dividing the raw images by the best-fitting $\beta-$models to analyze gas perturbations relative to the smooth 'unperturbed' background. Although a single $\beta-$model is a reasonable choice of the underlying 'unperturbed' profile for relaxed clusters, it may poorly fit SB profiles due to its oversimplification. Figure A.2 shows the SB profiles we extracted from the region near bow shock (left) and upstream shock (right). We compare them with the SB profiles within the sector from $225 - 260°$

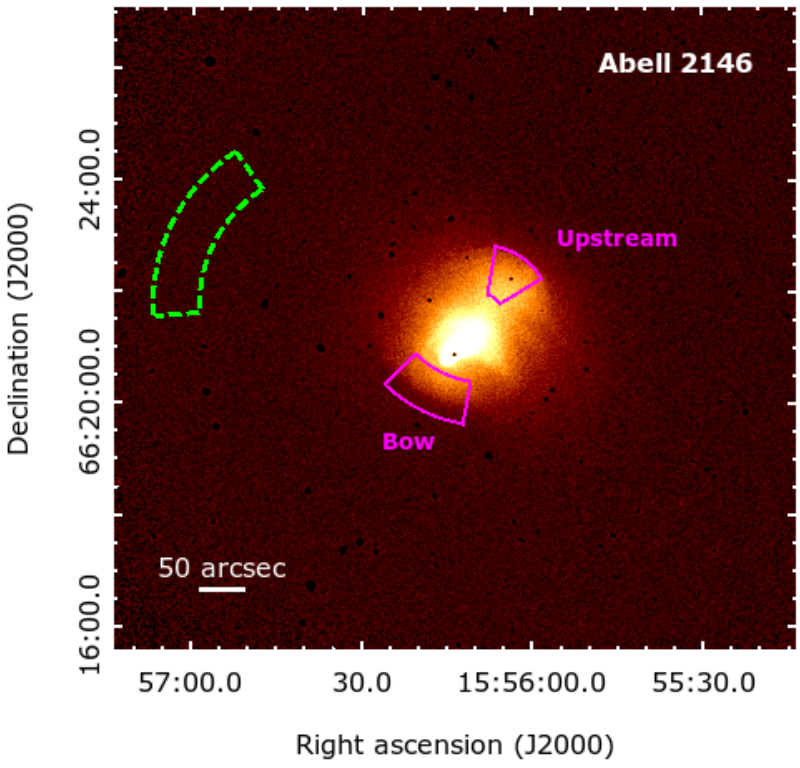


Figure A.1: Background-subtracted exposure-corrected Chandra image of Abell 2146 in $0.5 - 4$ keV. The background has been estimated and subtracted with the flux of the on-chip blank region (green dashed region). The magenta regions show the bow shock and upstream shock we analyzed in this work. The image is smoothed by 3" for display. The bright point sources and central AGN are masked out.

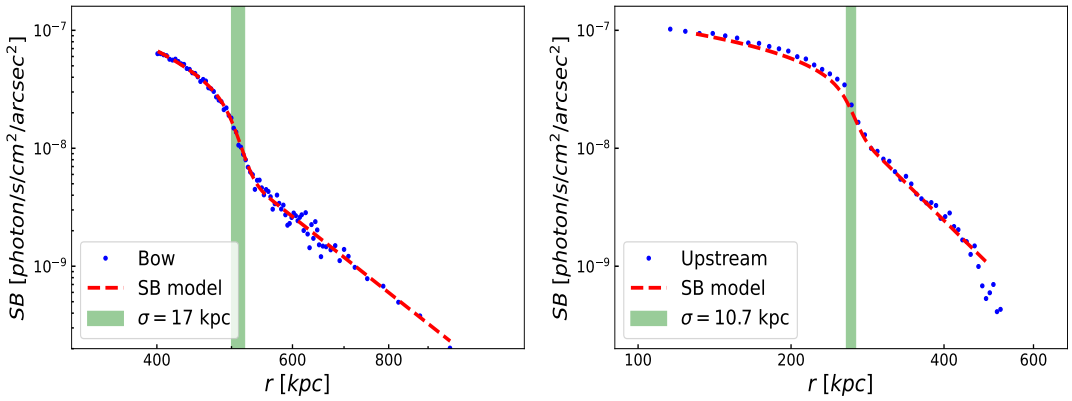


Figure A.2: The surface brightness profiles extracted from a $225 - 260°$ sector across the bow shock (left) and a $55 - 80°$ sector across the upstream shock (right) in the $0.5 - 4$ keV band. The dashed red lines indicate the surface brightness profiles measured by Russell et al. (2022). The vertical green bands represent the location and width of each shock front, measured to be 17 ± 1 kpc for the bow shock and 10.7 ± 0.3 kpc for the upstream shock.

at the bow shock and from $55 - 80°$ at the upstream shock measured by (Russell et al., 2022), respectively. These two profiles are consistent with each other at each radius.

A.2 Results

This section presents the analysis results from the Chandra X-ray observations, focusing on the power spectra of density fluctuations and the derived gas motion velocities in Abell 2146. The power spectra of surface brightness fluctuations between $0.5 - 4$ keV are measured, and then the amplitudes of density fluctuations as a function of wavenumber k are obtained after 2D-to-3D deprojection. Figure A.3 displays the amplitude of density fluctuations near the bow shock (left) and the upstream shock (right) of Abell 2146. The dotted lines represent the average amplitude across different spatial scales, with the shaded regions indicating 1σ statistical uncertainties. Only scales minimally affected by Poisson noise are included.

The smallest measurable scale reaches approximately 71 kpc at the bow shock and 46 kpc at the upstream shock. The results are summarized in Table A.1. The typical

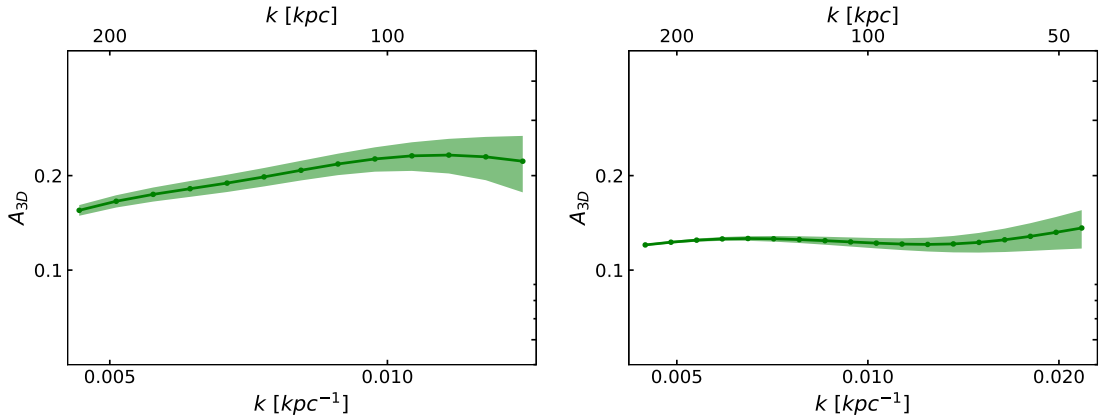


Figure A.3: The amplitudes of density fluctuations near the bow shock (left) and the upstream shock (right) in Abell 2146. The dotted line is the average amplitude of density fluctuations at each spatial scale. The width of regions shows 1σ uncertainties. Only scales on which the amplitudes are least affected by Poisson noise are shown here.

amplitude of density fluctuations ρ_0/ρ at the bow shock is $\sim 22\%$ on ~ 60 kpc scale, and it is higher than that at upstream shock ($< 15\%$ over the entire range of probed scales). This indicates that the perturbations are stronger at the bow shock region, in agreement with the sharper SB and density jump of the bow shock.

Using the measured power spectrum of density fluctuations, the amplitude of the one-component velocity of gas motion can be derived on each spatial scale $l = 1/k$. Zhuravleva et al. (2014b) have argued that a linear relation exists (see equation(2.9) between the power spectra of gas density fluctuations and the velocity spectra in relaxed clusters across a wide range of scale. Figure A.4 shows the indirectly measured one-component velocity power spectra at bow shock (left) and upstream shock (right), respectively. The red dashed line shows the turbulent velocities estimated with the mean temperature and the mean amplitude of density fluctuations at the shocks. The width of regions reflects 1σ statistical uncertainties and the temperature variance across the shock areas. The green hatched region shows the turbulent velocity σ_t derived from the shock widths using:

$$\Delta R = \sqrt{Rl}\ (\sigma_t/v_s), \tag{A.1}$$

where ΔR is the RMS radial displacements in the shock front, v_s is the shock velocity, and the coherence length l is typical $\sim 0.1R$ the shock radius. The turbulent velocities are similar ahead of both shock fronts, $\sigma_{\rm turb} \sim 290 \pm 30$ km s^{-1} derived by (Russell et al., 2022). For a bow shock radius R ~ 500 kpc, width $\sigma \sim 20$ kpc and bow shock velocity

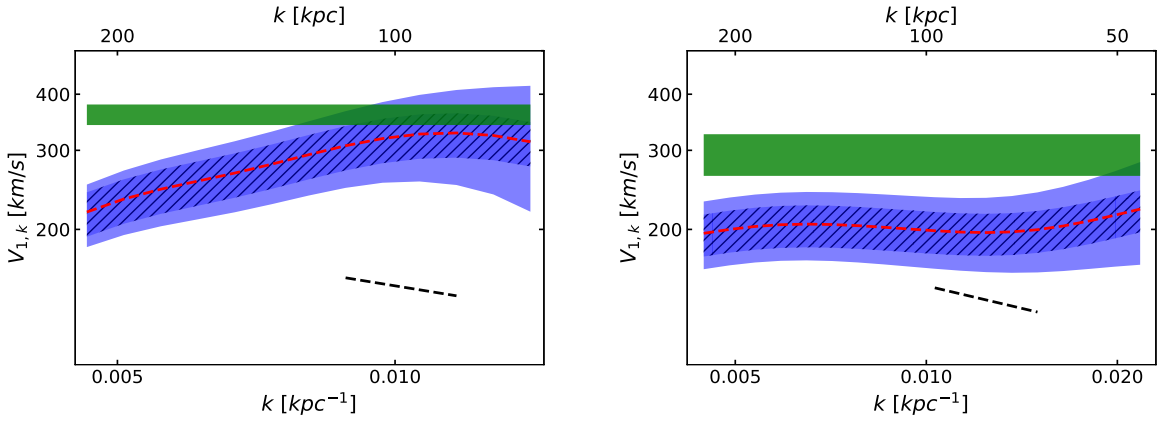


Figure A.4: The amplitude of one-component velocity of gas motions versus wavenumber at the bow shock (left) and the upstream shock (right). The red dashed line presents the velocities calculated from the mean density fluctuations and the mean temperature across the shocks. The solid blue regions represented velocity amplitudes when maximum and minimum temperatures were used. Black Dashed lines show the Kolmogorov slope $-1/3$. The green hatched region shows the turbulent velocity derived from the shock widths, which are 355^{+25}_{13} km s^{-1} and 290^{+30}_{-30} km s^{-1} at bow shock and at the upstream shock, respectively.

$v_{sh} = 2800^{+200}_{-100}$ km s^{-1}, we estimate $\sigma_{\rm turb} \sim 355^{+25}_{13}$ km s^{-1} at bow shock, which is higher than value given in Russell et al. (2022). The turbulent velocity at the upstream shock is estimated to be $\sim 290^{+30}_{-30}$ km s^{-1} by using upstream shock radius R $\sim$ 270 kpc, width $\sigma \sim 10.7$ kpc and upstream shock velocity $v_{sh} = 2300^{+300}_{-200}$ km s^{-1}.

Our indirectly derived gas turbulent velocities for the bow shock are 219^{+33}_{-36} km s^{-1} on scales of $\sim$ 216 kpc to 313^{+104}_{-94} km s^{-1} on scales of $\sim$ 71 kpc. The velocities measured at upstream shock lie below the measurements at bow shock on the same scales, varying from 196^{+35}_{-33} km s^{-1} on scales of $\sim$ 224 kpc to 222^{+61}_{-55} km s^{-1} on scales of $\sim$ 46 kpc with significant scatter. In Figure A.4, we can see that our results at the large-scale end agree with the turbulent RMS velocity derived from the shock width in the bow shock region within the uncertainties. However, the measured velocities on the range of scales we can probe are lower than the estimation given by (Russell et al., 2022).

Region	Scales	T_{pre}	T_{post}	$V_{1,k}(l_{max})$	$V_{1,k}(l_{min})$	$\frac{\delta\rho}{\rho_0}$
	kpc	keV	keV	km s^{-1}	km s^{-1}	per
(a)	(b)	(c)	(d)	(e)	(f)	(g)
Bow shock	71∼216	$5.9^{+0.8}_{-0.4}$	$9.3^{+0.2}_{-0.2}$	219^{+33}_{-36}	313^{+104}_{-94}	$15.5 \sim 22.2$
Upstream shock	46∼224	8^{+2}_{-1}	$12.3^{+1.7}_{-1}$	196^{+35}_{-33}	222^{+61}_{-55}	$12.0 \sim 13.6$

Table A.1: Summary of the measurements on the gas perturbations in Abell 2146: (a). Region, (b). Spatial scales least affected by Poisson noise, (c). Pre-shock temperature, (d). Post-shock temperature, (e). One-component turbulent velocity on the smallest probed scale, (f). $V_{1,k}$ on the largest probed scale, (g). the amplitude of density fluctuations

A.3 Conclusion

In this analysis, we examined gas perturbations near the bow shock and upstream regions in Abell 2146. The turbulent velocity spectra of gas motions were derived from the amplitude of gas density fluctuations, as indicated by the power spectra of X-ray surface brightness fluctuations. These velocities were compared with those estimated from the shock widths. Our principal conclusions are:

- The amplitudes of density fluctuations range from 15 to 22 per cent on scales of 71 to 216 kpc and from 12 to 14 per cent on scales of 46 to 224 kpc at the bow shock and upstream shock, respectively. The relatively high density fluctuation in the bow shock region correlates with its pronounced density and surface brightness jumps.

- The one-component turbulent velocities measured at the bow shock are 219^{+33}_{-36} km s^{-1} on scales of ∼216 kpc to 313^{+104}_{-94} km s^{-1} on scales of ∼71 kpc. At the upstream shock, the turbulent velocities vary from 196^{+35}_{-33} km s^{-1} on scales of ∼224 kpc to 222^{+61}_{-55} km s^{-1} on scales of ∼46 kpc, showing significant scatter. These typical velocity amplitudes align with the expected gas turbulent velocities measured directly in Perseus core by Hitomi (Hitomi Collaboration et al., 2016).

- Within the uncertainties, our results at the bow shock are consistent with the gas turbulent velocities derived from the shock width measurements. However, the velocity amplitudes at the upstream shock fall below 300 km s^{-1}, lower than the estimates provided by (Russell et al., 2022).

- Although the single $\beta-$model provides a convenient framework for reconstructing the density profile, it may inadequately describe SB discontinuities across shock regions. This oversimplification can lead to overestimation of gas perturbations on large spatial scales.